Electromagnetic measurements of steel phase transformations

Sherri Johnstone

ELECTROMAGNETIC MEASUREMENTS OF STEEL PHASE TRANSFORMATIONS

By

Sherri Johnstone B. Sc.

A Thesis submitted in partial fulfillment
of the requirements for the degree of Ph. D

School of Engineering
University of Durham
2002

Acknowledgements

I would like to thank Dr AJ Peyton from Lancaster University for agreeing to supervise my studies and supporting my transfer to Durham University.
I would also like to thank Dr WDN Pritchard for his industrial supervision and support and of course Corus for providing funding and facilities.

Finally, I would like to thank Prof MC Petty for supervising my studies at Durham.

DECLARATION

I hereby declare that the work carried out in this thesis has not been previously submitted for any degree and is not currently being submitted in candidature for any other degree.

Signed.....
Candidate

The work in this thesis was carried out by the candidate

Signed.....
Director of Studies

Signed.....
Candidate

ABSTRACT

This thesis describes the development of electromagnetic sensors to measure the phase transformation in steel as it cools from the hot austenite phase to colder ferritic based phases. The work initially involved investigating a variety of sensing configurations including ac excited coils, C-core arrangements and the adaptation of commercial eddy current proximity sensors. Finally, two prototype designs were built and tested on a hot strip mill.

The first of these, the T-meter was based on a C-shaped permanent magnet with a Gaussmeter measuring the magnetic field at the pole ends. Laboratory tests indicated that it could reliably detect the onset of transformation. However, the sensor was sensitive to both the steel properties and the position of the steel. To overcome this, an eddy current sensor was incorporated into the final measurement head. The instrument gave results which were consistent with material property variations, provided the lift-off variations were below 3Hz. The results indicated that for a grade 1916 carbon-manganese steel, the signal variation was reduced from 37% to 2%, and the resulting output was related to the steel property variations.

The second of these prototypes was based on a dc electromagnetic E-core, with Hall probes in each of the three poles. 'Cold' calibration tests were used to decouple the steel and the lift-off. The results indicated that there was an error of 3-4% ferrite/mm at high ferrite fractions. At lower fractions the error was higher due to the instrument's insensitivity to lift-off. The resulting output again showed a relationship with varying steel strip properties.

It was also shown that a finite element model could be calibrated to experimental results for a simple C-core geometry such that the output was sensitive to 0.2% of the range. This is required to simulate the sensor to resolve to 10% ferrite.

CONTENTS

Nomenclature

Symbol	Quantity	Units
A	Magnetic vector potential	Wbm^{-2}
B	Magnetic flux density	T
D	Electric flux density	Cm^{-2}
emf	Electromotive force	V
E	Electric field intensity	Vm^{-1}
F	Force	N
F_T	Fraction transformed	%
H	Magnetic field intensity	Am^{-1}
I	DC current	A
Idl	Current element	A.m
J_p	Magnetic polarisation	T
J	Volume current density	Am^{-2}
J_D	Displacement current density	Am^{-2}
J_s	Surface current density	Am^{-1}
L	Displacement	m
dl	Line element	m
mmf	Magnetomotive force	A
M	Magnetisation	Am^{-1}
m	Magnetic dipole moment	Wb.m
N	Number per unit volume	m^{-3}
P	Pole strength	A.m
Q	Point charge	C
Q	Charge	C
R	Radial distance	m
r	Distance	m
S	Area	m^2
T	Temperature	°C
dS	Area element	m^2
U	Magnetic scalar potential	A
u	General scalar potential	$J^{1/2}$

V	Electric scalar potential	V
W	Energy	J
X	Lift-off (distance)	M
α	Attenuation coefficient	m^{-1}
δ	Skin depth	m
ε	Permittivity	Fm^{-1}
ψ	Susceptibility	-
ϕ	Magnetic flux	Wb
Φ	Phase angle	rad
μ	Permeability	Hm^{-1}
ρ	Charge density	Cm^{-3}
σ	Conductivity	S
$d\tau$	Volume element	m^3
ω	Angular frequency	$rads^{-1}$

Notation

Symbol	**Description**
$\underline{a}_{direction}$	A unit vector
F	Magnitude of a vector
$\underline{F}$	A vector
F'	A scalar phasor field
$\underline{\underline{F}}$	A vector phasor field
$\overline{F}$	Fourier transform of a scalar phasor field

CHAPTER 1

INTRODUCTION

The steel industry is highly competitive, leading to increasing customer expectations. For the steel manufacturer this leads to the need to produce higher quality products whilst at the same time reducing costs. It is well known that the mechanical properties can be tuned by controlling the cooling rate of hot rolled steel. Thus, if the steel properties could be reliably measured during the cooling period, a cost effective solution to improving the mechanical properties of the products can be implemented relatively easily. The work presented in this thesis describes the research undertaken in developing an instrument to measure the material properties of steel, as it cools from the hot austenite phase to ferrite type phases. In particular, the aim is to be able to measure the percentage ferrite present in steel strip in a hot strip mill, while it undergoes a controlled cooling program. This can then be related to the microstructure, and hence the final mechanical properties of the steel product.

In chapter 2, the steel making process is described. From this, it can be seen how hot strip rolling fits into the manufacturing process. It also presents other manufacturing methods and products, to which the instrument could also be applied. These include the cooling of continuously cast slabs, universal beams, wire and the annealing of cold rolled strip. In chapter 3 a review of electromagnetic measurement and control methods in the rolling and finishing areas is presented. This is to identify existing electromagnetic technologies and to ensure the research in this project is novel. To complete the survey, non-electromagnetic on-line phase transformation measurement methods are included, since these would be needed to aid in assessing any instrument developed. The theory of magnetism and phase transformation in steel is described in chapter 4. There are various texts on either the theory of magnetism or metallurgy, but there is limited research in relating the magnetic properties of steel during the process of phase transformation. During the development of the instrument this was investigated by comparing its output with other measurement techniques such as dilatometry and optical microscopy.

Several instrument prototypes were developed based on inductive and magnetic type measurements. To aid with the design process finite element modeling was used. Thus a chapter is included which covers electromagnetic theory for both magnetostatic and eddy current systems. Since the geometries of the transformation meters do not lend themselves easily to analytical solutions, a section on numerical methods including finite element analysis is included. The remaining chapters describe the research undertaken in developing phase transformation detectors.

The initial investigation focuses on different types of sensors and geometries to test the underlying principle that the permeability of steel can be related to the fraction of ferrite. A selection of both hot and cold tests are presented in chapter 6. Experiments to research permanent magnet (ferrite and alcomax III) type designs are then described in chapters 7 and 8, concluding with plant trials on a hot strip mill. To put this work into context, a second design based on a E-core electromagnet is described in chapter 9, together with calibration / verification methods. The final piece of work to be recorded in chapter 10, is that of the use of finite element analysis to calibrate magnetic sensors in general.

The measurement principles researched in this thesis were filed on November 2, 2001, with the European Patent office.

CHAPTER 2

THE STEELMAKING PROCESS

2.1 Overview

The steelmaking process involves several stages. Because of this, it is produced in large quantities to reduce costs, eg the Teesside Blast furnace produced 10,000 tonnes per day in 1999. This means that large plants with high capital costs are required. To remain competitive, steel producers have over the last few decades considerably reduced their labour forces in favour of automated systems. Due to the hazardous nature of some processes, this has been challenging.

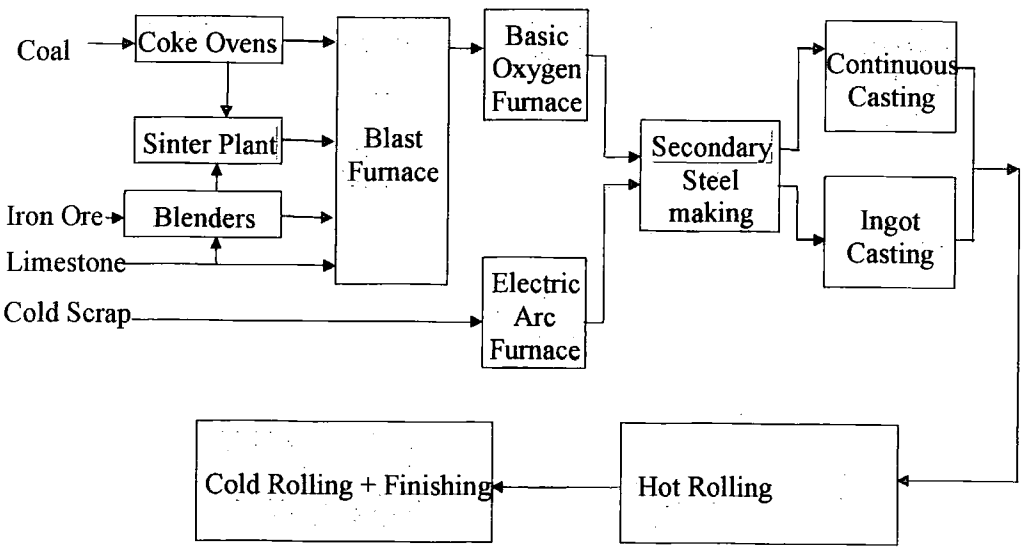

Fig. 2.1.1 Schematic of steelmaking process

The processes often require large amounts of energy. To minimise costs in this area and meet environmental standards waste gases are often recycled. This chapter describes the steel making process from the basic raw materials to the final finished products, which are delivered to customers such as the construction industry, automotive manufacturers, transport companies etc. A schematic of the process is shown in fig 2.1.1. It can be divided into 5 main processes, ironmaking[1,2], steelmaking[1], casting[1,3], hot rolling[4-6], cold rolling and finishing[4,7,8,9].

The work undertaken in this study is concerned with the rolling and finishing areas, therefore these will be described in detail. For completeness, brief descriptions will be given of the other processes.

2.2 Ironmaking

The main aim of this process, is to extract molten iron from naturally occurring iron ore in a chemical reactor known as a blast furnace. The iron ore, coke, sinter and limestone are charged into the top of the furnace, and a high-pressure hot air blast is injected into the base of the furnace through a number of nozzles, known as tuyeres. To improve efficiency, oxygen, oil or coal may also be injected. The iron ore is reduced directly and indirectly (as shown in equations 2.2.1, to 2.2.3) into molten iron.

Direct reduction

$$FeO + C = Fe + CO \qquad (2.2.1)$$

Indirect reduction

$$Fe_3O_4 + CO = 3FeO + CO_2 \qquad (2.2.2)$$

$$FeO + CO = Fe + CO_2 \qquad (2.2.3)$$

The limestone combines with the impurities in the ore to form a liquid slag, which being less dense than the iron floats on top of it. The molten iron often referred to as 'hot metal' and slag are tapped off from a taphole at the base of the furnace, with a skimmer being used to separate the two liquids. The slag is either granulated or pelletised and sold.

2.3 Steelmaking

In this stage of the process, the aim is to change the analysis of the incoming metal to produce a liquid steel with the desired chemical composition. There are two processes, basic oxygen and electric arc steelmaking. After both these stages, further refinement can take place depending on the grade of steel required. These further processes are known as secondary steelmaking.

2.3.1 Basic oxygen steelmaking (BOS)

This process uses hot metal from the blast furnace and is used to produce bulk steels. It takes place in a tilting vessel known as a converter, which is charged with good quality steel scrap then molten iron. Oxygen is then blown at high pressure into the metal to oxidise the carbon to carbon monoxide. Lime is used to help carry off these and other oxidised impurities as a floating layer of slag. To further aid in the

refinement, other gases including argon, nitrogen and carbon dioxide are injected through the base of the furnace.

2.3.2 Electric arc steelmaking

This process takes place in an electric arc furnace, which consists of a circular bath with a removable lid through which three graphite electrodes can be lowered. The first stage is to charge the furnace with cold scrap. The lid is closed and the electrodes lowered. A large electric current is passed through the circuit resulting in an arc. The heat generated melts the scrap. As with the BOS process, oxygen is blown into the melt and lime and fluxes are added to remove the impurities as a liquid slag. Alloys are also added during tapping to again finally adjust the composition.

2.4 Casting

There are two methods of casting the steel into slabs, billets or blooms; ingot and continuous casting. A schematic of a typical continuous caster is shown in fig. 2.4.1. Steel is poured from the ladle, through a gas-tight refractory nozzle to a tundish. The tundish supplies a continuous flow of steel to the water-cooled copper mould through a submerged entry nozzle (SEN). The steel solidifies as it comes into contact with the copper mould walls, thus forming a solid steel shell. The steel is continuously drawn from the base of the mould as more steel is introduced in the top.

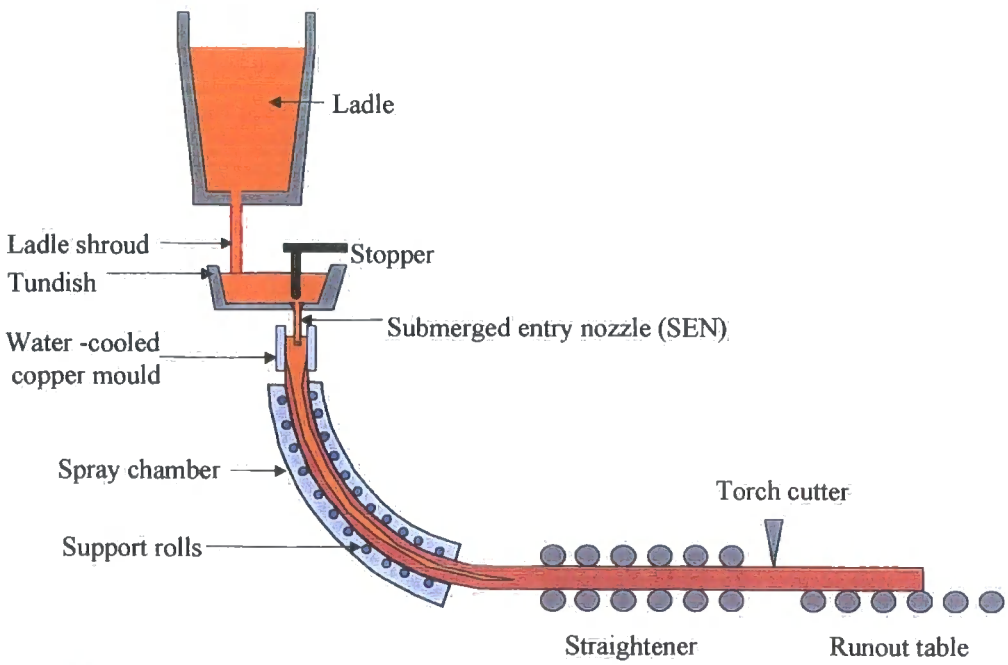

Fig. 2.4.1 Schematic of a continuous casting machine

(Reproduced from ' A Chown,'Continuous casting', Instrumentation & control engineering course, Ashorne Hill management college, Sep. 1997)

By the time the steel has passed right through the mould, a shell has formed around the steel, which is thick enough to support the liquid core. This semi solid structure is now referred to as the strand. The core gradually solidifies as the strand moves through the casting machine. A series of sprays down the length of the caster ensure that the strand solidifies completely before it is cut.

2.5 Hot rolling

In this section, the various stages in which the steel is shaped into the different product shapes are described. These include reheating, primary rolling, section rolling, plate rolling and hot strip rolling.

2.5.1 Reheating

In this stage, the steel is reheated to about 1200 °C. This reduces the yield strength of the material such that it can be shaped more easily. It also heats the steel above the phase transformation point, thus allowing the metallurgical properties to be controlled by the appropriate rolling and cooling schedules. Two types of furnace are in common use, the pusher furnace and the walking beam furnace. In the pusher furnace, the stock is pushed onto skid rails. This pushes the existing pieces in the furnace until they reach the other end. These furnaces are relatively cheap to install, run and maintain and are robust. The disadvantages are that there is local cooling on the steel pieces, where they are in contact with the skid rails. This can lead to unevenness in width, gauge and mechanical properties. Also, the output rate is limited by the furnace length. The walking beam furnace was designed to overcome the problems of the pusher furnaces. In these furnaces the stock is walked through using rotating supports. This means the output rate is now independent of the furnace length. Also because the stock is not pushed through, the effect of skid chills and the associated effects are markedly reduced. Both types of furnace can use a mixture of fuels, thereby making use of the most economic option at any time. These include recycled gas, natural gas and oil.

2.5.2 Primary rolling

The aim is to roll the slab, bloom or billet into a more suitable shape for the next rolling operation. The tolerance on the dimensions is not critical therefore a single pair of rolls, known as a 2-high stand, is used. To conserve space, the mills are often reversing and apply loads in the order of mega-Newtons in order to achieve large drafts (percentage reductions in gauge). Scale produced in the furnaces is removed

using high-pressure water jets before entering this mill. After rolling, the shapes of the product ends are often undesirable, therefore these are cut off using a crop-shear.

2.5.3 Section rolling

This section includes the rolling of universal beams, piling, and special sections including Caterpillar track. The layout for a typical Universal beam mill is shown in fig. 2.5.1. The roughing or primary mill has a series of pockets through which the slab passes to form a beam blank. Knifing passes are used to increase the gauge of the edges. The manipulators either side of the mill are used to guide the piece into the correct pocket and rotate it by 90 degrees to ensure all four sides are shaped. The piece can pass through the mill as many as 40 times depending on the required dimensions.

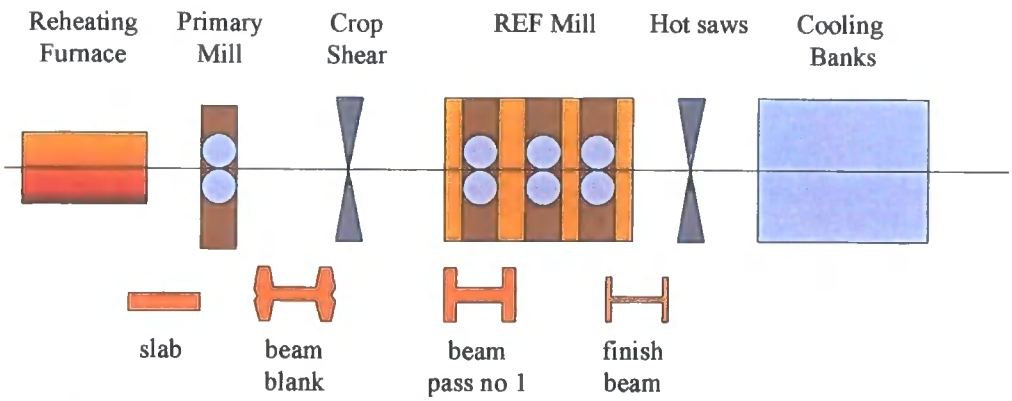

Fig. 2.5.1 Layout of a universal beam mill showing cross-sections across the beam width

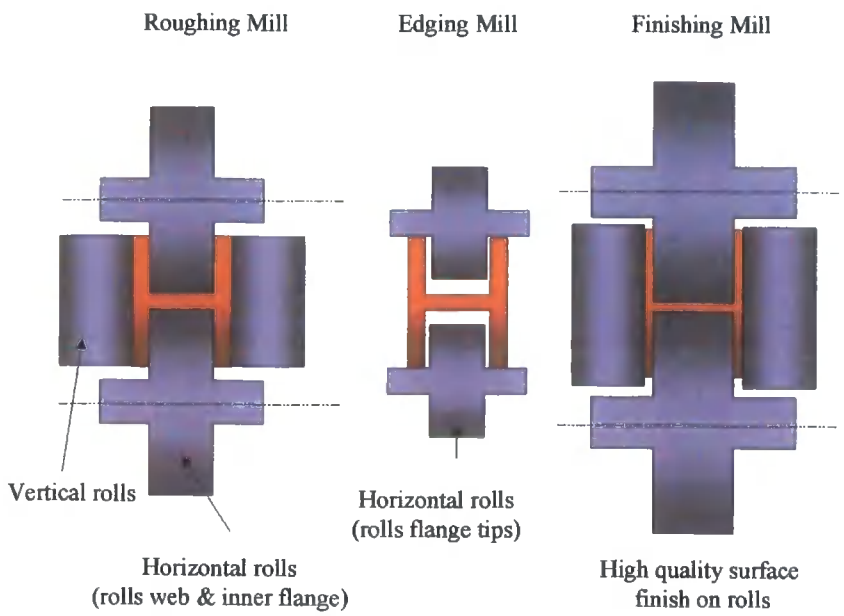

Fig. 2.5.2 Side view of the rolls in a REF mill

The next rolling operation takes place in the rougher, edger and finishing stands, collectively known as the REF mill. These 3 stands are coupled together as shown in fig. 2.5.2. The roughing and finishing stands contain vertical as well as horizontal rolls. The edger only rolls the flange tips of the beam. The steel passes between 7 and 15 times through these reversing mills. The finishing stand is only used in the final pass to improve the surface quality and produce the required dimensional tolerance. The beams are then cut to length and guided to the cooling banks where they are left to air-cool.

2.5.4 Plate rolling

This is the rolling of steel to widths up to 5m and gauges of between 5 and 50mm. A schematic of a typical mill is shown in fig. 2.5.3. The slabs are discharged from the furnace and are descaled using high-pressure water jets. The slab reduction takes place in a single stand, reversing mill, which has turn-tables and position-controlled sideguides on both sides of the mill for turning and centralising the piece.

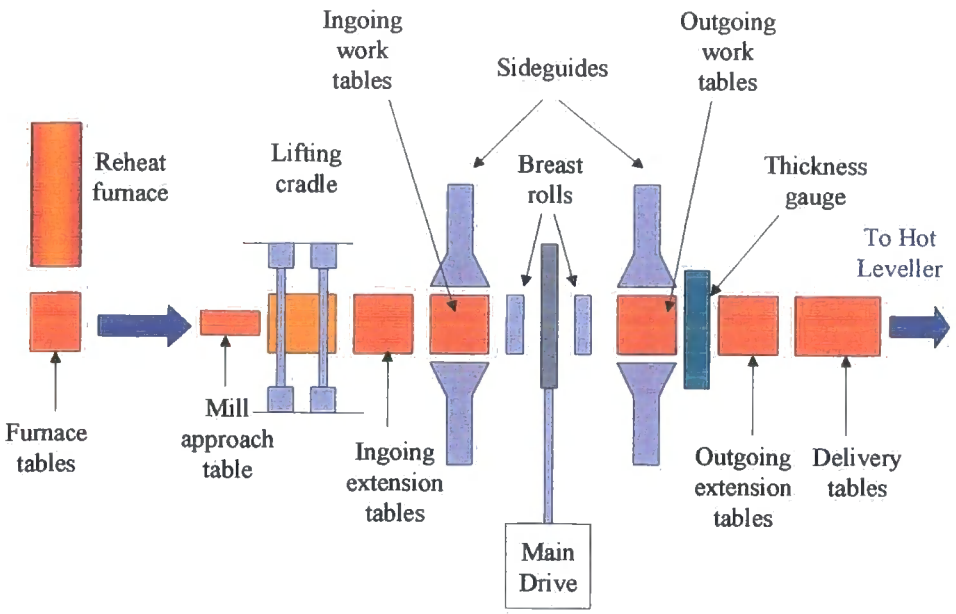

Fig. 2.5.3 Plan view of a plate mill

(Reproduced from 'A plate mill modernisation project', GEC Electrical Projects Ltd. Pub. No. 3493-348 1988)

During rolling, the piece becomes longer but the width is relatively unaffected. Therefore to increase the width of the piece, it is turned such that it is rolled broadside in some of the early passes. This 2-dimensional rolling reduces the directionality of the metallurgical properties which acts to improve them. The rolled product is referred to as the 'pattern' at this stage. The plan-view and gauge of the pattern are monitored

during and after rolling. It is then passed through a hot leveller which flattens and stress relieves the product. The piece is then left to cool on a cooling bank, after which it is sent to the shear line where plates are cut from it.

2.5.5 Hot strip rolling

This is the rolling of slabs to widths up to 1.2m and gauges of usually between 1 and 3mm, although the same process can be used to produce a thicker product of up to approximately 30mm. A typical layout is shown in fig. 2.5.4. After the slab has been primary rolled, it is either coiled to equalise the temperature of the bar before entry into the finishing mill, and /or passed under heat insulation Enco panels to reduce head to tail temperature losses, and reduce gauge variations owing to temperature differentials. The crop shear is used to remove the coil ends. The finishing mill consists of a number of 4-high stands coupled together such that the strip runs continuously through it. The number of stands varies from mill to mill, but is usually between 6 and 8. As the gauge of the strip reduces from stand to stand, the strip speed increases. The roll speeds of each stand therefore have to be controlled to match those of neighbouring stands.

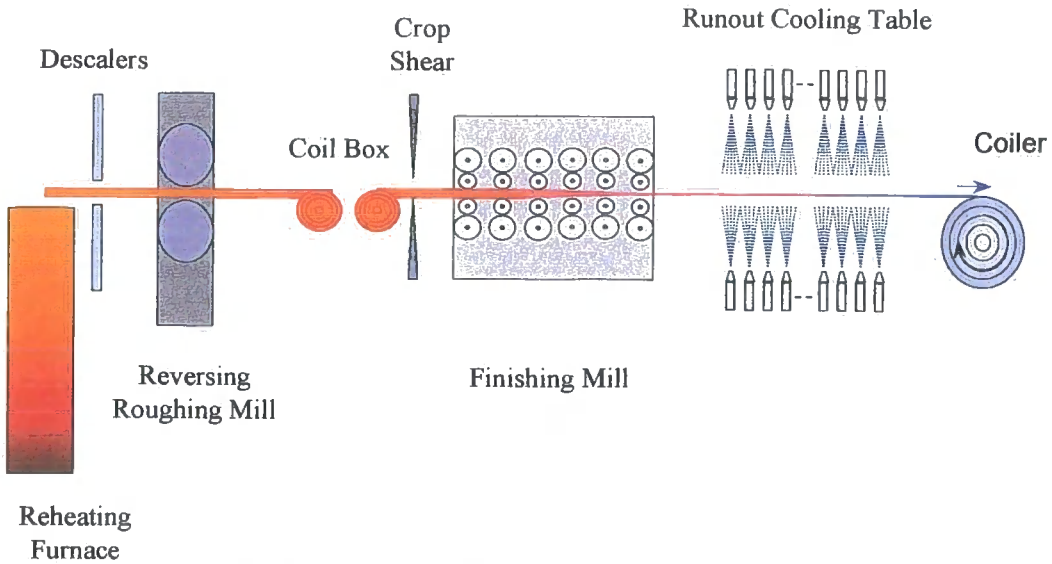

Fig. 2.5.4 Layout of a hot strip mill

Loopers are placed between the stands to compensate for changes in strip tension due to any mismatches in the roll speeds. The gauge of the strip is only measured after the primary and finishing mills, therefore the roll gap required to produce the necessary draft at each stand is calculated and controlled using the rolling load. When leaving the last finishing stand, the strip speed can be as high as 17 ms^{-1}. Its surface temperature is in the region of 700 to 900°C. The strip then passes through a series of

water cooling banks which cool the strip to about 400 – 500°C. It is then coiled to either be dispatched to external customers, or to be sent to the next process stage. Except for the head and tail ends, the strip is under tension between the finishing stands and the coiler. The amount of water applied is controlled using mathematical models which predict the metallurgical properties of the product using, typically, surface temperature measurements. If the phase transformation of the steel could be measured at this stage of the process, then the metallurgical properties of the steels could be more tightly controlled.

2.6 Cold rolling and finishing processes

This section describes the final processes which are applied to hot rolled products to meet the customer requirements. These include cold rolling, (tandem and temper mills), levelling of plates and straightening of sections, coating processes and welded tubes.

2.6.1 Cold rolling

This process is used to reduce the gauge of hot rolled strip to as low as 0.15mm. At the same time it is used to improve the shape and surface finish, together with the forming qualities of the product. A majority of mills are coupled stands which operate together as shown in fig. 2.6.1. However, reversing cold mills are still operated due to the lower cost. To improve throughput, coils are welded together at the mill entry. The strip is pickled to remove scale before entering the work rolls and as with hot rolling, the roll force is used to control the gauge of the strip. In temper rolling, the main aims are to produce the desired mechanical properties, the required surface texture and a flat strip. It can be carried out either wet or dry. However, wet rolling improves the surface cleanness. Strip products usually only undergo a slight gauge reduction, typically 0.7%, in a temper mill known as a skin pass mill. After any cold rolling process, the product is annealed by heating at carefully controlled temperatures in an inert atmosphere. This reduces the hardness which was caused from the cold rolling process.

2.6.2 Levelling and straightening

If a steel product has been hot rolled such that its shape and /or temperature distribution is uneven, it will experience non-uniform cooling, resulting in the build up of internal residual stresses and shape distortion. The aims of the straightening/ levelling operations are to remove the residual stresses and produce either a straight

section or a flat strip. The principle is to bend the work piece such that it is plastically deformed and then repeat the bend in the opposite direction as shown in fig. 2.6.2. This stress relieves the product and lowers the yield stress to enable straightening/levelling.

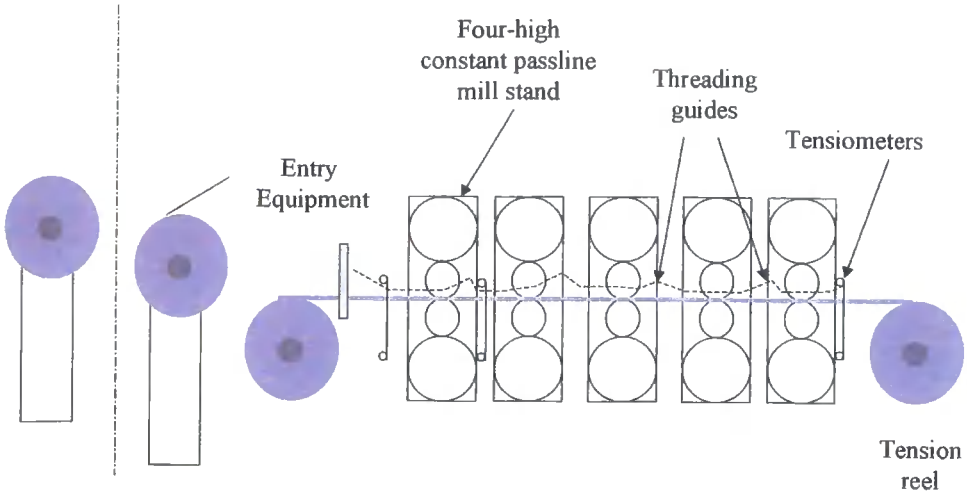

Fig. 2.6.1 Components of a five – stand tandem cold mill

(Reproduced from ' KJ Brown, 'Cold strip rolling', Instrumentation & control engineering course 2, Ashorne Hill management college, Sept 1994.)

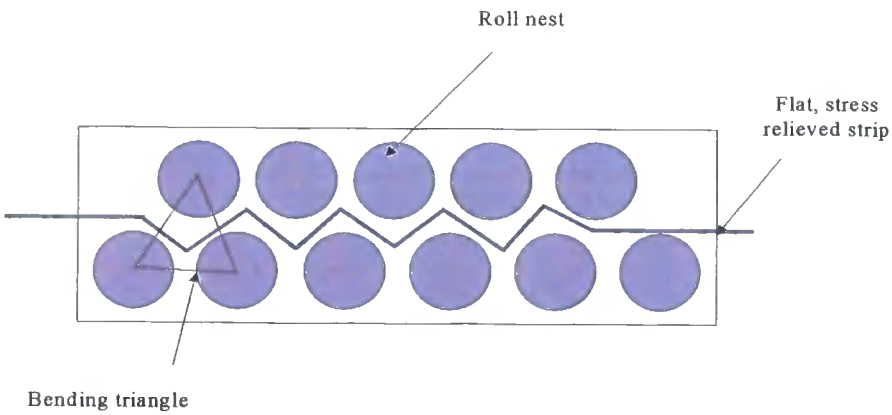

Fig. 2.6.2 Principle of plate levelling

2.6.3 Coatings

Coating prevents rusting and lengthens the product life; it can also dramatically improve the product appearance. There are three main types of coating, hot dip, electroplated and organic. The coating lines have basically the same components, the differing feature being the coating process.

Hot dip coating. This is used to apply metallic coatings of thicknesses in the range 7 to 45 μm. The most commonly used materials are zinc and tin due to their good

corrosion and chemical resistances. Here, the coating process is combined with a heat treatment stage to produce the desired metallurgical properties and give product flexibility.

Electroplated coatings. This is used to produce metal coating thicknesses of 0.1 to 10 μm thick. After cold reducing, the strip is annealed and temper rolled. It is degreased by passing through several solvent baths then pickled in the electrolyte before passing through a series of electroplating cells. This technique produces much thinner and tightly controlled coating thicknesses than the hot dip method. Also, the surface finish is smoother.

Organic coatings. There are two methods of organically coating steel. In the first method either uncoated or metallic coated strip is cleaned, tension levelled and chemically pre-treated to improve bonding. It is then coated with a range of specially formulated paints such as plastisols, polyesters and fluorocarbons. Primers and final coatings are applied by passing the strip through coating heads and are cured in ovens with temperatures up to 410°C. The second method involves applying adhesives and plastic film to the steel surface. This is known as laminating.

2.7 Summary

This chapter has described the processes to convert iron ore into steel products such as beams, tubes and strip products. To meet increasing customer demands, the process routes are continually being updated, with a view to improving efficiency, product specification and manufacturing new products.

2.8 References

1 -, 'Making Steel', British Steel plc.

2 *Taylor A*, 'Blast furnace control', Instrumentation & control engineering course 5, Ashorne Hill management college*, Sep. 1997

3 *Chown A*, 'Continuous casting', Instrumentation & control engineering course 5, Ashorne Hill management college*, Sep. 1997

4 -,'Shaping steel', British Steel plc.

5 *Dale J*, 'Sections', Instrumentation & control engineering course 5, Ashorne Hill management college*, Sep. 1997

6 -,'A plate mill modernisation project', Dalzell Works, Glasgow, GEC Electrical Projects Ltd, Pub. No. 3493-348, 1988

7 *Brown KJ*,'Cold strip rolling', Instrumentation & control engineering course 2, Ashorne Hill management college*, Sept 1994

8 *Wilkinson D*, 'Coatings', Instrumentation & control engineering course 5, Ashorne Hill management college*, Sep.1997

9 -,'Shotton Works', 'Advertising poster, British Steel plc.

* Address of College: Ashorne Hill, Leamington Spa, Warwickshire CV33 9QW. Further details are available on www.steel-training.co.uk (accessed 05/09/02)

CHAPTER 3

REVIEW OF ELECTROMAGNETIC MEASUREMENT SYSTEMS

3.1 Overview

The present trend in the major steelmaking companies is to produce more value-added products. In order to achieve this, it is necessary to control the product properties within tighter tolerances. To prove the product quality to the customer, off-line destructive testing with agreed standards and practices are used. This is costly, adds no value and is often not representative of the whole product. For example, in the case of steel strip, samples are only taken from the head or tail ends. Therefore, it is becoming more commonplace to develop on-line non-destructive measurement of parameters, which can be related to the final mechanical properties of the product. In this area, electromagnetic sensors have had a big impact. In developing these technologies, it is first necessary to understand the relationship between the magnetic and electrical properties of the steel product with the desired present or final property. The next stage is to develop the electromagnetic non-destructive testing technique using appropriate mathematical modelling tools where necessary[1]. In this section the following areas are reviewed, residual stress measurement, the measurement of phase transformation in hot rolled strip as it cools, hardness measurement, fracture toughness, formability, crack and defect detection, thickness and distance measurement and the detection of magnetic heterogeneity in steel sheets. Non-electromagnetic methods for measuring phase transformation are also included for completeness.

3.2 Residual stress measurement

The existence of residual stresses in hot and cold rolled steel products plays a crucial part in the final performance of the material. Qualitative predictions and model insights[2] have been used to identify the main mechanisms which contribute to distortion of plate and strip products on cutting, ie a plate can appear flat, but when cut the internal stresses are relieved, resulting in a curved piece. In special cases, inducing residual stresses is part of the design; for instance shot peened steel puts the surface into compression so that tiny surface cracks cannot grow into the material.

Destructive techniques such as hole drilling and sectioning[3] are well established and widely used. These are often accepted as the standard for comparison with the results of other techniques. However, they are time consuming and are not suitable for portable or on-line measurement. X-rays can only give measurements of surface stresses (up to a depth of 0.1mm)[4] and there are now reasonably portable units available. Greater penetration can, however, be achieved using neutron diffraction, which also gives through thickness and 3D absolute stress profiles[5]. The need for high flux reactors or accelerators limits its use due to lack of portability and cost. There has been much development of ultrasonic techniques, which are non-destructive, and have the potential of measuring in depth triaxial stress states. Although there are many standard probes of relatively low cost on the market, there remains a difficulty of separating the effects of microstructure and texture from stress effects. The magnetic techniques are of great interest in this area due to the fact that they are non-destructive, relatively cheap and portable. There are several commercial systems on the market.

3.2.1 Stress induced magnetic anisotropy

A technique, which has been studied in detail, is that of stress induced magnetic anisotropy (SMA). When a uniaxial stress is applied to a steel sample and a magnetic field applied, the $\underline{H}$ field is rotated, unless the poles of the applied field are parallel or perpendicular to the direction of maximum permeability. Langman[6-9] developed a rotation rig to investigate this effect. It consisted of a C-core and two pick up coils orientated parallel and perpendicular to the applied field, and was able to detect the ratio of the $\underline{H}$-field component in the two directions. He concluded that the maximum reading for a particular uniaxial stress is at about 45° to the direction of stress. He also studied the shape of the hysterisis loops for annealed mild steel with different applied tensile stresses. Examples of these for the $\underline{B}$-fields in directions parallel and perpendicular to the applied stress are shown in fig. 3.2.1. It can be seen that the parallel loop does change, but not as significantly as the perpendicular loop, which significantly decreases in area and rotates in a clockwise direction as the stress increases.

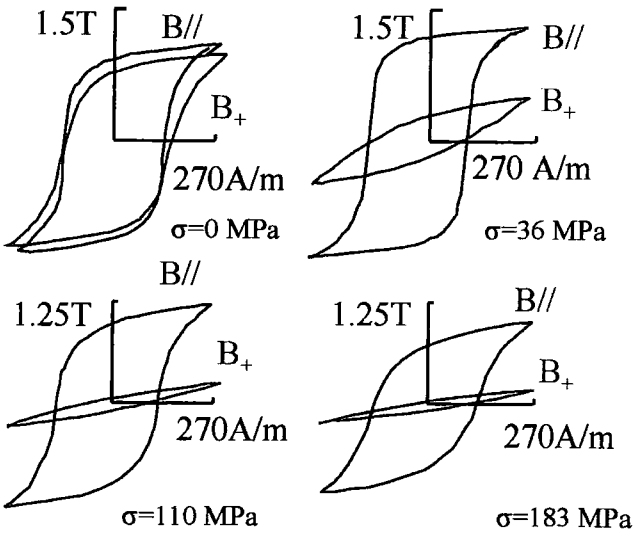

Fig. 3.2.1 B v H loops for annealed steel, B// is the loop measured parallel to the stress, B_+ is the loop measured normal to the stress and σ is the applied stress

(Reproduced from Langman R, 'Measurement of the mechanical stress in mild steel by means of rotation of magnetic field strength, NDT International, Oct. 1981)

Measurements revealed that the maximum rotations of these loops occur at about the yield stress, and that there is a non-linear relationship between their rotation and applied stress.

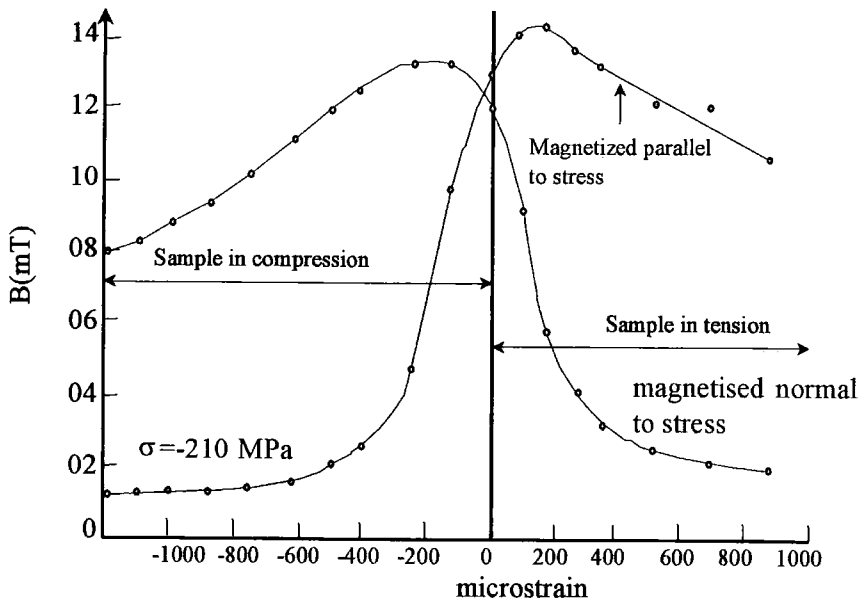

Fig. 3.2.2 Height (peak flux density) of B v H loop v strain for annealed mild steel in elastic region at H=270 A/m

(Reproduced from Langman R, 'Measurement of the mechanical stress in mild steel by means of rotation of magnetic field strength, NDT International, Oct. 1981)

The results, shown in fig. 3.2.2, show that tension parallel or compression perpendicular to the applied field have a smaller effect on the flux density compared with parallel compression or perpendicular tension which reduce the B-field considerably. Plastic strains decrease the rotation giving rise to an ambiguity. In studying biaxial applied stresses[7], he concluded that when steel is stressed elastically the output voltage of his rig was related to the difference in principal stresses. If the rig was rotated on the steel, its reading fluctuated between positive and negative. At a maximum positive reading, the more positive (tensile) stress was about 45° anticlockwise relative to the axis of the rotation rig. During his experiments, he found that the surface conditions of the samples had to be identical if comparisons were to be made. This is one of the major problems with magnetic stress measurement.

3.2.2 Magnetoacoustic emission

When a ferromagnetic material, such as steel is cycled through its hysterisis loop, the magnetisation of the steel takes place by the creation of domains, movement of their boundaries and subsequent annihilation of these domains. In steel, the effect of magnetostriction (ie the change in dimension due to an applied magnetic field) is to cause each domain to be strained longer along its direction of magnetisation, and shorter in the orthogonal directions[10]. There is thus a small strain field associated with domain magnetisation. Consequently, if the direction of the magnetostrictive strain changes as a result of abrupt domain wall movement, elastic waves will be generated locally.

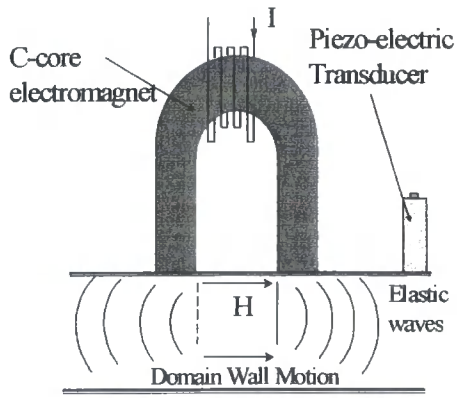

Fig. 3.2.3 Schematic of MAE transducer

This results in a magnetoacoustic emission (MAE), which is composed of many millions of discrete acoustic emissions, which together form a continuous largely incoherent noise signal. A schematic of a transducer[11]. which generates and detects

MAE is shown in fig. 3.2.3. The electromagnet applies a magnetic field which sweeps from –H to +H across the sample. At a certain value , say, $-H_1$ and again at, say, $+H_2$ there will be maximum amplitudes of MAE; the amplitude at the $-H_1$ point is referred to as the initial peak and that at the $+H_2$ point , the final peak. The dip in the middle (around H=0) is the central level. Any of these parameters and the area of the profile can be used.

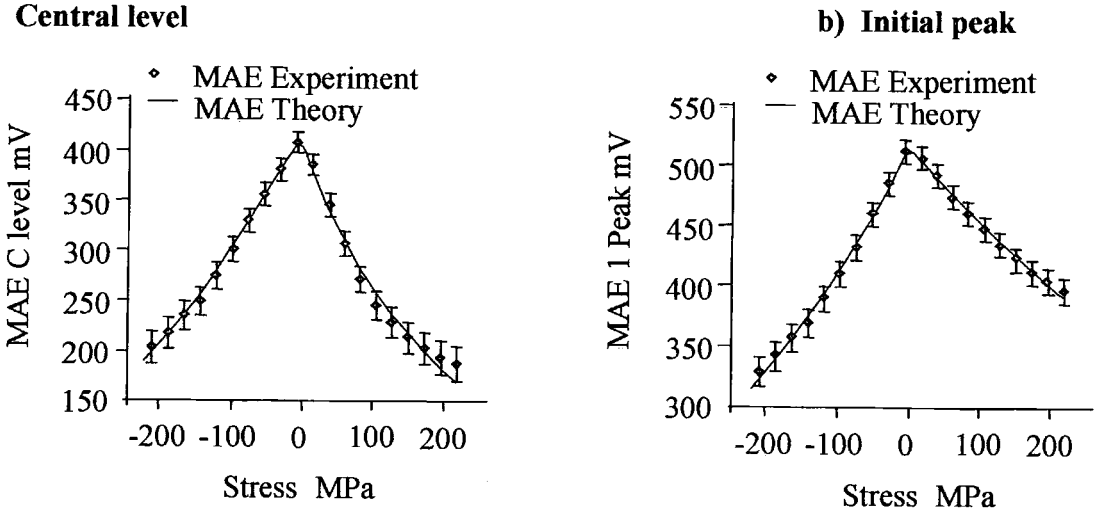

Fig. 3.2.4 Experimental MAE parameters and theoretical curves as functions of applied uniaxial stress

(Figs 3.2.3 and 3.2.4 both reproduced from Buttle DJ, Hutchings MT, 'Residual Stress Measurement at NNDTC', British Journal of NDT, Vol.34, No.4 Apr. 1992)

If the steel is subjected to stress, either residual or applied, this will interact with the magnetisation process resulting in partial alignment of the domain magnetisation vectors towards the tensile axis, or away from the compressive axis. The presence of the stress therefore, results in a larger permeability parallel to the most tensile axis compared to other directions, ie an induced magnetic anisotropy. Magnetoacoustic emission (MAE) is highly sensitive to stress, due partially to this domain alignment. The MAE signal amplitude decreases for both increasing tension and compression[11] as shown in fig. 3.2.4. The AEA Maps system[12-14] uses both stress induced magnetic anisotropy as described in Section 3.2.1 and magnetoacoustic emission. to measure biaxial stresses. It is now a commercial system , which cost in the region of £60,000 in September 1991.

3.2.3 Barkhausen emission (BE)

Barkhausen electromagnetic noise can also be calibrated to stress. It is detected by placing a coil of conducting wire near a sample while the domain walls move. The resulting change in magnetisation induces electrical impulses (Barkhausen noise) into the coil. It can be calibrated to both uniaxial and biaxial stresses. Its accuracy is limited by the similarity of the calibration and test sample microstructures[15]. The Stresscan system uses this technology. Work has been reported[16] in which two peaks occur on the BE and MAE curves. These correspond to the knees of the magnetisation curve, where domain nucleation and annihilation occur. When the ratio of the initial to final peak amplitude of the BE is greater than one, and the corresponding ratio for the MAE is about 1.3, then the steel is still in the elastic state. For plastically deformed steel, the BE peaks ratio is less than 1 with the MAE ratio larger than 1.3.

A method employed by British Steel, (Corus UK) [17-19] was to apply a low frequency ac magnetic field to the steel sample using a C-cored electromagnet. When a stress was applied to the sample, the permeability changed. This in turn changed the inductance of the coil, and hence the current. The principle of operation was to measure the change in current in the directions of the two principle stresses. These were assumed to be parallel and perpendicular to the rolling direction. The instrument was developed to the point, where a pair of 'magnetic stress indices' could give an indication of the stress trends. These were consistent with finite element stress simulations[20]. Since only uniaxial calibrations were carried out, it was not possible to distinguish between tensile and compressive stresses. The development was stopped at this stage, due to the estimated amount of work that was envisaged to obtain a reliable working system, balanced against the fact that commercial systems were becoming available. A device called the Sigmatron[21] uses the same property of anisotropic permeability. In this device, a primary coil generates the magnetic field, and a secondary coil is used to detect the signal dependent upon the magnetic properties of the material and the stress in it. It relies on a four point bending rig for its calibration. Tests at British Steel (Corus UK) showed that the device had a linear response to uniaxial stresses. The correlation for biaxial stresses was found to be unsatisfactory.

3.3 Phase transformation detection

This section reviews work carried out in detecting the percentage of steel transformed from the hot austenite phase to the colder ferrite and cementite phases, as hot strip cools after it has been hot rolled. The most common way of estimating this phase transformation is to use pyrometers to measure the surface temperature of the strip at two or more locations along the run-out table. Although this is only an indicator of the fraction transformed, it has been successfully used to control the cooling rate[22,23] of hot rolled steel, such that products with the desired mechanical properties have been produced within European tolerances. There are several limitations with the use of pyrometers, such as varying emissivity due to, for example, scale formation on the strip surface, obscuration due to the presence of copius amounts of water and steam, or dirt on the lens, and unwanted reflections from the mill sides and rolls etc. These factors reduce the number of suitable installation locations, and hence the number of measurements.

In 1971 at BISRA[24], laboratory experiments were undertaken, to investigate how the magnetic properties of steel changed as it was heated and cooled to and from 900 °C. The equipment consisted of a primary coil used to supply a 56kAm^{-1} field to a rod of steel with a thermocouple inserted to its midpoint and a pickup coil wound around it. The sample rested on the bottom of a quartz dilatometer tube incorporating an LVDT. Analogue circuitry was used to output the coercivity, H_c, the remanence, B_r, and the maximum induction B_m. The results are shown in fig. 3.3.1. Inflections in the curves were observed, some of which were shown to coincide with the phase transformations. Because the relationship between $\underline{B}$ and $\underline{H}$ is non-linear, a sinusoidal $\underline{H}$-field produces a non-sinusoidal $\underline{B}$-field. A waveform analyser was used to determine the amplitude and phase of the B-field in the frequency domain. The first 7 harmonics were used in the analysis. The 5th harmonic was found to reveal the Curie point of the cementite content of the sample when plotted against temperature. The reason for this was not given, but it could be that the cementite is magnetically harder than the ferrite. It was found that increasing the cooling rate, shifts the magnetic curves to lower temperatures. This is consistent with the phase transformations shifting with increased cooling rates and only the ferrite and cementite having ferromagnetic properties. However, it was observed that the gradient of the fifth harmonic of the $\underline{B}$-field remained unchanged with cooling. This could then be used to

determine cooling rates. The probe design mentioned for an on-line application involved maintaining a fixed distance between the probe and strip by means of an air cushion.

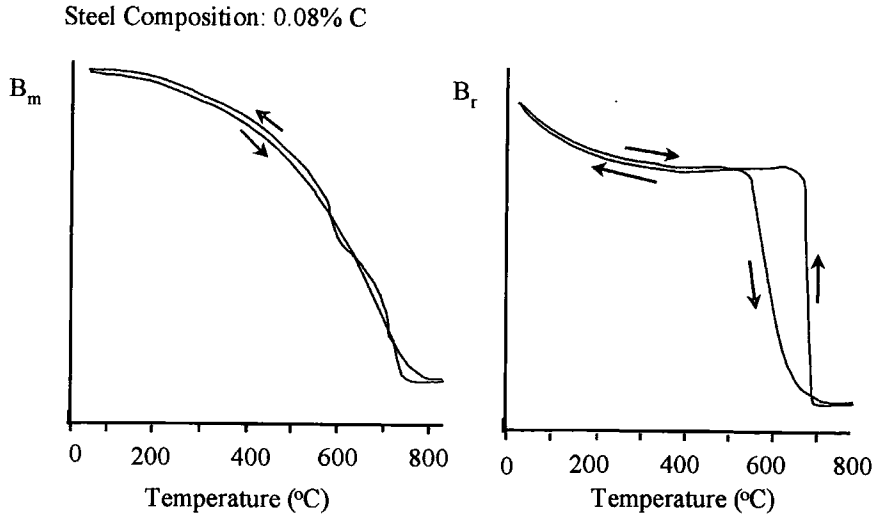

Fig. 3.3.1 Temperature dependence of magnetic properties

(Reproduced from Davis N, Norris P,'A magnetic technique for on-line measurement of temperature and metallurgical state', BISRA Internal Report Phys/TN/11/71, 1971)

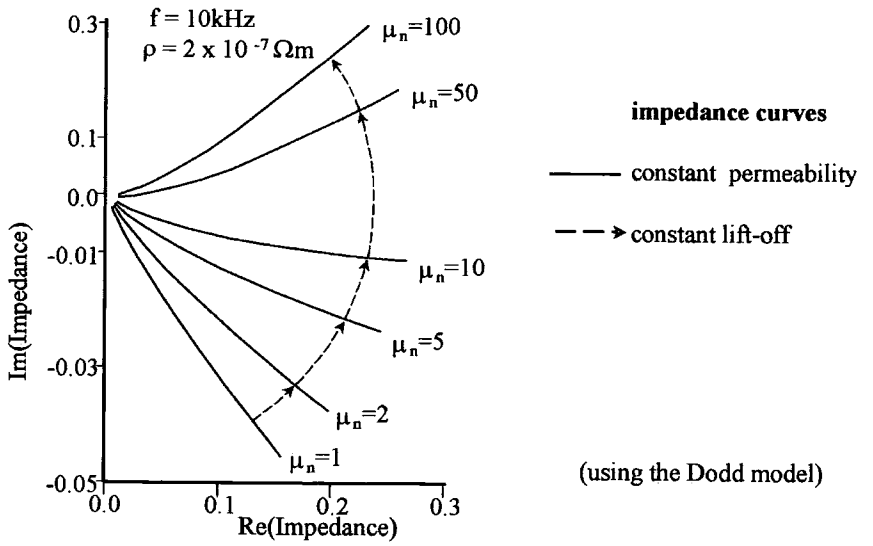

Fig. 3.3.2 Example of development of the coil impedance during transformation

(Reproduced from Dodd CV, Deeds WE, 'Analytical solutions to eddy current probe coil problems', Journal of Applied Physics Vol. 39, No. 6 (1968))

Irsid installed an on-line transformation detector[25-27] in the 1970's. The sensor consisted of an exciting and pick up coil situated under the strip. The variations in the coil impedance were analysed using an analytical model[28]. The probe was excited at 10kHz and the electrical phase information was used to compensate for the effect of lift-off (distance between the sensor and steel target) as shown in fig. 3.3.2. The sensor performed well in the production environment with a lift-off of ~20mm enabling satisfactory protection. The lift-off compensation also proved to work adequately, enabling satisfactory measurement of the permeability. It was found that the sensor was extremely sensitive to the first ferrite fractions, causing rapid saturation of the signal, making it difficult to interpret the fraction transformed. However, it did detect the start of transformation. The saturation was possibly due to the skin effect, which would be very significant at 10kHz.

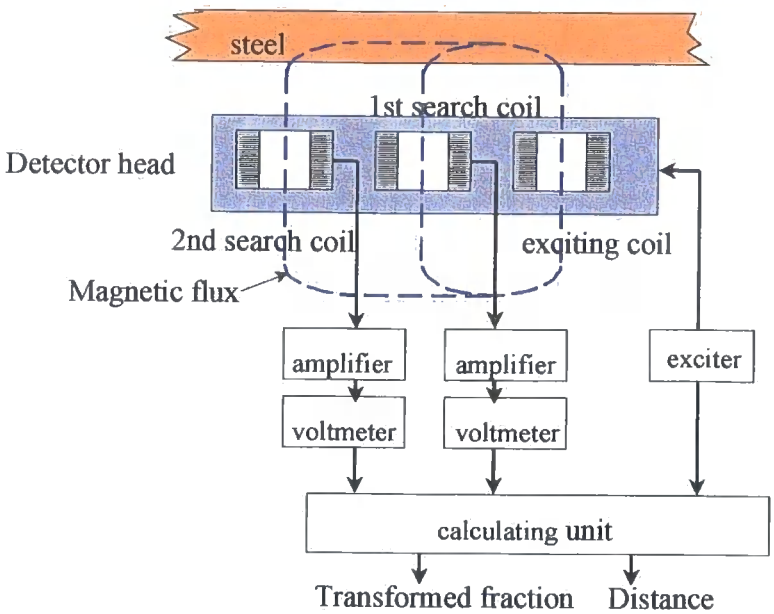

Fig. 3.3.3 Block diagram of an on-line transformation detector

(Reproduced from Morita M, Hashiguchi K, Hashimoto O, Nishida M, Okano S, 'On-line transformation detector for property control of hot rolled steel', Proc Of Met Soc of AIME Symp on Acc Coiling of Steel, Pittsburgh Aug. 1985)

NSC[27] proposed the use of two coils with one either side of the steel strip, and measuring the coil impedance as in Irsid's development. It was proposed that this would overcome the problem of extreme sensitivity to the initial transformed fraction. It would involve one coil being above the strip, which would be difficult to protect. Other limitations include sensitivity to the steel strip inclination and the signals becoming very low as soon as the steel becomes magnetic.

Kawasaki Steel have reported the development[29] and use [30]of a magnetic transformation detector at Mizushima Works hot strip mill for improved coiling temperature accuracy and better product uniformity.

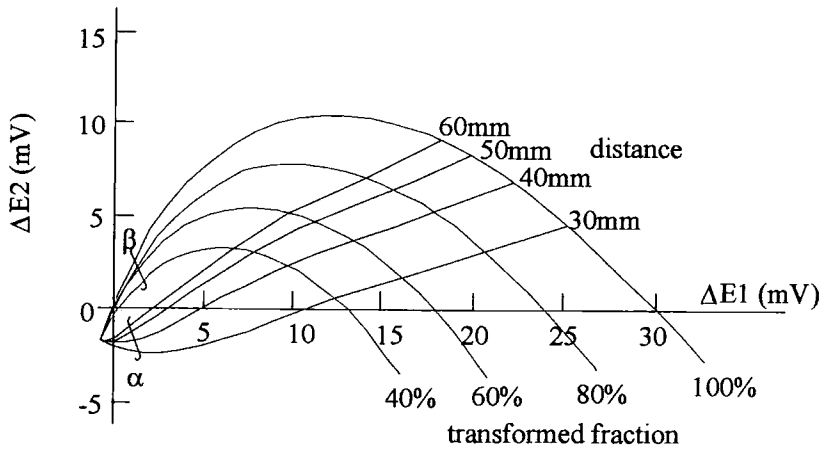

Fig. 3.3.4 Nomogram to determine % transformed and lift-off using induced voltages in pick-up coils

(Reproduced from Morita M, Hashiguchi K, Hashimoto O, Nishida M, Okano S, 'On-line transformation detector for property control of hot rolled steel', Proc Of Met Soc of AIME Symp on Acc Coiling of Steel, Pittsburgh Aug. 1985)

The detector consists of an exciting coil and two search coils as shown in fig. 3.3.3. The size of the fields generated or the cores of the coils are not mentioned. The principle of the measurement is that the exciting coil is driven by an ac signal. The flux linkage between the exciting and detector coils is determined by the magnetic reluctance of the steel, the air gap between the steel and search coil and the air gap between the exciting and search coil. The magnetic reluctance of the steel depends on its permeability and conductance, which in turn is dependent on the fraction of steel transformed to ferrite and cementite. If each detector coil is a different distance from the exciting coil, then each will see different contributions of the steel sample, and will have different voltages induced. Both induced voltages are functions of the transformed fraction and lift off and can hence, be used to decouple these two parameters as shown in fig. 3.3.4. The sensor can detect with lift off variations from 20mm to 120mm. Regression analysis was used to relate the rate of transformation procession in intervals of 10% to the mechanical properties. It was found that the variation in mechanical property prediction was improved by a factor of 3 over the conventional temperature measurement method (pyrometry).

The principle of magnetic reluctance using an electromagnet was proposed and dismissed by the researchers at Irsid[27]. The limitations they defined include the presence of an air gap, which greatly reduces the sensitivity, and the decoupling of air gap and material property.

A magnetic method of determining percentage phase transformation off-line was reported in 1996[31] and has been used by British Steel (Corus UK) at their technology centres with limited success. The apparatus is shown in fig. 3.3.5.

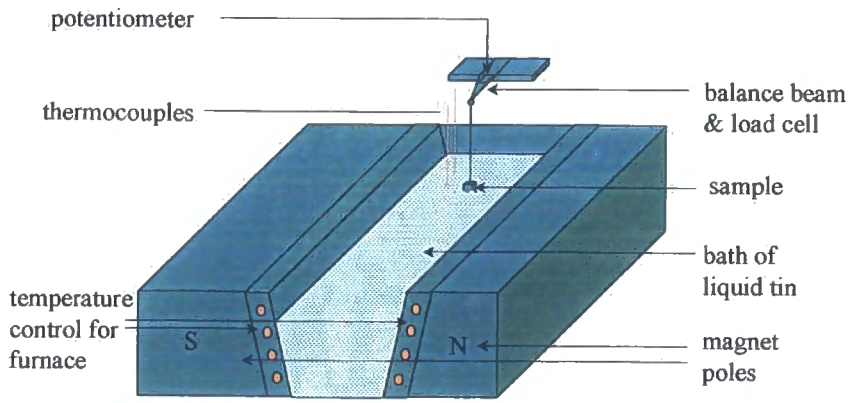

Fig. 3.3.5 A balance magnetometer for measuring phase transformation

(Reproduced from Khlestov VM, Konopleva EV, McQueen HJ, 'The hot working and transformation to ferrite of V-Mo, Nb and Nb-V steels', Canadian Metallurgical Quarterly, Vol. 35, No. 2, pp. 169-180, 1996)

The hot sample is placed in the tin bath to ensure isothermal transformation. The poles of the magnet produce a non-uniform magnetic field in the region of, 0.6T - 0.7T, which exerts a downward force on the specimens, resulting in a deflection of the load cell. The principle behind the method is that the higher the fraction of the magnetic ferrite phase, the greater the force. The isothermal transformation for two high strength, low alloy, (HSLA) steels at 700°C, which have been pre-rolled at known temperatures, are shown in fig. 3.3.6. ε represents the percentage reduction in the thickness of the sample during the rolling process They indicate an initial rapid increase in the percentage transformed then a gradual tailing off. This could be due to three reasons; the rate of transformation decreases as the percentage increases, the magnetic device becomes less sensitive to increases in the ferrite content and/or there is a non-uniform phase transformation across the sample. More information on this device needs to be found.

In 1997 research into transformation detection was restarted at British Steel (Corus UK) and Lancaster University. This work will be reported in detail in later sections.

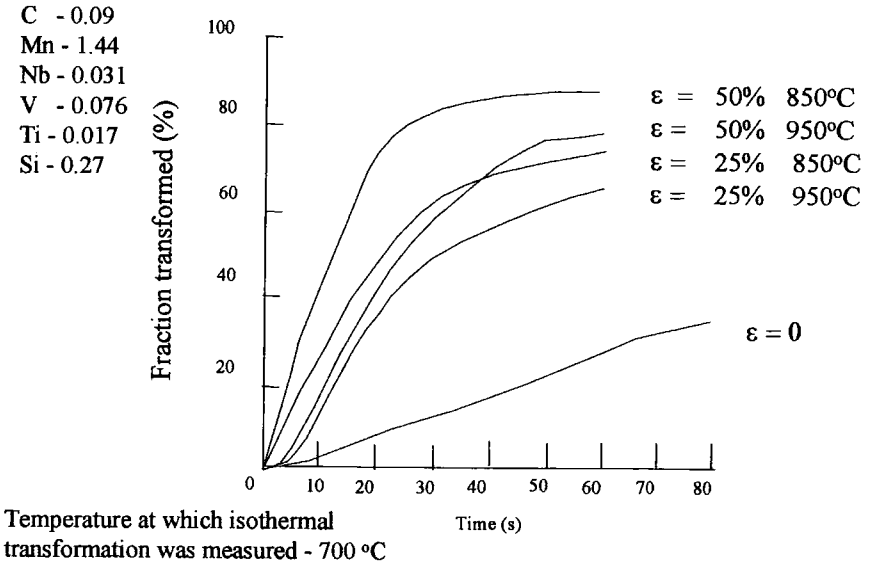

Fig. 3.3.6 Fraction of austenite transformed for different processing conditions

(Reproduced from Khlestov VM, Konopleva EV, McQueen HJ, 'The hot working and transformation to ferrite of V-Mo, Nb and Nb-V steels', Canadian Metallurgical Quarterly, Vol. 35, No. 2, pp. 169-180, 1996)

Patents[32,33] have been filed by NKK Corporation, Japan for a meter which measures the transformation of a sample by placing either a two or three pole electromagnet underneath the steel and using a flux-gate type sensor, which they have developed, to measure the small changes in magnetic field about one metre above it. The reason behind this, is that the sensor is extremely sensitive to changes in the magnetic field due to the phase transformation, but is relatively insensitive to variations in lift-off. This is because the lift-off will have an extremely small effect on the magnetic field at that distance. The final advantage to this arrangement, is that the sensor is far enough away from the steel not to be knocked by it, and the temperature will be lower.

3.4 Mechanical property measurement

In developing on-line hardness measurements using magnetic methods, it is common in the research to use commercially available equipment. These are used to measure the magnetic parameter(s) of interest, which are then related to the results of standard off-line destructive tests including Vickers and Rockwell hardness tests, Charpy impact and tensile tests. Examples of reported developments are outlined in this section.

It has been reported that regression equations using the output of the KIFM-1 coercimeter have been successfully used to predict hardness on the 2000 mill of Cherepovets Metallurgical Plant[34], and replace tensile tests at the Nizhni Tagil Metallurgical Combine[35]. Tests on over 10,000 plates at Nizhni suggest the possibility of also predicting impact strengths at -40°C using the KIFM-1 output in a tenth order polynomial fit, thus completely eliminating the need to cut samples for tensile and impact destructive testing[31].

A magnetic flaw detector MS-2 IFM has been used to predict the hardness of high chromium steels[36]. Magnetic parameters measured include the relaxation coercivity, H_r, the level of magnetisation corresponding to the field H_r on the limiting magnetic hysterisis loop, (the relaxation magnetisation) and the mean magnetic susceptibility on the recovery curve in the statically demagnetised state. These were related to the hardness measurements using regression equations. The agreement between the predicted and measured values was reported to be good. The tests described were performed off-line. The same flaw detector MS-2 IFM was modified by placing a 'ferroprobe' in the magnetic circuit[37]. Using this device, correlations were established between both irreversible and reversible magnetic processes and test parameters such as hardness. The quality of surface finish was considered an important factor when determining the accuracy of the predictions.

An on-line power loss tester was installed at Orb Works, British Steel to measure the hardness of electrical steels[38,39]. It employs digital processing such that, complete data is available for the whole of each hysterisis cycle. Therefore, it is relatively easy to obtain the remanence, coercivity, power loss and permeability from the data. A special voting algorithm was developed to improve the hardness predictions from the various magnetic parameters.

Work has been reported[40] in which Barkhausen Emissions (BE) have been correlated with the carburisation concentration gradient, and hence hardness within tool grade steels (fig. 3.4.1). The initial and final peaks of the BE characteristic are shown to merge at low temperatures. It is the height of these peaks that are used in the analysis.

An EMAT (Electromagnetic Acoustic Transducer) sensor, installed on two continuous annealing lines at Sumito Metal Industries Ltd, has been used to measure the

texture(characterised by the r-value) by creating Lamb waves at 0, 45 and 90 degrees to the rolling direction[41]. Two sensing techniques were considered to produce the waves: the Lorentz force and magnetostriction.

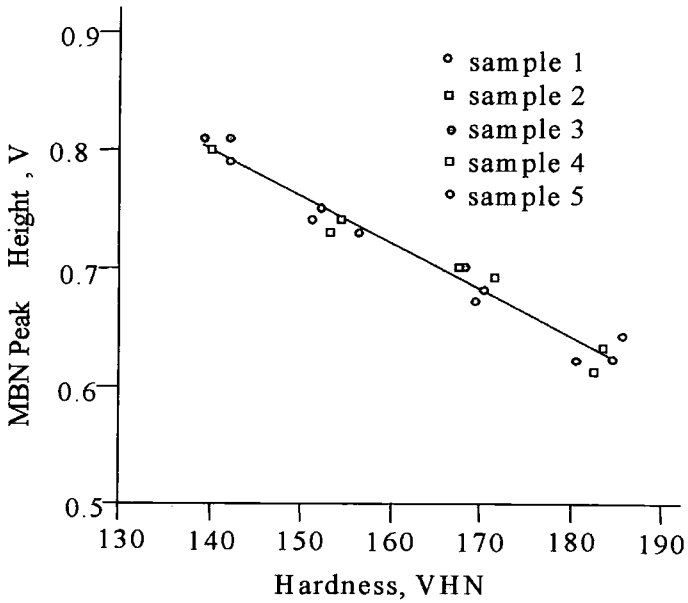

Fig. 3.4.1 MBN v Hardness in the carburised region

(Reproduced from Vaidyanathan S, Moorthy V, Jayakumar T, Raj B, 'Evaluation of carburisation depth in service exposed ferritic steel using magnetic Barkhausen noise analysis'' Materials Evaluation, Mar. 1998, pp.449-452)

An EMAT based on the Lorentz force principle is a coil excited by a high voltage radio frequency burst, which induces eddy currents into the steel. A permanent magnet or an electromagnet provides a dc magnetic bias perpendicular to the sheet, such that Lorentz forces act on the induced currents to generate mechanical vibrations, giving rise to Lamb waves. Detection occurs by using the reverse process.

An EMAT based on magnetostriction can only be used with ferromagnetic materials. Again a coil is excited by a radio frequency signal, but this time the static magnetic field is applied parallel to the steel sheet. The rf field induced in the steel causes the magnetic domains to align, giving rise to a dimensional change, ie magnetostriction. This produces periodic patterns of tensile and compressive strains, which convert to a Lamb wave. The detection process occurs due to the Lamb wave causing a periodic change in the permeability, which causes the oscillation of the magnetic flux density. This can be detected using electromagnetic induction.

The EMAT using magnetostriction was considered to be superior for cold rolled steel sheets. The driving frequency was chosen to be 280kHz, in the low frequency range, to minimise the effects of lift-off and sheet thickness. A gap of 3mm was maintained between each sensor using rollers to stabilise the steel sheet. There was good correlation with mechanical tests. A system installed on a hot dip galvanising line at Thyssen Stahl AG [42] consists of 2 sensors:

1 an EMUS (elecromagnetically excited ultrasound) device. This was used to measure the time of flight of shear horizontal waves and relate them to the change in r value (which represents a measure of direction dependent flow behaviour in the plane of the strip). The sensor head consists of one transmitting and two receiving transducers situated 60mm apart. This device appears to be similar to an EMAT.

2 a sensor to measure the incremental permeability, (and hence the coercive force) which is then related to the yield strength. The measuring head consists of an electromagnet which generates an ac magnetic field in the steel, a Hall sensor , and a measuring coil driven with a current in the kHz range. This generates a small field superimposed on the larger ac field. The ac resistance of the measuring coil is measured as a function of the larger ac field strength, and is a maximum when the field strength equals the coercive force.

Good correlations were observed with both sensing techniques. No interaction was observed between the two sensing heads. Strip speed did affect the output but correlations were still possible.

The 3MA (Micromagnetic Multiparameter Microstructure and Stress Analysis) device[43] consists of various transducers and a yoke, which provides the magnetic excitation. The idea is to measure quantities, which can be related to the reversible and irreversible magnetisation processes, which contribute independent information. The probe measures magnetic Barkhausen noise, acoustic Barkhausen noise, incremental permeability, longitudinal magnetostriction, dynamic magnetostriction and coercivity. A back propagation neural network with 14 inputs, representing these micromagnetic measuring parameters, was used to predict tensile strength, hardness, yield strength, and impact strength.

3.5 Defect detection

To detect defects in slabs, steel strip, rod etc there are several electromagnetic techniques available; eddy current inspection, magnetic flux leakage, the four probe potential drop method, magnetic particle inspection and EMATs. Other technologies reported include visual and optical inspection[44] and ultrasonic methods[45].

Eddy current systems are available, which are capable of detecting longitudinal and transverse cracks above the Curie temperature[46]. However, for these systems to operate effectively, surface descaling is required. The BHP system[47] uses multi - frequency probes housed in water cooled ceramic and stainless steel, and mounted on an oscillating beam. An industrial device has been developed by Irsid, which inspects the large sides of slabs below the Curie temperature[48]. The geometrically anisotropic probes transversally scan the slab and their outputs are used to build an image. Image processing algorithms can then be applied to recognise cracks or the signals can be compared with a reference crack. The system was successfully trialled at Sollac Fos.

Research has been undertaken to combine ultrasonic and eddy current technology to produce a 'Universal Digital Inspection System[49]'. This hybrid approach has been undertaken to reduce the physical size of an ultrasonic phased array unit.

In eddy current inspection a coil carrying an alternating current is placed close to the steel surface under inspection. Eddy currents are induced into the steel and flow near the surface, penetrating to a distance defined by the skin depth. A material discontinuity or defect near the surface affects the eddy current pattern, and is detected by a change in impedance of the coil. The eddy currents are also strongly affected by the distance between the sensor and the steel (lift-off). Phase sensitive detection enables the discrimination between lift-off and defects. The sensitivity of the system is increased by the use of small probes, high frequencies and limiting the lift-off variations. This limits the scanning speed for on-line use, as it becomes difficult to compensate for lift-off changes[44]. To improve the sensitivity to sub-surface flaws in steel samples below the Curie temperature, a saturating dc magnetic field can be applied to suppress the effect of the magnetic variables[50,51].

Systems using rotating probes and encircling coils have been developed for the inspection of rod and wire[51]. A 3 pole electromagnet (one exciting coil and two

differential secondary coils) situated within a permanent magnet has been developed by NKK to inspect defects throughout steel pipe walls[50]. A schematic is shown in fig. 3.5.1.

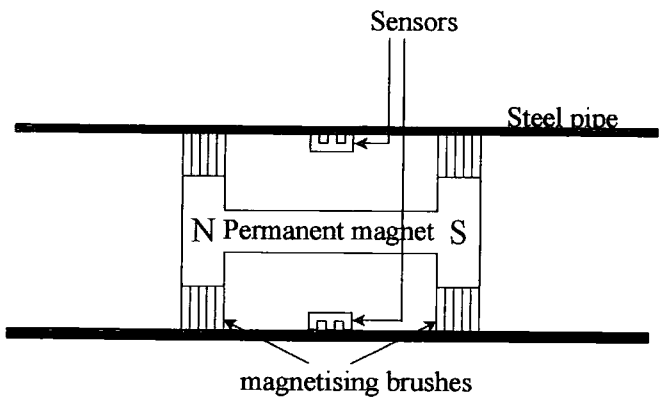

Fig. 3.5.1. Schematic of sensor to detect defects in steel pipe walls

(Reproduced from Kondo M, Murashita K, Honma H, Kurashima M, Toye M, Nishinno S, 'Magnetizing eddy current tool', NKK Tech. Review, No.76 ,1997)

The magnetic leakage method involves applying a saturating uniform magnetic field to the steel. The presence of a defect will cause a change in the level of the leakage flux, which is related to the volume of the defect. This leakage can be detected using a suitable sensor, eg Hall effect device, magnetic resistor or a magnetic diode.

An off-line system using this technique is in operation at Hoogovens[46]. However, the leakage flux is measured using coils. An on-line system at the No. 2 shear line at Fukuyama works, NKK also uses detector coils[52]. Both systems require constant lift-offs. The detection coil was developed by NKK because the sensitivities of other commercial devices were not considered adequate (see fig. 3.5.2). It is based on the principle shown in fig. 3.5.3. It consists of a coil, excited with an ac current, wound around a saturable ferromagnetic core. The voltage drop across the coil is given by e_o where e is the supply voltage, Z the series impedance and Z_o the impedance of the coil. When another magnetic flux is superimposed on the sensor, a difference in amplitude occurs between the positive and negative side of the voltage. This differential voltage is proportional to the leaked magnetic flux.

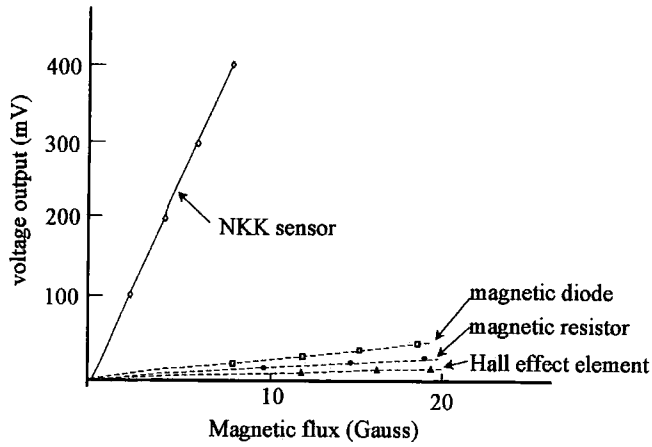

Fig. 3.5.2. Comparison of detector performance

(Reproduced from Maki H, Tsunozaki Y, Matsuffuji Y, 'Magnetic on-line defect inspection system for strip steel', Iron and Steel Engineer, Jan. 1993)

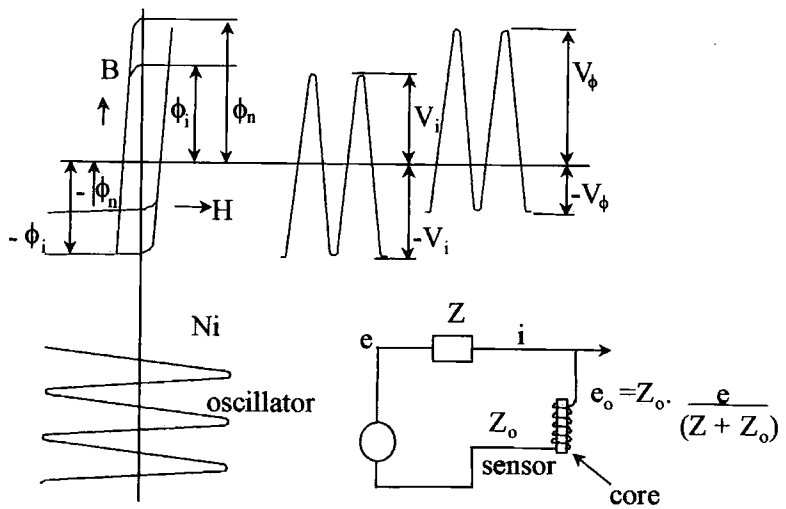

Fig. 3.5.3. Diagrams showing detection principle of NKK sensor

(Reproduced from Maki H, Tsunozaki Y, Matsuffuji Y, 'Magnetic on-line defect inspection system for strip steel', Iron and Steel Engineer, Jan. 1993)

This NKK system consists of an array of sensors (up to 1500) which can detect defects up to $5x10^{-4}$ mm^2. The constant lift off is maintained by placing the exciting and sensing coils in hollow guide rolls. The system is sensitive to speed.

The magnetic particle inspection method is an off-line defect detection method. The presence of an internal defect is achieved by magnetising the steel strip, and then applying a magnetic powder dissolved in liquid[49] over the defect region. The defect

produces a stray-flux, into which the magnetic particles cluster to form a visible indication of the defect. After the liquid has dried, the image can be taken from the steel strip using adhesive tape, or detected using image processing techniques.

The four point probe potential drop method is used to determine the depth of a crack (the influence of the width is assumed to be negligible). Unlike the other methods already described it relies on good contact with the steel sample[53]. The frequency of the injected current should be sufficiently high, such that it travels along the surface of the sample and follows the crack. However, the frequency should not be too high, since this introduces screening problems, and the permeability is frequency dependent. For this method to work successfully, the crack must be at least twice the length of the distance between the probes.

The quality of butt welds for joining coils on continuous lines such as cold rolling and pickling lines have been detected using a commercial system (Temate 2000[54]). It consists of an EMAT, producing shear horizontal waves, which travel along the length of the strip to the weld. This wave provides 100% inspection of the weld area, and is sensitive to both defects within and on the surface of the weld. The defects cause reflections of the wave energy. Therefore, by monitoring the amplitude of the transmitted signal and setting a threshold level, good and bad welds can be distinguished.

3.6 Distance and thickness measurements

Eddy current sensors are available for distance measurement, but need to be calibrated for ferromagnetic or non-ferromagnetic targets eg Kaman™ and Micro-Epsilon™ devices. This problem was overcome by the manufacturer Bruel and Kjaer™ by making use of the electrical phase information[55]. However, the resulting sensor was too difficult to manufacture and has thus been withdrawn from the market. Single coil devices are the cheapest , but for greater temperature stability, dual-coil devices are more satisfactory.

There is a report of a sensor, which can measure the coating thickness of galvanised steel strip being installed on a continuous galvanising line at the end of the coating process, where the strip temperature is 40°C, and immediately after the coating operation, where the strip temperature is 300°C[56]. The sensor consists of a primary

coil wound on an open magnetic core with an excitation frequency of 500 kHz and a secondary coil which is divided into two parts, the active part and the reference path (fig. 3.6.1). A metallic shield is used to reduce flux leakage. The distance between the sensor and the strip (lift-off) is about 20mm. An analytical small perturbation, complex reluctance model has been derived enabling the sensor to detect coating thickness with lift-off variations of +/-5mm. This is achieved by separating the in-phase and quadrature components of the output using a phase sensitive detector. Experimental and theoretical predictions compare well (fig. 3.6.2).

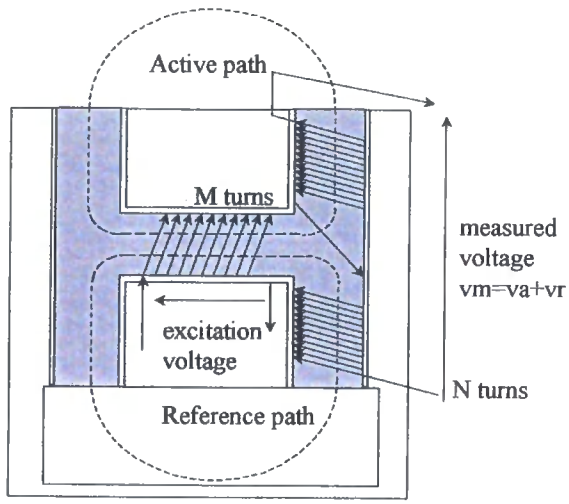

Fig. 3.6.1 Sensor to measure the coating thickness of galvanised steel strip

(Reproduced from Placko D, Clergeot H, Santander E, 'Physical modelling of an eddy current sensor designed for real time distance and thickness measurement in galvanisation industry', IEEE Trans on Magnetics, Vol. 25, No.4 , July 1989)

3.7 Material heterogeneity

In electrical steels, the magnetic properties are measured using Epstein frames or single sheet testers. These all use averaging techniques. A method known as magnetovision has been developed, which gives a picture of the non-uniformity of the magnetic properties in a sheet. This gives the capability, for example, of determination of rotational losses and the causes of eventual quality deterioration[57]. The system measures the variation in magnetic field intensity, by using one or two C-cores to magnetise the strip, and a scanning permalloy magnetoresistive sensor (fig. 3.7.1). The advantage of using this sensor is that it is small, (1 x 1mm) and can measure both dc and ac fields directly with sensitivities of $16VT^{-1}$. There are no reports on using this system on line to date.

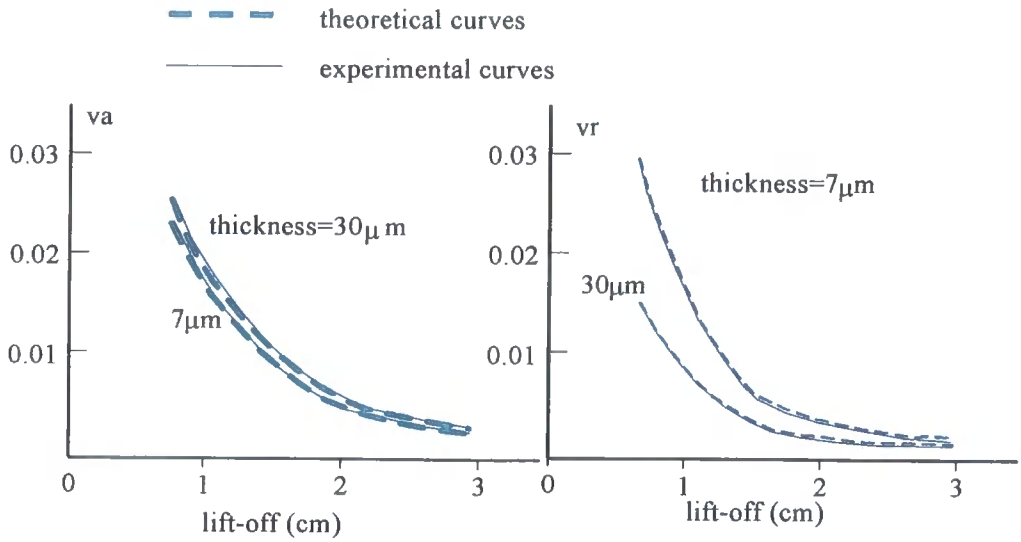

Fig. 3.6.2 Comparison of theoretical and experimental data from sensor to measure coating thickness of galvanised strip steel.

(Reproduced from Placko D, Clergeot H, Santander E, 'Physical modelling of an eddy current sensor designed for real time distance and thickness measurement in galvanisation industry', IEEE Trans on Magnetics, Vol. 25, No.4 , July 1989)

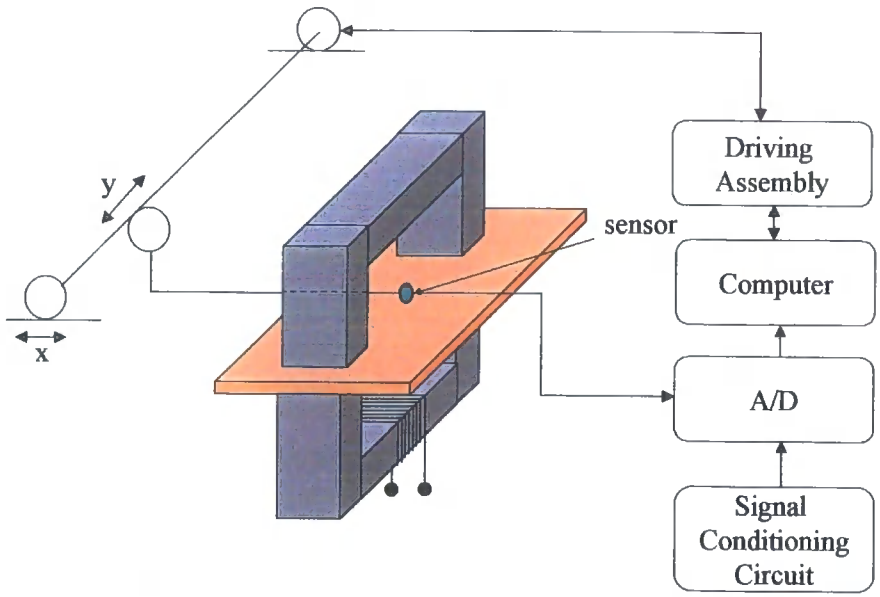

Fig. 3.7.1 Schematic of Magnetovision system

(Reproduced from Slawomir Tumanski, Marek Stabrowski, 'The magnetovision method as a tool to investigate the quality of electrical steel', Meas Sci. Technol. 9 (1998) 488-495)

3.8 Non- electromagnetic phase transformation sensing techniques

This section covers non-electromagnetic techniques, which have been used to measure or infer the austenite-to-ferrite phase transformations in steel as it cools on-line. Laboratory methods such as optical microscopy, dilatometry etc are not included. Thus three types of measurement are reported, X-ray techniques, laser ultrasonics and temperature.

3.8.1 X-ray techniques

X-rays can be used to measure phase transformation in two ways[58,59]; ionising radiation absorption and X-ray diffraction in both reflection and transmission.

Radiation absorption. In 1991 Irsid[27] measured the fraction transformed using the technique of ionising radiation absorption. The basic principle is that the flow of gamma photons emanating from an object is related to the object thickness, the apparent density and the flow of incident photons. The transformation of austenite during cooling causes a change in the thickness and volume of the product. The percentage transformation can therefore, be detected by noting the intensity of the gamma photons passing through the steel. It was found that the measurement of the quantity transformed by this method of radiation absorption worked well in the laboratory, but difficulties were encountered when transferring the technology onto a production environment, due the limited stability of the source and measurement speed of commercial production apparatus.

X-ray diffraction. This technique is based on the Bragg diffraction principle in which a collimated X-ray beam is directed at an angle to the crystallographic planes. The beam is reflected from the planes and will constructively interfere at an angle known as the Bragg angle. This is determined by the lattice spacing and the X-ray frequency ie

$$n\lambda = 2.d.\sin\theta \qquad (3.8.1)$$

where λ is the wavelength, d is the crystal spacing, θ is the grazing angle of the X-ray beam and n is an integer. Measurement of the lattice spacing gives a measure of the phases present. This is achieved by either placing detectors in fixed positions, and noting the change in intensity or using image capturing and processing techniques to determine the Bragg angles. Because steel is polycrystalline, diffraction cones are formed, but the same information can still be extracted. Laboratory equipment using this technique usually uses the reflected beam from steel samples as shown in fig. 3.8.1(a). Since most of the energy is reflected by the first few crystal layers, this reflection method only enables a very thin layer (up to 0.1mm) to be tested. The use of reflection X-ray diffraction for monitoring an austenitic production line has been reported[58]. A laboratory prototype[27] was produced, which consisted of an excitation tube and three detectors; one in the Bragg position for martensite, one for the austenite

angle and the third was used to measure the background noise. The equipment could measure variations in the martesite/austenite ratio along a steel strip. However, variations in the texture prevented comparison from one piece of strip to the next. X-ray in transmission is shown in fig. 3.8.1(b). As can be seen in the diagram, the rays are still reflected off the crystallographic planes to form a diffraction pattern. The methods of detection are identical to the reflection method. The advantage with this arrangement is that the measurement is no longer restricted to the surface layer. This method has been reported to work online in measuring texture[59].

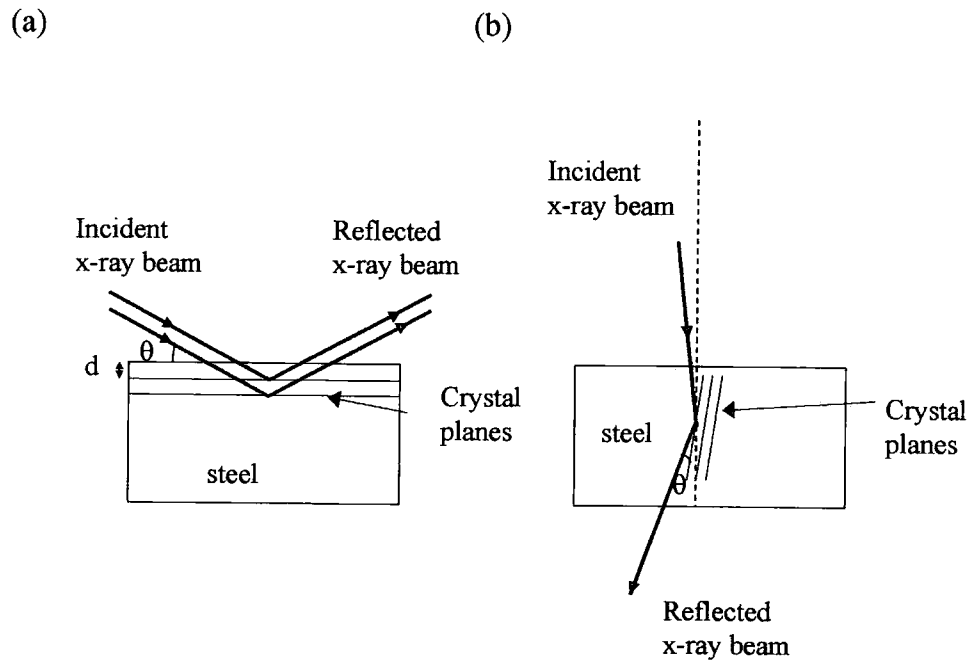

Fig. 3.8.1 X-ray diffraction in reflection (a) and transmission (b) geometries.

3.8.2 Laser ultrasonics

In this method ultrasonic waves are induced into the steel as pulses using a high energy excitation laser. This can cause visible marking on the surface, but does not significantly affect the thickness[60]. The resulting wave, which has passed through the steel, is detected by a low power laser and a Fabry-Perot interferometer. In[60] the attenuation of the wave is measured, and related to the grain size to give an indication of phase transformation. The form of the relationship depends on the ratio of the wavelength to average grain size. Work has been reported by AEA[61] on using laser ultrasonics to measure phase transformation, grain size and recrystallisation. To achieve this, wave velocity, and pulse rise times were measured in addition to attenuation.

3.8.3 Temperature

In chapter 4, it will be shown that temperature and cooling rate affect the transformation of austenite-to-ferrite and hence the final microstructure. It therefore follows that if the temperature of the steel product is measured during processing, which includes both rolling and cooling, it should be possible to calculate and hence control the percentage phase transformation of the steel on-line. British Steel (Corus UK) produced a semi-quantative predictor of profile and microstructure after the hot rolling of transformable steels[62]. The model was limited by insufficient knowledge of the roll/product frictional conditions. Hoogovens Groep BV (Corus NL) also produced an on-line model[63]. They also found limitations with their model, in that the temperature measurements were not satisfactory and the processing conditions were not totally reproducible. Since this work there have been numerous reports of the use of mathematical models to control the microstructure of steel in hot strip mills, using temperature as the input measurement. Good agreements are reported[64,65]. However, the research into other methods to measure the phase transformation directly suggests a requirement for more accurate inputs into these control models.

3.9 Summary

This chapter has cited literature which shows it is possible to measure the material properties of steel using electromagnetic sensing techniques. A summary of the methods is given in table 3.9.1. Information from this research has been used in both the design of the T-meter (chapters 7 and 8) and the MagTran (Chapter 9).

Table 3.9.1

Residual stress measurement	
Stress induced magnetic anisotropy	Unable to decouple biaxial stresses. Requires prior knowledge of principle stress directions. Surface conditions cause problems. Not suitable for on-line measurements.
Magnetoacoustic and Barkhausen emissions	Unable to decouple biaxial stresses. Require contact sensors. Not suitable for on-line measurements.
Phase transformation	
BISRA system (AC coil)	Not suitable on-line. Significance of 5^{th} harmonic not clear.
IRSID system (10kHz coil)	Only detects transformation start – skin depth effect. Electrical phase used to compensate for lift-off variations. Proven on-line. C-core design. Measures effect of phase transformation on both conductivity and permeability.
NSC system (AC coils)	Problems with protecting a coil above strip. Too sensitive to the start of transformation. Too sensitive to strip inclination.
Kawasaki system (Three ac coils)	Proven on-line. Compensates for lift-offs up to 120mm. AC method causes skin depth to change during phase transformation. Measures effect of phase transformation on both conductivity and permeability.
Force method (Permanent magnet)	Not suitable on-line. Measures permeability changes only. Measures all the way through the sample. Results validated by thermal methods.
NKK system (Two ac coils)	Sensor geometry suitable for on-line measurement. Insensitive to lift-off – no compensation required. Requires patented sensor. AC method causes skin depth to change during phase transformation. Measures effect of phase transformation on both conductivity and permeability.
Mechanical property measurement	
Magnetic flaw detector (AC coil)	Commercial instrument. Position of ferroprobe not clear. Affected by quality of surface finish. Possibly suitable for on-line measurement. Correlation with mechanical properties good.
On-line power tester (AC coils)	Commercial instrument. Algorithm required to relate to hardness. Requires contact with steel.
EMATs	Magnetostrictive type EMAT performs best. Good correlation with texture. Unaffected by strip speed. Suitable for on-line measurement.
3MA (Various methods)	Requires neural network to relate measurements to mechanical property. Needs calibrating for each sample type. Not suitable for on-line measurement.
Defect detection	
Eddy current (AC coil)	Only examines surface. Sensitive to surface cracks. Can compensate for lift-off. Measurement depth increased using saturating dc field. On-line measurement possible.
Magnetic leakage	Requires small sensors.

(AC)	Lift-off needs to be constant and small. On-line systems available.
Magnetic particle inspection	Off-line measurement only. Requires vision system for real-time measurements.
Four point probe	Off-line measurement only. Requires direct contact with test sample.
Coating thickness sensor	It has lift-off compensation using differential coils. Can be used on-line. Used for non-ferromagnetic coatings.
Magnetovision system	Only suitable for use on cold strip mills. Can detect changes in the magnetic properties of a strip.
Non-electromagnetic phase transformation measurement	
X-ray absorption	Worked well in the laboratory. Problems applying on-line due to the limited stability of the source.
X-ray diffraction	In reflection mode the measurement depth is limited. Suitable for on-line measurement. Texture variations in samples prevent comparisons being made. Expensive.
Laser ultrasonics	Suitable for on-line measurement. Expensive. Can also be used to determine grain size and recrystallisation.
Pyrometry	Indirect measurement. Only measures surface temperature. Suitable for limited number of locations on a mill. It is the most widely used measurement in the steel industry.

Summary of measurement methods

3.10 References

1. *Mikheev MN, Gorkunov ES,* 'Relationship of magnetic properties to the structural condition of a substance - the physical basis of magnetic structure analysis (review)',Inst. of Metal Physics, Ural Scientific Centre, Translated from Defektoskopiya, No.8, pp. 5-22, Aug. 1981
2. *Kusakabe T, Mihara Y,* 'Analysis of residual stresses in hot-rolled H-shapes' Trans. ISIJ, Vol. 20, 1980
3. *Wang, N,* 'Residual stress measurements - Report on a survey of residual stress measurement activities within BS technology centres', TL/RF/TN/T2214/2/98/D, Internal Report, 1998
4. *Thomas JT,* 'Residual stress in cold rolled strip and their influence on subsequent processing operations', Technical Report No.1 and 3 to 6, 1854, 1973, 2087, 2117, 2197, WL/RF/ECSC/323/1-6/92-94/D, Mar. 1992 to Feb 1994
5. *Finch DM,* 'A review of non-destructive residual stress measurement techniques', ERA Report 94-0101R, Mar. 1994
6. *Langman R,* 'Measurement of the mechanical stress in mild steel by means of rotation of magnetic field strength', NDT International, Oct. 1981
7. *Langman R,* 'Measurement of the mechanical stress in mild steel by means of rotation of magnetic field strength - part 2 : biaxial stress', NDT International, Apr. 1982
8. *Langman R,* 'The effect of stress on the magnetisation of mild steel at moderate field strengths', IEEE Trans on Magnetics, Vol. Mag-21 No.4 1985

9. *Langman R*, 'Measurements of the mechanical stress in mild steel by means of rotation of magnetic field strength - part 3: practical applications', NDT International, Apr. 1983

10. *Chikazumi S*, 'Physics of magnetism', Wiley, New York,1964

11. *Buttle DJ, Hutchings MT*, 'Residual stress measurement at NNDTC', British Journal of NDT, Vol.34, No.4 Apr. 1992

12. *Wood, MJ*, 'AEA MAPS Residual stress meter', Internal memo, BS Nov. 97 (Internal report)

13. *Buttle DJ, Dalzell W*, 'Measurement of absolute stress levels in 136 RE rail using the MAPS System', AEA Technology, AEA-TSD-0380, Dec. 1994 (Internal report)

14. *Buttle DJ, Dalzell W*, 'Measurement of absolute stress levels in 136 RE rail using the MAPS System', AEA Technology, AEA-TSD-0779, Jun. 1995 (Internal report)

15. *Titto S*, 'Residual stress handbook', Chap. 8, American Stress Technologies, Inc. Pittsburgh, PA, USA

16. *Ng HT, Yu CC, Ng DHL*, 'Domain nucleation and annihilation in a steel bar subjected to an increasing tensile load', IEEE Trans on Magnetics, Vol.32 No.5 Sep. 1996

17. *Pritchard WDN, Mallinson SL*, 'Development of a stress transducer: progress report for the period 10/3/95 to 1/9/95', TL/CI/TN/T1792/52/95/D, Aug. 1995 (Internal report)

18. *Johnstone S*, 'Residual stress sensor', TL/CI/T1797/8/96, Feb. 1996 (Internal technical brief)

19. *Johnstone S*, 'Control of straightening operations for optimisation of product' Properties submission to ECSC, Report, Jun. 1996

20. *Johnstone S*, 'Residual stress sensor', TL/CI/T1792/8/96/2, April 1996 (Internal technical brief)

21. *Middleton J C*, ' The evaluation of a magnetic device for the measurement of residual stress', SL/SF/TN/9/-/91/D, May 1991

22. *Bodin A, Marchet PA*, 'The use of thermal analysis techniques for the validation of phase transformation models', Steel Research, Vol. 65, No.3, 1994

23. *Bodin A*, 'Mechanical properties of hot rolled strip and transformation detection',Eur Com tech steel research, Report EUR 16625En, Jun. 1993

24. *Davis N, Norris P*,'A magnetic technique for on-line measurement of temperature and metallurgical state', BISRA, Internal report, Phys/TN/11/71, 1971

25. *Lacroix M, Abrigo J, Arnault L*, : Inter conf. on steel rolling, 1980, Tokyo, Vol. 2 , pp 1286-1296, 1980

26. *Labbe G, Lebon ONE, Maeder C*, 'Application of Foucault currents to the detection of the alpha transformation during the cooling of hot laminated strips', Internal report, Irsid

27. -, *IRSID*, 'On-line detection of the alpha-gamma transformation point' Draft Final Report, MCA.RCA 91318, Sep. 1991

28. *Dodd CV, Deeds WE*, 'Analytical solutions to eddy current probe coil problems', Journal of Applied Physics Vol. 39, No. 6, 1968

29. *Morita M, Hashiguchi K, Hashimoto O, Nishida M, Okano S*, 'On-line transformation detector for property control of hot rolled steel', Proc Of Met Soc of AIME symp on Acc coiling of steel, Pittsburgh, Aug. 1985

30. *Yahiro K, Yamasaki J, Furukawa M, Arai K, Morita M, Obashi M*, 'Development of coiling temperature control system on hot strip mill', Kawasaki Steel technical report, No.24, Apr. 1991

31. *Khlestov VM, Konopleva EV, McQueen HJ*, 'The hot working and transformation to ferrite of V-Mo, Nb and Nb-V steels', Canadian Metallurgical Quarterly, Vol. 35, No. 2, pp. 169-180, 1996

32. Yasuhiro M, Seigo A, 'Transformation rate-measuring method and device', Patent abstracts of Japan, 28.07.95

33. *Yasuhiro M, Akio N*, 'Method and apparatus for measurement of transformation rate', Patents abstracts of Japan, 08062181A, 08.03.96

34. *Pyatunin GA, Slavov VI*, 'Nature of the relationship between the mechanical and magnetic properties of carbon steel', Translated from Defektoskopiya, No. 11, pp. 98-103, Nov. 1978

35. *Aronson E V, Bida G V, Kamardin V M, Mikheev M N Samokhvalova L Z*, 'Possibility of magnetic testing of the impact strength of low -carbon and low alloy steel rolled products ', Defektoskopiya, No. 6 , pp. 66-72, Jun. 1978

36. *Bida GV, Sazhina EY, Tsar'kova TP*, 'Magnetic properties of quenched and tempered high-chromium steels and their potential for nondestructive evaluation', Russian Journal of Nondestructive Testing, Vol. 32, No. 8, 1996

37. *Bida GV, Kamardin VM, Tsar'kova TP, Sazhina EY*, 'Improving the informativeness of magnetic methods of checking the structures and mechanical properties of products', Russian Journal of NDT , Vol. 31, No. 12, 1995

38. *Soghomonian ZS*, 'A novel interactive computerised technique for predicting and monitoring the magnetic and mechanical properties of non-orientated silicon iron materials in real time', Pan-Armenian Science Review, 1993

39. *Beckley P, Moses AJ*, 'On-line hardness assesment of CRML steels', 13th Annual conf. on properties and applications of magnetic materials', 7-14, Illinois, Inst.of Tech, Herman Hall, Chicago, May 1994

40. *Vaidyanathan S, Moorthy V, Jayakumar T, Raj B*, 'Evaluation of carburisation depth in service exposed ferritic steel using magnetic Barkhausen noise analysis', Materials Evaluation, pp. 449-452, Mar. 1998

41. *Murayama R, Fujisawa K, Fukuoka H, Hirao M*, 'Development of an on-line evaluation system of formability in cold-rolled steel sheets using electromagnetic acoustic transducers (EMAT's)', NDT & E Int., Vol. 29, No. 3, pp.141-146, 1996

42. *Borsutski M, Thoma C, Bleck W, Theiner W*, 'On-Line determination of the material properties of cold-rolled steel strip', Stahl & Eisen, 1993, 113 (10, 13th Oct., pp..93-99

43. *Theiner WA, Fielder U, Kröning M*, 'Non-destructive evaluation of material parameters using neural networks', Mat Sc Forum, Vols. 210-213, pp.343-348, 1996

44. *Allen D R*, ' Instrumentation for inspection and quality control', Steel Times International, Dec. 1986

45. *Ploegaer H T, Van der Stel J*, 'Small inhomogeneities in flat steel products: to be seen or not to be seen?' La Revue de Metallurgie-CIT, Jan .1996

46. *Knox TJ*, 'Measurement and analysis - a basis for steel quality and customer confidence', Ironmaking and Steelmaking, Vol.18, No.3, 1991

47. -, 'Slab Defect Detector', BHP Instruments advertising booklet.

48. *Mayos M, Turon JM, Alexandre P, Salon JL, Depeyris M, Rios JC*, ' Nondestructive on-line inspection of the whole surface of continuously cast slabs', La Revue de Metallergie - CIT, Jun. 1993

49. *Hauser T, Schenk G, Bertus N, Erhard A*, 'Universal digital inspection systems for ultrasonic and pulsed eddy current techniques', Materialprufung, Vol 38, Nos. 7-8,1996

50. *Kondo M, Murashita K, Honma H, Kurashima M, Toye M, Nishinno S*, 'Magnetizing eddy current tool', NKK Tech. Review, No.76 ,1997

51. *Roberts B*, 'Computer integrated testing of rod and wire', Wire Journal Int, Sep. 1998

52. *Maki H, Tsunozaki Y, Matsuffuji Y*, 'Magnetic on-line defect inspection system for strip steel', Iron and Steel Engineer, Jan. 1993

53. *Deutsch V, Ettel P, Platte M, Cost H*, 'Crack depth measurement - state -of -the-art measurement technology for an established method', Materialprufung, Vol. 38, Nos.7-8, pp. 306-310, 1996

54. *Lang DD, Geier DP Shultz BL*, 'Butt weld inspection and weld machine diagnostic system for continuous coil processing lines', Iron and Steel Engineer, Jun. 1996

55. -, New Document Flyer by Bruel and Kjaer

56. *Placko D, Clergeot H, Santander E*, 'Physical modelling of an eddy current sensor designed for real time distance and thickness measurement in galvanisation industry', IEEE Trans on Magnetics, Vol. 25, No.4 , Jul. 1989

57. *Tumanski S, Stabrowski M*, 'The magnetovision method as a tool to investigate the quality of electrical steel', Meas Sci. Technol. Vol. 9, pp. 488-495, 1998

58. *Kitagawa H, Sohmura T*, 'An X-ray diffraction method for quantitative determination of retained austenite in the production line of metastable austenitic stainless steel', Trans. Iron Steel Inst. Jpn Vol. 23, No. 6, 1983

59. *Kopineck H-J*, 'Nondestructive testing and measuring techniques for rolling mills and rolled products', Stahl und Eisen 113. No 11 pp. 73-81

60. *Dubois M, Moreau A, Militzer M, Bussiere JF*, 'Laser-ultrasonic monitoring of phase transformation in steels', Scripta Materiala, Vol. 39, No. 6. pp. 735-741, 1998

61. *Astill AG, Tweed JH, Stacey K, Moss BC*, 'Prospects for on-line structure monitoring by laser ultrasonics for process control in rolling and heat treatment', IoM Conference on 'Measuring up to customers needs: Advances in on-line instrumentation for finishing processes in strip production',27-28 April, 1999

62. *Howe A, Beckitt F, Husain Z, Farrugia D, Ingham P, Watts G,* 'Control of microstructure and properties of wrought transformable steels', European commission technical steel research, Mechanical working (Rolling mills) EUR 14789 EN, Final Report, 30 June 1991

63. *Bodin A,* 'Mechanical properties of hot rolled strip and transformation detection', European Commission Technical Steel Research, Mechanical working (Rolling Mills) EUR 16625 EN, Final Report, 30 June 1993

64. *Colas R,* 'Mathematical modelling of hot rolling steel strip', Materials Science and Technology, Vol. 14, No. 5, pp. 388-393, May 1998

65. *Han HN, Park SH,* 'Model for cooling and phase transformation behaviour of transformation induced plasticity steel on a run-out table in hot strip mill', Materials Science and Technology, 17(6); 721-726, Jun 2001

CHAPTER 4

MAGNETISM AND STEEL

4.1 Introduction

This section describes the different types of magnetism with theories behind their existence. It introduces basic concepts used to describe ferromagnetic properties and then focuses on the metallurgical properties of steel. Finally, existing knowledge about the link between steel processing and magnetic properties is discussed. However, this is an area still under investigation.

4.2 Types of magnetism

Five basic types of magnetism exist, diamagnetic, paramagnetic, ferromagnetic, antiferromagnetic and ferrimagnetic. This section describes each of these types with particular emphasis on ferromagnetic materials.

4.2.1 Diamagnetism

All materials are magnetic. It is an extremely small effect in which the value $(\mu_r - 1)$ is small, negative, and independent of the B-field and temperature. In the atoms of an unmagnetised material, the planes of the electron orbits are orientated at random. When a magnetic field is present, these orbits precess around the field direction producing a very small field in opposition to the applied field. The effect disappears on removal of the applied field.

4.2.2 Paramagnetism

The effect of paramagnetism can be 10 to 100 times greater than diamagnetism. In this case, the orbital and spinning motions of electrons produce magnetic moments. Thermal agitation causes the individual moments to be randomly orientated. When a magnetic field is applied the moments are partially aligned, resulting in $(\mu_r - 1)$ being small, positive, linear and decreasing with temperature.

4.2.3 Ferromagnetism

This effect is much larger than either para- or dia- magnetism. It results in a relative permeability, μ_r, which is large, positive, nonlinear and dependent on previous history. Ferromagnetic materials are metallic and become paramagnetic above a

temperature known as the Curie point. The ferromagnetism is due to exchange forces between neighbouring atoms causing the magnetic moments to be aligned parallel to each other. The sign of the exchange forces (determined by the atomic separation) affects whether a material is ferromagnetic or not, and the magnitude determines the Curie temperature, at which ferromagnetism breaks down. The number of electron spins per atom that can be aligned, determines the saturation magnetisation.

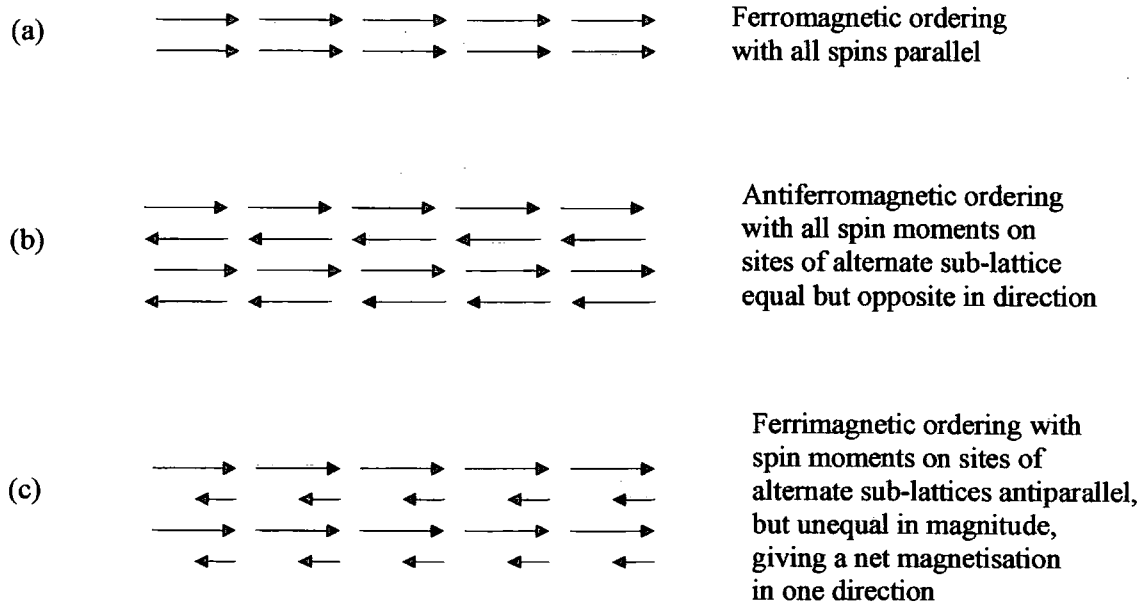

Fig. 4.2.1 Schematic of ferro-, antiferro-, and ferri- magnetic mechanisms

(Reproduced from 'M McCaig, 'Permanent magnets theory and practice', Pentech Press,1977)

4.2.4 Antiferromagnetism

In these materials, the moments in alternate atoms are ordered in an antiparallel manner. The magnetic behaviour has similarities to that of paramagnetic materials. A temperature known as the Néel point (which is analogous to the Curie point) exists, at which the antiferromagnetism is destroyed by thermal agitation. Above the Néel point, the material is paramagnetic; at the Néel point, the permeability is a maximum; and below the Néel point, the permeability falls as the temperature is reduced.

4.2.5 Ferrimagnetism

This is a class consisting of mixed oxides of iron known as ferrites. Barium, strontium and lead ferrites can be used to make permanent magnets, whereas those of manganese, nickel and zinc can be used for radio frequency transformer cores.

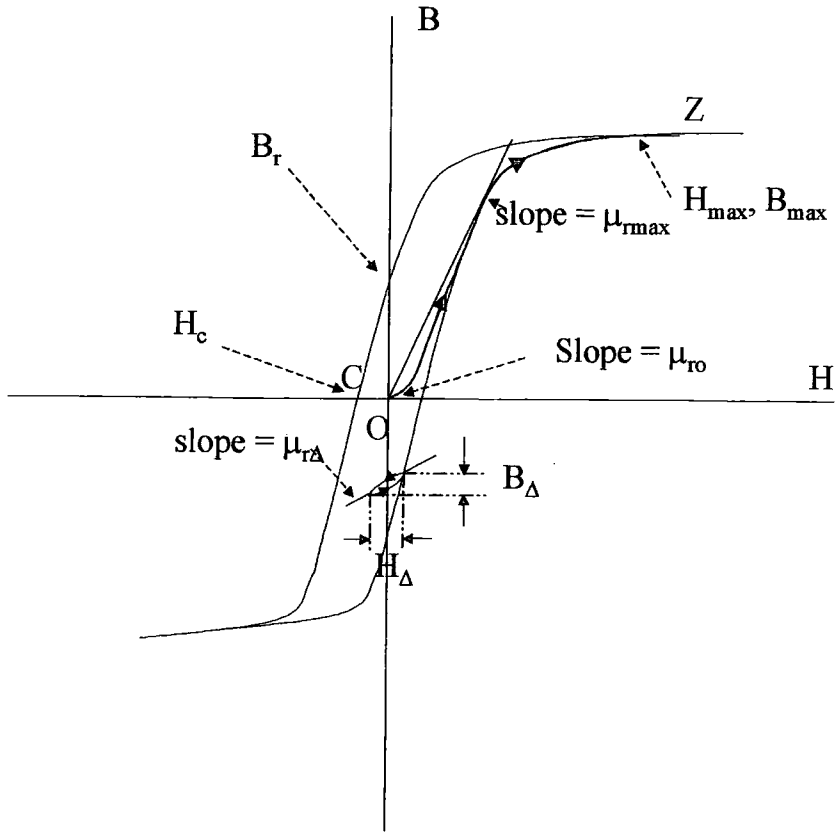

Fig. 4.3.1 Magnetisation curve (black line) and hysteresis curve (blue line)
(Reproduced from 'RM Bozorth, 'Ferromagnetism', Bell Laboratory Series, 1964)

In these materials, the magnetic moments are ordered regularly in an antiparallel sense, such that the sum of the moments pointing in one direction exceeds that of the sum pointing in the opposite direction. Fig. 4.2.1. shows a schematic of the differences between ferro-, antiferro-, and ferri- magnetic materials.

4.3 Concepts used to describe ferromagnetic materials

4.3.1 Magnetisation

The magnetisation, $\underline{M}$, is the magnetic moment per unit volume of a magnetised material at a point. If there are N atoms per unit volume, each possessing a magnetic dipole moment, $\underline{m}$ orientated in a given direction, then

$$\underline{M} = N\underline{m} \tag{4.3.1}$$

4.3.2 The magnetisation curve and hysteresis loop

If an unmagnetised ferromagnetic material is subjected to a gradually increasing $\underline{H}$-field, then $\underline{B}$ increases following path OZ (fig. 4.3.1) until the material saturates and the magnetisation increases no further. This curve is known as the magnetisation curve. If the field is then reduced, the $\underline{B}$-field now follows path ZC. Cycling the $\underline{H}$-

field between positive and negative saturation levels produces the hysteresis loop for a material. (Cycling between smaller fields produces smaller loops.) The intercept on the B-axis is called the remanence and is a measure of the retained magnetisation in the material. Permanent magnets have a large remanence. The intercept on the H-axis is called the coercivity. This is the value of the reverse field needed to demagnetise the material.

4.3.3 Relative permeability and susceptibility

The B field in a magnetic material is due to the internal magnetisation, M and the externally applied H-field as shown in equation 4.3.2.

$$\underline{B} = \mu_o(\underline{H} + \underline{M}) \qquad (4.3.2)$$

If the susceptibility, ψ_m is defined as: -

$$\underline{M} = \psi_m \underline{H} \qquad (4.3.3)$$

then the relative permeability, μ_r, can be defined as

$$\mu_r = 1 + \psi_m \qquad (4.3.4)$$

such that

$$\underline{B} = \mu_r \mu_o \underline{H} \qquad (4.3.5)$$

Due to the complex nature of the relationship between B and H in a magnetic material, several different definitions for the permeability have been produced. Four of them are described in this section. These are shown in fig. 4.3.1.

(1) The term relative permeability, μ_r, is the ratio $\underline{B}/\mu_o\underline{H}$ on the magnetisation curve, possibly over some specified range.

(2) The maximum relative permeability, μ_{rmax}, is $\left[\underline{B}/\mu_o\underline{H}\right]_{max}$.

(3) The initial relative permeability, μ_{ri}, is the ratio $\underline{B}/\mu_o\underline{H}$ at very weak fields.

(4) The differential or incremental relative permeability, $\mu_{r\Delta}$, is the ratio $d\underline{B}/\mu_o d\underline{H}$, or the slope of the magnetisation curve divided by μ_o at a given point on the hysteresis loop.

4.3.4 Demagnetisation curve

This is the part of the hysteresis loop, which lies in the second quadrant, where B is positive and H is negative (fig. 4.3.2). It is used to describe the operating region of permanent magnets (hard magnetic materials), since they are subject to fields, which tend to reduce the magnetisation. The optimal working point occurs when the product |BH| is a maximum. This gives the strongest flux density with the smallest volume of material. A 'keeper' of soft iron with a high relative permeability is used to reduce the demagnetising field to almost zero.

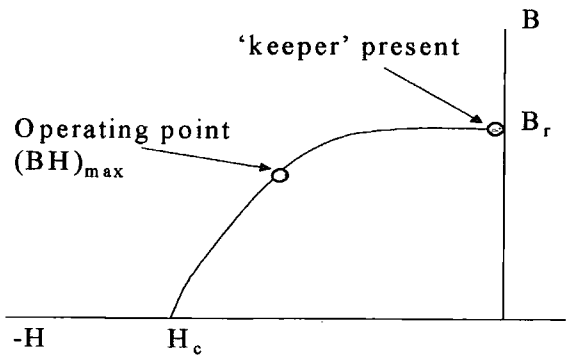

Fig. 4.3.2 Demagnetisation curve

The demagnetising field is dependent on the geometry of the sample. For short cylinders or rectangular blocks with uniform magnetization, the mean demagnetising field is usually calculated numerically and then a mean demagnetization factor derived.

4.3.5 Domain theory

A domain can be described by considering crystals of iron and nickel in the absence of any external magnetic fields or stresses as shown in fig. 4.3.3. In iron, the direction of magnetisation proceeds most easily along the crystal axes. It is therefore concluded that in a domain of crystal iron, the magnetisation is always parallel to only one of the crystal axes, provided there are no external fields or stresses. This gives rise to six possible directions. Therefore, 1/6 of the domains will be in each of these easy directions. In nickel, there are eight easy directions since the direction of magnetisation proceeds most easily in the direction parallel to the body diagonal of the cube. Therefore, 1/8 of the domains in unmagnetised nickel will be each of these easy directions. In each domain, the magnetisation, M, is equal to the saturation

magnetisation of the material at a given temperature. The magnetic moment of a domain depends on both the magnitude and direction of magnetisation and the volume of the domain as shown in equation 4.3.1.

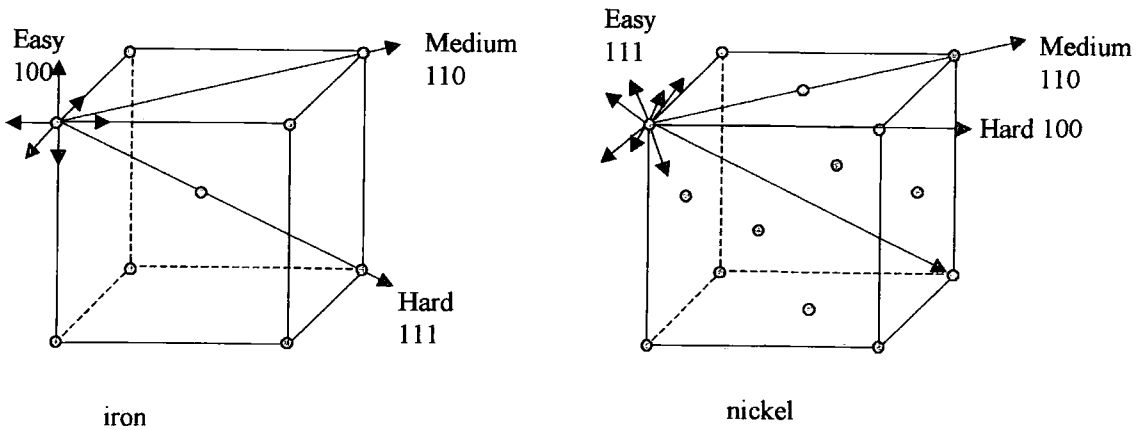

Fig. 4.3.3 Ease of magnetisation in directions, 100,110 and 111 in iron and nickel
(Reproduced from 'RM Bozorth, 'Ferromagnetism', Bell Laboratory Series, 1964)

The bulk magnetisation of a ferromagnetic object is changed by either a change in the direction of the magnetisation of the domain by 'rotation,' and/or a change in the volume of the domain by 'moving boundaries.' The magnetisation curve can be identified using the following processes (fig. 4.3.4):

1) Reversible boundary displacement
2) Irreversible boundary displacement
3) Reversible rotation.

(A detailed survey of theories of domain boundary movement is given in Mikheev and Gorkunov[1]).

4.4 Steel

4.4.1 Definition of steel

Steel is the term given to an alloy of iron and carbon. The carbon content is typically below 1%. To tune the properties, other alloying additions can be added. These include manganese, chromium, molybdenum, nickel, niobium, titanium, vanadium, aluminium and nitrogen. Steel can be divided into three main categories which are determined by the alloy content.

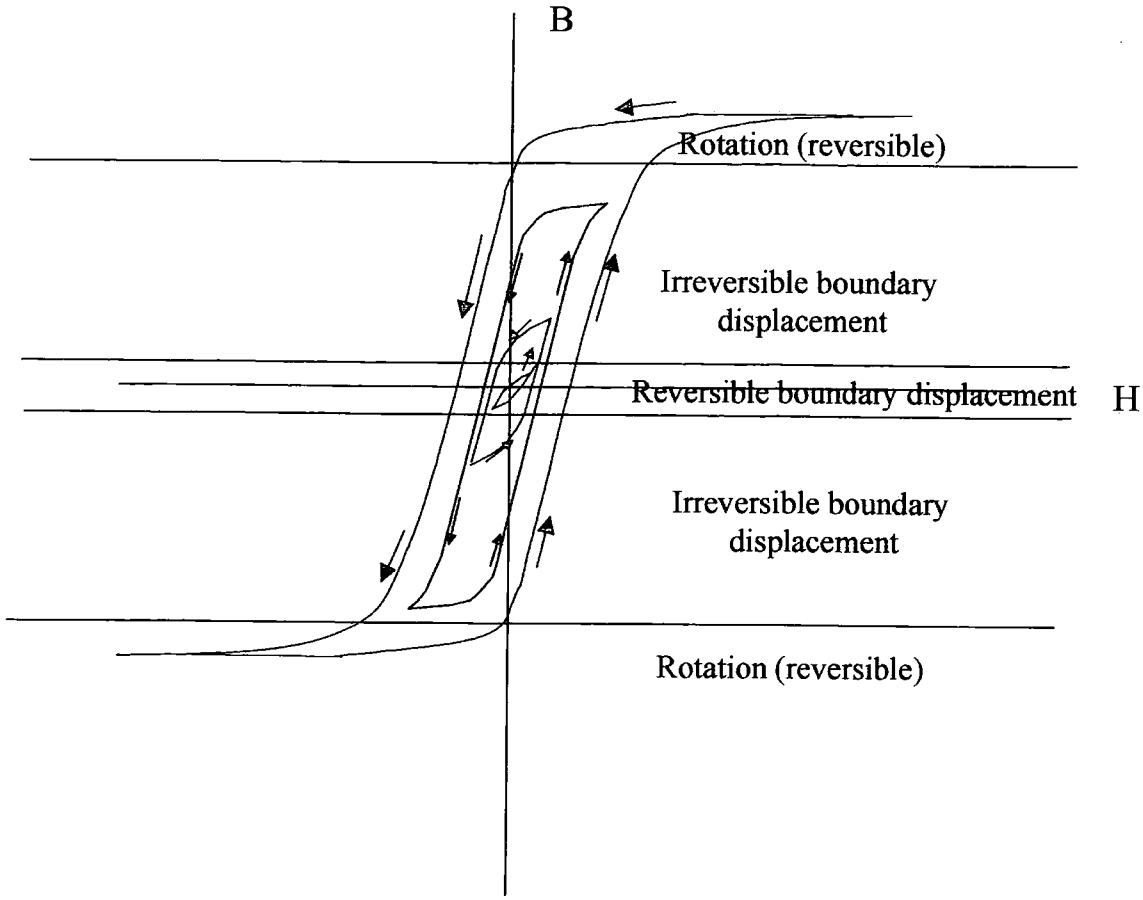

Fig. 4.3.4 Relationship between domain processes and hysteresis loops

(Reproduced from 'RM Bozorth, 'Ferromagnetism', Bell Laboratory Series, 1964)

1) **Microalloyed** steel. This contains less than 0.2% of carbon and 1.75% of manganese; the total percentage of niobium, aluminium, titanium and vanadium is less than 0.1% and possibly about 0.002% of boron.

2) **Low alloy** steel. This contains up to 1% carbon and a total maximum of 5% of manganese, chromium, molybdenum and nickel.

3) **High alloy** steel. In this type, the total alloy content is between 5 to 50%, eg stainless steel.

4.4.2 Crystal structure

Pure iron consists of two different crystal structures depending on the temperature. There exists a high temperature phase called austenite or gamma-iron. It exists above 910°C and has a face centred cubic structure as shown in fig. 4.4.1(a). Each cube has one atom in the centre of the cube face, which gives it a close packed structure in which the atoms are stacked in layers. It has a density of 8.0×10^3 kg/m^3. Below 910°C, a low temperature phase known as ferrite or alpha–iron exists. It also exists

between temperatures of 1400 and 1535°C. This phase has a body centred cubic structure as shown in fig. 4.4.1(b). It is not close packed and has a density of 7.8×10^3 kg/m^3. The austenite has a larger cube length and is more dense. Hence, when there is a phase change there is a volume change associated with it. This is the principle behind dilatometry.

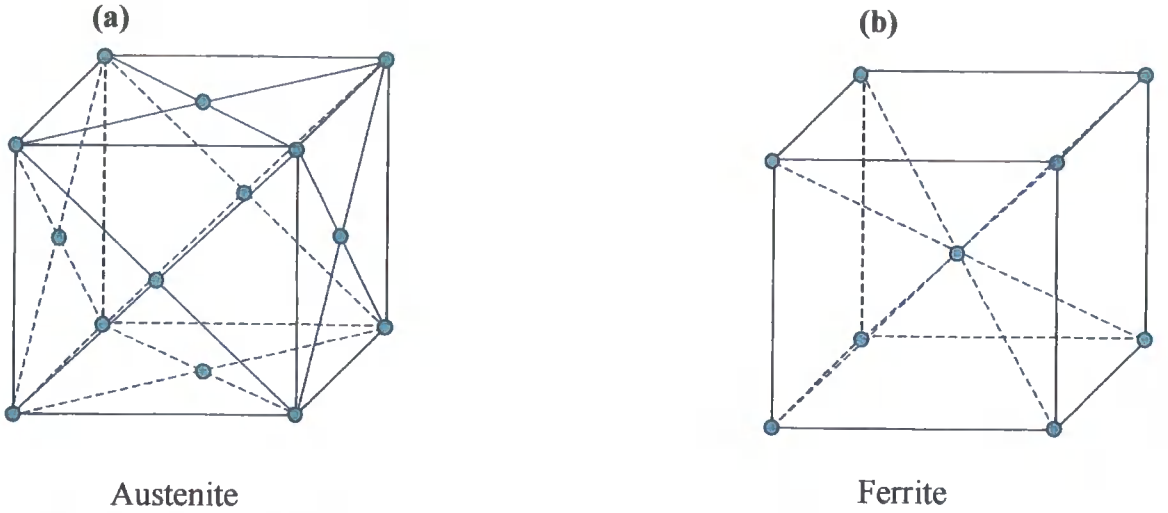

Fig. 4.4.1 Crystal structure of iron

(Reproduced from 'PF Morris,'Basic metallurgy course', Teesside Tech Ctr. British Steel Dec. 1998)

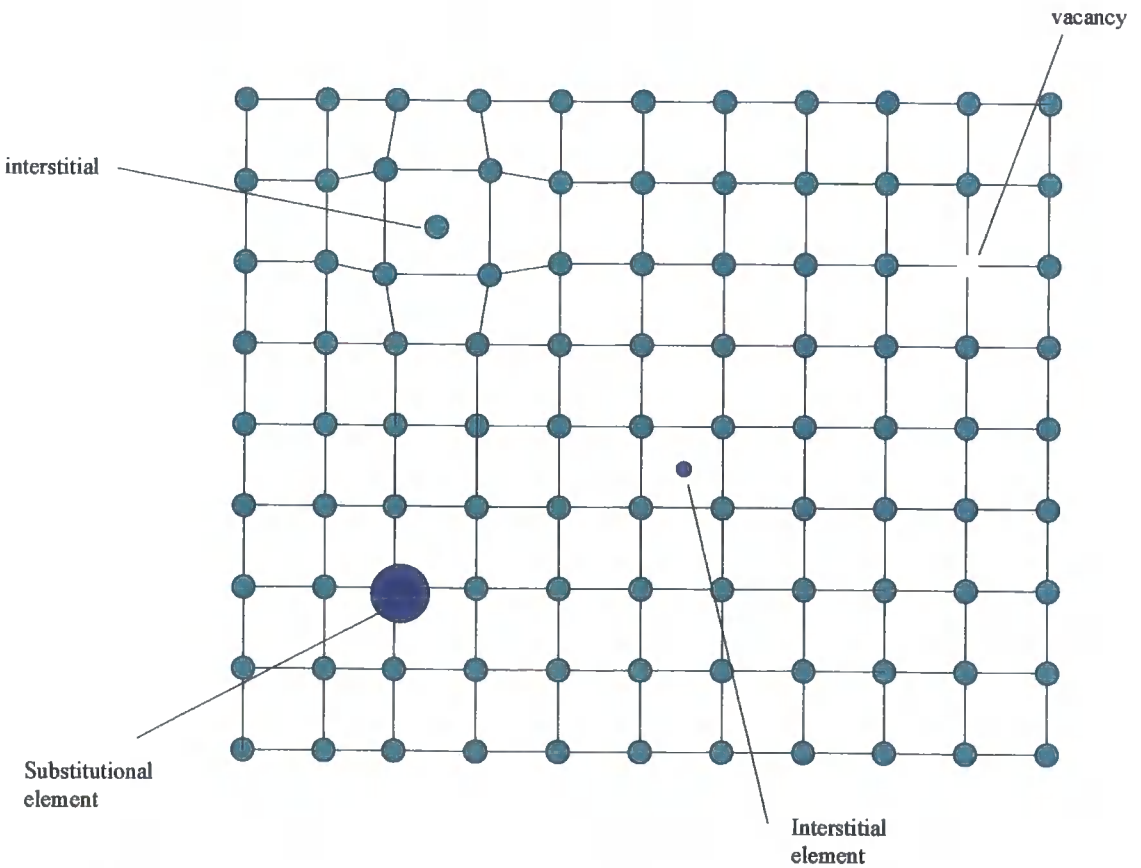

Fig. 4.4.2 Alloying elements and lattice defects in steel

(Reproduced from 'PF Morris,'Basic metallurgy course', Teesside Tech Ctr. British Steel Dec. 1998)

To produce steel, alloying additions are added. These are dissolved into the iron lattice in the form of precipitates to enhance the mechanical properties. However, compounds can be present in the form of inclusions. These are usually unwanted and worsen the steel properties. Additions can be 'dissolved' into the crystal lattice by two mechanisms. Small atoms such as carbon, nitrogen and boron fit in the spaces between the iron atoms as shown in fig. 4.4.2. These are known as interstitial elements and the resulting structure is referred to as an **interstitial solid solution**. Atoms such as manganese, chromium and titanium, which are too large to fit into the spaces, replace the atoms in the main lattice to form a **substitutional solid solution**. Fig. 4.4.2 also shows two other features which can occur in the lattice. The first is that the iron atoms themselves can occupy interstitial sites. The other is a vacancy, ie an unoccupied lattice site. Vacancies exist naturally in steel. However, the amount of them increases rapidly during deformation processes, eg hot rolling. It is the presence of vacancies and intersticials, which allows atoms to move around or **diffuse**. It should be noted, however, that interstices move faster than vacancies.

To complete the picture of a crystal lattice, the concept of imperfect lattices and dislocation movement is needed. Dislocations occur when there are incomplete planes of atoms which results in a dislocation core (fig. 4.4.3). When a stress is applied the atom (A) at the end of the plane bonds with atom (B) in the next plane, and the dislocation moves one plane through the crystal. This process repeats itself until the dislocation has moved to the edge of the crystal. In a typical steel undergoing hot rolling, there are about 10^{11} - 10^{12} dislocations per m^2. The structure then becomes unstable and recrystallisation occurs (see section 4.4.3).

4.4.3 Recrystallisation and grains

Section 4.4.2 dealt with concepts relating to regular crystal lattices. Steel is a polycrystalline material. It does contain atoms arranged in regular crystal lattices, but the regions in which the lattice is maintained are relatively small. These individual metal crystal regions are known as **grains**. They are separated by disordered boundaries, which are narrow (four atom diameters) and strong. New grains are defined when one solid crystalline structure recrystallises and forms regions of the new structure. To illustrate this process, the deformation of austenite at high temperature will be used. As the austenite is deformed, the new crystal structure

nucleates as embryos on suitable sites. In this case, it is the existing disordered grain boundary regions. An interface is therefore created between the embryo and the original (parent) austenite lattice. This interface moves outwards, as individual atoms move across it to take up their new positions in the crystal structure. The final grain size associated with the recrystallised structure depends on two factors:

1) The grain size of the parent structure. This determines the number of boundaries and hence nucleation sites. Large grains have fewer boundaries and hence the final structure will be coarse.
2) The temperature at which recrystallisation occurs.

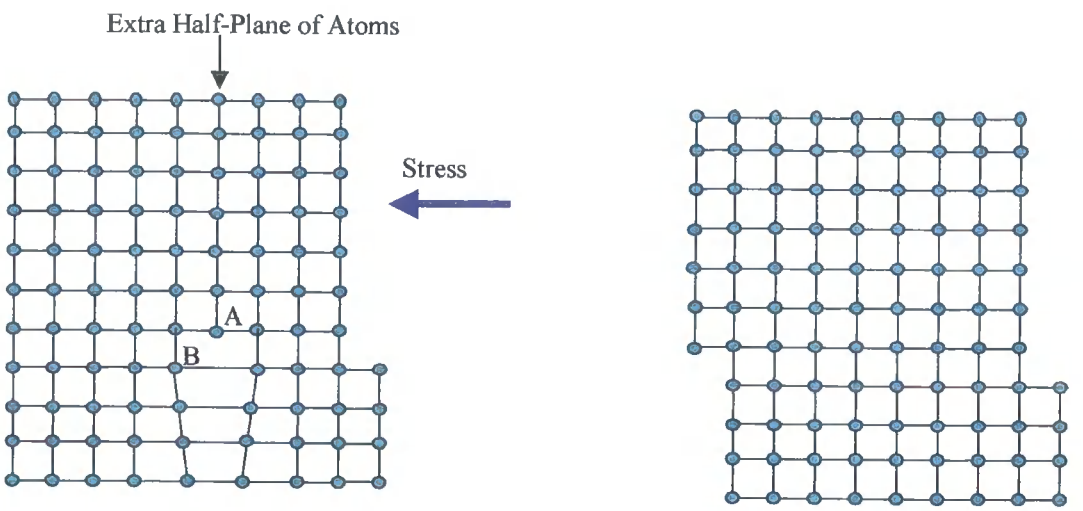

Stress induced Dislocation Movement **Crystal after passage of Dislocation**

Fig. 4.4.3 Dislocation movement in a crystal lattice

(Reproduced from 'PF Morris,'Basic metallurgy course', Teesside Tech Ctr. British Steel Dec. 1998)

At high temperatures, there are high diffusion rates, which results in the elimination of the newly formed boundaries. This reduces the number of nucleation sites, and increases the grain growth. The result is a coarse grain structure. At low temperatures, many nuclei become active. However, because of the low diffusion rates the grains grow slowly. The result is a fine grain structure. Controlled rolling, in which the steel is rolled at lower defined temperatures, is used to produce a finer austenite grain structure. Finer structures are associated with products with better mechanical properties such as high tensile strength, good ductility and toughness. However, electrical steels have larger grains since these structures have better magnetic properties, eg higher permeabiliy, low power loss etc.

4.5 Ferritic phases

4.5.1 General concept of phase transformation

Four distinct phases feature in this category: pearlite, upper and lower bainite and martensite. To explain the general concept behind the phase transformation from austenite to ferrite, the iron-carbon equilibrium diagram is required (fig. 4.5.1). Consider steel containing 0.2% carbon cooling from 900°C (ignoring the cooling kinetics). Because the austenite crystal lattice is larger than that of ferrite, all of the carbon can be dissolved in its interstices. At point A, ferrite nucleates. Ferrite can only hold 0.02% carbon, hence the unwanted carbon dissolves back into the remaining austenite, which then has a higher carbon content. This is represented by point B. This process of ferrite nucleating and the austenite carbon content increasing, proceeds until the eutectoid temperature at point C is reached. At this stage, the remaining austenite transforms to a mixture of ferrite and iron carbide (cementite). The resulting structure depends upon the grain size of the austenite and the rate of cooling. During the phase change heat is released. This is known as recalescence.

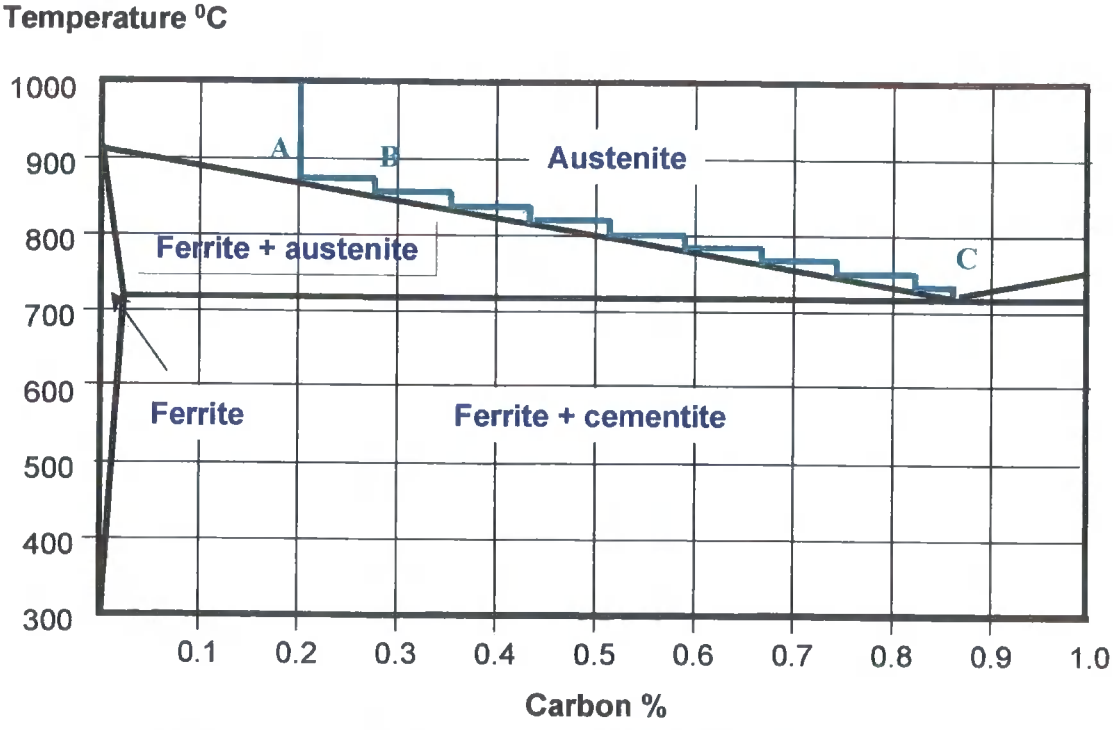

Fig. 4.5.1 Iron-carbon equilibrium diagram

4.5.2 Pearlite

This structure occurs when the cooling rate is sufficiently slow or at a suitable temperature of isothermal transformation, such that the carbon atoms can diffuse rapidly enough to precipitate out from the austenite together with the ferrite as shown

in the iron-carbon diagram. In eutectoid steels (steels of composition C in fig 4.5.1), the pearlite nucleates on austenite grain boundaries. In lower carbon steels, the nucleation occurs on the ferrite-austenite grain boundaries. In either case, growth occurs by carbon and iron atoms crossing the interface of the pearlite and austenite. The cementite and ferrite layers grow such that they can maintain contact with the interface to avoid the energy needed for renucleation. The resulting structure is a planar structure (fig. 4.5.2 (a)). Increasing the cooling rate or lowering the isothermal transformation temperature results in more nucleation and slower diffusion of the carbon. Thus, the platelets of carbide are thinner and more closely spaced.

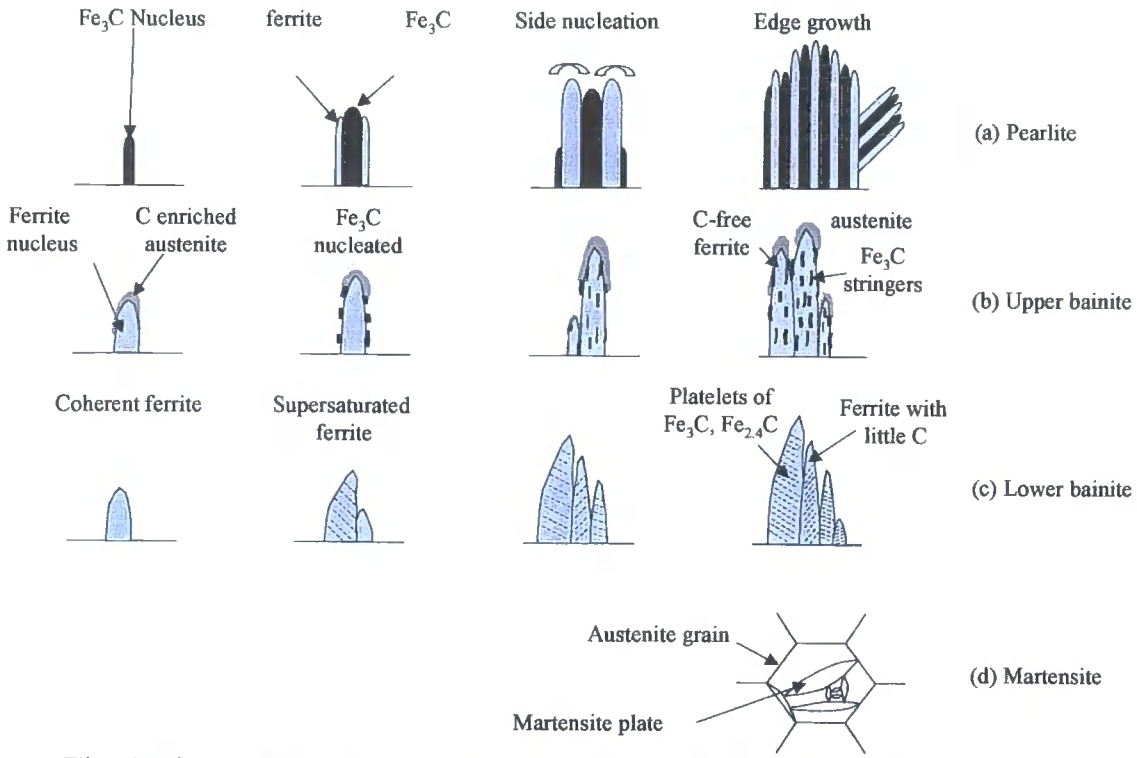

Fig. 4.5.2 Diagrammatic representation of the formation of pearlite, bainite and martensite on grain boundaries

(Reproduced from 'PF Morris,'Basic metallurgy course', Teesside Tech Ctr. British Steel Dec. 1998)

4.5.3 Bainite

This exists in two main forms: upper and lower bainite. It occurs when the austenite is cooled faster, or when the isothermal transformation temperature is lower, than that causing ferrite and pearlite. Increasing the rate of cooling depresses the transformation temperature. In upper bainite, plates of ferrite form by again nucleating on the parent austenite grain boundaries, but this time they grow into the austenite lattice. Due to the lower transformation temperature, there is less atomic movement across the ferrite

austenite interface. Therefore, the ferrite grain grows fastest, when both it and the austenite are orientatated, such that the resulting atomic displacements within the crystal lattice are small. Because of this, the transformation is said to be 'orderly' and the carbon atoms form carbides by growing between the bainite ferrite plates (fig. 4.5.2(b)). Lower bainite occurs at lower transformation temperatures. In this phase, the ferrite transformation becomes more orderly, to the extent that most of the ferrite-austenite interfaces have a regular crystallographic relationship. In this case, the carbon atoms are retained within the ferrite where they form iron carbides by reaction within the newly formed bainitic ferrite. The carbides are precipitated as a fine dispersion within the bainite with a well-defined crystallographic orientation relationship between the carbide and the parent ferrite crystals (fig. 4.5.2(c)).

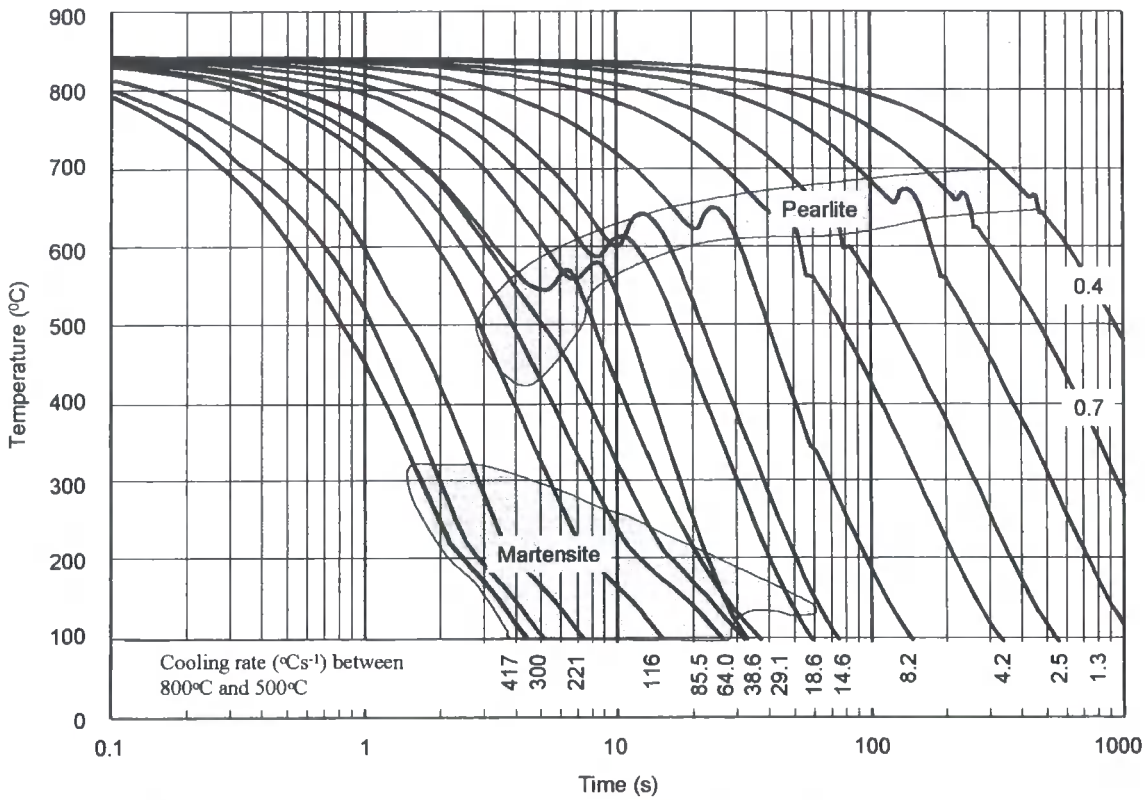

Fig. 4.5.3 Continuous Cooling Transformation Diagram

4.5.4 Martensite

This occurs at very high cooling rates, such that there is not enough time for any diffusional movement of either the iron or carbon atoms. In this phase, the ferritic lattice forms as a series of platelets by a process of local shearing of the austenite crystal structure. The crystallographic relationship between the austenite and ferrite is good. However, there is no time for the carbon atoms to form carbides, thus the

carbon is retained within the ferrite lattice by distorting it. The resulting structure (fig. 4.5.2(d)) is supersaturated ferrite, which has a crystal structure closely related to, but distinct from body centred ferrite. To ensure this phase transformation is complete, the temperature must continuously decrease. The resulting structure is hard and brittle.

4.5.5 The isothermal transformation diagram

When controlling the structure of steel, both the transformation temperatures and the time taken for the phase transformation to complete are needed. These are chosen using an isothermal transformation diagram. To construct such a chart, small specimens are heated until they are austenised. Then they are quenched rapidly to the chosen temperature and held for a specified time. The structure is then quenched to room temperature to examine the extent of the transformation. These diagrams are of great use when the type of cooling rates encountered during processing is superimposed on it (fig. 4.5.3). They are often referred to as continuous cooling diagrams and give more useful information about the structure than the equilibrium iron-carbon diagram.

To show how these diagrams work in practice, consider fig. 4.5.3. The start of the pearlite transformation at 500°C, occurs when the sample has been quenched rapidly to 500°C and held at that temperature for about 2.8s. Hence the equivalent cooling rate is calculated as 825/2.8 which gives $116°Cs^{-1}$ as shown on the diagram.

4.5.6 Steel processing and magnetic properties

In this section, existing knowledge on how the processing of steel affects magnetic properties is presented. However, the research to develop a transformation meter and other ongoing projects, IQUEST (Improving Quality Using Electromagnetic Sensing Techniques) should reveal more detailed information.

4.5.6.1 Heat treatment

It has been shown that the rate of cooling or the temperature of isothermal transformation affects the final crystal structure. It was found that as the cooling rate increases, in general, the resulting structure was more 'ordered'. In the case of martensite, the resulting structure is a distorted body centred ferrite structure. The rapid cooling needed to produce this structure not only produces a mechanically hard material, but also one that is magnetically hard (ie large remanence and coercivity).

Because the direction of a domain is determined by the directions of the crystal lattices, a single lattice of steel (if it were to exist) would have only six preferred directions of magnetisation (see section 4.3.5 for iron). Therefore, the energy needed for the domains to either rotate or grow will be less than if the material is polycrystalline. Therefore, increasing the grain size in polycrystalline steel increases the permeability and remanence but decreases the coercivity. Annealing a martensitic steel enables the carbide to be precipitated from the supersaturated ferrite lattice. The higher the annealing temperature, the more pronounced the precipitation. This acts to produce a small increase in the remanence, but a significant decrease in the coercivity.

4.5.6.2 Composition

Commercial steels contains carbon additions up to 0.8% wt. Although iron carbide or cementite is itself magnetic below 200 ^{0}C, increasing the percentage carbon in steel increases the distortions in the martensite lattice and produce more carbide precipitates in bainite and pearlite structures. The net result is a decrease in the average magnetic moment of the iron atoms, which in turn decreases the saturation B-field, and the permeability. This decrease is more pronounced in quenched rather than annealed steels. Manganese is usually added to steel to facilitate the hot rolling process. Steels which contain about 0.8% wt. of manganese are often referred to as carbon-manganese steels. The addition of this element acts to move the eutectoid point in the iron-carbon equilibrium diagram, ie no new phases are produced. Thus metallurgists often calculate an equivalent carbon content from both the carbon and manganese percentages. It is assumed that manganese has little effect on the magnetic properties of carbon steels.

4.6 Summary

This chapter has covered the basic magnetic and metallurgical concepts which are needed in the design of an instrument to measure phase transformation. It can be seen that the sections linking magnetic and metallurgical properties are limited. This is because the research in this area is also limited and emphasises the need for further work in this area.

4.7 References

1 *MN Mikheev, ES Gorkunov*, Relationship of magnetic properties to the structural condition of a substance – the physical basis of magnetic structure analysis (review), Defektoskopiya, No 8 pp5-22, August 1981

4.8 Bibliography

McCaig M, 'Permanent magnets in theory and practice', Pentech Press 1977

Lorrain P, Corson DP, Lorrain F, 'Electromagnetic fields and waves', 3rd Ed. WH Freeman & Co. 1988

Morris PF, 'Basic metallurgy course', Teesside Tech Ctr. British Steel, Dec.1998

Bozorth RM, 'Ferromagnetism', Bell Laboratory Series, 1964

Craik D, 'Magnetism: Principles and applications', Wiley, 1998

Jones IP, 'Material science for electrical and electronic engineers', Oxford University Press 2001

CHAPTER 5

ELECTROMAGNETIC THEORY

5.1 Introduction

This chapter reviews the basic electromagnetic theory required for designing and analysing the phase transformation detectors described in Chapters 6 – 9. This section can be excluded for readers experienced in electromagnetics. Since numerical methods are assessed for the calibration of the T-meter in Chapter 10, its theory and the Ansoft Maxwell package are also described. To put numerical methods in context, sections on analytical methods are included for completeness.

5.2 Maxwell's equations

The general form of Maxwell's differential equations are shown in table 5.2.1. They therefore apply to nonhomogeneous, nonlinear and nonisotropic media. The corresponding integral equations are shown in table 5.2.2.

Table 5.2.1

$\nabla \cdot \underline{D} = \rho$	$\nabla \cdot \underline{B} = 0$
$\nabla \times \underline{E} = -\frac{\partial \underline{B}}{\partial t}$	$\nabla \times \underline{H} = \underline{J} + \frac{\partial \underline{D}}{\partial t}$

Maxwell's equations in differential form

Table 5.2.2

$\oint_S \underline{D} \cdot \underline{dS} = \int_\tau \rho . d\tau$	$\oint_S \underline{B} \cdot \underline{dS} = 0$
$\oint_L \underline{E} \cdot \underline{dl} = -\frac{d}{dt} \int_S \underline{B} \cdot \underline{dS}$	$\oint \underline{H} \cdot \underline{dl} = \int_S \left[\underline{J} + \frac{\partial \underline{D}}{\partial t} \right] \cdot \underline{dS}$

Maxwell's equations in integral form

5.3 Vector potential

The magnetic flux density can be expressed in terms of a vector known as the vector potential, $\underline{A}$. Since $\nabla . \underline{B} = 0$, there exists a function, which satisfies equation

$$\underline{B} = \nabla \times \underline{A} \tag{5.3.1}$$

$\underline{A}$ is not uniquely defined by $\underline{B}$, but it does have a definite value for a given current distribution, ie

$$\underline{A} = \frac{\mu_0}{4\pi} \int_\tau \frac{\underline{J}}{r} d\tau \tag{5.3.2}$$

where r is the distance between the current source and observation point. The Laplacian of $\underline{A}$ for static fields is given by

$$\nabla^2 \underline{A} = -\mu \underline{J} \tag{5.3.3}$$

This is Poisson's equation. It can also be shown that for static fields and currents of finite extent the divergence of $\underline{A}$ is zero. Since the curl of the electric field intensity is dependent on the time derivative of $\underline{B}$, and $\underline{B}$ is dependent on the curl of $\underline{A}$, it follows that $\underline{E}$ and $\underline{A}$ are parallel and that the time derivative of $\underline{A}$ contributes to $\underline{E}$ giving

$$\underline{E} = -\nabla V - \frac{\partial \underline{A}}{\partial t} \tag{5.3.4}$$

5.4 Boundary conditions

Consider a boundary between two media. Let the tangential components in medium 1 be $\underline{H}_{T1}$ and $\underline{E}_{T1}$ and the normal components be $\underline{D}_{N1}$ and $\underline{B}_{N1}$. Similarly for medium 2 the components are $\underline{H}_{T2}$, $\underline{E}_{T2}$, $\underline{D}_{N2}$ and $\underline{B}_{N2}$. If J_s and ρ_s are the surface current and charge densities, and $\underline{a}_n$ is the vector normal to the boundary, then the boundary conditions can be defined as shown in table 5.4.1.

Table 5.4.1

Tangential components	Normal components
$\underline{a}_n \times (\underline{H}_1 - \underline{H}_2) = \underline{J}_S$	$(\underline{D}_1 - \underline{D}_2) \cdot \underline{a}_n = \rho_s$
$\underline{a}_n \times (\underline{E}_1 - \underline{E}_2) = 0$	$(\underline{B}_1 - \underline{B}_2) \cdot \underline{a}_n = 0$

Boundary conditions

5.5 Time harmonic form of Maxwell's equations

This form of the equations describes sinusoidal steady-state fields as phasors with both an amplitude and phase. Thus Maxwell's differential equations can be re-written in phasor form as shown in table 5.5.1.

Table 5.5.1

$\nabla \cdot \underline{\underline{D}} = \rho$	$\nabla \cdot \underline{\underline{B}} = 0$
$\nabla \times \underline{\underline{E}} = -j\omega\mu \underline{\underline{H}}$	$\nabla \times \underline{\underline{H}} = \underline{J} + j\omega\varepsilon$

Time harmonic Maxwell's equations in differential form

5.6 Finite element methods

In this section two equations, which are frequently used to describe potential distributions in electromagnetic problems are considered, the Laplace and Poission equations.

5.6.1 Source free region

Potentials in source free regions can be described by the Laplace equation which is of the form

$$\nabla^2 u = 0 \qquad (5.6.1)$$

As shown in section 5.8, it can be solved by the separation of variables or finite difference methods. However, an approximate solution can be found for a potential distribution u, by considering the stored energy W(u) as a simple function, which can be minimised to determine the unknown parameters. Virtually all finite element methods follow some variation of this technique which is outlined below.

Let u(x,y) be the solution of the problem, and the boundaries defined as either a value of u or its derivative *d*u/*d*n. A function h(x,y) is defined and has the properties:

1) It is sufficiently differentiable.
2) It has a value of exactly zero at every boundary point where a value of u has been prescribed. Therefore, the value of (u+kh) where k is a scalar parameter has the same prescribed boundary values as u.

The energy W(u) associated with u in two dimensions is given by

$$W(u) = \frac{1}{2}\int |\nabla u|^2 \, dS \qquad (5.6.2)$$

This is referred to as a functional of u (the function of the function, u). The energy associated with W(u+kh) is given by

$$W(u+kh) = W(u) + k\int \nabla u \cdot \nabla h . dS + \tfrac{1}{2}k^2 \int |\nabla h|^2 \, dS \qquad (5.6.3)$$

Applying Green's theorem to the middle term on the right gives

$$W(u+kh) = W(u) + k^2 W(h) - k\int h\nabla^2 u\, dS + k \oint h\frac{\partial u}{\partial n}\, dS \qquad (5.6.4)$$

The third term vanishes due to u being an exact solution to Laplace's equation. The last term on the right also vanishes since either h or *du/dn* equals zero at every boundary point. The resulting equation therefore reduces to

$$W(u+kh) = W(u) + k^2 W(h) \qquad (5.6.5)$$

Since k^2 is always positive the minimum of the function is W(u).

5.6.2 Construction of elements

Two dimensional, first-order elements are described to show the principles behind their construction. The basic idea is to subdivide the region into triangular elements and then approximate the potential u within the elements. The potential distributions then have to be interrelated in the various elements such that the potential is continuous across inter-element boundaries.

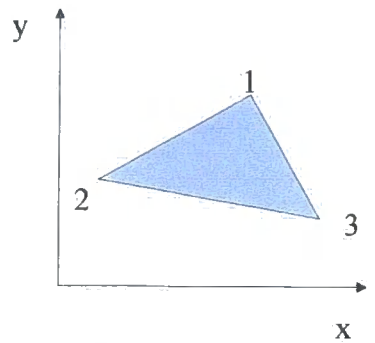

Fig. 5.6.1 Typical triangular element in the x-y plane

In the first order case, the potential at each node (or vertex) of a triangle (fig. 5.6.1) is given by

$$\begin{bmatrix} U_1 \\ U_2 \\ U_3 \end{bmatrix} = \begin{bmatrix} 1 & x_1 & y_1 \\ 1 & x_2 & y_2 \\ 1 & x_3 & y_3 \end{bmatrix} \begin{bmatrix} a \\ b \\ c \end{bmatrix} \qquad (5.6.6)$$

Where a,b and c are coefficients and the subscripts identify the nodes. The potential at any point in the element, u(x,y) can then be found by solving for a,b,c . The element energy, W^e, can then be calculated by substituing U into

$$W^e = \tfrac{1}{2}\int |\nabla U|^2\, dS \qquad (5.6.7)$$

and solving for W^e. Therefore, the total energy from all the elements is given by

$$W = \sum_{allelements} W^e \tag{5.6.8}$$

To ensure continuity across the triangles the potentials at common nodes are forced to be equal.

5.6.3 Modelling regions with sources

Poisson's equation can be used to describe regions in which source distributions are present. An example of this is the vector potential equation for static fields as described in Section 5.3.

$$\nabla^2 \underline{A} = -\mu \underline{J} \tag{5.6.9}$$

For the case of a two-dimensional current source problem giving a potential distribution u the energy functional which can be minimised to solve Poisson's equation is given by

$$F(u) = \tfrac{1}{2}\int |\nabla u|^2 dS - \mu_0 \int uJ\, dS \tag{5.6.10}$$

Green's theorem and consideration of boundary conditions can be used to reduce equation 5.6.10 to equation 5.6.11

$$F(A+kv) = F(A) + \tfrac{1}{2}k^2 \int |\nabla v|^2\, dS \tag{5.6.11}$$

where A is the correct solution, k is a scalar parameter and v is a differentiable function which vanishes at the boundaries. It can be seen that a minimum is reached when k=0. However, it should be noted that the field energy is still calculable using

$$W = \tfrac{1}{2}\int |\nabla A|^2 dS \tag{5.6.12}$$

or

$$W = \frac{\mu_0}{2}\int AJ\, dS \tag{5.6.13}$$

The current densities at the element nodes are prescribed and are therefore known. As in the case of the potentials, the value of J at a particular location (x,y) within and element is given by

$$J(x,y) = \begin{bmatrix} 1 & x & y \end{bmatrix} \begin{bmatrix} 1 & x_1 & y_1 \\ 1 & x_2 & y_2 \\ 1 & x_3 & y_3 \end{bmatrix}^{-1} \begin{bmatrix} J_1 \\ J_2 \\ J_3 \end{bmatrix} \tag{5.6.14}$$

This is then substituted into the second term on the right-hand side of equation 5.6.10. In general, there is no need for source densities to be continuous across inter-element boundaries. The first term on the right hand side is identical to the energy term used to solve the Laplace equation, and therefore the solution process for this term is also the same.

5.6.4 Functionals

Corresponding to any electromagnetic partial differential equation, it is possible to derive a functional F, which can be expressed in terms of the dependent variables of the equation. These can be field or potential variables. The functional is obtained by integrating over the volume of the problem space. It has the property of being stationary, as either a maximum, minimum or point of inflection about the correct set of functions representing the required solution, subject to the boundary constraints. Functionals for both Laplace's and Poisson's equations have been used. These equations are both special cases of the inhomogeneous Helmholz equation given in equation 5.6.15

$$\nabla \cdot (p\nabla u) + k^2 u = g \qquad (5.6.15)$$

where u is a scalar potential which is a function of position, k is a constant, p(x,y,z) is a function representing the material properties, and g(x,y,z) is a driving function.

Suitable boundary conditions for this type of problem are either

i) **Dirichelet**, where the value of u(x,y,z) is given on the boundary C(x,y,z)

ii) **Neumann**, where the normal derivative $\partial u/\partial n$ is given on C.

Problems can have a mixture of the two types. The general form of the functional for equation 5.6.15 is

$$F(U) = \tfrac{1}{2}\int_{\tau} p(\nabla U)^2 - k^2 U^2 + 2gU \, d\tau \qquad (5.6.16)$$

where U=u+θh (h is a differentiable function with the properties mentioned in section 5.6.1). However, this functional is restricted to functions which satisfy the Dirichelet boundary conditions on the closed surface C. There is no restriction with respect to the Neumann conditions.

For the case of vector potentials

$$\nabla^2 \underline{A} = -\mu \underline{J} \qquad (5.6.17)$$

this can be solved using the functional in equation 5.6.10, if it is considered as a set of scalar equations.

5.7 Magnetostatic problems with permanent magnet sources

This section describes mathematical models used to calculate the magnetic fields due to permanent magnet systems. Firstly, the analytical methods are considered together with their various merits, and then numerical methods are described. Specific details relating to the Ansoft Maxwell ™ software package are dealt with in Section 5.9.

5.7.1 Analytical solutions

The definition of a magnetic dipole moment $\underline{m}$, in a volume of material $d\tau$ is given by

$$m = \underline{M} d\tau \qquad (5.7.1)$$

Where $\underline{M}$ is the average magnetisation in a dipole. The field at any external point is then the vector sum of the contribution of all the elements of volume. This section deals with different analytical mathematical representations used to calculate fields due to permanent magnets. They include the dipole model, the pole model,the volume and surface current loop models and finally, the magnetic circuit model.

5.7.2 The dipole model

This model can be used to calculate fields both inside and outside of the magnet. To define the equations for this model, it is first necessary to establish the link between a magnetic dipole moment and a current loop dipole moment.

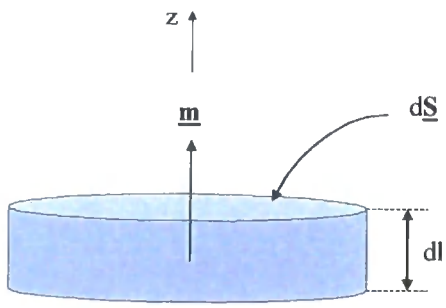

Fig. 5.7.1 A magnetic dipole

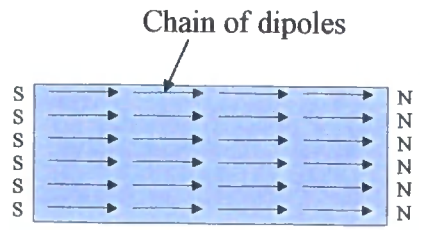

Fig. 5.7.2 The pole model

Consider a dipole as shown in fig. 5.7.1. Then the dipole moment $\underline{m}$ can be expressed in cylindrical coordinates as $M.dl.dS.\underline{a}_z$. Now consider the dipole as a current loop with a surface current $J_s.\underline{a}_\phi$. Then the current dipole moment is $J.dl.dS.\underline{a}_z$.
Comparing these two expressions gives

$$J_\phi = M_z, \quad \text{or} \quad \underline{J} = \underline{M} \times \underline{a}_n \tag{5.7.2}$$

The magnetic field strength, $\underline{H}$ at any point in space can then be calculated for a magnetic dipole, $\underline{m}$, using equation 5.7.3, provided R>>radius of the dipole. The resulting equation in spherical coordinates is

$$\underline{H} = \frac{m}{4\pi R^3}(\underline{a}_R 2\cos\theta + \underline{a}_\theta \sin\theta) \tag{5.7.3}$$

Note: the derivation is given in Karmel et al[1]. For regions outside the magnet (ie source free regions) the scalar magnetic potential due to a dipole can be calculated by finding the line integral of $\underline{H}$ to give equation 5.7.4.

$$U = \frac{m\cos\theta}{4\pi R^2} \qquad \text{or} \qquad U = \frac{\underline{m} \cdot \underline{a}_R}{4\pi R^2} \tag{5.7.4}$$

If the distribution of $\underline{M}$ over the magnetic material is known, then in theory this equation can be integrated over the volume of the magnet, to find the total scalar potential due to all the dipoles. However, except for a few simple geometries, this can only be achieved numerically. Analytical calculations using this method tend to be complicated and cannot be used to calculate the fields within magnetic materials.

5.7.3 The pole model

This model is only applicable to magnets with uniform magnetisation, such that all the dipoles have the same dipole moment. It can only be used to calculate fields external to the magnet. The dipoles are all assumed to line up to form chains, in which the north pole of one dipole neutralises the south pole of the next. The result is that for any one chain, there is only one north pole and one south pole at either end of the chain, as shown in fig. 5.7.2. This method is most reliable for long needle shaped magnets. However, for other shapes it can be assumed that there is a uniform distribution of poles on the ends of the magnet. Therefore, the model basically assumes that the two poles of a dipole moment are separated by a displacement, $\underline{L}$, such that the pole strength, P is given by

$$P = \frac{\underline{m}}{\underline{L}} \tag{5.7.5}$$

The equations used to describe the fields due to poles are then analogous to those used for point charges in electrostatics, ie

$$U = \frac{P}{4\pi R} \tag{5.7.6}$$

and $$\underline{H} = \frac{P\,\underline{a}_R}{4\pi R^2} \qquad (5.7.7)$$

The potential can then be integrated over the pole area to give the total field strength. This method can be used to give an exact solution for any point, P, on the axis of a cylindrical magnet, where the poles are represented as two circles (fig. 5.7.3). The resulting equation is

$$H_z = \frac{M}{2}\left\{1 - \frac{z/a_o}{\left(1+\frac{z^2}{a_o^2}\right)^{\frac{1}{2}}}\right\} \qquad (5.7.8)$$

where M is also in the z direction. To calculate the magnetic field off the axis of cylindrical magnets is considerably more involved. Two methods available[2] are briefly described.

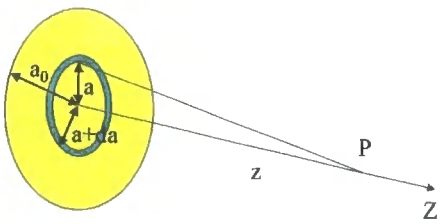

Fig. 5.7.3 The pole of a cylindrical magnet

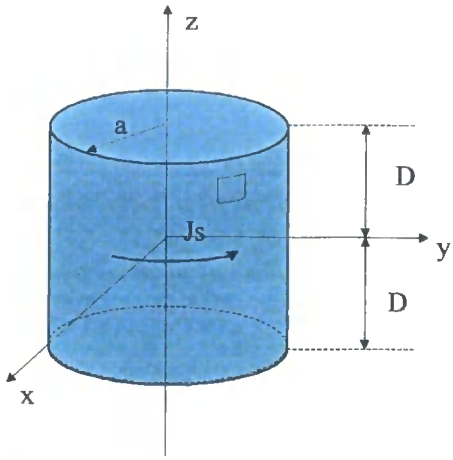

Fig. 5.7.4 Surface current model

The first is to calculate the components of the H-field at a point using an expansion of Legendre polynomials. The answer is in series form involving zonal harmonics, which can be found in look-up tables. The method deteriorates when R and a_o are about the same value due to the series converging too slowly. A second method is to numerically integrate over the circular surface of the pole. However, each term in this integration involves using look-up tables, to find values of complete elliptical integrals of the second kind. This method can be used when R and a_o are approximately equal. Similar methods can be used to calculate radial components.

The exact values of the H-field components can be evaluated for a magnet with a rectangular cross-section and uniform magnetisation normal to the pole surface.

5.7.4 The current loop model

Care must be taken when using the magnetic dipole moment of a current element to calculate fields within a magnetic material, because it is in the opposite direction to that of a magnetic dipole. It can be shown[3] that the vector potential A, at a displacement R from a magnetic dipole is given by

$$\underline{A} = \frac{\mu_0}{4\pi}\int_S \frac{\underline{M}\times\underline{a}_n}{R}\,dS + \frac{\mu_0}{4\pi}\int_\tau \frac{\nabla\times\underline{M}}{R}\,d\tau \qquad (5.7.9)$$

where $\underline{a}_n$ is the outward normal unit vector to the surface area S of the magnetised material. By comparing both components on the right hand side of the equation with equation 5.3.2, equations for the surface and volume current densities can be derived, ie

$$\underline{J}_s = \underline{M}\times\underline{a}_n \qquad (5.7.10)$$

$$\underline{J} = \nabla\times\underline{M} \qquad (5.7.11)$$

The magnetic material can therefore be represented as equivalent surface and volume currents. If the material is uniformly magnetised then external fields can be calculated using a surface current model.

Volume current model. This is required if the magnetisation within the material is not uniform. Equations 5.7.3 and 5.7.4 can be used to calculate the fields and potentials using current dipole moments.

Surface Current Model. In this model, the magnet can now be considered as a solenoid with a surface current density $\underline{J}_s$. However, it should be noted that these surface currents cannot be used to calculate the magnetomotive force of the magnet in a magnetic circuit. It represents a magnet with a uniform magnetisation but a non-uniform B-field or H-field. The H-field on the axis of a solenoid shown in fig. 5.7.4 is given by

$$\underline{H} = \underline{a}_z\frac{J_s}{2}\left[\frac{z+D}{\sqrt{a^2+(z+D)^2}} - \frac{z-D}{\sqrt{a^2+(z-D)^2}}\right] \qquad (5.5.12)$$

In the centre of the magnet $\underline{H} \sim J_s \underline{a}_z$ and halves at the pole ends. The fields off the axis can similarly be found by summing the contributions from the surface current. The vector potential can be used to obtain solutions in terms of elliptic integrals, or Legendre polynomials.

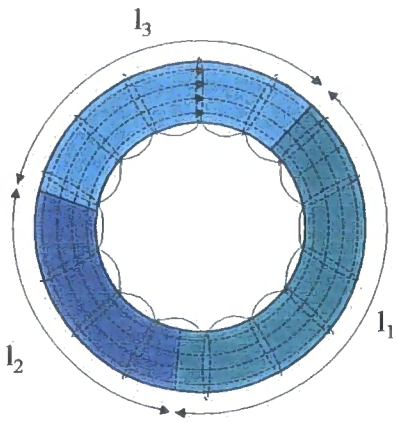

Fig. 5.7.5 Torus with Different Permeability Cores

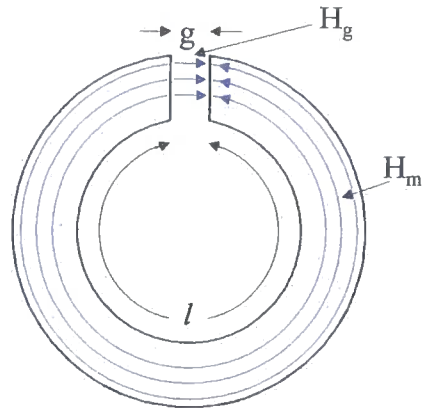

Fig. 5.7.6 Permanent Magnet Torus with Small Air Gap

5.7.5 The magnetic circuit model

This method draws on analogies with electrical circuits. Consider a toroidal coil as shown in fig. 5.7.5 which is wound around lengths, l_i, of different permeabilities, μ_i, and cross-sectional areas, A_i. If the ring is ferromagnetic then there will be little flux leakage and the magnetomotive force (mmf) can be given by

$$mmf = \sum H_i l_i \tag{5.7.13}$$

For each length

$$H_i l_i = {B_i l_i}/{\mu_i} = \phi {l_i}/{\mu_i A_i} \tag{5.7.14}$$

substituting into equation 5.7.13 gives

$$mmf = \phi \sum \frac{l_i}{\mu_i A_i} \tag{5.7.15}$$

The flux around the circuit is assumed constant and is analogous to current in an electric circuit. The term ${l_i}/{\mu_i A_i}$ is analogous to the resistance and is known as the reluctance. The rules combining series and parallel resistances therefore apply to reluctances. Because of flux leakages and μ not being a constant, the magnetic equations are not as exact as the electrical case. To apply this to a permanent magnet,

consider a torus with a small air gap as shown in fig. 5.7.6. Because the magnetomotance is zero it follows that

$$H_{gap}\, g = -H_{magnet}\, l \qquad (5.7.16)$$

and H_{magnet} is in the opposite sense to H_{gap}. H_{magnet} is known as the demagnetising field.

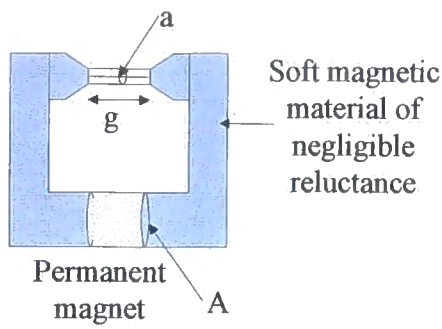

Fig. 5.7.7 A magnet with soft ferromagnetic pole pieces

This method can be used to calculate the minimum volume of magnetic material required to give a required B-field. To demonstrate this, consider a magnet as shown in fig. 5.7.7, in which part of the circuit is made from a soft ferromagnetic material of negligible reluctance, such that equation 5.7.16 still applies. If the pole pieces define a gap of cross-section a, then

$$\phi = B_{gap} a = B_{magnet} A \qquad (5.5.17)$$

The product of equations 5.7.16 and 5.7.17 gives

$$B_{gap} H_{gap} \tau_{gap} = -B_{magnet} H_{magnet} \tau_{magnet} \qquad (5.7.18)$$

where τ represents volume. The equation shows that the smallest volume of material required to give a defined value of B in the gap occurs when the product $B_{magnet}H_{magnet}$ is a maximum. This defines the operating point of a magnet.

5.7.6 Finite element solutions

Magnetostatic problems with complicated geometries or non-linear material properties can be solved using finite element solutions. The general problem can be solved for two and three dimensional problems using the techniques described in section 5.6. In these problems, however, there can exist permanent magnet sources and non-linear ferromagnetic materials. This section describes how these are incorporated into the methods.

Permanent magnet sources. If each element in a finite element model is considered as a magnetic dipole, and the demagnetisation curve is known, then the scalar potential at a point can be calculated by integrating the scalar potential equation.

Soft ferromagnetic materials. The simplest way of dealing with these materials is to assume they are linear and use a single value for the permeability. If, however, the non-linear nature is required, the magnetisation curve is used together with the magnetic dipole model. In this case, the energy functional must take account of the non-linear nature.

5.8 Eddy current problems

In this section, various methods are considered for determining the magnetic fields due to sinusoidal eddy current flow in conductors. Firstly, analytical methods for solving one and two dimensional cases for linear conductors are described then numerical techniques including one dimensional finite difference and two and three dimensional finite element methods are explained.

5.8.1 Analytical solutions

The diffusion equation for the H-field in conductors is

$$\nabla^2 \underline{H} = \sigma\mu \frac{\partial \underline{H}}{\partial t} \tag{5.8.1}$$

in which $\sigma\mu$ is the diffusion coefficient. The following sections show how this equation together with the diffusion equation in terms of the vector potential, can be used to calculate the fields generated due to eddy currents of known frequencies.

5.8.2 One-dimensional solution in a linear conductor

Fig. 5.8.1 shows a cross section of a semi-infinite plate in which the sinusoidal current J, flows in the x-direction with the resulting sinusoidal magnetic field H, in the z-direction. Since the directions of H and J are well defined, the resulting time harmonic diffusion equation can be written in scalar form as

$$\frac{d^2H'}{dy^2} = j\omega\sigma\mu H' = \alpha^2 H' \tag{5.8.2}$$

where

$$\alpha = (1+j)/\delta \tag{5.8.3}$$

δ is known as the skin depth. It is defined as the depth into the conductor in which the H- field decays by 1/e. As can be seen from equation 5.8.4, it decreases with frequency and is a function of the material properties.

$$\delta = \sqrt{2/\omega\sigma\mu} \qquad (5.8.4)$$

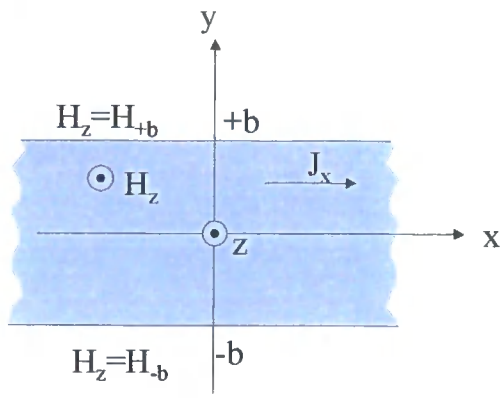

Fig. 5.8.1 Cross –section of a semi-infinite plane

Equation 5.8.2 is a second order homogeneous linear equation. The roots of its characteristic equation are distinct and real (in terms of α) and therefore it has a solution of the form

$$H' = k_1 e^{\alpha y} + k_2 e^{-\alpha y} \qquad (5.8.5)$$

where k_1 and k_2 are constants. To find the values of these either the flux per unit width of the plate can be specified (case 1) or the applied magnetic field strength (case 2).

Case1: Flux per unit Width of plate known

By using

$$\phi = \int_{-b}^{+b} \mu H' dy \qquad (5.8.6)$$

and invoking symmetry equation 5.8.5 becomes

$$H' = \frac{\alpha\phi}{2\mu} \frac{\cosh(\alpha y)}{\sinh(\alpha b)} \qquad (5.8.7)$$

Case 2: Applied Magnetic Field Strength known

If the magnetic fields strengths at +b and –b are defined as H_{+b} and H_{-b} respectively then the values of k_1 and k_2 are given by

$$k_1 = \frac{H_{+b}e^{\alpha b} - H_{-b}e^{-\alpha b}}{e^{2\alpha b} - e^{-2\alpha b}} \tag{5.8.8}$$

$$k_2 = \frac{H_{-b}e^{\alpha b} - H_{+b}e^{-\alpha b}}{e^{2\alpha b} - e^{-2\alpha b}} \tag{5.8.9}$$

5.8.3 Two-dimensional solutions in a linear conductor

There are two possibilities when considering two-dimensional systems:

1 the current only flows in the z direction. In this case J_z, H_x and H_y are functions of x and y,

2 the magnetic field only has a component in the z direction. In this case H_z, J_x and J_y are functions of x and y.

Case 1: Current in z-direction

Since the vector potential is parallel to the current and the current only has one component, it is easiest to solve for this. By assuming the displacement current is negligible in a conductor, the diffusion equation in terms of the vector potential is given by

$$\frac{\partial^2 A_z}{\partial x^2} + \frac{\partial^2 A_z}{\partial y^2} = \sigma\mu\left(\frac{\partial A_z}{\partial t} + \frac{\partial V}{\partial z}\right) \tag{5.8.10}$$

For sinusoidal variations equation 5.8.10 reduces to

$$\frac{\partial^2 A'}{\partial x^2} + \frac{\partial^2 A'}{\partial y^2} = \alpha^2 A' + \sigma\mu\frac{\partial V'}{\partial z} \tag{5.8.11}$$

where $A_z = \mathrm{Re}\left[A' e^{j\omega t}\right]$ and $V = \mathrm{Re}\left[V' e^{j\omega t}\right]$ (5.8.12)

The boundary conditions for this problem must be specified either as the flux density tangential to the boundary or the value of A_z and the total current enclosed. To define the boundary of interconnected regions, extra information is required in the form of the normal component of $\underline{B}$ and the tangential component of $\underline{H}$.

Case 2: Magnetic field in z-direction

Because there is only one component of the magnetic field, it can be calculated directly. In this case for a sinusoidal excitation, equation 5.8.1 can be represented in its time harmonic scalar form

$$\frac{\partial^2 H'}{\partial x^2} + \frac{\partial^2 H'}{\partial y^2} = \alpha^2 H' \tag{5.8.13}$$

where H' is the z component of the vector phasor field. This form of the diffusion equation is referred to as the homogeneous Helmholz equation. The boundary conditions for this case should be specified as either H_z' or $\partial H_z'/\partial n$ where n represents the direction normal to the boundary. Methods which can be used to solve this equation are outlined in this section.

Separation of variables.

Let $$H' = X(x)Y(y) \tag{5.8.14}$$

Substituting into equation 5.8.13 gives

$$\frac{1}{X}\frac{d^2X}{dx^2} + \frac{1}{Y}\frac{d^2Y}{dy^2} = \alpha^2 \tag{5.8.15}$$

Therefore, equation 5.8.15 can be re-written as

$$\frac{1}{X}\frac{d^2X}{dx^2} = -\frac{1}{Y}\left(\frac{d^2Y}{dy^2} - \alpha^2 Y\right) = -p^2 \tag{5.8.16}$$

where p is a constant, to yield two ordinary differential equations whose solutions are

$$\begin{aligned} X &= C_1\cos(px) + C_2\sin(px) \\ Y &= C_3\sinh(\sqrt{(\alpha^2+p^2)}y) + C_4\cosh(\sqrt{(\alpha^2+p^2)}y) \end{aligned} \tag{5.8.17}$$

The solutions for X and Y can be reversed by equating the the Y term to $-q^2$, say. There will also be a range of separation constants, which give valid solutions. Therefore the general form of the solution is

$$H' = \sum_{m=0}^{\infty}\{K_m\sin p_m x + L_m\cos p_m x\}\times\left\{M_m\sinh\sqrt{(\alpha^2+{p_m}^2)}\,y + N_m\cosh\sqrt{(\alpha^2+{p_m}^2)}\,y\right\} +$$
$$\sum_{n=0}^{\infty}\{P_n\sin q_n y + Q_n\cos q_n y\}\times\left\{R_n\sinh\sqrt{(\alpha^2+{q_n}^2)}\,x + S_n\cosh\sqrt{(\alpha^2+{q_n}^2)}\,x\right\} \tag{5.8.18}$$

The constants K_m through to S_n and p_m and q_n are found by application of the appropriate boundary conditions.

The Finite Fourier Transform Method. This method includes all the boundary conditions in one double series. To demonstrate it, consider a long rectangular bar as shown in fig. 5.8.2 excited by a uniform axial field, which varies sinusoidally in time with a peak value H_s. Therefore, the boundary conditions are H'=H_s for x=+/-a and y=+/-b. The problem has even symmetry, therefore cosine transforms will be used.

(The same method using sine transforms can be used for problems with odd symmetry).

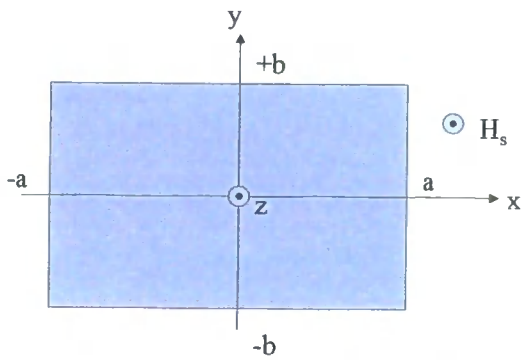

Fig. 5.8.2 Cross-section of rectangular bar

The finite cosine transform of H' with respect to y is defined as

$$\overline{H}(n,y)=\int_{-b}^{+b}H'\cos\frac{n\pi y}{2b}dy \qquad (5.8.19)$$

where n is an integer and the finite cosine transform of $\overline{H}$ with respect to x is defined as

$$\overline{\overline{H}}(m,x)=\int_{-a}^{+a}\overline{H}\cos\frac{m\pi x}{2a}dx \qquad (5.8.20)$$

where m is an integer. Equation 5.8.13 is firstly multiplied by cos(nπy/2b) then integrated between +b and-b. The boundary conditions in the y-direction are then applied. The resulting equation is then multiplied by cos(mπx/2a) and the same procedure carried out in the x-direction to calculate $\overline{\overline{H}}$. The inverse transform is then calculated using

$$H'=\frac{1}{ab}\sum_m\sum_n\overline{\overline{H}}\cos p_m x\cos q_n y \qquad (5.8.21)$$

where p_m=mπ/2a and q_n=nπ/2b, which gives the solution

$$H'=\sum_m\sum_n K_{mn}\cos p_m x\cos q_n y \qquad (5.8.22)$$

where

$$K_{mn}=\frac{16H_s}{mn\pi^2}\sin\frac{m\pi}{2}\sin\frac{n\pi}{2}\left[\frac{p_m^{\,2}+q_n^{\,2}}{p_m^{\,2}+q_n^{\,2}+\alpha^2}\right] \qquad (5.8.23)$$

For quasi-static problems, the solution in equation 5.8.22 can be assumed and substituted into equation 5.8.13, for example, to obtain the unknown coefficients. For

homogeneous boundary conditions, it can be used directly. For other cases, it can be combined with the separation of variables method to include the boundary conditions by superposition.

Equivalent circuit method. This method uses the concept of eddy-current modes from the double series form of the solution as shown in equation 5.8.22. Considering the case of $\underline{H}$ in the z direction, the spatial distributions of field and current are regarded as being made up of a number of superimposed modes

$$\begin{aligned} H'_{mn} &= K_{mn}\cos p_m x \cos q_n y \\ J'_{mnx} &= -q_n K_{mn}\cos p_m x \sin q_n y \\ J'_{mny} &= p_m K_{mn}\sin p_m x \cos q_n y \end{aligned} \tag{5.8.24}$$

Since these terms are a set of orthogonal functions, it is assumed that each mode is a separate R-L circuit with no coupling between the modal circuits. The modal resistance, R_{mn}, represents the eddy-current loss and the modal inductance, L_{mn}, represents the stored magnetic field energy. For a unit length of the bar shown in fig. 5.8.2 the equations are

$$\begin{aligned} I^2_{mn}R_{mn} &= \frac{1}{2\sigma}\int_{-b-a}^{+b+a}\int\left(\left|J'_{mnx}\right|^2 + \left|J'_{mny}\right|^2\right)dxdy \\ \tfrac{1}{2}I^2_{mn}L_{mn} &= \frac{\mu}{4}\int_{-b-a}^{+b+a}\int\left|H'_{mn}\right|^2 dxdy \end{aligned} \tag{5.8.25}$$

where I_{mn} is the rms current in each modal circuit. Once the circuit parameters have been determined for the particular problem this analysis is relatively simple to use.

The power-series method. This method solves eddy current problems by the successive approximation method which is outlined below:

1) Calculate the $\underline{H}$-field, $\underline{H}_0$ in the absence of eddy currents using

$$\nabla \times \underline{H} = \underline{J} \tag{5.8.26}$$

2) Using the time variation in $\underline{H}_0$, calculate an eddy current density J_1 using

$$\nabla \times \underline{E} = \frac{\partial \underline{B}}{\partial t} \tag{5.8.27}$$

3) Calculate the field $\underline{H}_1$ based on $\underline{J}_1$ using equation 5.8.26.

4) Calculate $\underline{J}_2$ from $\underline{H}_1$ using equation 5.8.27.

5) Continue to generate pairs of $\underline{J}_k$, $\underline{H}_k$ until they are negligible.

6) The final magnetic field is the sum of all the terms.

5.8.4 Numerical solutions

Two methods are available, finite difference and finite element methods.

5.8.5 Finite difference method

These can be used to solve both one- and two-dimensional linear problems and one-dimensional non-linear problems. To explain the method consider the one-dimensional diffusion equation (equation 5.8.28) for the z-component of the magnetic field inside a conductor with uniform conductivity as shown in fig. 5.8.1.

$$\frac{\partial^2 H_z}{\partial y^2} = \sigma\mu \frac{\partial H_z}{\partial t} \tag{5.8.28}$$

Let the length of the conductor, 2b, be divided into equal sections of length h, and the corresponding nodes be numbered i (i=1,2,3....M). Also, consider time steps of length p which are numbered j (j=1,2,3....N).

ie $y=(i-1)h \qquad i= 1,2,3...M$

and $t=(j-1)p \qquad j= 1,2,3....N.$

Using the Taylor series, and ignoring higher order terms the second derivative of H_z can be expressed as

$$\left.\frac{\partial^2 H_z}{\partial y^2}\right|_{i,j} = \frac{H_{z(i+1,j)} - 2H_{z(i,j)} + H_{z(i-1,j)}}{h^2} \tag{5.8.29}$$

The time derivative can also be expressed in terms of a first order Taylor's expansion. Using a forward difference formula gives

$$\left.\frac{\partial H_z}{\partial t}\right|_{i,j} = \frac{H_{z(i,j+1)} - H_{z(i,j)}}{p} \tag{5.8.30}$$

Substituting equations 5.8.29 and 5.8.30 into equation 5.8.28 gives

$$H_{z(i,j+1)} = rH_{z(i+1,j)} + (1-2r)H_{z(i,j)} + rH_{z(i-1,j)} \tag{5.8.31}$$

where $r=p/(\sigma\mu h^2)$. This equation can be solved explicitly. However, to ensure stability $r<=1/2$. An equation using centre-difference formulae can be derived (the Crank-Nicolson equation), which has the advantage of being stable for all values of p and h. The advantage of this is that the time step can be increased, and hence the computation time decreased.

5.8.6 Finite element method

In finite element eddy current problems, time harmonic diffusion equations 5.8.41 and 5.8.42 are solved in conductors.

$$\nabla^2 H' = j\omega\sigma\mu H' \qquad (5.6.41)$$

$$\nabla^2 \underline{A} = -\mu \underline{J} \qquad (5.6.42)$$

The divergence of $\underline{A}$ is often assumed to be zero in near-field steady state eddy current problems since this gives a unique solution. However, it should be noted that this condition actually applies to static fields and currents of finite extent. Non-linear and magnetic materials can be included. More detail is given in the next section, which describes the software package used by the author in this research.

5.9 Maxwell Ansoft software package

This section describes the package used in the research detailed in this thesis. It enables solutions to complex geometries to be calculated numerically, in both two and three dimensions. The two-dimensional magnetostatic and eddy current options, solve for the vector potential, from which the other field quantities can be calculated. Three-dimensional problems use the components of the $\underline{H}$-field. The simulation involves the following series of steps:

1) Define the model geometry
2) Define the material characteristics
3) Define the boundary conditions and field sources
4) Define the finite element mesh
5) Solve the problem numerically
6) Perform further calculations using the field solutions if necessary.

In this section, the finite element method used in this package will be described together with the boundary conditions and algorithms used to solve both magnetostatic and static eddy current problems.

5.9.1 Finite element method

To illustrate this procedure the two-dimensional vector potential method is used, ie the vector potential can be considered as a scalar in the z direction. The associated diffusion equation is

$$\nabla^2 \underline{A} = -\mu \underline{J} \tag{5.9.1}$$

The problem region is broken up into simple shapes called finite elements, with the aim of calculating the field in each of these. Equilateral triangles are used in this package, since they are most suitable for the second order polynomial function used by the software. The method used to create the triangles is the 'Delaunay Tessellation[4]', which maximises the sum of the minimum angles, and hence practically eliminates thin isosceles triangles.

The desired field in each element is approximated with a second order polynomial

$$A_z(x,y) = a_0 + a_1 x + a_2 y + a_3 x^2 + a_4 xy + a_5 y^2 \tag{5.9.2}$$

The vector potential, A_z is calculated for the three corners and three midpoints of each triangle. As shown in section 5.6.3, the energy functional for the vector potential is

$$F(A) = \frac{1}{2}\mu \int_{\tau} \left(\frac{\nabla A \cdot \nabla A}{\mu} - AJ \right) dS \tag{5.9.3}$$

This functional is calculated and then minimised with respect to A_z at each node in every triangle. The number of equations produced is that of the number of nodes. Since each element's energy is determined from the local node values, the resulting matrix equation (equation 5.9.4) consists of a sparse coefficient matrix, [S], ie it has relatively few non-zero entries.

$$[S][A] = [J] \tag{5.9.4}$$

This can be solved directly using the Sparse Gaussian Elimination method or using an indirect iterative type solver such as the pre-conditioned Conjugate Gradient Method. The resulting values of $\underline{A}$ are substituted into Poisson's equation to calculate the error, R, in each triangle, ie

$$\nabla^2 A^{approx} + \mu J = R \tag{5.9.5}$$

The absolute values of the errors in each triangle are summated and expressed as a fraction of the total energy to give a percentage energy error. Thus,

$$\%EnergyError = \sum_{i=1}^{n} \frac{|R_i|}{TotalEnergy} \times 100\% \tag{5.9.6}$$

This value can be used to define when the solution is complete. Alternatively, the number of iterations can be defined. The method of reducing the energy error is to refine the mesh.

5.9.2 Magnetostatic 2D solver

In these type of problems the current density, J is assumed to have only a z component, thus the vector potential, A, only has a z component. Therefore, the two quantities can be treated as scalars in the calculations. Because the fields are static and the currents assumed to be of finite extent, the divergence of A is assumed zero. Hence, Poisson's equation can be rewritten as

$$J_z(x,y) = \nabla \times \left(\frac{1}{\mu_r \mu_o} \right) \nabla \times A_z(x,y) \qquad (5.9.7)$$

This equation is solved for A_z. B and H are then calculated. The sources for this problem need to be specified in terms of a current density. In the case of permanent magnets, equations 5.7.10 and 5.7.11 are used to give the link for the linear and non-linear cases using the surface and volume current models respectively.

5.9.3 Eddy current 2D solver

This solver again assumes that all current densities exist only in the z direction. This results in the vector potential, A, and the electric field intensity E also only having z components. Therefore the voltage, V, over the cross section of each conductor in the problem is constant, and is not calculated for every node. All quantities in the problem must be at the same frequency. However, they can have different phases. The steady state (assuming zero divergence of A) time harmonic field equation used is

$$\nabla \times \frac{1}{\mu_r} (\nabla \times \underline{A}) = (\sigma + j\omega\varepsilon_o)(-j\omega \underline{A} - \nabla V) \qquad (5.9.8)$$

From this equation, a second equation can be derived which computes the total current flowing in any conductor that is connected to an external source,

$$I = I_s + I_e + I_d \qquad (5.9.9)$$

where I_s is the source current $-\int_{\omega} \frac{1}{\mu} \sigma \nabla V d\omega$

I_e is the induced current and $-\int_{\omega} \frac{1}{\mu} j\omega\sigma A d\omega$

I_d is the displacement current $\int_{\omega} \frac{1}{\mu} j\omega\varepsilon(-j\omega \underline{A} - \nabla V) d\omega$

5.9.4 Boundary conditions for 2D solvers

Both the magnetostatic and eddy current simulators have the same boundary conditions. In the eddy current case, however, both the magnitude and the phase must be defined. The default condition for the outer problem region boundary is for the tangential component of the H-field to be forced to zero. Since the outer boundary is not a perfect conductor and therefore cannot support a surface current density, this implies that there are no external tangential H-fields to the boundary. Hence, the H-field will always be normal to the boundary. It is referred to as a **Neumann** boundary because the H-field is the curl of the vector potential A_z. It can be assigned by calling the **balloon** boundary command. The default boundary condition between objects are those described in section 5.4. These are known as the **natural** boundary conditions. To specify external fields, values can be assigned to the value of the vector potential, A_z. This type of boundary is referred to as a **Dirichlet** or value boundary. Since the B-field is the curl of the vector potential, it and hence the H-field is therefore defined for both the normal and tangential directions to the boundary. The external fields can therefore be specified. To produce half and quarter symmetry models, it is necessary to have symmetry boundaries. An even symmetry causes the H-field to be perpendicular to the boundary (and in phase for the eddy current case), while and odd symmetry causes the H-field to be tangential (and out of phase for the eddy current case). These are produced by using the Neumann and Dirichlet, with A_z =0, boundaries respectively. **Master/slave** boundaries force the H-field of the slave boundary to have the same magnitude, direction (or opposite direction) and phase (if applicable) of that of the master boundary. **Impedance** boundaries are used to simulate the induced currents in a conductor without directly computing them. It is used when the skin depth is at least two orders of magnitude smaller than the object dimensions, the induced current is small or the ac current source is relatively far away from the conductor surface relative to the skin depth. Firstly, the object is excluded from the calculation region by defining an outer boundary as an impedance boundary. The skin depth is then calculated. Finally, the H-field for the rest of the problem is solved. The ohmic loss can be then be calculated using

$$Loss = \sqrt{\frac{\varpi\mu}{8\sigma}} \int_s H_{\tan} \cdot H_{\tan}^{*} dS \qquad (5.9.10)$$

where the power loss is in Watts. H_{tan} is the tangential component of H and H_{tan}^{*} is the complex conjugate of the tangential component of H.

5.9.5 Magnetostatic 3D solver

This solver has two parts to the calculation:

Conduction current solution. In this part, the current density J is calculated from dc currents inside the conductors. If a permanent magnet is used as a source, equations 5.7.10 or 5.7.11 are used to calculate J. Surface currents are calculated for perfect conductors. The equation used to calculate J for non-perfect conductors is

$$\nabla \cdot (\sigma \nabla V) = 0$$
$$(derivation: \underline{J} = \sigma \underline{E} = \sigma \nabla V : \nabla \cdot \underline{J} = \frac{d\rho}{dt} = 0) \qquad (5.9.11)$$

This can be calculated for each element using the functional for Laplace's equation

$$W(V) = \frac{1}{2}\int |\nabla V|^2 dS \qquad (5.9.12)$$

Magnetic field solver. This is implemented using the equations

$$\nabla \times \underline{H} = \underline{J}$$
$$\nabla \cdot \underline{B} = 0 \qquad (5.9.13)$$
$$\underline{B} = \mu_o \mu_r \underline{H}$$

It should be noted that the displacement current is ignored since the fields are static. The solution process is summarised in fig. 5.9.1.

5.9.6 Eddy current 3D solver

The sources used in this calculation are either the current in a conductor or the current density, J. In either case, they must be defined by both the magnitude and the phase. It is assumed that the displacement current is zero in all regions of the problem as is usually the case in near-field eddy current problems, thus the form of Maxwell's equations are

$$\nabla \times \underline{H} = \underline{J}$$
$$\nabla \times \underline{E} = -\frac{d\underline{B}}{dt} \qquad (5.9.14)$$

To solve for H, the model is split into two regions:

Conductors in which source and eddy currents occur. In this region the H-field is directly computed from the source currents and applied magnetic fields. Combining the H-field equations in table 5.5.1, and using J=σE gives the time harmonic field equation

$$\nabla \times \left(\frac{1}{\sigma} \nabla \times \underline{H} \right) + j\omega\mu \underline{H} = 0 \tag{5.9.15}$$

Non-current bearing regions. Here the curl of the B-field is zero and therefore the magnetic scalar potential, U, has a single-valued path-independent value (analogous to the electric potential). This enables the use of a simpler calculation

$$\begin{aligned} &\nabla \cdot (\mu \nabla U) = 0 \\ &(\textit{derivation}: \underline{H} = -\nabla U : \underline{B} = -\mu \nabla U : \nabla \cdot \underline{B} = 0) \end{aligned} \tag{5.9.16}$$

On the boundaries of the two types of regions, the H-field is forced to be continuous. The flowchart in fig. 5.9.2 summarises the algorithm.

5.9.7 Boundary Conditions for 3D solvers

As in the 2D case the boundary conditions for the magnetostatic and eddy current solvers are the same. Again, in the case of the eddy current solver both the magnitude and phase must be considered. **Natural** boundaries are used for all surfaces between objects. The outer surface of the problem space can be defined using Neumann, Dirichlet or symmetry boundaries. These labels do not describe the same conditions as in the 2D simulator, but are merely used to describe how the field is defined (value, derivative etc). In the **Neumann** boundary the normal derivative of the H-field is forced to zero, hence the magnetic field is always tangential. This prevents the flux crossing the boundary due to the B-field being continuous. In the **Dirichlet** (or magnetic field) boundary, values or functions of the H-field are defined, enabling external fields to be included. An **odd symmetry** boundary forces the flux to be tangential and is the same as the Neumann boundary. An **even symmetry** boundary forces the flux to be normal by using a Dirichlet condition. **Master/slave** boundaries force the H-field of the slave boundary to have the same magnitude, direction (or opposite direction) and phase (if applicable) of that of the master boundary. As in the 2D simulator, **impedance** boundaries are used to simulate the induced currents in a conductor without directly computing them. It is also used in the same conditions with the same method.

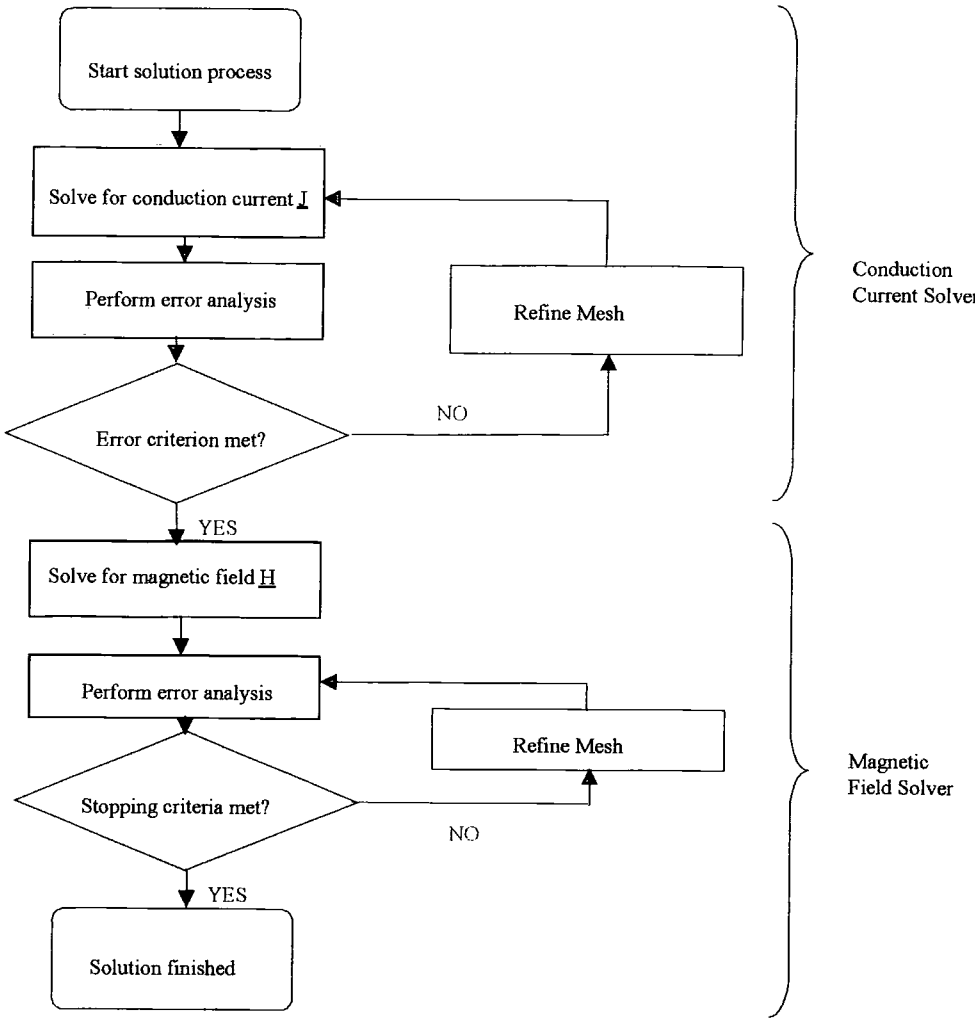

Fig. 5.9.1 Flow chart of 3D magnetostatic solver in Ansoft Maxwell

(Reproduced from the Technical Notes in Ansoft Maxwell Software Package, 1999)

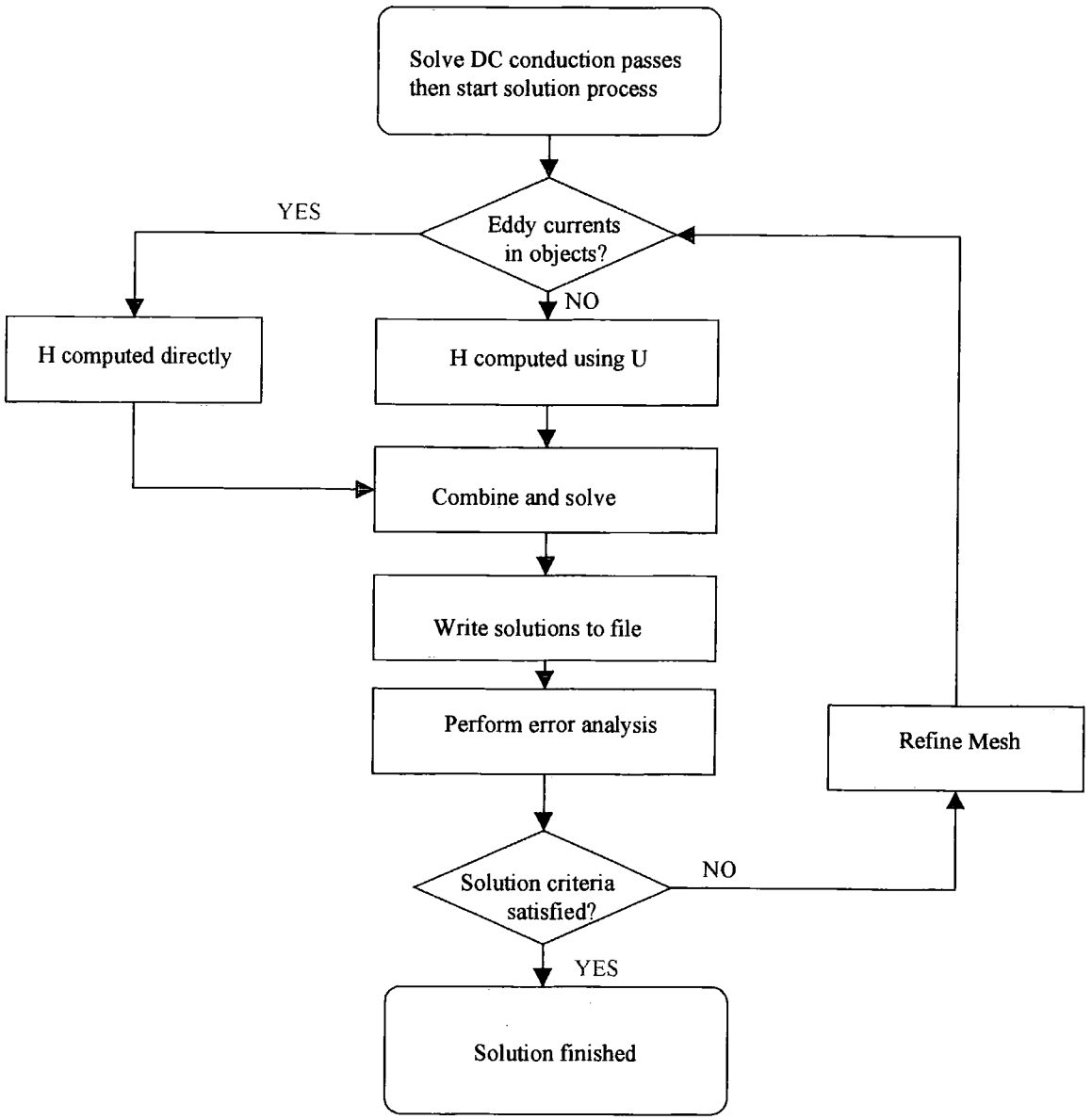

Fig. 5.7.2 Flow chart of 3D eddy current solver in Ansoft Maxwell

(Reproduced from the Technical Notes in Ansoft Maxwell Software Package, 1999)

5.10 References

1 *Karmel PR*, GD Colef, RL Camisa, 'Introduction to electromagnetic and microwave engineering', John Wiley & Sons, Inc 1998

2 *McCaig M, Clegg AG*,'Permanent Magnets in theory and practice', Pentech Press 1987

3 *Lorrain P, Corson DP, Lorrain F*, 'Electromagnetic fields and waves', 3rd Ed. WH Freeman & Co. 1988

4 *Woodward A*, 'Introduction to the finite element method', Presentation Notes from Ansoft, Nov. 1998

5.11 Bibliography

Duffin WJ, 'Electricity and magnetism', 3rd Ed. McGraw-Hill Book Co. 1980

Silvester PP, RL Ferrari, 'Finite elements for electrical engineers', Cambridge University press, 1983

Stoll RL, 'The analysis of eddy currents', Clarendon Press, Oxford 1974

Kreyszig E, 'Advanced engineering mathematics', Sixth Edition, John Wiley & Sons 1988

Technical notes in Ansoft Maxwell software package, 1999

CHAPTER 6

DEVELOPMENT OF A TRANSFORMATION DETECTION SYSTEM

6.1 Introduction

This chapter describes the initial investigations undertaken to develop a system which detects the austenite-to-ferrite phase transformation in hot steel. Chapters 7 to 9 describe the prototypes subsequently produced, together with experimental data and plant trials. Although the development has concentrated on steel strip with gauges between 1 and 5mm, it is hoped that the detector can be adapted to detect the phase transformations in other steel products, such as sections or rods.

A summary of various electromagnetic techniques in steel rolling and finishing processes is given in chapter 3. Included in this are phase transformation measurement systems. To date, there are no reports on the successful implementation of on-line phase transformation detectors using permanent magnets or dc electromagnets. These appear on the surface to be simple, cheap, robust methods and have therefore been researched by the author in detail with the aim of implementing them on a hot strip mill, eg Port Talbot hot strip mill, Corus Strip.

6.2 The measurement problem

The final mechanical properties of hot rolled products are dependent on the final microstructure, which itself is related to the rate of the austenite-to-ferrite phase transformation. The factors affecting these are steel composition, process history, ie how the product was rolled, and cooling rate. After the strip has been rolled, it leaves the finishing stand at about 900°C, and enters the run-out-table (ROT). It is here that the final mechanical properties are tuned by controlling the water flow. The measurement parameter used for this is temperature. Due to the high temperature of the strip, (500 °C – 900°C) and its high speed, (>10m/s) this has to be done using a non-contact method, the most common being radiation pyrometry. This measurement, however, can lead to quite significant errors (+/- 20°C). Due to the method of water cooling, there are copious amounts of steam obscuring the view of the pyrometer.

This limits the number of suitable locations for installing the pyrometers, which in turn reduces the accuracy to which the cooling rate can be predicted. The water and air also react with the strip surface to produce iron oxides, which are referred to as scale. This acts to give unknown variations in the surface emissivity, and thus contributes further to the errors in temperature measurement. Radiation reflected from the mill sides also create unwanted variations.

Once the temperature reading is available, there are further errors in relating it to the percentage ferrite present in the steel. The ferrite fraction at any region within the steel product will be dependent on the temperature. Since only the surface temperature is measured, then the temperature profile throughout the product needs to be evaluated. For thicker products finite difference calculations could be used. However, for thin strip of less than 3mm, the cross thickness temperature variation is usually below 5°C. Thus, within an acceptable error, the surface temperature can be assumed to be the bulk temperature. A metallurgical model is then needed to calculate the ferrite fraction. The accuracy of prediction will depend on the validity of the model, and the degree of accuracy to which other parameters, such as composition and dimensions, are measured or assumed. One significant factor affecting the output is that a point temperature measurement does not correspond to a unique fraction of ferrite. This is due to heat being released during the transformation process, ie recalescence.

Due to these limitations, the research has focused on finding a direct measurement of the phase transformation as shown schematically in fig. 6.2.1. The proposed transformation system includes both magnetic detectors and optical pyrometers as shown in fig. 6.2.2. It includes at least four magnetic detectors to identify the non-transformed level, the transformation rate and the end of transformation. More detectors may be needed since the transformation region will change from product to product. The optical pyrometers are needed to improve the accuracy of the system. In future schemes, sensors could be placed along the width of the strip to give even tighter control of the material properties. This would only be an advantage, however, if the cooling system has the required flexibility.

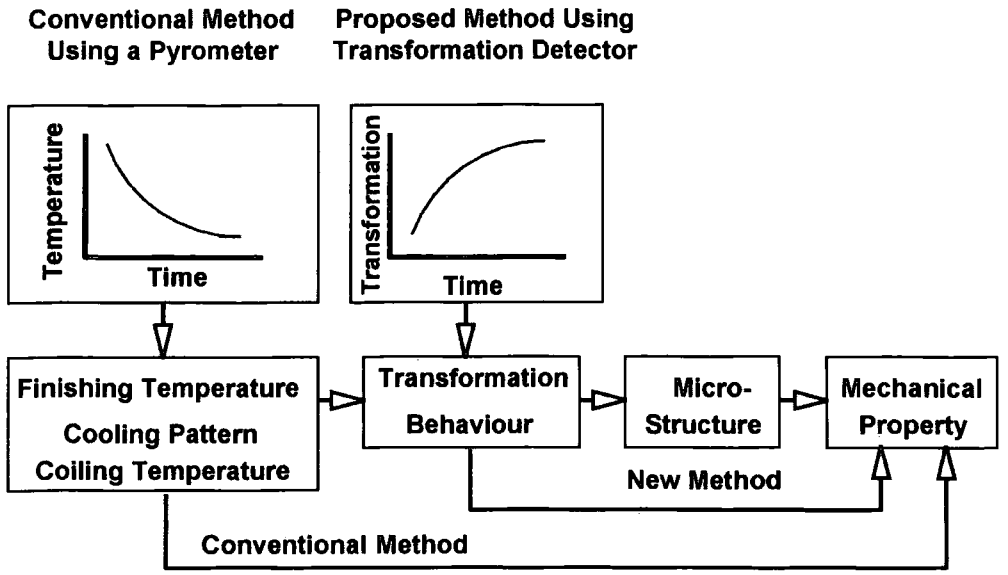

Fig. 6.2.1 Schematic comparing conventional and proposed mechanical property control

(Reproduced from Morita et al, On-line transformation detector for property control of hot rolled steel, Proc of Met. Soc. of AIME Symposium on Accelerated cooling of steel, Pittsburgh 1985)

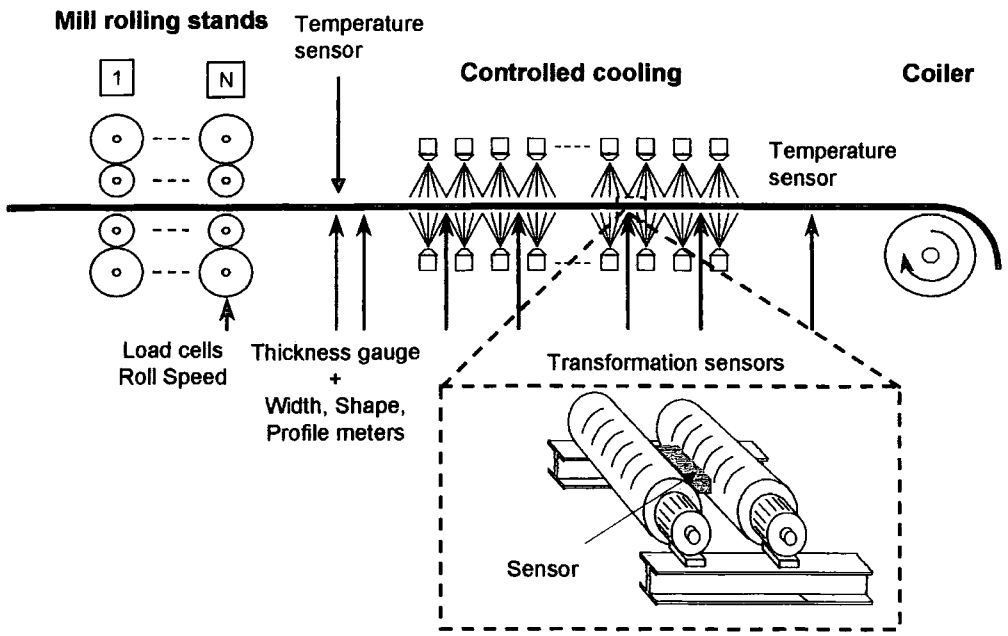

Fig. 6.2.2 Proposed transformation detection scheme

6.3 Instrument requirements

The instrument must be designed to meet the following requirements:

i) The measurement needs to be non-contact. Due to the temperature of the steel strip and its speed, it is not practical to place probes on it since most importantly they would mark the strip. Other considerations would be the life of a contact sensor due to, for example, frictional effects and cooling requirements. A practical mounting distance of 50mm below the strip, with a range of 10mm to allow for strip height variations was considered acceptable.

ii) The instrument must be mechanically robust, such that it can survive the impact from a hot strip.

iii) It must be manufactured such that if a steel strip hits it, the steel strip is not marked.

iv) It should be small enough to be mounted between neighbouring rolls on the ROT.

v) It must be waterproof so that it can be placed in the quenching zone.

vi) The presence of copious amounts of water and dirt should not affect the instrument performance, ie it should be able to 'see' through it.

vii) It should be easily maintainable, ie it should be self-cleaning and capable of remote calibration.

viii) Each sensor head should be cheap and readily replaceable, but able to withstand temperatures of several hundred degrees Celsius.

ix) The output should be a direct measure of the ferrite fraction present in the steel strip. It should have a range of 100%, a resolution of at least 10%, good repeatability and reliability.

x) The output is recorded digitally at 0.1s intervals, therefore the response time (10% to 90%) of the sensor output, should be less than half of this, ie 50ms.

6.4 General measurement principle

In section 4.2.3 it was explained that the exchange forces between neighbouring atoms in a material, which determine whether a material is ferromagnetic or not, are extremely sensitive to atomic separation. This is the reason why austenite is paramagnetic, and ferrite is ferromagnetic. It is this difference in the magnetic properties of the two crystal structures, which is exploited in magnetic transformation detectors. The detectors provide a measure of the steel's permeability. In section 4.5, the mechanism behind the austenite-to-ferrite phase transformation was described. In general, the higher the carbon content, or the faster the cooling rate, the cooler the temperature at which the phase transformation occurs. Therefore, for the case of a slowly cooled low carbon sample, the phase transformation will occur at a relatively high temperature. If this is above the Curie temperature, then the sample permeability will remain unchanged, since both the austenite and ferrite will be paramagnetic. If, however, the cooling rate is increased, or a sample with a higher carbon content is considered, then the ferrite will start forming below the Curie temperature. Since the ferrite is ferromagnetic, then the increase in permeability of the sample should be directly related to the amount of ferrite present. The general measurement principle behind all the sensors investigated is to generate a magnetic field which passes through the steel sample. The sample's change in magnetic properties will affect this field, which can then be measured. Possible sensor configurations include C-core permanent magnets or dc electromagnets with magnetic field detectors such as Hall probes, magnetoresistive devices or magnetic diodes. Others include the generation of ac magnetic fields using exciting coils, and detection using either measurement of the exciting coil impedance, or pick-up coils. Fig. 6.4.1 shows examples of possible sensing arrangements. The ac methods measure both the permeability and conductivity of the sample, whereas the dc method just measures the magnetic permeability. However, they are all sensitive to both the steel and the distance between the steel and detector.

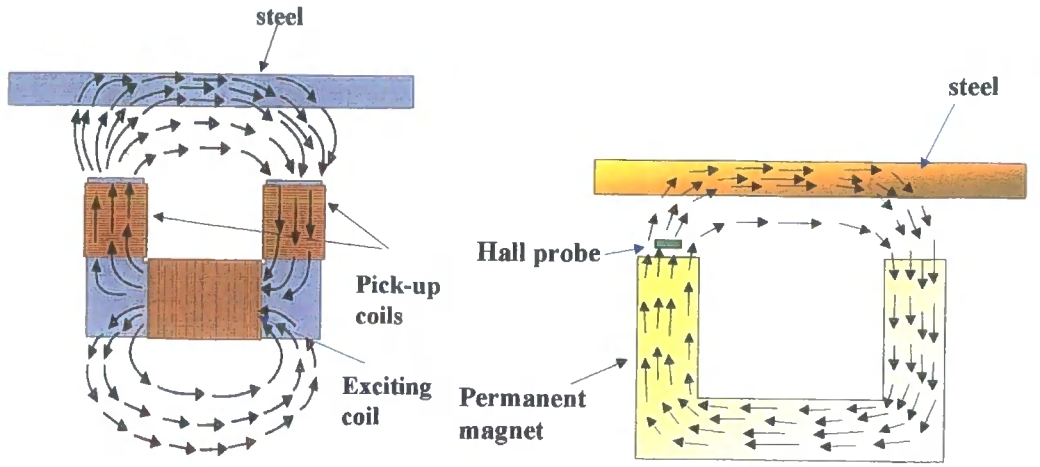

a) AC exciting coil with pick-up coils **b) Permanent magnet with Hall probes**

Fig. 6.4.1 Possible sensing configurations

6.5 Initial investigations

The remainder of this chapter describes investigations of various sensor configurations. Where possible, cold and hot laboratory tests have been carried out. However, to complete the investigations finite element simulations were used. These reduced the costs of investigating different magnet and coil geometries. Four basic types of sensor were considered: ac coils, dc coils, permanent magnets and commercial ac proximity sensors. The work in this section forms the basis of the prototypes, which have been trialled on a hot strip mill.

6.6 AC single coil sensor

This consisted of a laminated HWR electrical steel C-core, around which was wound a coil as shown in fig. 6.6.1. A C-core geometry was used since previous work by Lacroix et al[(1)], Kawasaki Steel[(2)] and NKK[(3)], have shown this to be a suitable geometry. The reason being that the sample under investigation forms a significant part of the magnetic circuit. Thus, the whole assembly can be located safely below the hot steel strip in a rolling mill. This prototype was used to investigate the sensitivity of electromagnet type sensors to steel samples and look at the effect of speed. The principle of operation was to excite the coil with a constant amplitude voltage from a custom made signal generator (supplied by Mallinson Engineering), and note the change in current through the coil using an Hitachi VC6050 oscilloscope. The supply voltage and resulting current could then be related to the coil impedance.

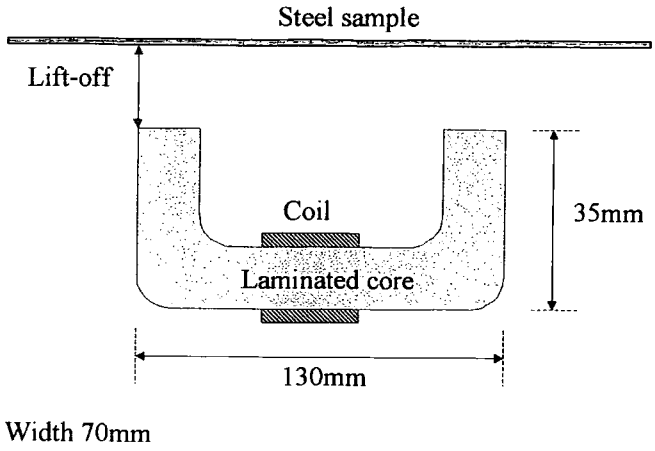

Fig. 6.6.1 AC single coil type sensor

The experimental set-up and equivalent circuit are shown in fig. 6.6.2. The electrical properties of the probe were calculated using the phase shift and amplitude of the current signal at two frequencies of 32Hz and 64Hz. The resistance and inductance were found to be 0.70Ω +/− 0.01Ω and 37.2mH +/- 0.1mH at 64Hz. During experimentation a constant amplitude rms voltage of 3.87V +/- 0.01V was used to excite the coil. To measure the current a 1Ω +/−1% sensing resistor was placed in series with the coil. Using the assumed electrical properties of the coil, it was predicted that a current of about 0.7A would flow with no sample present. The presence of a fully transformed sample would appear as an increased inductance to the circuit and hence, decrease the output current.

Table 6.6.1

Frequency (Hz)	32 Hz	64Hz	100Hz	500Hz	500kHz
Skin depth of ferritic steel	4.45mm	3.11mm	2.52mm	1.13mm	0.04mm
Skin depth of austenitic steel	88.97mm	62.89mm	50.32mm	22.50mm	0.71mm

Calculated skin depths for austenitic and ferritic steel phases

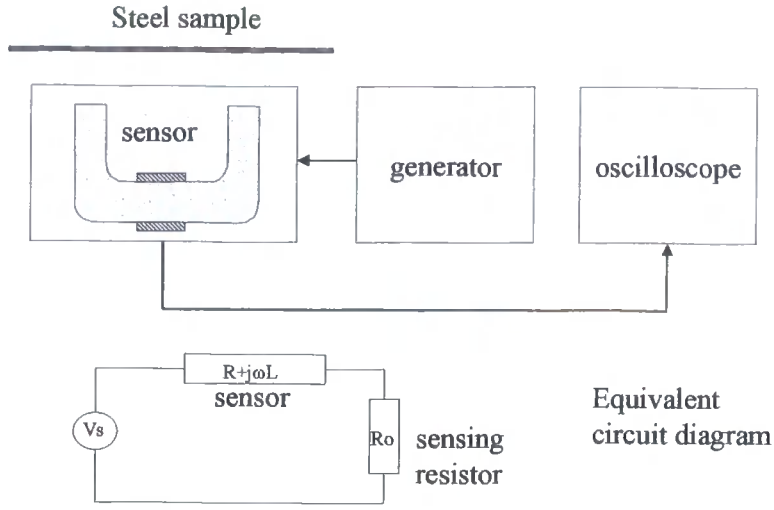

Fig. 6.6.2 Experimental set-up and equivalent circuit

The effect of changing the excitation frequency, is to alter the skin depth in the sample. The exact value will depend on its transformed state, ie the permeability and to a smaller extent the conductivity. Typical values of skin depth, calculated using equation 5.8.4 for various frequencies of both transformed and non-transformed states, are given in table 6.6.1. For these calculations, the conductivity of steel was assumed to be 10^6 S/m and the relative permeability of ferritic steel, 400. These were used to select the operating frequency of the sensor. Values of 32Hz and 64Hz were chosen. These were considered to be low enough to significantly penetrate, and hence measure the permeability of as much of the sample as possible. They also, gave minimum skins depths in the region of a typical steel strip thickness. This gave the advantage of minimising the effect of a changing penetration depth, through the phase transformation from austenite to ferrite. The final advantage of using such low frequencies, is that eddy current losses would be minimised, and hence effects due to variations in conductivity.

6.6.1 To test the effect of strip speed

From Faraday's law, an increase in the strip speed will further increase the induced eddy currents in the sample which in turn will reduce the current in the exciting coil. The tests involved manually passing a steel sample of approximate dimensions 10mm x 30mm x 3mm at a constant lift-off over the sensor using a slide rail, as shown in fig. 6.6.3. For this, excitation frequencies of 32Hz and 64Hz were used. The speed was not guaranteed to be constant and was inferred from the time t2 on the output traces.

The shape of a typical output is shown in fig. 6.6.4, where I1 and I2 indicate the changes in rms current as the sample starts and finishes overlapping the sensor and t1, t2 and t3 are time intervals. The trace shows a change in current in the negative direction, as the strip edges pass over the sensor. This is consistent with Faraday's law and also the presence of a ferromagnetic sample, which would act to concentrate the flux lines within the sample. However, as the body of the strip passes, there is a general increase in the sensor output. When the strip was reversed, the trend was in the reverse direction. This implies that there was a gradual change in the lift-off of the strip and/or the material properties had a gradual change. An indication of the strip speed was given by the detection period.

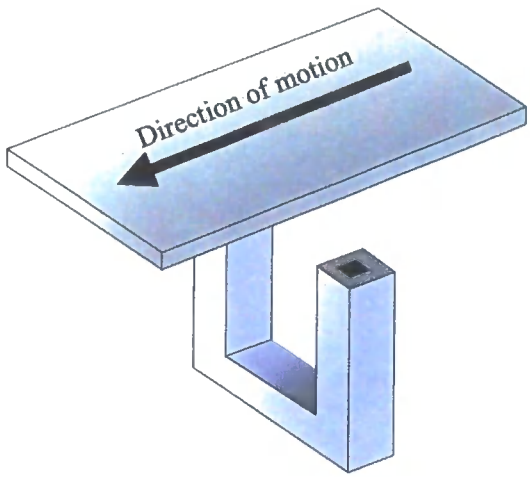

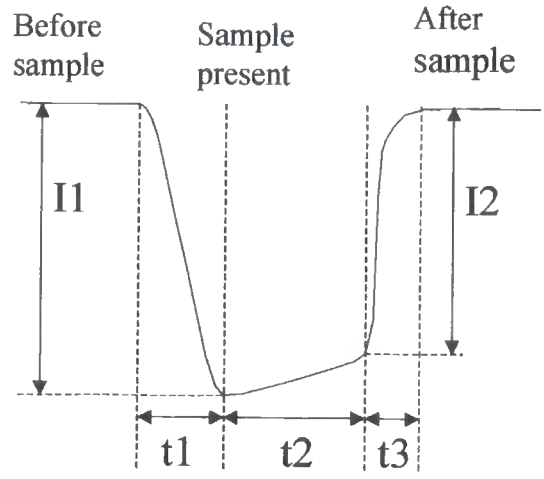

Fig. 6.6.3 Speed test set-up

Fig. 6.6.4 Typical Output from speed test

The results are shown in table 6.6.2 . It can be seen that increasing the strip speed by over a factor of 4, only produced a 2% variation in I1 and I2 at 32Hz. Thus, the sensor is sufficiently insensitive to speed to be used without compensation. However, increasing the sensor frequency, increased the sensor sensitivity to steel samples. This is as expected from Faradays law, and explains why high frequencies are used in inductive proximity sensors. The results also show that the sensor was relatively insensitive to an aluminium sample when compared with the steel. This can be explained by noting the fact that the magnetic flux density increases in steel, due to it being highly permeable, whereas it does not in aluminium. Thus the rate of change of flux, required to generate the eddy currents, will be greater for steel.

Table 6.6.2

Test No.	Excitation frequency (Hz) +/- 5%	t1 (s) +/- 1ms	t2 (s)) +/- 1ms	t3 (s)) +/- 1ms	Change in current, I1(A) +/- 0.001A	Change in current, I2 (A) +/- 0.001A
1	64	0.175	0.335	0.175	0.928	0.846
2	64	0.080	0.160	0.090	0.928	0.842
3	64	0.335	0.765	0.450	0.936	0.842
4	32	0.165	0.485	0.340	0.490	0.420
5	32	0.077	0.125	0.077	0.478	0.426
6	32	0.060	0.110	0.060	0.480	0.426
aluminium	32	Not recorded			<0.02	

Results of speed tests

Therefore, it can be concluded that the sensor is sensitive to the presence ferromagnetic samples, and therefore has the potential to detect phase transformation. To achieve this, low excitation frequencies should be used to ensure penetration into the sample and insensitivity to sample speed. However, it should be noted at this stage, that reducing the frequency can significantly reduce the sensor range.

6.6.2 Comparison with other research

Work performed by Lacroix et al[1] at 10kHz showed that ac inductive sensors were sensitive to the acceleration and deceleration of hot steel strips. The actual percentage change was not quoted, and it is unclear from their work whether the speed and transformation changes were decoupled. This appears at first to contradict this research. However, the reason for the increased sensitivity to speed of their results, is the higher excitation frequency used, which in turn decreases the skin depth and concentrates the flux in the surface of the steel. Thus the rate of change of flux will be greater and hence more sensitive to speed variations.

The sensors described by Morita et al[2] and NKK[3] do not mention the problems with the effects of speed. Although the excitation frequency is not mentioned by Morita et al[2] the NKK system was reported to be operating at a frequency of 40Hz, which is in a similar range to the ac system in this research. Therefore, the decision to use low frequencies to increase the penetration depth also appears to have the added advantage of desensitising the system to sample speed.

From these results and previous research[4,5,6] this approach to measuring phase transformation was felt to be feasible, and further analyses of custom-built ac type prototypes were continued by Richard Binns from Lancaster University as part of his PhD studies. However, the research cited by Lacroix et al[1] does mention a severe degradation in sensitivity after the steel surface has transformed. Also, the issue of a changing skin depth, can complicate the measurement. For this reason dc methods were chosen as the main measurement technique to be researched in this study.

6.7 DC coil sensor

Lacroix et al[1] stated that the magnetic reluctance of the air gap attenuates the magnetic field in the sample to such a degree that it is not suitable for the measurement of phase transformation of a steel sample. With advances in magnetic field measurement devices, it was felt that it would be appropriate to re-examine this technique. To do this, two sensors were built and finite element simulations were used to extend the investigations.

The first sensor used dc excitation and Lohet Hall probes (see Appendix A for specification) to detect the presence of a ferromagnetic material. A schematic is shown in fig. 6.7.1. The pole gap was 100mm and the number of turns on the exciting coil was 260; these filled the pole gap and were multilayered. A dc constant current source was used to ensure the magnetomotive force driving the magnetic circuit was constant. The orientation of the Hall probe was such that it only measured the component of the B-field normal to the pole face. The output was fed through a differential amplifier circuit with variable gain. It should be noted that the Hall probe output was very sensitive to sensor location and the amplifier gain was used to optimise the output range for different sensor setups, ie the readings from two different experiments cannot be directly compared.

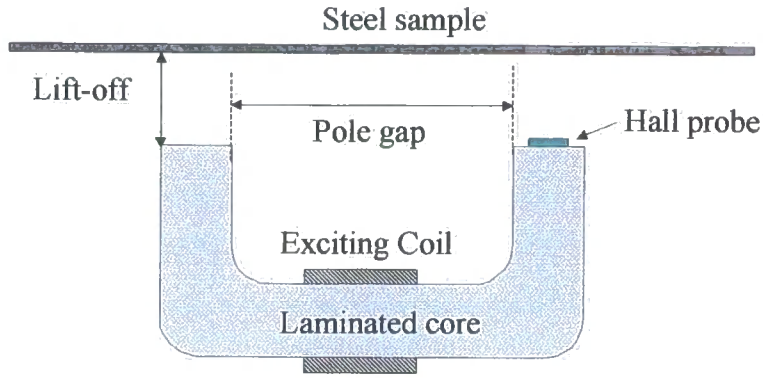

Fig. 6.7.1 **DC coil based sensor**

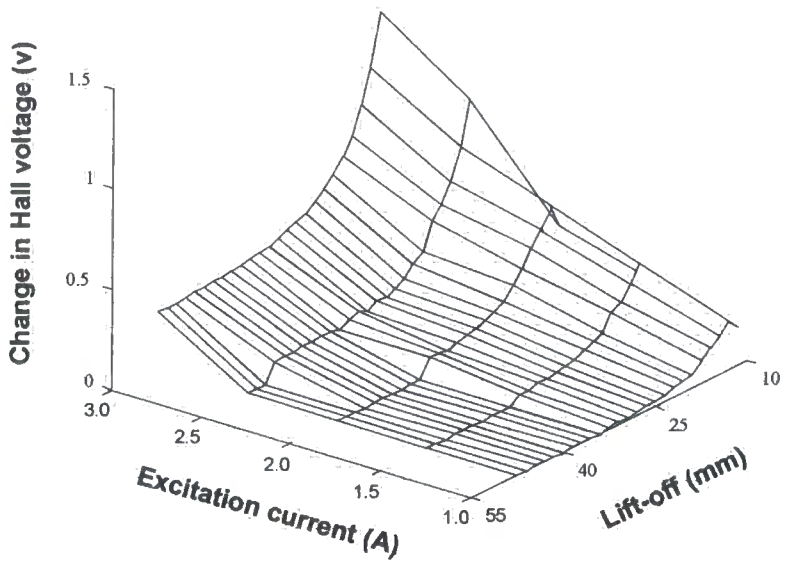

Fig. 6.7.2 **Lift-off characteristics for different excitation currents**

6.7.1 Characterisation of lift-off for different excitation currents

Experimental Work

Steel samples were placed at known distances above the sensor and the Hall output noted for different driving currents. The results are shown in fig. 6.7.2. They show that the Hall sensor detected the steel plate, with the sensitivity decreasing as the distance (lift-off) increased, eg with a 3.0A driving current, at a lift-off of 50mm the detecting range is about 6% of the sensor range. Therefore, to resolve percentage transformation to better than 10%, the sensor needs to be stable to better than 0.6%. Also, increasing the driving current increased the lift-off range of the sensor.

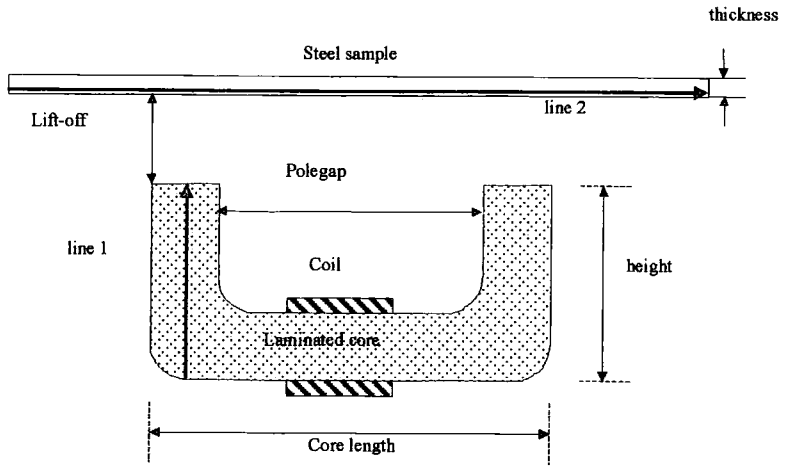

Fig. 6.7.3 Two-dimensional model of DC coil

Finite element Simulations

To investigate these results further, two-dimensional simulations were set up in Ansoft Maxwell™. Before the simulations were carried out, the validity of the model setup needed to be investigated. The main concern was how to define the magnetic properties of the sensor core and the sample material. The sensor core was assumed to be high permeability transformer steel with very low hysteresis loss. Therefore, it was assigned a relative permeability of 5000, ie it was assumed to be in the linear region. To model the material properties of a cold piece of steel, the magnetisation curves of steel types 1008 and 1010, supplied by the Ansoft software, were investigated. These steel grades were unfamiliar, so firstly the relative permeabilities in the linear regions of the curves were calculated; they were both about 400. This value is too low for electrical steel and too high for ferritic stainless steel. It was therefore concluded that these steels were possibly carbon steels, and applicable to the grades rolled at Port Talbot hot strip mill and therefore to this research.

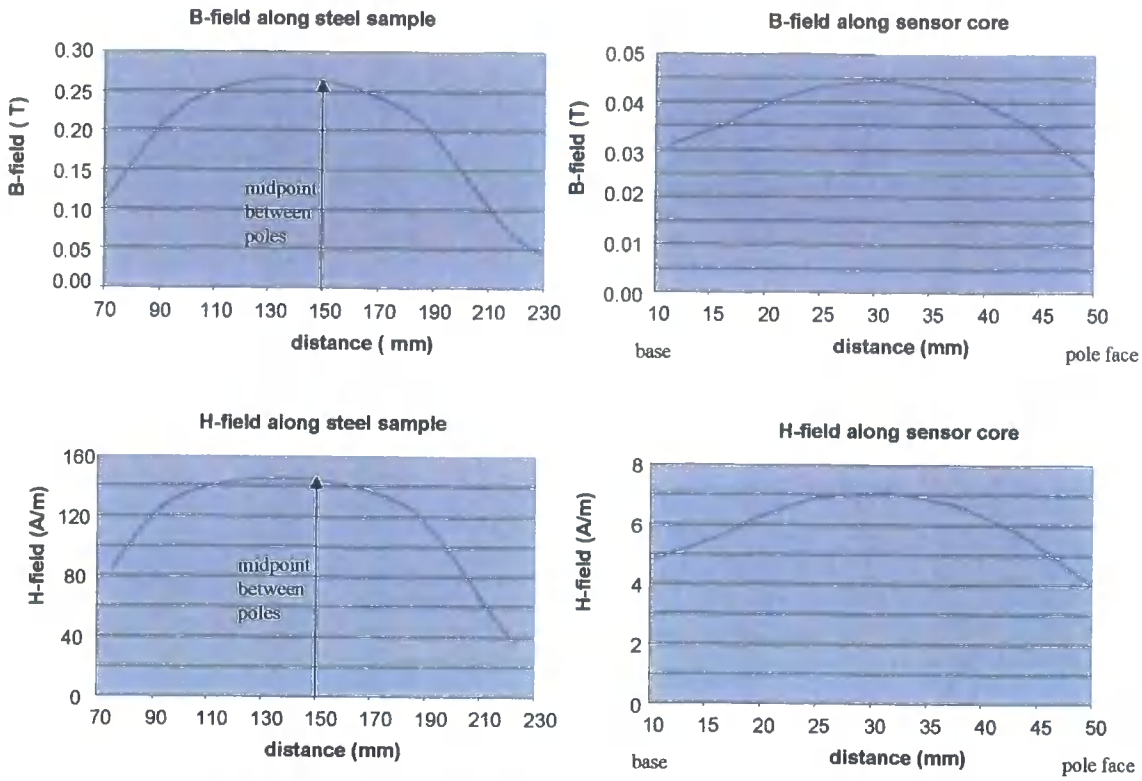

Fig. 6.7.4 Characterisation of B and H-Field magnitudes along sensor and steel sample

A two-dimensional model of the setup shown in fig. 6.7.3 was produced with the following parameters: lift-off = 10mm, coil current = 4A, polegap = 100mm, core relative permeability = 5000, steel B-H curve = steel_1008, steel thickness = 5mm, magnet length = 150mm and coil winding area = 50mm x 0.5mm. Due to the low lift-off value, it was expected that this would be a reasonable representation of higher values of B- and H-fields to be measured. These were measured in the sensor core (as shown by line 1) and steel sample (as shown by line 2) . The results are shown in fig. 6.7.4. They show that the B- and H-fields in the steel sample are well within the linear region of the steel hysteresis curves, ie B is below 1.6T and H is below 3.2 kA/m. This implies that a single value of relative permeability can be used to represent the cold steel samples. The B- and H-fields within the core were also very low, and assumed again to be in the linear region. However, to confirm these findings, an electrical steel expert at Orb Electrical Steels, Corus was consulted. The model was then used to simulate the B-fields measured by the Hall probe for different excitation currents at lift-offs between 10mm and 50mm, and the results, as shown in fig. 6.7.5, compared with the measured values shown in fig. 6.7.2. The model shows that the changes in output are consistent with the experimental data, and that the relationship

continues for larger currents. These results give further confidence in using two-dimensional finite element simulations for future predictions of this sensor arrangement.

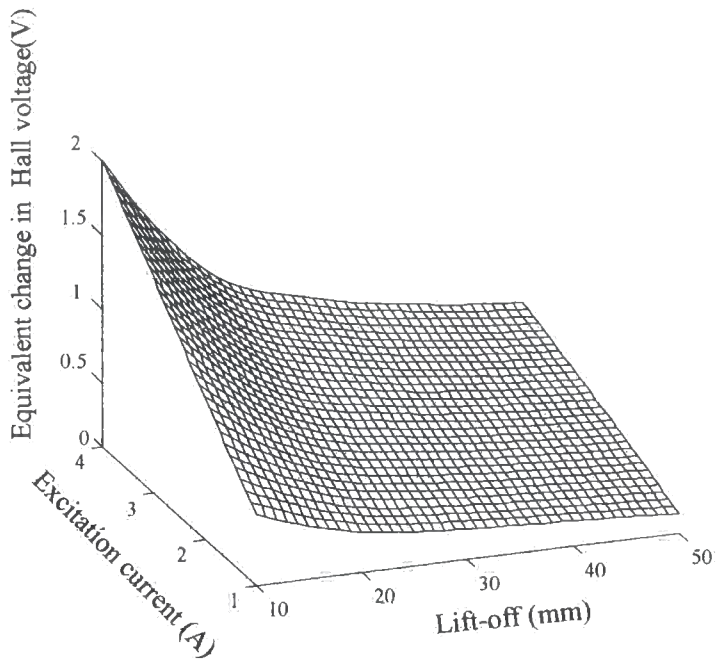

Fig. 6.7.5 FE simulation of lift-off characteristic with applied excitation current

6.7.2 Characterisation of lift-off for different polegaps

Experimental work

The previous results showed that the sensitivity could be considerably improved by increasing the field strength. Another factor which could have an effect was the length of the polegap. This was investigated by winding coils with almost the same number of windings onto C-cores with polegaps of 18mm and 30mm. Lohet Hall probes were used to detect the B-field changes. The results are shown in fig. 6.7.6.

It can be seen that the output of the larger polegap is lower. This was thought to be because the magnetic circuit is longer. However, the sensitivity to the sample's lift-off is greater and the sensor's range longer. The actual range of any of the sensors will be defined by the detecting circuitry and noise levels. In this case it was defined as 50mV for comparison purposes only.

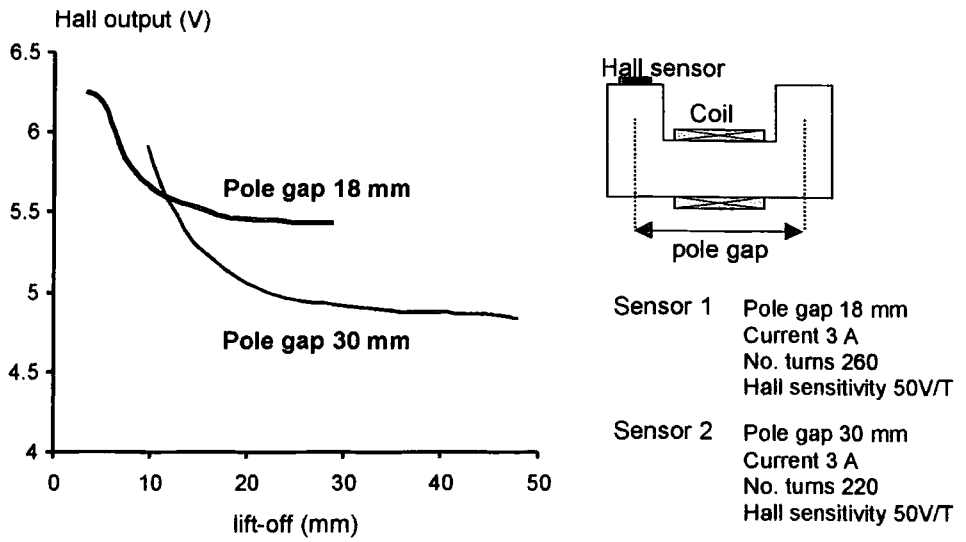

Fig. 6.7.6 Comparison of ac electromagnet type sensors with different polegaps

Finite Element simulations

To investigate further the effect of changing the polegap, finite element simulations were carried out. The normal B-fields at the centre of the pole faces were measured and the results averaged. Firstly, the sensitivity to lift-off was investigated and then the sensitivity to the sample permeability changing. The results from the lift-off versus polegap simulations are shown in fig. 6.7.7. Typical mesh sizes were between 20,000 and 30,000 elements. The graph shows that the B-field range for a corresponding lift-off range between 10mm and 50mm, was 15.22mT +/-0.04mT and has no apparent relationship with polegap. This does not appear to agree with the experiments. To investigate this further the B-field for a sample at 50mm lift-off was examined. An example is given in fig. 6.7.8.

It shows that the normal B-field initially increases and then decays. This can be explained by considering the diagrams in fig. 6.7.9. At polegaps smaller than the lift-off, the route with the smallest reluctance is directly between the poles. Therefore, there will be a strong x-component and a weak y-component of the B-field. At pole gaps comparable to the lift-off, the field will split between the two paths, resulting in a stronger y-component and weaker x-component. For pole gaps greater than the lift-off, the x-component becomes negligible as the path of least reluctance is through the target material. As the pole gap increases further, the circuit length increases thus the y-value decreases. This now explains the experimental data since the curves in fig.

6.7.6 are closer together when the polegaps are greater than the lift-offs, ie at low lift-offs.

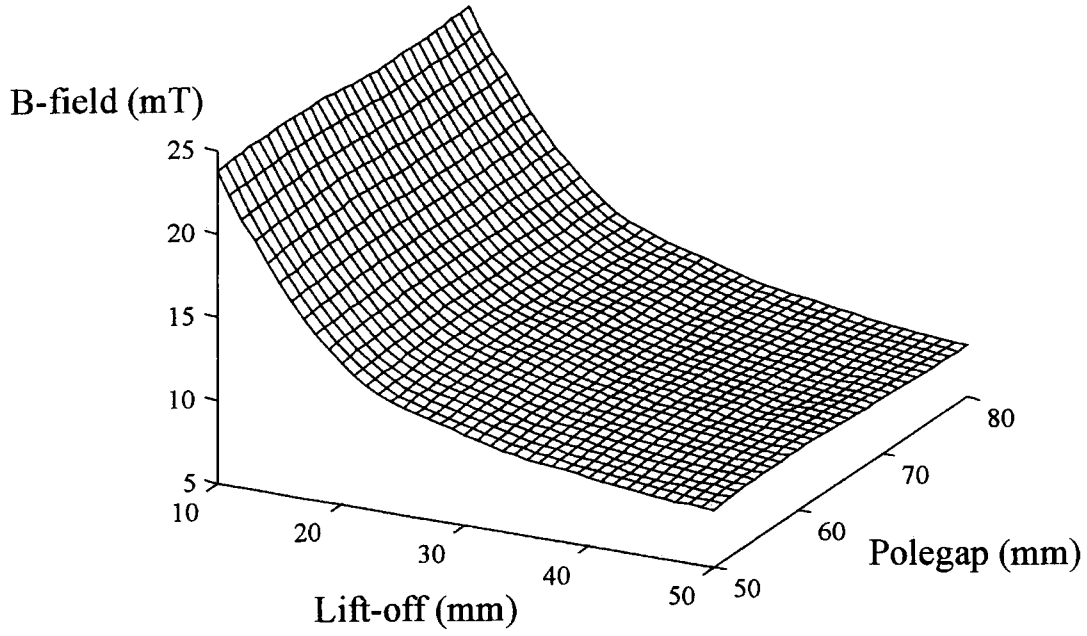

Fig. 6.7.7 FE simulation of lift-off characteristic with increase in polegap

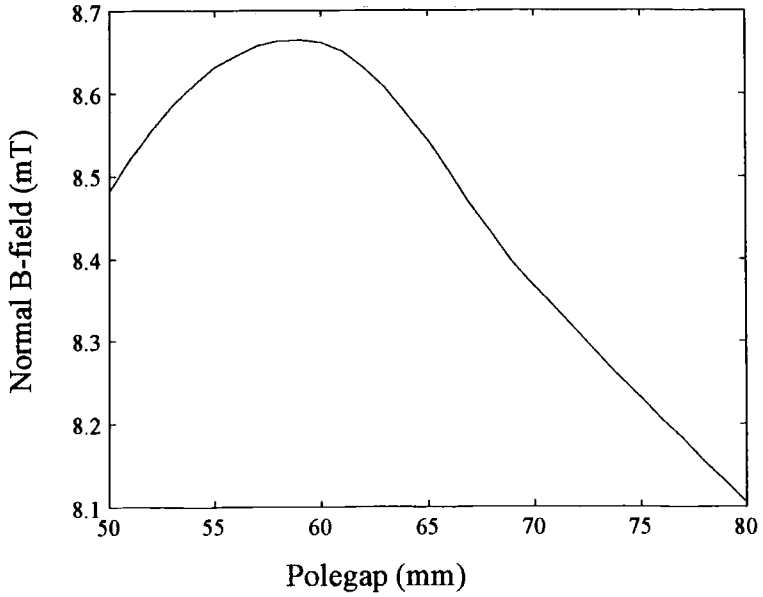

Fig. 6.7.8 Normal B-field at 50mm lift-off for varying polegaps

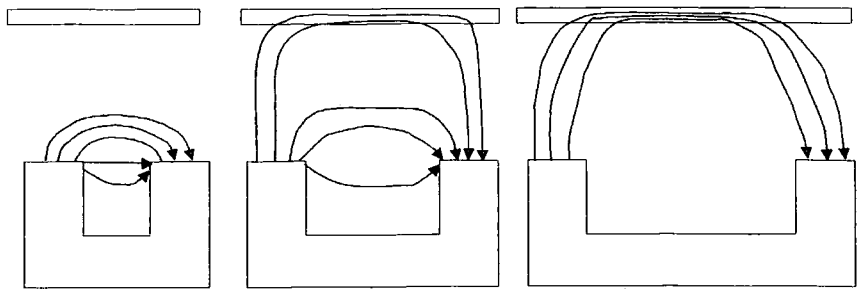

Polegap < lift-off Polegap = lift-off Polegap > lift-off

Fig. 6.7.9 Flux diagrams for sensors with different polegaps

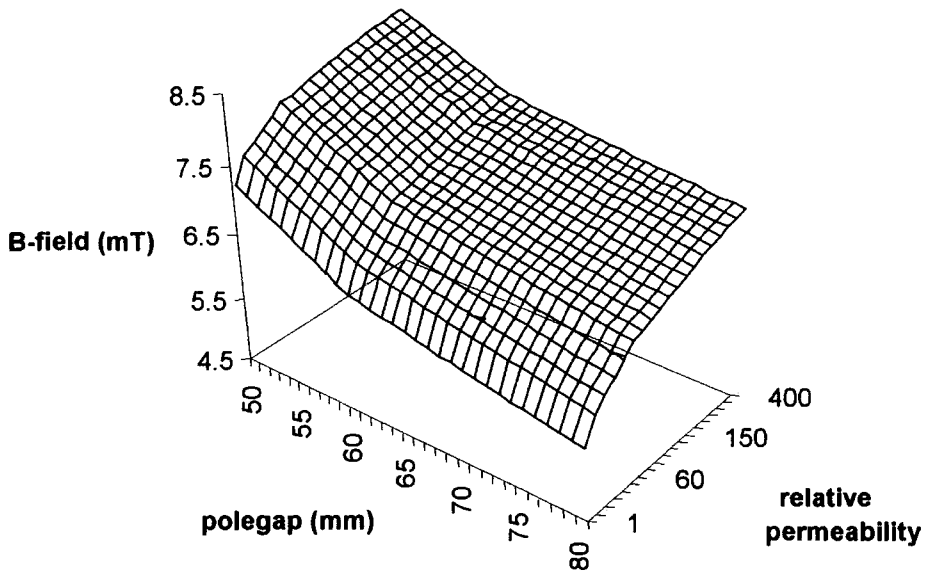

Fig. 6.7.10 FE simulation of permeability characteristic with increase in polegap

To complete the investigation into the effect of the pole gap a final set of simulations were produced, in which the permeability of the sample was varied at a constant lift-off of 50mm, for different pole gaps. The results are shown in fig. 6.7.10. They show that increasing the pole gap, increases the sensitivity to the sample's permeability. This can be seen more clearly in fig. 6.7.11, where the difference in B-field for $\mu_r = 1$ and $\mu_r = 400$, the range, is plotted against pole gap. Initially, the range increases at a steady rate. This is due to the flux preferentially travelling through the sample as μ_r increases, as well as the flux density in the sample increasing. When the pole gap is sufficiently greater than the lift-off such that the flux would pass through the sample for most values of μ_r, the rate of increase of range decreases. This is because the only factor affecting the range now is the flux density in the sample.

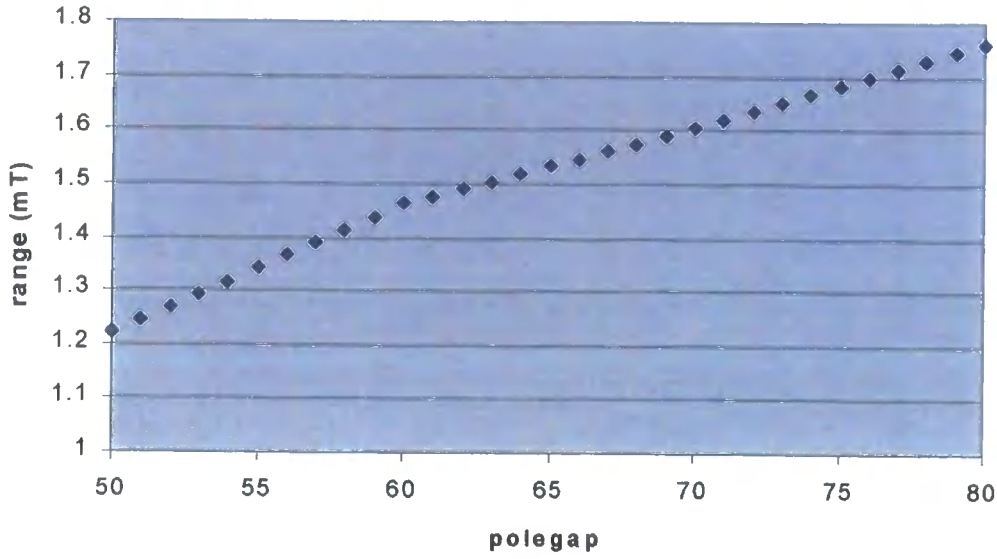

Fig. 6.7.11 Permeability sensitivity as a function of polegap

The increase in range was not solely due to an increase in the length of the magnetic circuit, since work by Macovsci and Poupot[7] showed that simply increasing the length of the circuit (by increasing the pole lengths) with a constant polegap had negligible effect on the sensitivity to the sample.

6.7.3 Conclusions

Using a dc circuit eliminates problems due to changing skin depth with phase transformation. In this section, work was carried out to optimise the magnetic circuit parameters. It was found that increasing the number of turns per unit length and the current in the driving coil, (the magnetomotive force) increased the flux density around the magnetic circuit. This resulted in the Hall sensor output being more sensitive to changes in components, such as the sample permeability, size and position within the circuit. The effect of increasing the gap between the sensor and sample (the lift-off) was also examined. The results showed that increasing the lift-off, decreases the sensitivity of the Hall output to the sample. This is due to the flux decaying with distance from the sensor and preferentially travelling directly to the other pole.

Changing the polegap does have an effect on the normal B-field component at a poleface. However, the relationship is dependent on the sample lift-off, with the field

increasing while the polegap is less than or comparable to the lift-off, and decreasing when it is greater. Regardless of this, the sensitivity of the sensor to the sample permeability at a constant lift-off, increases with increasing polegap. For smaller polegaps, the increase is due to the flux redirecting through the sample, and the sample becoming more permeable, whilst for larger polegaps, just the latter mechanism applies. It can therefore be concluded from these investigations, that the optimum polegap should be as large as possible to fit between the rolls on the roller table.

6.8 Permanent magnet sensor

To look at the effect of further increasing the B-field, a readily available permanent magnet (of unknown magnetic characteristics) was tested. The use of permanent magnets for sensor applications is commonplace, with examples including tachometers, torque sensors and metal flow meters[8,9,10]. The results are shown in fig. 6.8.1. They show that the range is increased further still, when compared to the electromagnet systems. The limiting factor at this stage being the Lohet Hall probe, since it has a built in amplifier limiting the range to +/-40mT.

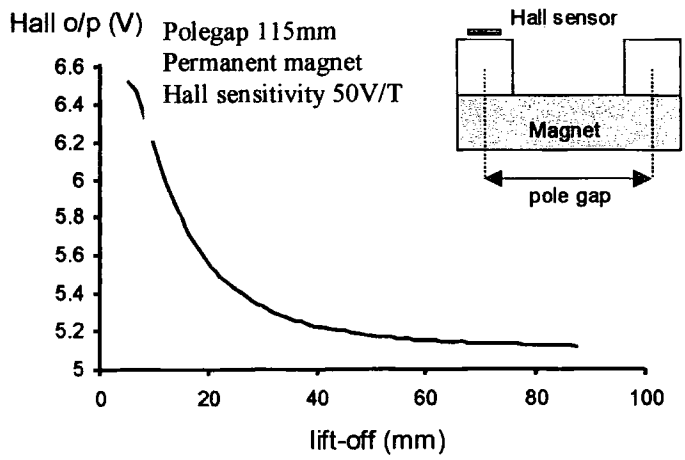

Fig. 6.8.1 Lift-off characteristic for a permanent magnet

6.9 Commercial eddy current sensor

The sensor used for this investigation was a Kaman 10CU dual coil proximity sensor, which was part of an inductive bridge. A schematic of the measurement system is shown in fig. 6.9.1. When a sample is placed within range (25mm) of the sensor, the sensor's impedance changes with distance. This changes the magnitude and phase of the output voltage from the bridge circuit. This is demodulated using a phase sensitive

detector to gives a logarithmic curve, which is then linearised to give an output proportional to distance. The manufacturer recommended different calibrations for different sample materials. Also, the literature[4,11,12] showed evidence that eddy current sensors were sensitive to the material microstructure and defects. Therefore, the possibility of using the sensor's sensitivity to the sample electromagnetic properties was examined for the purpose of measuring phase transformation in steel.

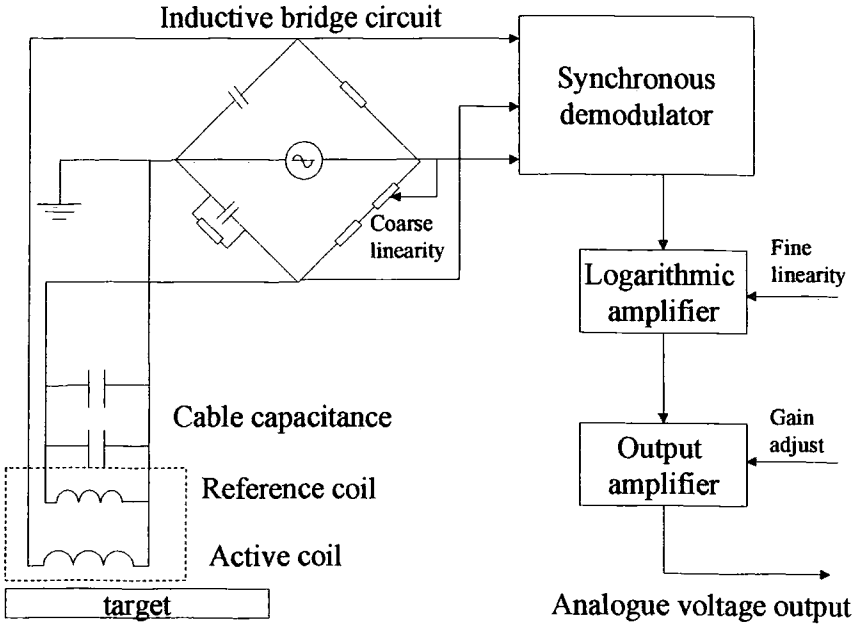

Fig. 6.9.1 Kaman inductive bridge measuring system

(Reproduced from Kaman Measuring Systems Seminar Workbook SWB 865, 1993, Kaman Instrumentation Corp.)

The sensor was excited by a 1MHz signal, and as such had calculated skin depths ranging from 25μm, for a transformed sample, to 503μm for an untransformed sample (assuming a conductivity of 10^6 S/m and a relative permeability of 400). Therefore, it would be expected to be extremely sensitive to the transformation of the sample surface. To investigate this sensor, different metal samples with varying thicknesses were placed at known distances from the sensor using Tufnol spacers. The results are shown in fig. 6.9.2. They show that when the samples were at distances greater than about 11mm from the sensor, all the traces were approximately parallel with a spread (from steel to brass) of around 6% of the sensor output range. At distances less than 11mm the steel trace deviated from the rest which tended to converge. This is because the sensor is more sensitive to the samples' permeability and conductivity when they are closer to it, since the magnetic coupling is greater. To explain the spread of the

curves, the resistivities of the samples were considered. They were found to be in the range of 2 x $10^{-8}\Omega$m (for aluminium) to 66 x $10^{-8}\Omega$m (stainless steel). This can give a difference in the induced current, and hence the output of around 25%. This was not consistent with the 6% spread found from the measurements, thus another factor was considered, that of sample thickness. The reason for this, is that the sample resistance is affected by both the resistivity and geometry. It was found that the measured curves of the paramagnetic materials were in order of their resistance, brass having the highest value due to it being considerably thinner than the other samples. The ferromagnetic sample, steel, however, did not follow this relationship. This is due to the steel having a permeability of at least 400 times greater than the other metals. This will act to concentrate the magnetic flux through the sample, which will increase the rate of change of flux, and hence the resulting eddy currents. Therefore, as predicted, steel gave the greatest change in the coil impedance and hence the highest output.

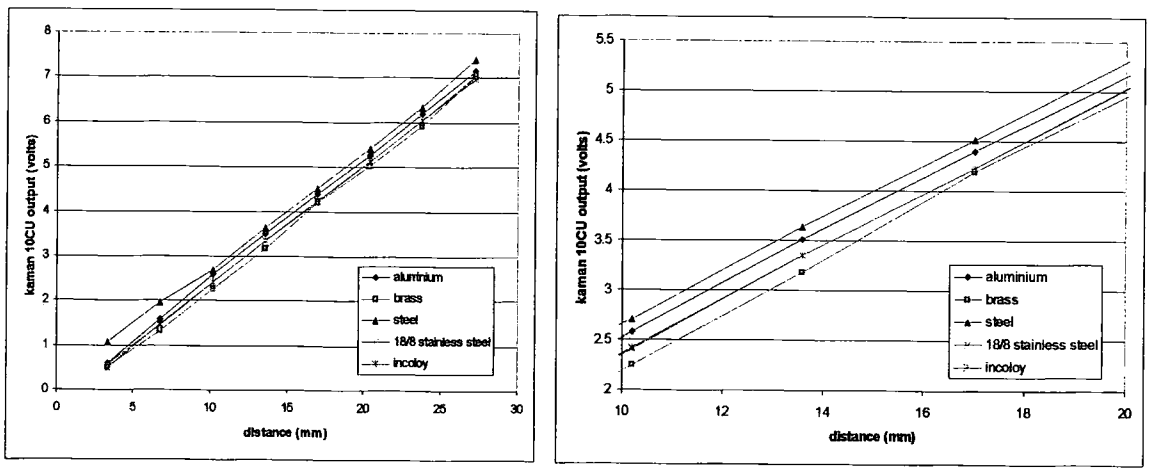

a) Full range of results b) Close up of results between 10 and 20mm

Fig. 6.9.2 Output of Kaman 10CU with different target materials

From these results, it would be expected that the sensor should be able to detect steel transforming with the sensitivity increasing as the lift-off decreases. The range of the sensor output would be in the region of 800mV or less depending on lift-off and sample thickness.

6.10 Laboratory tests using hot samples

6.10.1 Comparison of sensors

The work so far has shown that there are three sensor arrangements, which have the potential of measuring phase transformation; a dc C-core electromagnet, a C-core permanent magnet and a commercial eddy current proximity sensor. (There is also the ac C-core electromagnet which is not covered here). To assess the sensors, further tests were performed in the laboratory using hot samples. The experimental setup is shown in fig. 6.10.1 for a dc electromagnet of polegap 90mm, with a 300-turn coil and a driving current of 1.6A, and a permanent magnet sensor of polegap 115mm. Lohet sensors were used to measure the B-field for both arrangements.

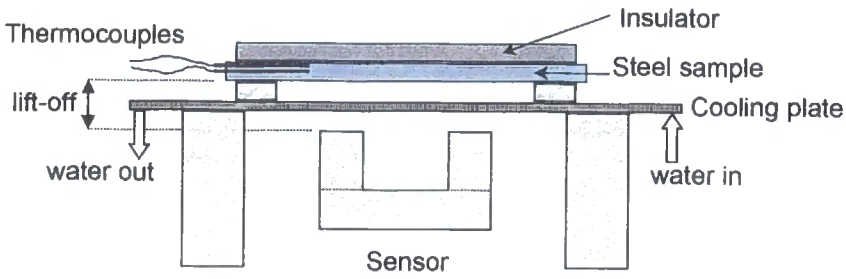

Fig. 6.10.1 Experimental setup for hot samples

The test consisted of heating a steel sample to about 1000°C in an inductively heated furnace. The size of the sample was such that it was greater than the sensor, but small enough to fit in the furnace. The sample size determined the soaking time in the furnace which was chosen to ensure that the entire sample had an austenitic microstructure. However, because the sample was heated in air, prolongued heating caused decarburisation, which affected the surface microstructure. The sample was then removed from the furnace and placed on refractory supports, under which was situated an aluminium cooling plate. A thermocouple was inserted into a pre-drilled hole in the sample, and the sample was then left to cool. The sample temperature and sensor output were logged using a Squirrel data logger at a rate of 1Hz. This logging rate was thought to be sufficient due to the slow cooling rate.

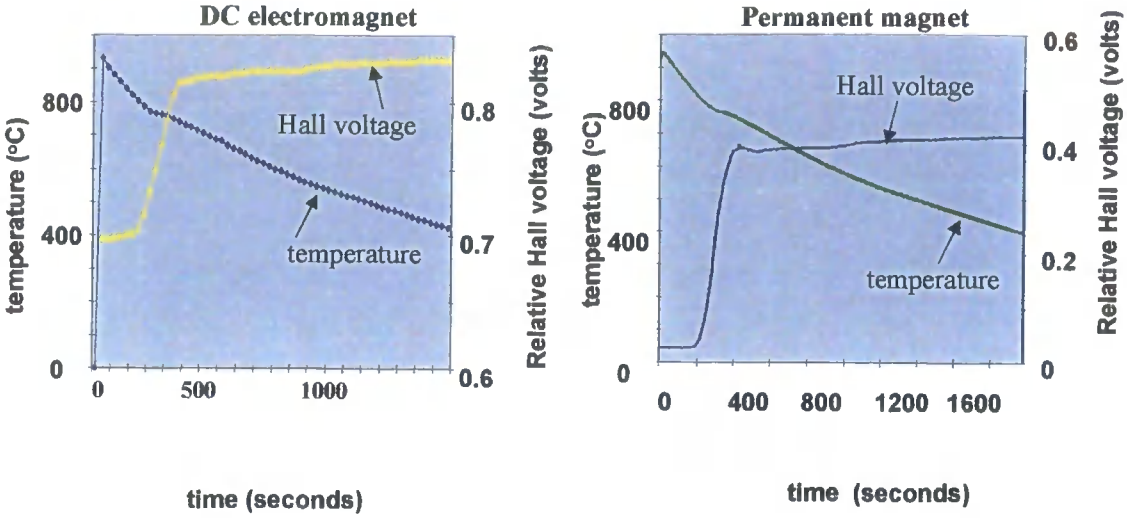

Fig. 6.10.2 Results from Hot tests

The steel used in these tests was a grade 43A structural steel from a 10mm thick flange of a Universal beam. Its carbon content was approximately 0.2%. This sample was chosen, since it was thick enough to prevent excessive buckling which would vary the average lift-off as the test progressed. A soak time of 20 minutes was chosen to ensure the centre of the sample was austenised. The results are shown in fig. 6.10.2.

The temperature traces show inflections at around 750 – 760 °C. This is due to the heat given out during the change of phase from austenite to ferrite. The exact start and end of transformation will occur over a range of temperatures, since the surface will be cooler and will therefore transform first. This will release energy, which will increase the bulk temperature. The net effect is the transformation of the sample centre will occur at a measured lower temperature than the surface. A detailed explanation of the transformations in slowly cooled steel is given by Bodin[13]. At around 600°C there appears to be another much smaller inflection. This is possibly due to a pearlite transformation. The metallurgy of this steel would have to be analysed further to corroborate this explanation.

The dc electromagnet used was the sensor shown in fig. 6.7.1. The Hall voltage trace shows that at the start of the experiment, there was a slight upward trend before the large swing in voltage. Finally, there was a further gentle increase. The large swing in voltage of 0.15V occurred around the expected phase transformation period, as suggested by the temperature curve. This showed that this sensor had an output which

could potentially be related to the percentage fraction transformed. The experiment was repeated with the permanent magnet sensor described in section 6.8. The trace showed a similar characteristic to the dc sensor but with a greater voltage swing of 0.4V as expected due to the larger field strength. There also appeared to be a small inflection in the 'transformation region'. Only the dc electromagnet showed an upward drift before transformation due to the resistance of the driving coil decreasing as it heated up. This had the effect of increasing the driving current and hence the resulting magnetic field. This is further confirmed by the fact that no drift was observed before transformation for the permanent magnet system, ie this sensing system is less temperature sensitive. The gentle upward trends in the traces after the transformation region in both systems were, therefore, probably due to a combined effect of temperature dependent sensor drift and sample permeability as described in Bozorth[14].

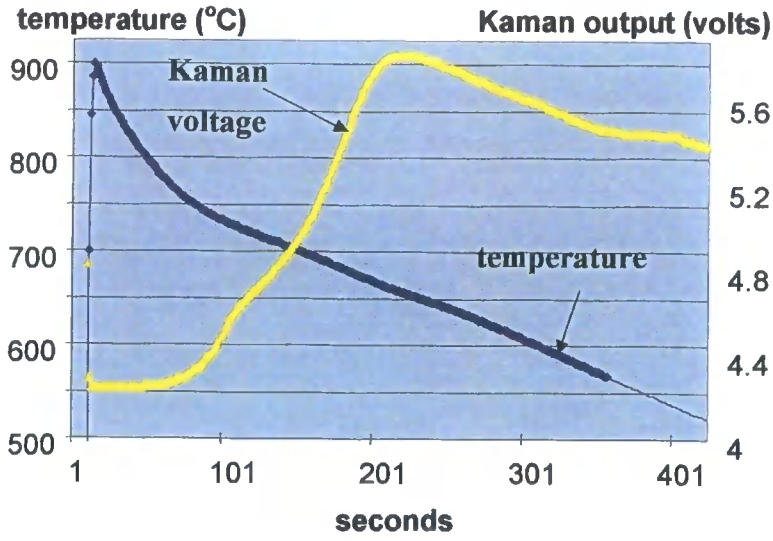

Fig. 6.10.3 Results from Hot tests with Kaman 10CU

The results of the tests carried out with the Kaman 10CU are shown in fig. 6.10.3. In this test the sensor was placed 20mm below the sample. The aluminium cooling plate could not be used, since it would act to shield the sensor from the hot steel sample. Therefore, a 10mm refractory board was used to protect the sensor against the heat. (If the sensor had been waterproof, it could have been immersed in water.) A grade H559 piece of steel (See Appendix B) was placed on the refractory board. Due to the limited measuring range of the sensor, refractory spacers could not be used. This meant that the cooling of the sample was significantly greater on the top, and since the sample

was only 4mm thick, it buckled as the experiment progressed. Due to the low carbon content in this particular steel grade, it was not possible to determine how the major increase in the Kaman sensor output related to the start and end of transformation. However, the output did change significantly (18% of range) around the expected transformation region. Therefore, this sensor showed a potential for measuring phase transformation of the sample surface which is defined by the skin depth. Other features were observed in the trace. A low frequency oscillation of period greater than 100s appeared to be present. It was possible that this could be a result of the material properties fluctuating, since the output was influenced by a combination of both the permeability and conductivity of the material. However, the instrumentation system itself could not be ignored. The logging frequency was limited to 1Hz by the Squirrel data logger, thus the observed frequency could, in fact, be aliased. An anti-aliasing filter would be needed to remove this. Another factor to be considered was that the sensor electronics were designed to give a linear relationship with distance. Due to the material properties changing, this was certainly not the case in this experiment. Thus, the output signal could have been distorted.

6.10.2 Comparison of different cooling rates

This experiment was undertaken, to try to assess whether the magnetic property changes observed during the cooling of hot steel samples, had a consistent relationship with the austenite-to-ferrite phase transformation. The sensor used for this was the dc electromagnet with a polegap of 90mm, and 300 turns. A driving current of 1.6A was used and the $\underline{B}$-field measured using a Lohet sensor. The experimental arrangement was as shown in fig. 6.10.1.

A Squirrel data logger was used again to collect the data at a rate of 1Hz. The results are shown in fig. 6.10.4. The average cooling rates were fast, 4°C/s; medium, 2°C/s; slow, 0.6°C/s. It can be seen that the curves are similar in shape to transformation curves derived from dilatometry tests[15], in that the gradient is initially steep and then reduces towards the end. To further explain the curves, the differentiated traces are considered, since it is easier to identify points in both the temperature and magnetic traces.

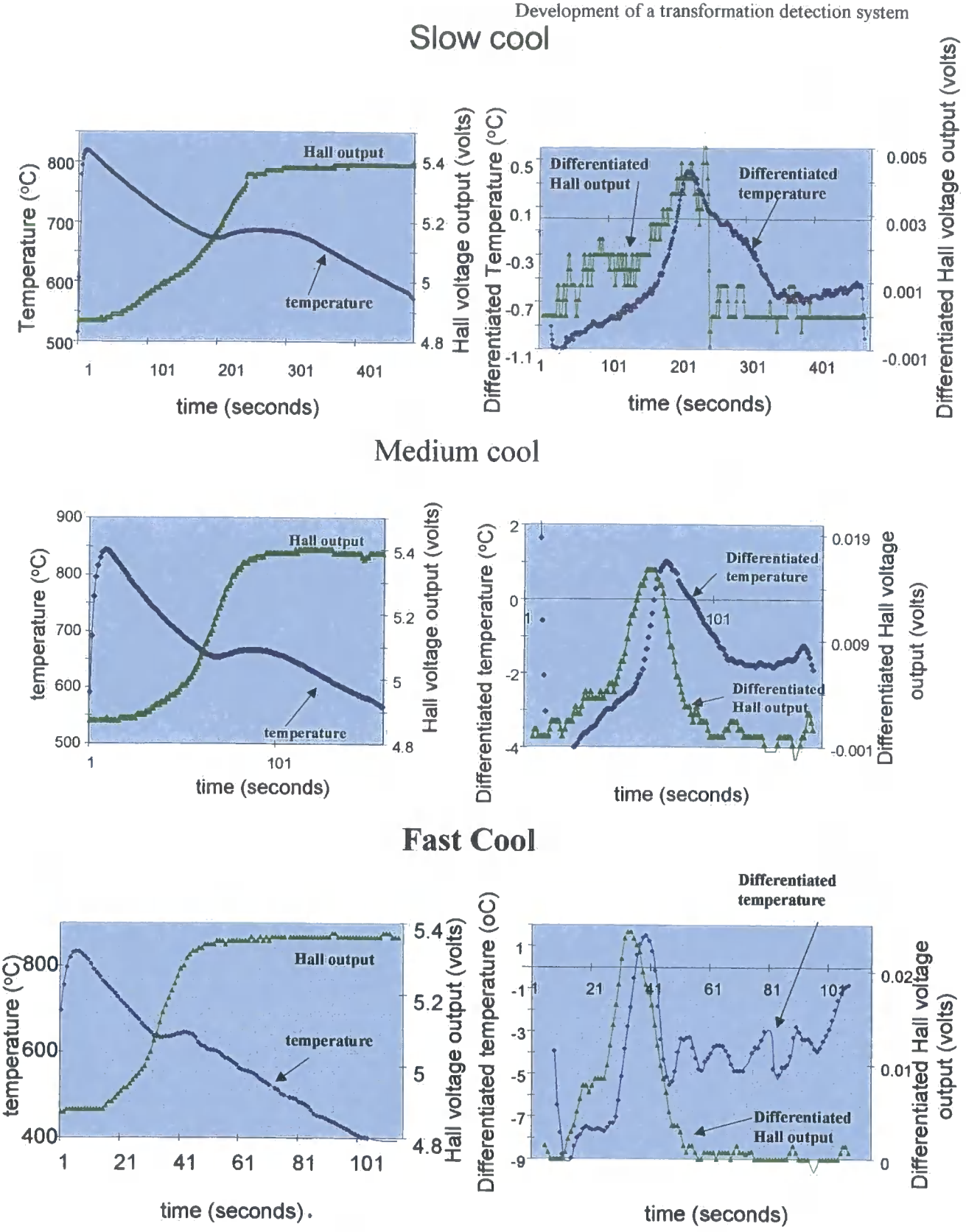

Fig. 6.10.4 Comparison of different cooling rates

The first points to note are those of the locations of the largest maxima since on both traces they can be related to the maximum rate of transformation. On the slow cool trace these occur at the same time within the resolution of the sample rate. On the medium and fast cool traces, the magnetic trace peaks before the temperature trace. In an attempt to explain this, the sensor reponse times were considered. It was found that the sensor response of the magnetic sensor was similar to the thermocouple. Thus, the difference in time (6-10s) was too large to be accounted for by this effect. Time differences of less than a logging interval of one second would have been expected, since the thermocouple has a quoted response time in the order of milliseconds. The next factor to be examined was the metallurgical aspect. The ferrite transformation occurs before the pearlite transformation. Since the magnetic peak detects the ferrite transformation, and the temperature peak is related the maximum rate of increase of temperature, due to recalescence (ie a combination of the ferrite and pearlite transformations), it is possible that the magnetic sensor should have its maximum rate of increase before the temperature. The exact kinetics would have to be studied more carefully to verify this. Finally, the measurement setup was reconsidered. The thermocouple was positioned in the centre of the sample, thus it measured the internal bulk temperature of the steel. The magnetic sensor was designed to detect changes in the magnetic properties throughout the sample. Since the surface would be the coolest part, it would begin to transform first, and hence be detected by the magnetic sensor before the thermocouple indicated a recalescence.

The second point of interest is that the widths of both sets of peaks have a tendency to become narrower as the cooling rate increases. This indicates that the rate of transformation increases with cooling rate. The raw traces show that the temperature at which transformation occurs decreases as the cooling rate increases. The start and finish of the change in magnetic properties also starts at lower temperatures for higher cooling rates, and corresponds to the continuous cooling diagrams, an example of which is shown in section 4.4. In general, the similarity in the occurrence of maxima on the differentiated curves, indicates a close link between the magnetic sensor output and phase transformation from austenite to ferrite.

6.10.3 Conclusions

Tests were successfully carried out, in which steel was cooled from the hot austenite to the cooler ferritic phases, with the magnetic properties measured using magnetic sensors. Both the dc electromagnet and permanent magnet implementations, showed a significant change in output during the phase transformation period. The change during the transformation period was relatively linear with respect to time, although the permanent magnet device did show a small inflection. The output from the electromagnet showed a tendency to drift, whereas the permanent magnet output did not. The commercial eddy current sensor produced a fairly linear output trace, but with fluctuations present in the transformation region. It was not established at this stage, as to whether these were due to the material property changes or the instrument. Further tests with the dc electromagnet at different cooling rates, showed that there was close agreement between the differentiated temperature and Hall probe traces. This indicates they are both registering the phase transformation at about the same time.

6.11 Summary

The role of radiation pyrometry in determining phase-transformation on-line has been described, together with its limitations. Thus the need for a direct on-line measurement of phase-transformation has been identified. In order to implement such a measurement, a specification has been produced, and a measurement principle identified. The most appropriate being a magnetic circuit in the shape of a C-core. Investigations were then undertaken to determine the advantages and disadvantages of using either ac or dc circuits. This was done by means of cold laboratory tests. It was found that the ac sensors were relatively insensitive to speed, and the meaning behind the measurement was complicated by the skin depth varying throughout the transformation process. The dc method was then pursued since there were no skin depth issues and only permeability changes were measured. Both laboratory tests and finite element simulations showed that increasing the magnetomotive force by increasing the current density increased the sensitivity of the circuit to the sample properties. The relationship with polegap was not so straight forward, with the lift-off / polegap ratio being a significant factor. It was, however, found that increasing the polegap, generally increased the sensitivity to the sample. This was due to the sample taking a proportionately larger part of the circuit length. Commercial eddy current

sensors were also considered. The cold tests on various metals showed a correlation between the output and sample resistance.

Hot tests were finally carried out to examine the relationship between phase transformation and sensor output. The only measurement available to aid in this investigation was the sample temperature. Both the dc magnetic circuit designs showed a reasonably linear relationship within the predicted phase transformation region. Comparison of different cooling rates also showed a close relationship between the differentiated Hall output and temperature. This indicates they are both registering the start of the transformation in the same region. The commercial eddy current trace similarly registered a distinct change in the transformation region but there were unexpected fluctuations which could be due to conflicting changes in the material properties or the instrumentation system.

To conclude, work has been carried out in this section, which positively indicates that magnetic sensor outputs can be related to phase transformation. Also, this sensor technology is potentially suited to satisfying the overall instrument requirements. However, the long term affects of using a permanent magnet in high ambient temperatures need to be considered.

6.12 References

1 *Lacroix M, Abrigo J, Arnault L*, 'On line instrument for ferritic transformation control: Inter Conf. On steel rolling', Tokyo, Vol. 2, pp. 1286-1296, 1980

2 *Morita M, Hashiguchi K, Hashimoto O, Nishida M, Okano S*, 'On-line transformation detector for property control of hot rolled steel', Proc of Met Soc of AIME Symposium on Accelerated cooling of steel, Pittsburgh Aug. 1985

3 *Yasuhiro M, Seigo A*, 'Transformation rate-measuring method and device', NKK Corp., Pub. No. 07190991 A Aug 1995

4 *Kim H-S, Park I-H, Wee S-B, Hahn S-Y, Han M-K*,'Eddy current methods for evaluating the transformed fraction of metals by voltage source', IEEE Trans. Mag., Vol. 26, No. 2, pp. 505-8, 1990

5 *Yahiro K, Yamasaki J, Furukawa M, Arai K, Morita M, Obashi M*, 'Development of coiling temperature control system on hot strip mill',

Kawasaki Steel Technical Report, No. 24, Apr. 1991

6 *Habiby F, Siddiqui TN, Khan SH, Haq A, Khan AQ*, 'Austenite determination by eddy current measurements in a maraging steel', NDT&E International Vol. 25, No. 3, 1992

7 *Macovschi M, Poupot C*, 'Study of variable inductance transducers as proximity sensors: I. Computer assited study', Meas. Sci Technol. Vol 1, pp. 1031-1039, 1990

8 *Rajagopal KR, Singh , BP Singh, Nvedachalam*, 'Novel methods of temperature compensation for permanent magnet sensors and actuators', IEEE Trans on Magnetics 2001, Vol. 37, Iss. 4, pp. 1995-1997

9 *de Silva C*, 'Sensor/transducer technology – Part 8 – Inductive motion transducers', Meas & Control 2000, Iss. 201, pp. 65-76

10 *Lemarquand V*, 'Synthesis study of magnetic torque sensors', IEE Trans. on Magnetics, Vol 35, Iss. 6, pp. 4503-4510, 1999

11 *Bartoletti C, Buonanni R, Fantasia LG, Frulla R, Gaggioli W, Sacerdoti G*, 'The design of a proximity inductive sensor', Meas. Sci. Technol. Vol. 9, pp. 1180-1190, 1998

12 *Dodd CV, Deeds WE*, 'Analytical solutions to eddy-current probe-coil problems' Journal of Applied Physics, Vol. 39, No. 6, May 1968

13 *Bodin A*, 'Mechanical properties of hot rolled strip and transformation detection', EUR 16625EN, European Commission Technical Steel report – mechanical working (Rolling mills)

14 *Bozorth RM*, 'Ferromagnetism', Bell Laboratory Series, 1964

15 *Prior GK*,' The role of dilatometry in the characterization of steels', Materials Forum Vol.18, pp. 265-276, 1994

CHAPTER 7

PERMANENT MAGNET PROTOTYPES

7.1 Instrument design using a ferrite magnet

The aim of this design was to produce a low cost unit which could be used to test the measurement principles on a hot strip mill. Therefore, drift, temperature or lift-off compensations were not present at this stage. Prototypes 1 to 3 were very similar, thus only prototype 3 will be described. A schematic is shown in fig. 7.1.1. It consisted of an electromagnet C-core, with ferrite magnets placed on each pole. On top of each magnet was a Lohet Hall probe. The outputs of the Hall probes were subtracted to double the sensitivity and reduce the effects of noise.

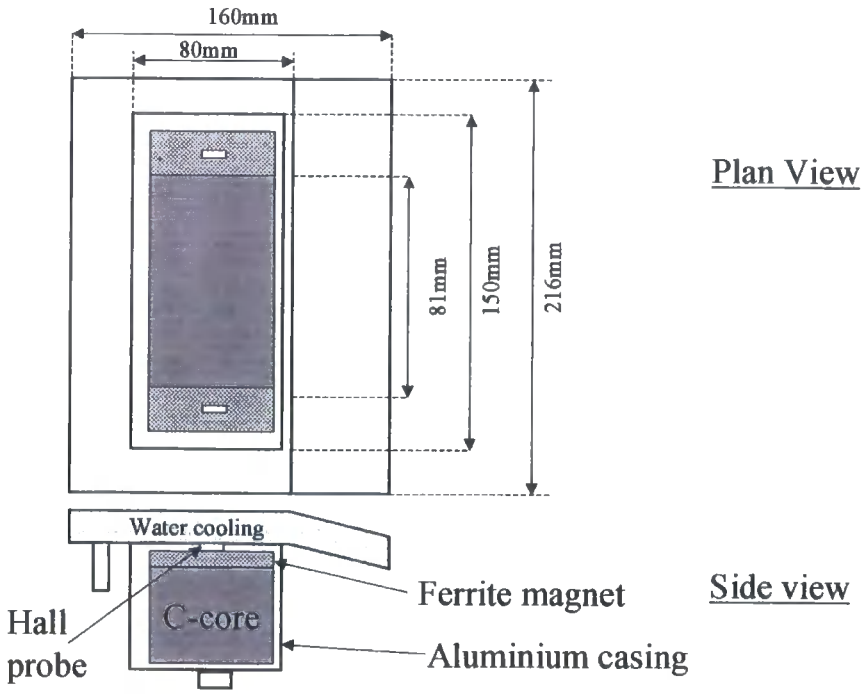

Figure 7.1.1 Schematic of prototype 3

Small anisotropic sintered ferrite magnets (Appendix C) were used since they were the most cost-effective magnets on the market with a high resistance to demagnetisation. They were also capable of producing the required field strength (limited by the range of the Hall probes) with a small volume of material, which again acts to reduce the cost. Using equation 5.7.18, and estimating an operating demagnetision field of about 100kA/m, the calculated range of the B-field was found

to be between 26mT (no steel sample present) and 30mT (a fully transformed steel sample with negligible reluctance at 50mm lift-off) which was within the 40mT range of the Lohet sensor. The main components were housed in an aluminium casing with a double skinned cooling plate on the top. The top plate was profiled to reduce the possibility of a hot steel strip catching on the edge. A schematic of the complete measurement system is shown in fig. 7.1.2.

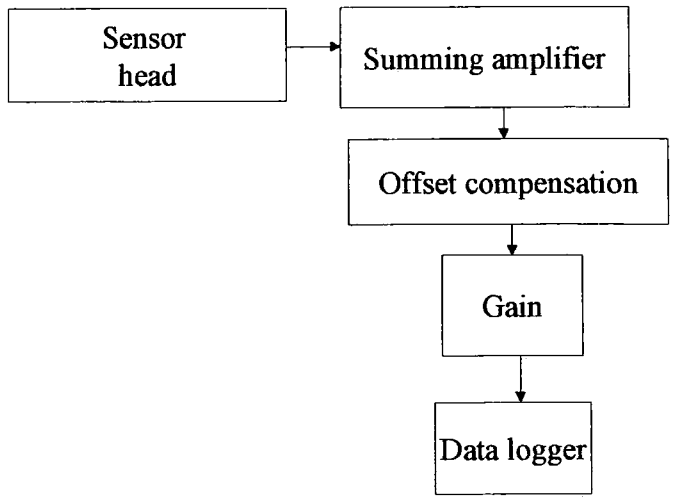

Fig. 7.1.2 Schematic of measurement system

7.2 Laboratory tests using 'cold' samples

These tests were carried out at the Welsh Technology Centre, Corus UK. They consisted of placing a steel sample 20mm and 50mm from the top of the aluminium casing for known periods of time and then removing them. Tests with a Fluke multi-meter showed that the sensor output took in the order of a few minutes to settle to its new value when a piece of steel was placed on it. To investigate this further, traces were recorded on a chart recorderas shown in fig. 7.2.1.

They show a sample being placed 20mm above the instrument for two minutes and then removed. After the first two cycles, the trace was offset to ensure it did not go off the scale. The next 4 cycles are directly comparable. The output range was found to be around 420mV. The instrument was calculated to have a response time of about 28s (assuming a first order system), which was unacceptably long since a coil on a strip mill only takes 90s to pass a point on the run-out-table. Another feature of the trace is that the sensor output gradually increased at the peaks of each cycle. In this case, after 4 cycles the output rose about 9mV, which is 2% of the range. For the case

where the lift-off was 50mm, the increase in peak output was 28% of the range (32mV) and clearly requires some compensation. When the sensor was left with no sample the signal also drifted back to the starting value. To explain these features the system was divided into three parts, the magnetic circuit, the amplification electronics and the chart recorder. The time constant of the electronics was calculated to be around 3ms so was eliminated as the cause.

The chart recorder was specified as having a time constant better than ten seconds. Therefore, the magnetic circuit was investigated in more detail. The drift and offset could be explained by the fact that increasing and decreasing the B-field cycled the magnet around a small hysteresis loop. The effect is particularly noticeable in this case due to the large amplification of the Hall output. The large time constant could be due to the small change in B-field, such that the energy change is small and there is a delay in some of the domain boundary displacements. Further investigation would be needed to confirm this.

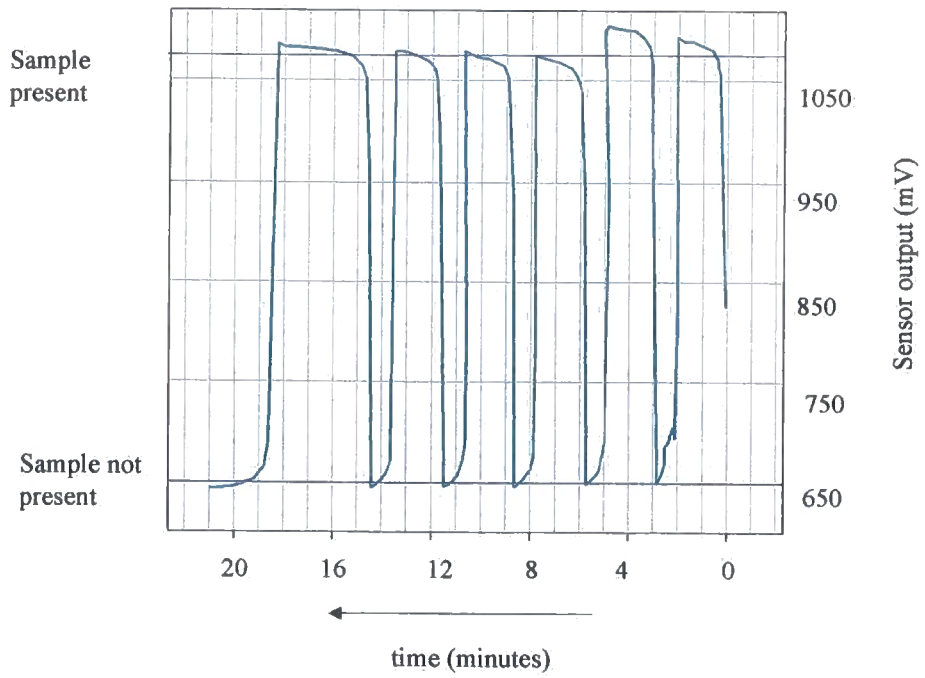

Fig. 7.2.1 Chart recording of prototype 3 output

7.3 Trial at Port Talbot hot strip mill

7.3.1 Method

Prototype 3 was tested at Port Talbot hot strip mill to assess the ruggardness of the sensor and to assess whether it could detect transformed steel strips in a mill environment. The installation bracket, shown in fig. 7.3.1, was designed to fit across the width of the roller table, about 2m in front of the coiler. The height of the meter was adjustable to ensure the lift-off was 50mm below the pass-line, as requested by the mill personnel. The meter could be pushed into or pulled out of the mill manually. Temperature strips were placed inside the casing to assess the effectiveness of the cooling plate.

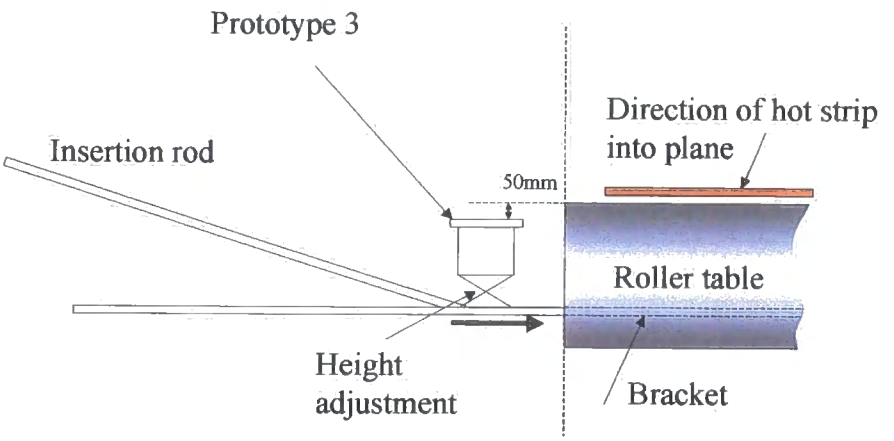

Fig. 7.3.1 Installation of prototype 3 onto Port Talbot hot strip mill

The meter was only pushed into the mill when the strip was under tension, to prevent the strip head and tail ends from hitting the meter. This meant the maximum period of time the meter was in the mill was about half to one minute. The temperature strip on the circuit board did not detect temperatures above 70°C. Therefore, it was concluded that the water-cooling plate was adequate for this trial. Recordings were then taken from several strips under tension as they passed over the sensor. The variations of the strip were estimated by eye to be of the order of a few mm for these particular steels at this mill position. The nominal composition by weight of the steel grade in this rolling round was 0.032%C, 0.001%Si, 0.011%P, 0.211%Mn. Typical results are shown in fig. 7.3.2.

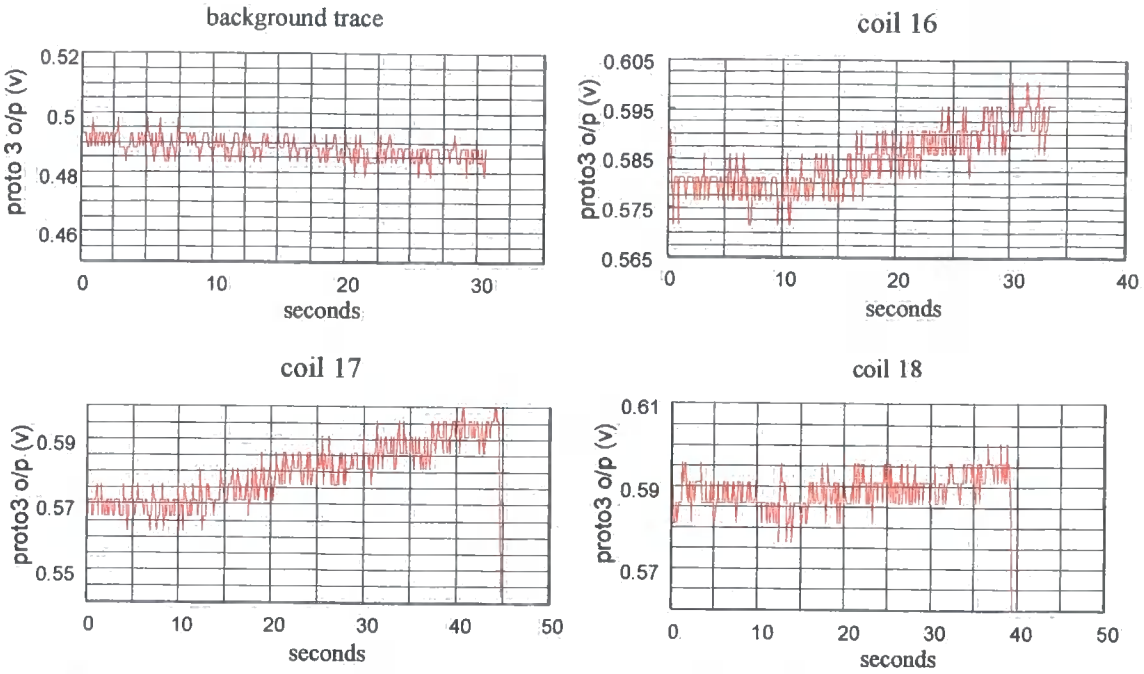

Fig. 7.3.2 **Prototype 3 results from Port Talbot hot strip mill**

7.3.2 Results

The outputs from the coils do show an increase from the background trace in the region of 90mV. The typical noise level (defined as two standard deviations) was 6mV giving a resolution of about 6%. Each of the traces showed a general upward trend as the coil progressed. The rate of increase (approximately 30mV/min) was considerably faster than that observed in the cold tests (2.8mV/min). Therefore, other causes were looked at. To do this, other plant signals such as the last finishing stand (F11) exit temperature, strip speed and F11 rolling load were compared with the transformation meter traces. Typical traces are shown in fig. 7.3.3. They show no apparent correlation with the strip speed. This was confirmed by analysing other strip traces. This shows one of the advantages of using a dc magnetic field as opposed to an ac since Lacroix[1] observed distinct acceleration and deceleration effects for their 10kHz system. However, there appears to be correlations with the temperature of the strip at the coiler and possibly the F11 mill load. These are both indicators of changing material properties. However, the temperature characteristic of the sensor was not known at this stage. Therefore, laboratory tests in which the meter was placed in an environmental chamber were carried out. The temperature coefficient was found to be approximately 0.6mV/°C. By considering the prototype 3 output trace in fig. 7.3.3, the maximum change in output when a strip was present is 15mV. This could be achieved by a corresponding temperature change of 25°C, and the temperature trace

shows an equivalent change of about 20°C. However, the temperature change between the 'no strip' and 'strip present' cases would be equivalent to a 480mV change on the sensor output. The reason this change in the output did not occur, is due to the fact that the sensor did not reach these temperatures, but heated up gradually due to the radiated heat from the strip. Previous temperature tests show that the temperature change of the sensor should be below 40°C. However, the temperature changes did not account for the upward trend in most of traces. Therefore, to carry out a more detailed analysis, temperature compensation is recommended.

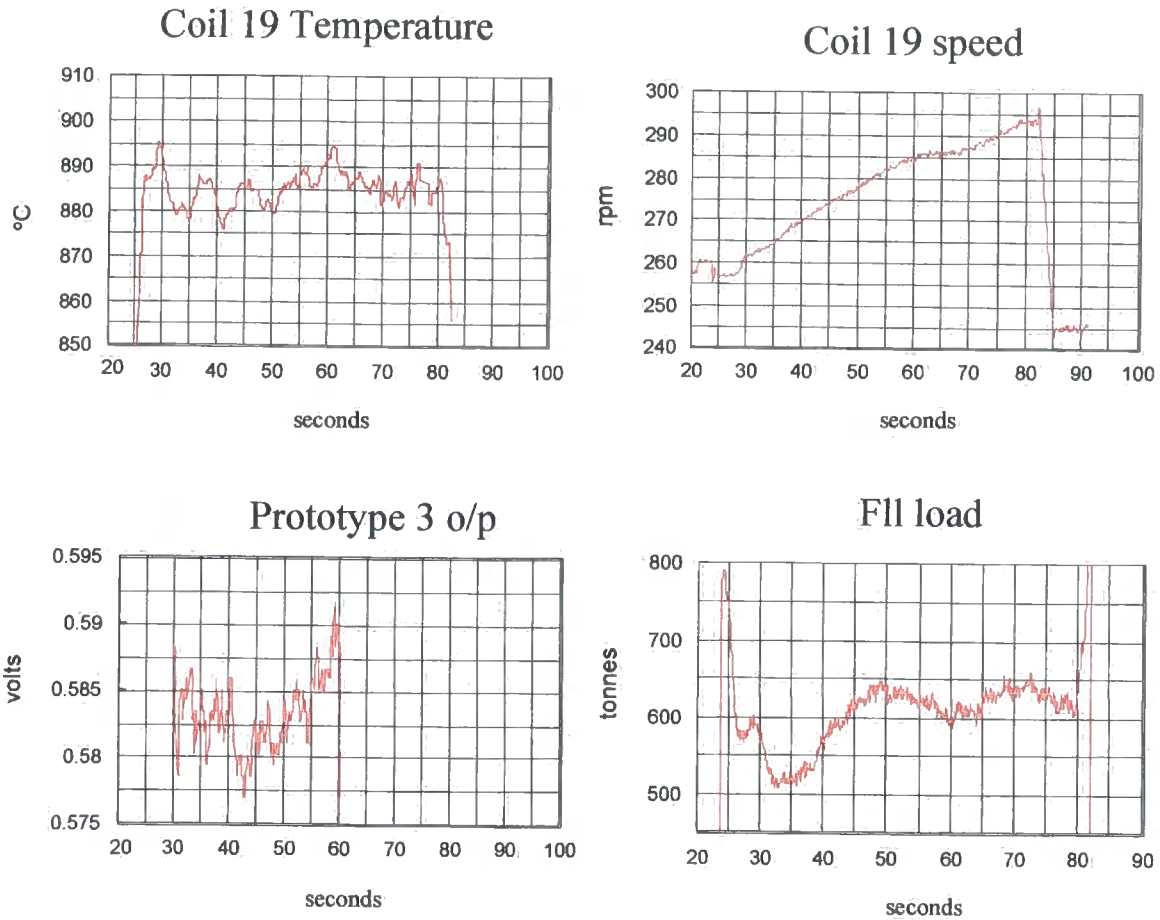

Fig. 7.3.3 **Comparison of prototype 3 output with plant signals**

7.4 Conclusions

It was found that the instrument was robust enough to withstand the mill environment and recordings were made for several coils. The analysis of the data was inconclusive, due to the lack of temperature compensation. Laboratory tests revealed that temperature changes alone could be responsible for the change in output, observed during the plant trial.

Prototype 3 gave an encouraging indication on which to build further prototypes. However, there were several issues, which needed to be addressed to obtain meaningful measurements on-line. These included the response time of the magnetic circuit, temperature, strip speed and lift-off compensation. Also the plant trial was limited, in that the transformed state of the steel was only assumed. To overcome this, more laboratory tests with specific steel grades were needed such that the plant trial could be designed to give more conclusive results.

7.5 Instrument design using an alcomax magnet

Based on the information gained from prototype 3, an improved version, referred to as the T-meter was designed, built and tested[2]. It is again based on a C-core magnet , but this time the issue of how varying lift-off affects the results is addressed. The areas researched were:

i) the permanent magnet
ii) magnetic field measurement
iii) lift-off measurement
iv) casing the components
v) cooling circuitry.

Photographs of the measurement head are shown in fig 7.5.1 and a schematic of the complete system in fig. 7.5.2.

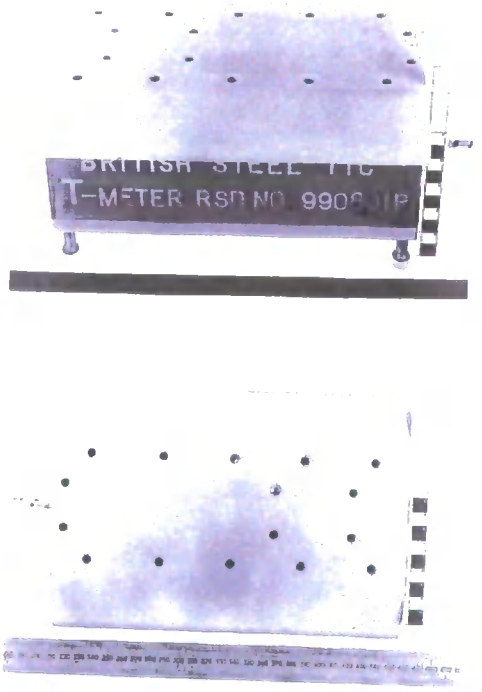

Fig. 7.5.1 Photograph of the T-meter measurement head

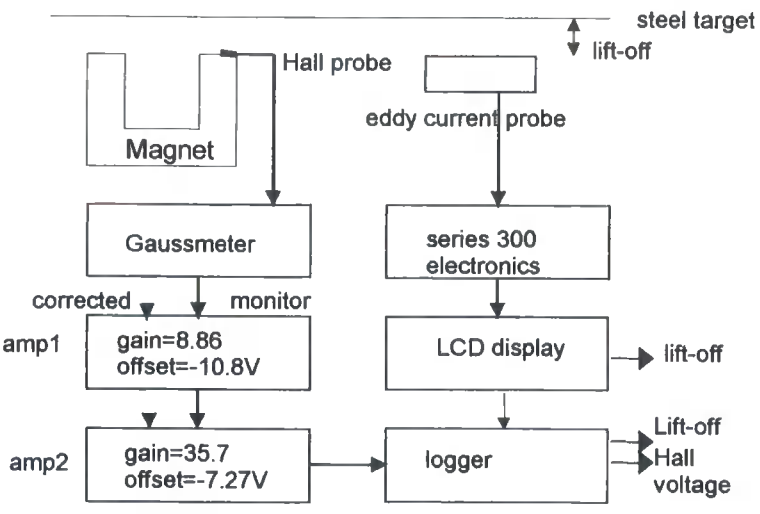

Fig. 7.5.2 Schematic of T-meter system

7.5.1 Permanent magnet

The ferrite magnet for prototype 3 was chosen such that the maximum B-field at the probe was within the range of the Lohet sensors. This severely reduced the sensitivity of the sensing system. Equation 5.7.18 shows that the external field at the pole of a magnet is not only dependent on the maximum $B_{magnet}H_{magnet}$ product but also on the volume and geometry of the magnet. To increase the pole B-field, the magnetic length of the magnet was increased by using a C-core permanent magnet.

Also, a material with a considerably higher remanance was chosen which also had the added advantage of having a lower reversible temperature coefficient. An 'off-the-shelf' alcomax III magnet was found to have the necessary characteristics. Again, using a small air-gap reluctance model (section 5.7.5), the calculated B-field range at the poles was between 130mT (with no sample present) and 160mT (with a negligible reluctance steel sample at a lift-off of 50mm). This simple estimation immediately shows the potential to increase the sensitivity of the system.

7.5.2 Magnetic field measurement

This instrument relies on measuring small field changes on a relatively large background field. This presents a challenge when trying to identify a sensor with a high sensitivity but a large range. The Lohet sensors were limited due to the on-chip amplification circuitry. Various probes were considered, including giant magnetoresistive type sensors. The probe eventually chosen was part of a commercial Gaussmeter. The specification sheet is given in the Appendix A. The probes contain a highly doped indium arsenide active material. From the data sheet, this material appears to have been used because of its good immunity to high energy radiation. This is not an issue with transformation detection. To increase the accuracy of the sensor, the manufacturers have programmed a calibration look-up table into an EPROM located inside the probe connector. Therefore, each probe has its own individual calibration curve. The probes are designed to be used with the Lakeshore 420 and 450 Gaussmeters. These can be configured to give several measurement ranges, each corresponding to an analogue output of +/-3V. There are two analogue outputs available. The first is a corrected output, which updates three times per second. This output is highly processed to compensate for drift and improve the accuracy of the reading. The second output is a monitor output, which gives a semi-processed signal but has an increased bandwidth of 400Hz. The first output was chosen since the logging rate of the final system was predicted as around 10-20Hz. It can be seen that both of the above outputs have been digitised and then reconverted back to analogue signals.

To achieve a good sensitivity from the system, the small changes on the large background field needed to be logged. Two amplification and offset stages were used to reduce the large offset and amplify the changes due the presence of a sample. Commercial strain gauge amplifiers were chosen. The specification sheets are shown

in the Appendix D. This enabled the use of a standard data-logging package (the Overpower Monitoring system) with an input range of +/-10v over a 12 bit A/D converter giving a resolution of 5mV.

7.5.3 Lift-off measurement

It has been stated in previous sections that the magnetic sensor is sensitive to both the steel property and the distance between the sensor and the steel, the lift-off. To decouple these two effects, two general methods were considered. The first was to measure the lift-off directly. This was the preferred method, since it would simplify the calibration of the instrument to phase transformation. The second was to measure two variables which are both influenced by the lift-off and material property and then decouple them graphically or by calculation. This method has been applied by other researchers: Pustynnikov and Anisimov[3] suggest a multi-frequency method together with small perturbations to develop a linear model to predict the permeability, conductivity and lift-off of a sample, Fielder et al[4] use neural networks to relate parameters obtained from acoustic Barkhausen noise, incremental permeability, coercivity etc to material parameters such as hardness, strength, residual stress etc. Although, the direct method is easier to apply, the evidence shows that indirect methods are as feasible although care is needed in identifying an appropriate mathematical model.

Direct measurement

To measure the lift-off directly, a sensing technique which could operate satisfactorily in the wet mill environment needed to be sourced. That meant it had to work in the presence of copious amounts of water, the presence of dirt, fluctuating high temperatures and a target moving at high speed. Therefore, laser, capacitance and contact systems were eliminated. This left eddy current and ultrasonic type measurements. The experiments in section 6.9 showed that the eddy current sensor had a sensitivity of 6% of the range between austenitic stainless and a low carbon steel. Also in section 6.10 the change in the sensor output due to a sample transforming was 18% of the range. If a sensor could be found with a reduced sensitivity, then it may be suitable for direct lift-off measurement. Such a sensing system was a με series 300 with a U40 probe and 500kHz exciting frequency. The cold and hot test results are shown in figs. 7.5.3 and 7.5.4.

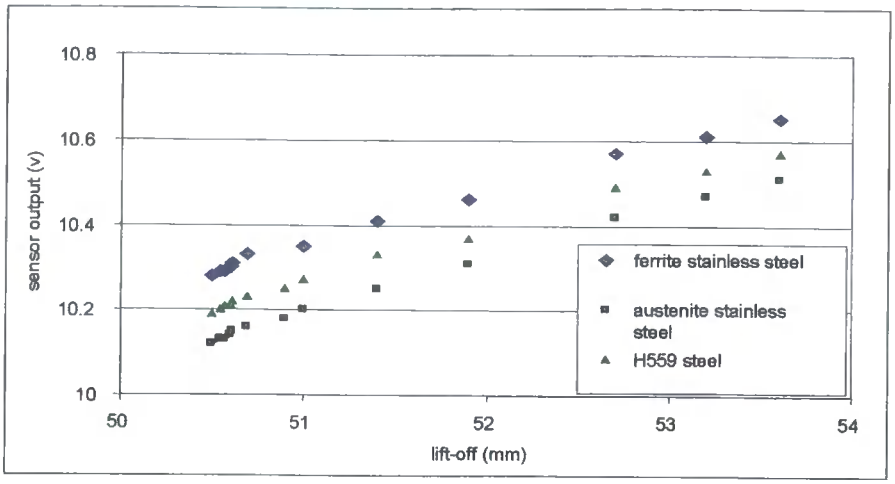

Fig. 7.5.3 Sensitivity of με eddy current sensor to different target materials

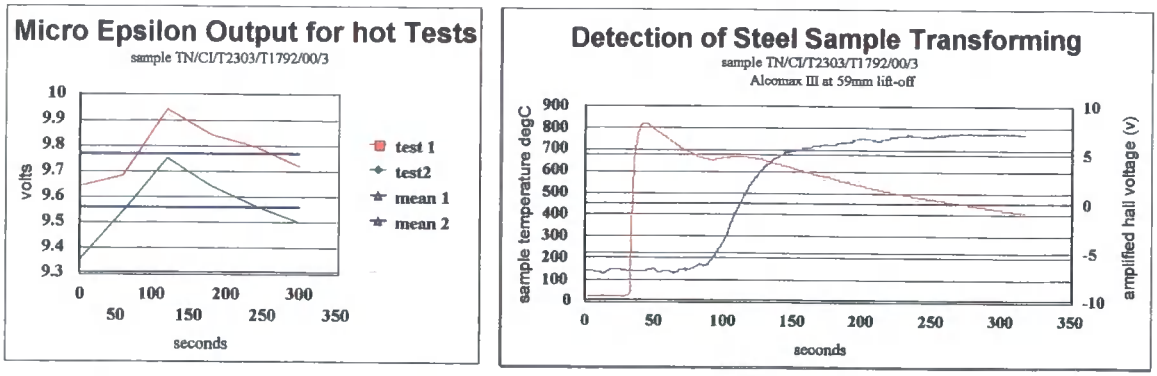

Fig. 7.5.4 με output when placed under hot steel transforming

Both sets of tests show a decrease in the με sensor sensitivity to material property of 20-30% of the Kaman values. Therefore, it was decided to use the με sensor. However, the ultrasonic option was not ruled out at this stage.

The next stage in the development was to look at how the ac and dc magnetic circuits interacted to determine an appropriate separation distance between them. The manufacturers recommend twice the sensor diameter from the outer edge of the με sensor. However, results showed that a distance of 70mm between the U40 centre and the centre of the nearest pole of the permanent magnet was sufficient. It was important to keep this distance as short as possible so that both sensors were looking at approximately the same part of the steel. It would have been preferable to place the sensor in the centre of the permanent magnet. This was not carried out since a magnet with a pole gap of at least 200mm would be required which would have to be

manufactured specifically for this application. This was not thought suitable for a prototype but could be considered for several commercial units.

Indirect measurement

This method is used when direct measurement of the lift-off is not possible. Methods include using magnets with three poles, or using two sensors with known calibration characteristics. These will be dealt with in later sections when further redesigns of the transformation detection system are described.

7.5.4 Casing the components

In prototypes 2 and 3 an aluminium casing could be used since only dc magnetic fields were involved. With the introduction of the eddy current sensor this was not a feasible option anymore. The two general designs considered were (i) a general aluminium case with a non-conductive window and (ii) a case moulded from a suitable non-conductive and non-magnetic material.

To test the first design, the eddy current sensor was placed below aluminium rings of increasing diameter to assess their effect on its range. It was found that even rings with inner diameters of 80mm were reducing the output by 12%. Since the maximum width of the meter could only be 100mm and problems were envisaged in manufacturing this composite case, this idea was rejected.

The second design involved finding a non-conductive case or moulding one. The challenge was to find a material which could withstand at least 200°C. It was not possible to find a pre-manufactured case, so the investigation steered towards finding a suitable material which could withstand the temperatures and was easy to mould. Two epoxy-resin type compounds were identified. Both could withstand up to 270°C and were curable at room temperature. One was defined as being a good thermal insulator and the other a good thermal conductor. Test pieces were moulded. The thermally conductive compound was placed next to the eddy current sensor to assess its effect. It did not reduce the sensor output. Both materials were placed under an electric heater and water poured over the surface of the compound. The air temperatures just above and within the material were then measured. The results showed that even when the air temperature was 285°C the temperature of the compound was only 45°C. Therefore, both the materials were found to be suitable. It was decided to make the upper skin of the meter closest to the hot steel from the

insulating type to try to prevent the heat from entering the measurement head and then to make the rest of the case from the thermally conductive material. This was to enable any heat, which had been transferred to the sensor body to conduct back out towards the colder sides and base. Work performed by Macovschi and Poupot[5] undertook similar considerations and identified materials such as epoxy resins and silicones as suitable. The instrument was proven to be robust in a mill environment thereby reinforcing the suitability of the choice of casing materials for the T-meter.

7.5.5 Cooling circuitry

To achieve repeatable results from the instrument and to protect it from the large amounts of radiated heat from the hot steel strips on the mill a suitable method of cooling was required[6,7]. The eddy current sensor range was limited to approximately 55mm. This meant that the casing above it needed to be as thin as possible. This prevented the use of a double skin as in prototype 3. Therefore it was decided to water-proof all the components by moulding them in the conductive epoxy and force water up a series of channels through the measurement head. The water emerging from the top would then form a cooling / insulating layer. For this reason, the shape of the head was not altered from the basic shape in prototype 3. However, it was found that the eddy current sensor was sensitive to the water flow. To eliminate this a carbon powder was sprayed over the surface above the eddy current sensor and polished. This acted to screen the sensor from the capacitive effects of the water layer.

7.6 Characterisation tests

The initial tests were carried out before the components were moulded into the housing. The set up parameters are shown in fig. 7.5.2. The criteria characterised were response time, long term drift, strip speed, temperature and lift-off.

7.6.1 Response time

To measure this parameter, the time taken for the output to respond from the no sample state to a sample present state was recorded. The test was carried out using a logging rate of 10Hz since the corrected output only updates at a rate of 3Hz. It was found that the response time was faster than 0.33s, which was thought to be adequate.

7.6.2 Long term drift

The long term drift of the Hall probe and magnet system was characterised by logging the output at 5 minute intervals over a 40 hour period and monitoring manually over a

series of weeks. The drift was found to be negligible. The results from the logged period show a standard deviation of 4μT.

7.6.3 Strip Speed

Variations in the strip speed were simulated using a flywheel with a diameter of 1m and a thickness of 140mm. Speeds of up to 200rpm or 10ms^{-1} could be achieved.

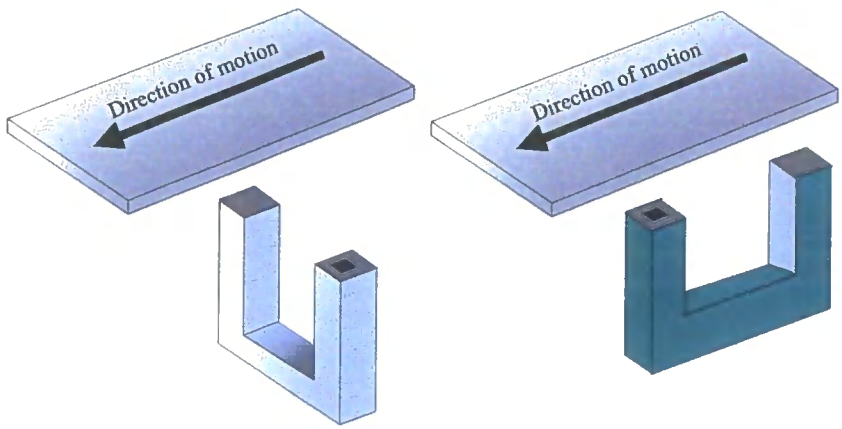

(a) field perpendicular (b) field parallel

Fig. 7.6.1 Experimental set-up to assess effects of speed

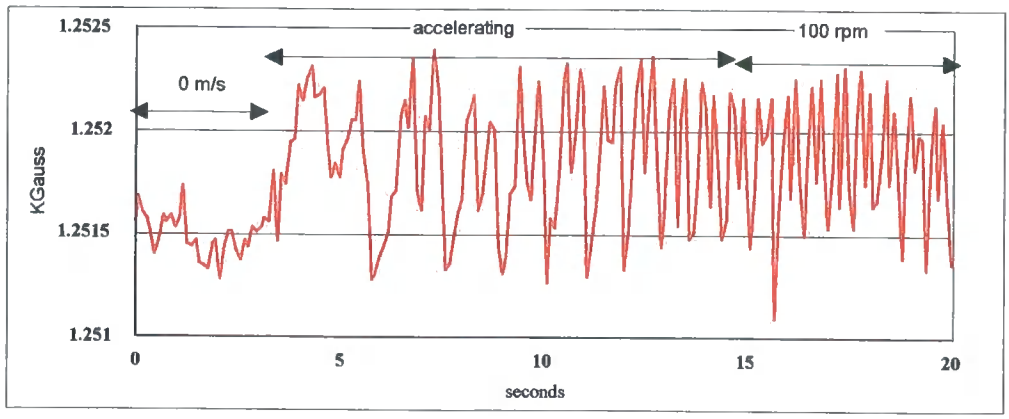

Fig. 7.6.2 Typical monitor output with B-field perpendicular to motion

The sensor was initially placed such that it produced a field perpendicular to the motion of the wheel as shown in fig. 7.6.1(a). The monitor output was used because the response of the corrected output was too slow (3 Hz). A logging frequency of 100 Hz was used. A typical trace is shown in fig. 7.6.2. It shows a periodic variation, which increases in frequency with increased speed. This could be due to eccentricity, material property or width variation around the circumference of the wheel. The change in output with respect to speed was found to be negligible as shown in fig. 7.6.3(a). Also altering the direction of the wheel did not affect the sensor output. A possible explanation is that the eddy currents are produced in the sample in such a way that the sum of their effects is negligible.

a) field perpendicular

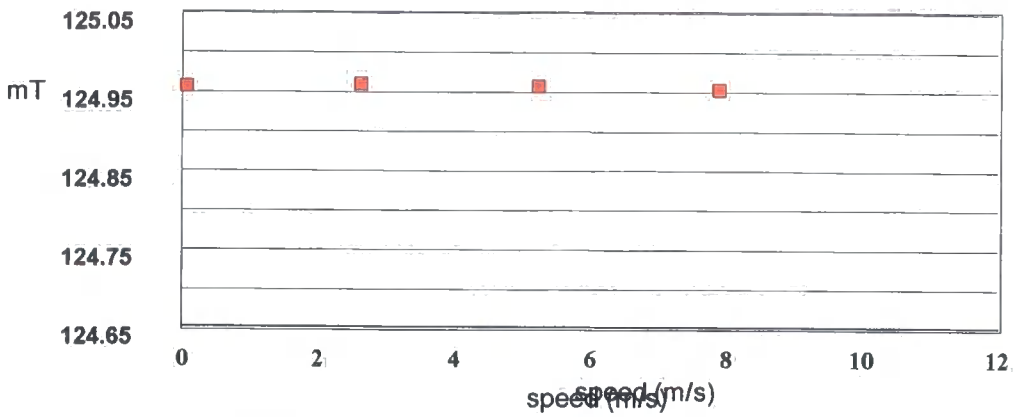

b) field parallel

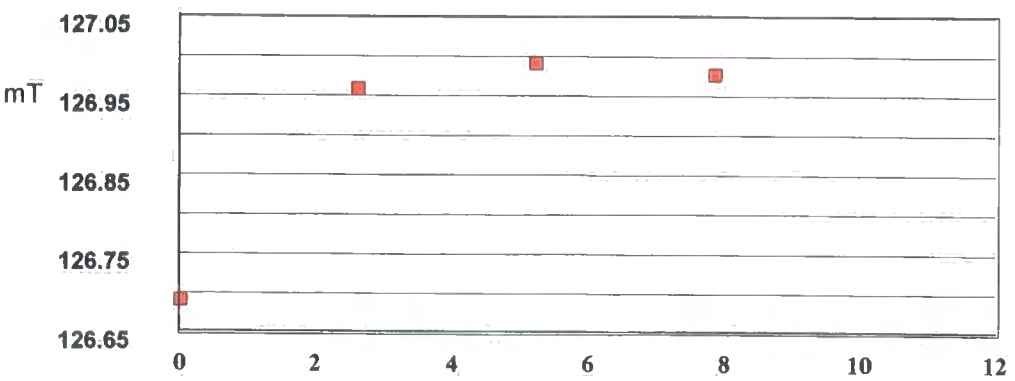

Fig. 7.6.3 Effect of speed on Hall probe output

The sensor was then placed such that it produced a field parallel to the direction of motion, as shown in fig. 7.6.1(b). A plot of the average output as a function of speed, fig. 7.6.3(b), shows the effect to be significant. Reversing the motion significantly affects the output. A possible explanation for this is that the eddy currents are

produced such that their associated fluxes add to give a greater effect. The change from the stationary case to $2ms^{-1}$ was about 0.25mT.

These results show that it is preferable to place the magnet perpendicular to the motion of the steel strip. This was an advantageous result since space constraints only allow this orientation without severely reducing the pole gap and hence the range of the sensor.

7.6.4 Temperature compensation

Although the gaussmeter was specified as having negligible temperature drift, it was characterised in the system including the magnet. This was carried out using an environmental chamber. The magnet had a large thermal inertia due to its large mass, therefore the temperature was set for a minimum of four hours before readings were taken. A resistive temperature device (RTD) was placed in a hole through the magnet pole to measure the magnet temperature as closely as possible. Measurements were logged at five minute intervals for two set-up conditions; no sample present and a mild steel sample at 65.0mm +/- 0.1mm lift-off. The average value of the amplified Hall voltage at each temperature was plotted as shown in fig. 7.6.4. It should be noted that the offsets were adjusted to investigate the gradient therefore the absolute values of the output cannot be compared with other experiments. A similar exercise was carried out for the eddy current sensor. The relationships were found to be highly linear as shown by R^2 values greater than 0.997. For prototype 4 the resulting equations were

$$V_{Hall} = V_{measured.Hall} + 1.38 \times (V_{RTD} - 2.00) \qquad (7.6.1)$$

$$V_{Eddy} = V_{measured.Eddy} + 0.431 \times (V_{RTD} - 2.00) \qquad (7.6.2)$$

where V_{Hall}, V_{Eddy} are the amplified Hall eddy current voltages at 25°C (V).

$V_{measured.Hall}$, $V_{measured.Eddy}$ are the raw values (V).

V_{RTD} is the RTD output voltage (V).

These tests were also used to characterise the noise level by noting the standard deviation of the signal at each temperature. The average was calculated to be 0.05V.

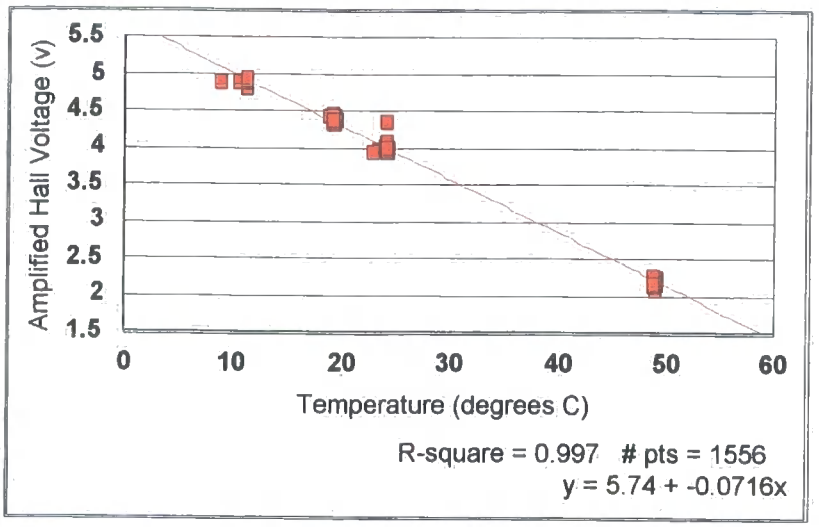

Fig. 7.6.4 Hall probe temperature characteristic of Prototype 4

7.6.5 Lift-off compensation

This section examines the errors associated with predicting the ferrite fraction when using the eddy current sensor to compensate for lift-off variations. The Hall and the eddy current sensors were moulded into the casing before this test took place. The output was logged at 10Hz over a period of time with a sample 50mm above it. The eddy current sensor gave an average output of 50.23mm with a standard deviation of 0.41mm. The lift-off sensitivity of the Hall sensor is shown in fig. 7.6.5. For safety reasons (ie to reduce the B-field on top of the sensor head) the corresponding operating lift-off for the Hall probe was 65mm. The sensitivity of the Hall probe at this value was 0.438 volts/mm (assuming a linear characteristic between 65mm and 75mm) which gives a standard deviation of 0.180 volts (equivalent to 0.41mm).

If the maximum error is assumed to be 2 x standard deviation then the total error in the Hall voltage output due to noise and lift-off is predicted to be:

$$\%error = \frac{\sqrt{\left((2\times 0.05)^2 + (2\times 0.180)^2\right)}}{9.37}\times 100 = 4.0\% \qquad (7.6.3)$$

where 0.05V is the standard deviation of the Hall sensor output,

0.180V is the standard deviation due to the eddy current sensor

9.37V is the range from 65mm to 'no sample'.

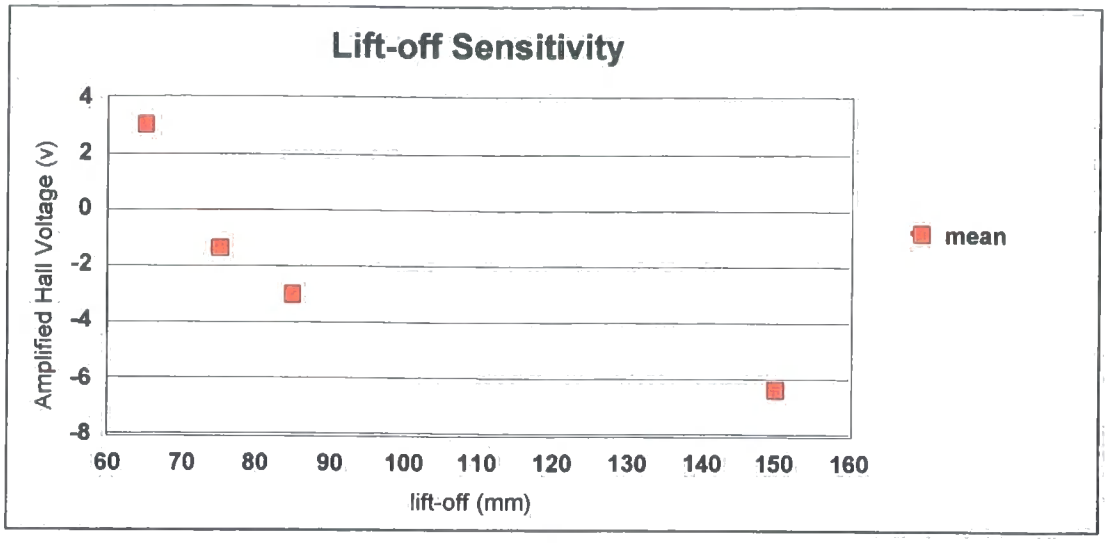

Fig. 7.6.5 Lift-off characteristic of Hall sensor

7.7 Conclusions

The T-meter design was based on the same principle as prototypes 2 and 3. Several modifications were made to address the problems encountered in the plant trials. The first of these was to increase the sensitivity to the magnetic field. It was achieved by replacing the Lohet sensors with a commercial Gaussmeter. Although this also acted to reduce the noise levels and increased the resolution, the bandwidth was severely compromised to 3 Hz. The second improvement was the addition of an eddy current sensor to directly measure and hence compensate for variations in lift-off. Initial tests and subsequent calculations revealed that this addition increased the measurement error to 4% of the range. RTD's were then added to characterise the effect of temperature on the output. A linear relationship was observed, thus a simple algorithm was used to compensate for this. Finally, it was found that if the orientation of the C-core was perpendicular to the direction of motion of the steel target, then the output was relatively insensitive to speed. Thus, no speed compensation was applied.

The work undertaken to produce a prototype to investigate the measurement of steel properties has been described in this chapter. It was necessary to ensure that the effect of unwanted factors such as lift-off, temperature etc were minimized sufficiently to facilitate the interpretation of further experiments and plant trials.

7.8 References

1 *Lacroix M, Abrigo J, Arnault L*, 'On line instrument for ferritic transformation control: Inter Conf. On steel rolling', Tokyo, Vol. 2, pp. 1286-1296,1980

2 *Johnstone S*, 'Transformation meter development - To characterise the main components of a prototype based on an Alcomax III magnet (Prototype 4)', Internal Technical Brief, TI/CI/TB/T2303/T1792/1/00/D, Jul. 1999

3 *Pustynnikov VG, Anisimov SD*, 'Multiparameter electromagnetic control of steel products', Zavadskaya Laboratoriya, Vol. 30, No. 10, pp. 1236-1239, 1964

4 *Fielder U, Kröning M, Theiner WA*, 'Nondestructive evaluation of material parameters using neural networks', Mat. Sc Forum, Vols. 210-213, pp. 343-348, 1996

5 *Macovschi M, Poupot C*, 'Study of variable inductance transducers as proximity sensors: II. Experimental study using 'C'-type magnetic circuits', Meas.Sci.Technol , Vol.1, pp.1291-1296, 1990

6 *Lacroix M, Abrigo J, Arnault L*, 'On line instrument for ferritic transformation control: Inter Conf. On steel rolling', Tokyo, Vol. 2, pp. 1286-1296,1980

7 *Yasuhiro M, Seigo A*, 'Transformation rate-measuring method and device', NKK Corp, Pub. No. 07190991 A, Aug. 1995

CHAPTER 8

EXPERIMENTS USING THE T-METER

8.1 Introduction

In this chapter tests are carried out both in the laboratory and on the hot strip mill at Port Talbot, with the aim of researching whether the phase transformation of steel can be measured using its relationship to its magnetic properties. The T-meter, described in chapter 8 was developed for this purpose.

8.2 Laboratory hot tests

This work was divided into two distinct parts. The first aim was to relate the output of the T-meter at a fixed lift-off to the phase transformation[1]. This involved the help of metallurgists Peter Morris and Cathy Bell at Swinden Technology Centre (STC), Corus R,D&T. The second part was to identify applications for the meter at the hot strip mills at South Wales[2]. Peter Evans, the product metallurgist at Welsh Technology Centre (WTC), Corus R,D&T helped with this.

8.2.1 To investigate the relationship between T-meter output and phase transformation

The aim of this investigation was to determine the response of the T-meter to a sample of eutectoid steel during cooling from a temperature where the steel was fully austenitic, to about 400°C when the steel should have transformed to a fully pearlitic microstructure. This type of steel was chosen because only one transformation, austenite to pearlite, is involved which occurs over a relatively narrow range of temperatures.

Defining the measurement accuracy of the T-meter is dependent on the comparison technique(s) chosen. Optical microscopy indirectly measures phase transformation[3,4] using correlations which have been established with reference to techniques such as X-ray diffraction, chemical analysis etc. It has also been reported[5] that neutron diffraction methods show a good correlation with a vibrating sample magnetometer. (Information on this particular magnetic measurement technique has not yet been found.) However, statistical methods are required to derive the percentage of each phase present. In dilatometry, a linear relationship between the change of length and

phase transformation is usually assumed[6,7] although a predicted error of up to 25% can be present if the increase in austenite carbon concentration and the difference in volumes of ferrite and pearlite are not taken into account[8]. The validity of other methods such as thermal, ultrasonics[9] and X-ray diffraction are also evaluated by either comparing with other methods and or relating to theory.

Dilatometry was chosen since the apparatus enabled replication of the thermal characteristic of the sample when measured by the T-meter, and is widely accepted in the industrial steel community. Optical microscopy was used to observe and compare the microstructures of the samples in both sets of tests. It was not used to measure the percentage of phases present.

8.2.2 T-meter experiment

The apparatus was set up as shown in fig. 8.2.1. The experiment consisted of placing a grade H603/8 (see Appendix B) sample with dimensions 328mm x 160mm x 5mm in a furnace at 1000°C for 20 minutes. This length of time was long enough for the sample to completely austenise but short enough such that any decarburisation was minimised. When the sample was placed on the frame above the T-meter, a thermocouple was inserted into a small hole drilled through the side. A K-type (NiCr/NiAl) was used since it has the required temperature range (-200°C to 1250°C). The measured temperature was assumed to be the average temperature of the steel sample. The Hall sensor, RTD and thermocouple outputs were logged at 10Hz using a Squirrel data logger. The output of the eddy current sensor was logged at one minute intervals for observation purposes only.

The experiment was repeated with a second sample with the same dimensions and from the same coil. It should be noted that the first test piece was not reheated since its microstructure would have changed during the first test. The RTD reading was used to apply temperature corrections using equations 7.6.1 and 7.6.2. The results for both samples are shown in fig. 8.2.2.

8.2.3 Metallurgical tests

Metallurgists at STC carried out this work. The two test samples plus another untested sample from the same coil were provided. The first stage was to characterise the microstructures from the two pieces. The second stage was to use this information,

together with the temperature curves, to reproduce the tests in a dilatometer such that the start and stop of the phase transformation could be determined.

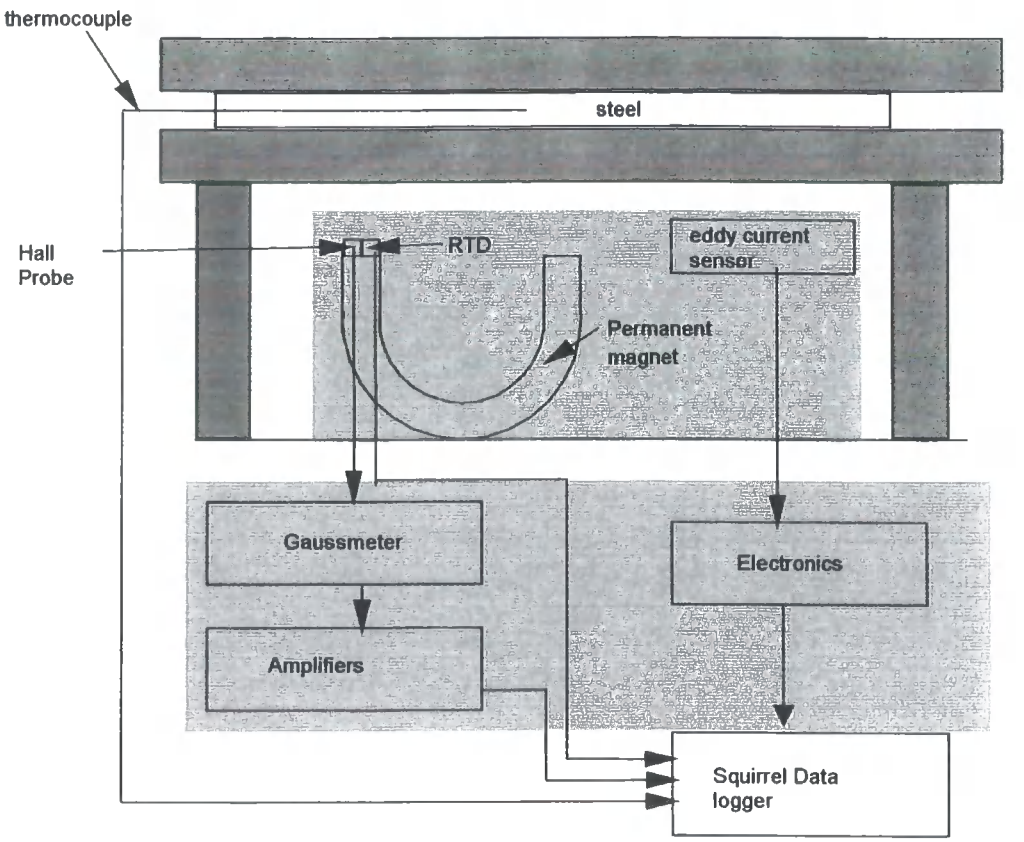

Fig. 8.2.1 **Hot test apparatus**

One of the hot test samples was sectioned to allow examination of the microstructure in the rolling direction at two locations; (i) the thermocouple hole and (ii) the centre of the plate. Decarburisation was present around the surface of the hole as shown in fig. 8.2.3 (a) and on the strip surface to a similar depth as shown in fig. 8.2.3 (b). This was due to the sample being heated in air. The microstructure adjacent to the hole, but clear of the decarburised regions and in the centre of the sample was found to be mainly irresolvable pearlite. These are shown in fig. 8.2.3 (a) and (b) respectively. However, relatively large regions of resolvable pearlite were also present at both positions.

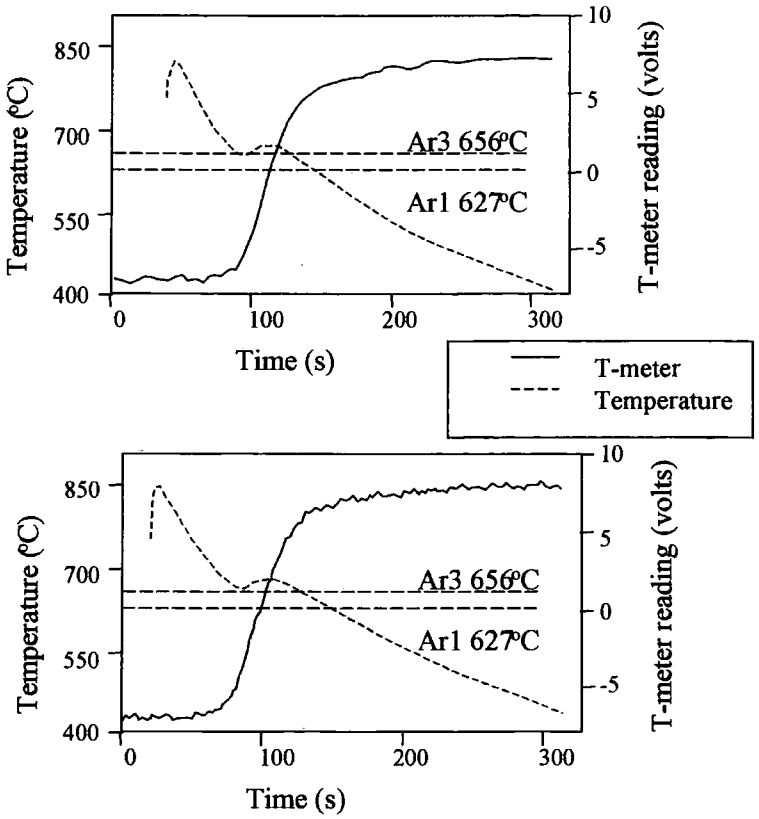

Fig. 8.2.2 Experimental data collected during transformation of a eutectoid steel

The dilatometer tests were carried out using solid rods of 3.5mm diameter from the untested sample. The thermal cycle was to designed to imitate the T-meter experiments by using the temperature data. From these tests, the temperatures corresponding to the start and stop of transformation (the Ar transformation temperatures) were established. The microstructure of the sample was examined to compare it with that of the T-meter test sample. It was similar in that it was mainly irresolvable pearlite with a small quantity of resolvable pearlite. However, the pearlite colony size was smaller as shown in fig. 8.2.4 (c). There was no decarburisation at the surface sample as expected since this experiment was carried out in a vacuum.

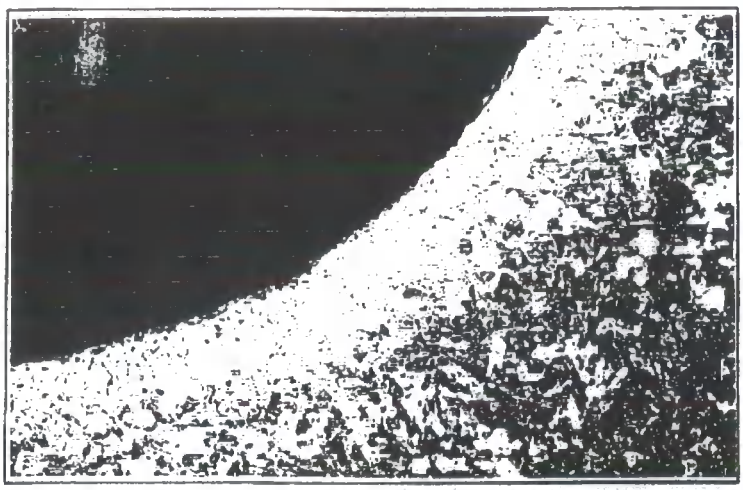

a) Hot test sample-thermocouple hole

x 100

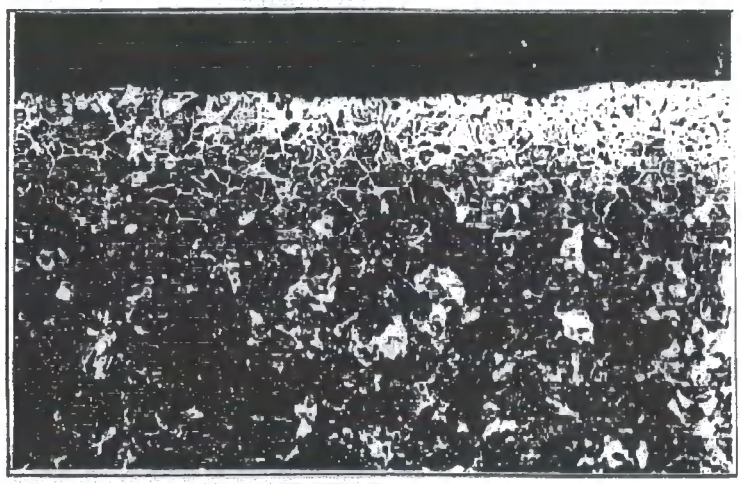

b) Hot test sample-surface of strip

x 100

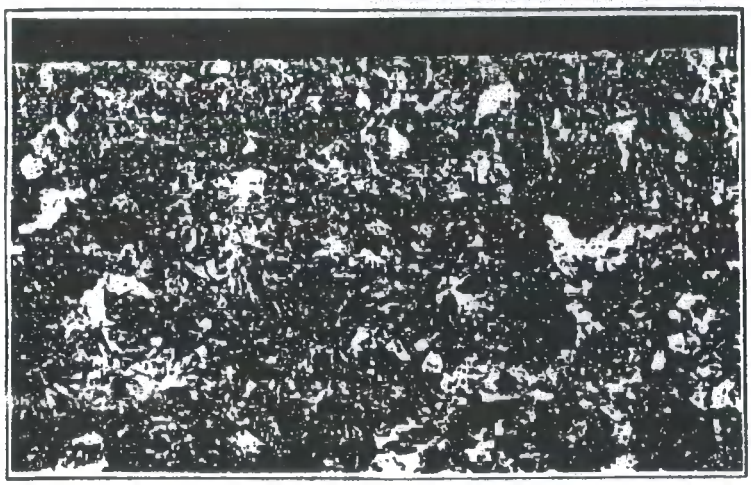

c) Hot test sample -surface

x 100

Fig. 8.2.3 Surface microstructures after heat treatment

a) typical microstructure at hole

x 500

b) typical microstructure at centre

x 500

c) typical microstructure -dilatometer sample

x 500

Fig. 8.2.4 Bulk microstructures after heat treatment

8.2.4 Discussion

The T-meter test results are very similar to those observed in previous tests. The Ar temperatures, determined from the dilatometer tests, show that the steel is in the austenitic phase above 656°C and transforms to pearlite down to a temperature of 627°C. This is consistent with the T-meter output. An explanation is given in the following section.

Above 656°C the T-meter registers no change in the magnetic property of the sample. This is consistent with it being austenitic. There is a rapidly increasing response close to and below the expected transformation temperature 656°C and this corresponds to the point at which recalescence is observed, ie the temperature rise which occurs because of the heat evolution associated with the transformation. The size of this temperature rise, 15°C indicates the onset of rapid transformation from austenite to pearlite. The output from the T-meter was very similar for the two tests carried out indicating good repeatability of the experimental setup and measurement. It does not, however, locate the start point as precisely as the dilatometer. This is possibly due to the samples in the T-meter tests being larger and hence the different regions of the steel will transform at different rates.

The slight deviation from linearity of the temperature/time curve at temperatures below about 750°C indicates that a small amount of transformation may have occurred at temperatures above 656°C. This is probably explained by the transformation of the 0.10-0.15mm decarburised layer at the surface of the strip used in T-meter runs as shown in fig. 8.2.3. These low carbon regions would be expected to transform at temperatures above those of the 0.82%C material in the bulk. The indications of transformation from the temperature/time curves are matched by a small increase in the response of the T-meter. For the 5mm strip in this work, the T-meter was sampling the full thickness. Therefore, the detection of transformation in these decarburised regions suggests that the technique is capable of detecting small volume fractions of ferrite-containing phases in austenite.

It was more difficult to determine the precise location of the end of transformation; however, this is the case even in a dilatometer, which is specifically designed for carrying out such measurements. There are several reasons for this. Firstly, as the permeability becomes larger then small changes will have less influence on changes in the $\underline{B}$-field. Also, the rate of transformation decreases as the fraction of pearlite

increases. This will be partly due to the lower temperature slowing diffusion rates and partly due to the lower numbers involved. The final factor which affects this is that the permeability of ferromagnetic materials is slightly temperature dependent below the Curie temperature and exhibits hysteresis.

8.2.5 Conclusions

Experiments have been carried out in which the Hall output due to a sample cooling and transforming from austenite to pearlite was compared with dilatometry tests and optical micrographs. The results indicate that the T-meter provides a means of detecting the onset of transformation from austenite to pearlite when it occurs below the Curie temperature. It does not give as precise a measurement as the dilatometer, but this could be due to differences in the sample sizes.

In high carbon steels the T-meter will detect the onset for all cooling rates, since the transformation will always occur below the Curie temperature. In very low carbon steels, particularly at low cooling rates, transformation may occur above the Curie point. In this case, the presence of ferrite will only be indicated when the temperature falls below the Curie point. Apart from low carbon, high strength and multiphase steels the T-meter should be able to accurately detect the onset of transformation.

8.3 To identify applications for the T-meter

8.3.1 Experimental set-up

The T-meter was placed in the annealing simulator at Welsh Technology Centre as shown in fig. 8.3.1. Pieces of steel of dimensions 100 mm x 370 mm x gauge were heated to about 960 ^{o}C by passing a large current through them. The temperature of the sample was measured using thermocouples spot-welded onto the steel surface. The current was then switched off and each sample cooled using one of three methods:

(i) simply leaving it to cool naturally in air,
(ii) applying an air purge to force cool it, and
(iii) lagging the coil to retard the cooling.

During these cooling periods, the Hall output, eddy current output and thermocouple output were logged at 10 Hz. The nominal chemistries, by percentage weight for the samples tested are shown in table 8.3.1. Only the Hall sensor output was analysed to assess the link between the magnetic properties and austenite-to-ferrite

transformation. The eddy current sensor output was not used since the lift-off was assumed constant.

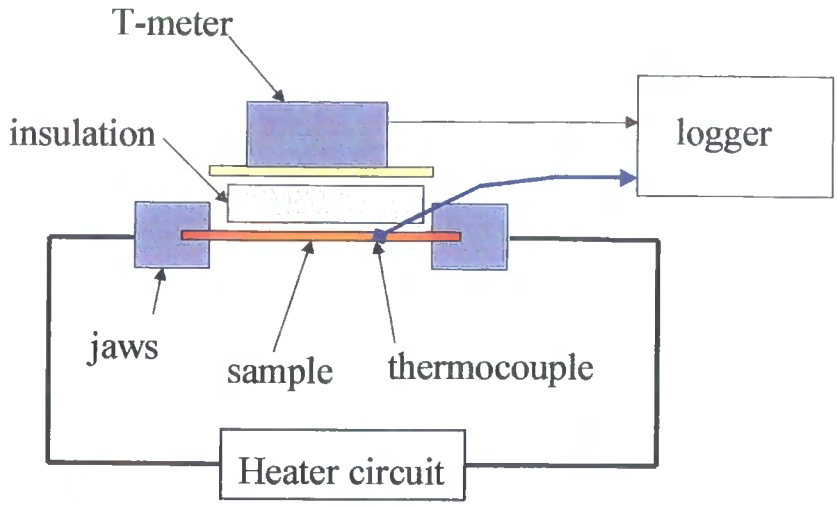

Fig. 8.3.1 Experimental set-up in annealing simulator

8.3.2 Results and discussion

The results for four of the steel types are shown in figs. 8.3.2 to 8.3.5. In all cases, the Hall output (referred to as the detector signal in the graphs) changed in a positive direction as the steel cooled and transformed from austenite to ferrite. In general, at the start of each test (ie the sample in the hot austenitic, paramagnetic state) the Hall output should give a repeatable output, provided the T-meter and sample are not moved. After each sample has cooled and the sample is fully ferritic and ferromagnetic, the Hall output will be dependent on the type of steel and the distance between the T-meter and sample.

Due to the jaws clamping the steel having a temperature limit of 150°C, there was always a temperature gradient across the steel samples. This resulted in variations in the fraction of ferrite present across the sample. Therefore as the steel cooled, the sides of the sample nearest to the jaws had a greater ferrite content than that in the centre where the thermocouple measurement was located; this was detected by the meter. The effect of this is that when the Hall output is plotted against the measured temperature, it could appear that it was detecting some of the samples transforming to ferrite above the Curie temperature. This was not the case, since the principle of operation of the T-meter is that the ferrite only becomes ferromagnetic below the

Curie temperature. It should also be noted that surface decarburisation affects the transformation start temperature (see section 8.2.3).

Fig. 8.3.2 shows the results for the H653/11(eutectoid steel) grade of steel for both natural and forced cooling conditions. This is a similar type of steel to that investigated in the previous laboratory tests, and hence the temperature traces from

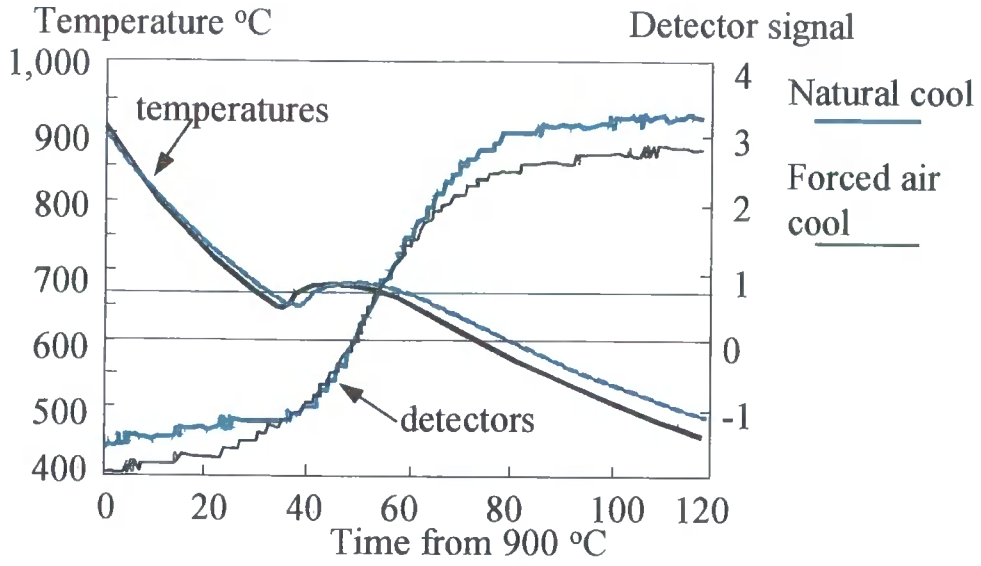

Fig. 8.3.2 Laboratory results for grade H653/11

the centre of the sample show a large recalescence. Therefore using temperature alone, there is an ambiguity as to whether the steel has started to transform or is partly or fully transformed to ferrite. To illustrate this, consider the temperature 665 °C in fig. 8.3.2. It occurs at three points in time, 26s, 38s and 54s. The Hall output detected a significant change in signal below the Curie temperature. This is consistent with the start of transformation, since this grade of steel is known to transform to pearlite below the Curie temperature. Due to the temperature gradient across the sample, the start of transformation was not well defined. However, at the 26s, 38s and 54s points it gave outputs, which could be uniquely related to the fraction of ferrite present. To conclude, this experiment shows the possibility of using the T-meter output as means of uniquely identifying the ferrite fraction in high carbon steels around transformation temperatures.

Table 8.3.1

	H653/11 0.8%C	RMS 235a 0.2%C	C65218 CMn	H636/2 HR1+B	51014/4 mild IF Ni-Ti	S8/0103 43A	H639/27 HR1+B
C	0.761	0.194	0.137	0.048	0.0013	0.169	0.04
Si	0.233	0.211	0.266	0.002	-	0.007	0.004
Mn	0.76	1.22	1.13	0.25	0.00.141 4	0.79	0.27
P	0.014	0.018	0.019	0.011	0.007	0.016	0.11
S	0.01	0.0055	0.002	0.006	0.008	0.008	0.006
Ni	0.009	0.013	0.015	0.008	-	-	0.008
Cu	0.02	0.01	0.026	0.016	-	-	0.022
Sn	0.003	0.003	0.005	0.002	-	-	0.003
N	0.0053	0.0058	0.007	0.0017	0.0017	0.0034	0.0019
soluble Al	0.032	0.042	0.039	0.03	0.045	0.05	0.036
Cr	0.192	0.023	0.038	0.012	-	-	0.013
Mo	0.003	0.001	0.002	-	-	-	0.003
Nb	-	0.001	0.002	<0.01	0.019	-	0.001
Ti	-	0.001	0.002	<0.01	0.029	-	0.001
B	-	0.0003	-	-	-	-	0.0027
test no.	101,112	13	678	45	181,920	161,721	2,324
gauge (mm)	2.2	1.9	1.83	1.75	0.8	1.9	1.35,1.8

Nominal Chemistry for material used in transformation studies at WTC, % Wt

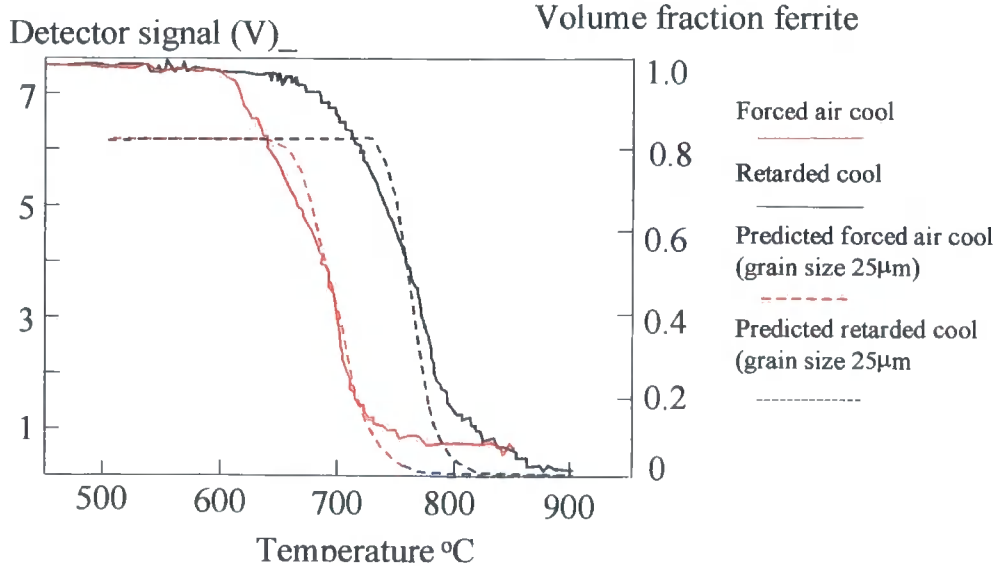

Fig. 8.3.3 **Laboratory results for grade S8/0103**

Fig. 8.3.3 shows the results for grade S8/0103 which is a general purpose steel grade. At the retarded cooling rate, the sample was predicted to start the austenite-to-ferrite transformation above the Curie temperature. Therefore, in theory, the Hall output should have been a step at the Curie temperature with a value equivalent to the percentage transformed at that point. Fig. 8.3.3 shows the curve to appear transforming above the Curie temperature. This is due to the temperature gradient of the sample masking this effect. The forced cooling rate was predicted to depress the transformation temperature below the Curie temperature, thus the instrument was able to detect the full change in that case.

A simulation software package provided by Welsh Technology Centre, Corus R,D&T, was used by P Evans to predict the ferrite fraction. Using knowledge of the sample, an appropriate grain size was assumed and the simulated cooling rate was matched to that of the retarded cooling rate. The grain size was then optimised to give the best fit to the data. To validate the T-meter data further, the model was used to calculate the fraction of ferrite when using forced cooling. This curve represented the experimental data well, and hence the T-meter output was validated as being a reasonable representation of the fraction of ferrite present.

Fig. 8.3.4 shows the results from grade C65218 which is a carbon-manganese steel. At both cooling rates, the sample transformed below the Curie temperature. The computer simulation was optimised and fitted the data for both cooling rates. Therefore, it was concluded that the T-meter output could be used to measure the percentage ferrite for all cooling rates. An inflection in the curve was also observed. This may have been due to the start of the pearlite transformation.

Fig. 8.3.5 shows the results for H639/27, which is a low carbon steel. At both cooling rates the ferrite was predicted to form above the Curie temperature. Therefore, the Hall output could not clearly define the start of transformation. This was further complicated by the temperature gradient across the sample. However, the simulation and experimental data matched reasonably well with the calculations predicting that the transformation started before the T-meter output detected a change.

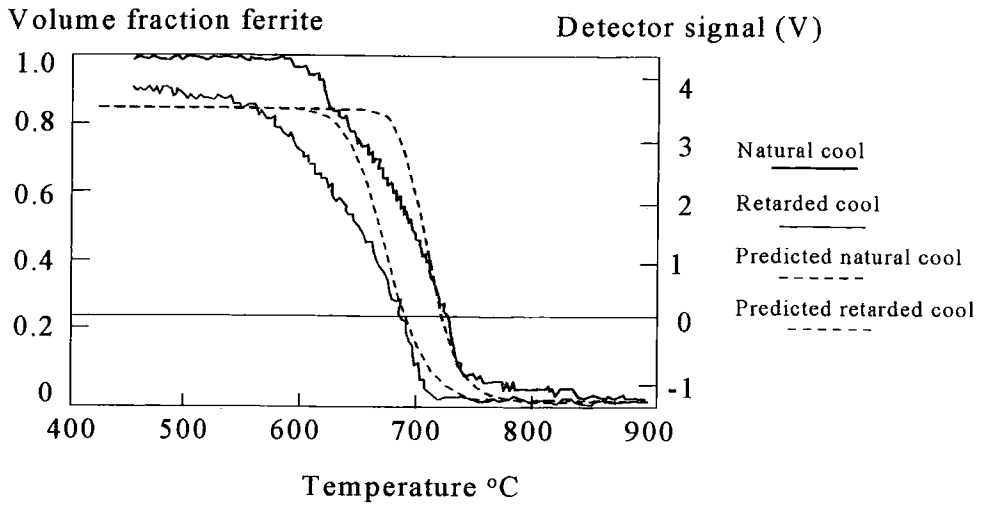

Fig. 8.3.4 **Laboratory results for grade C65218**

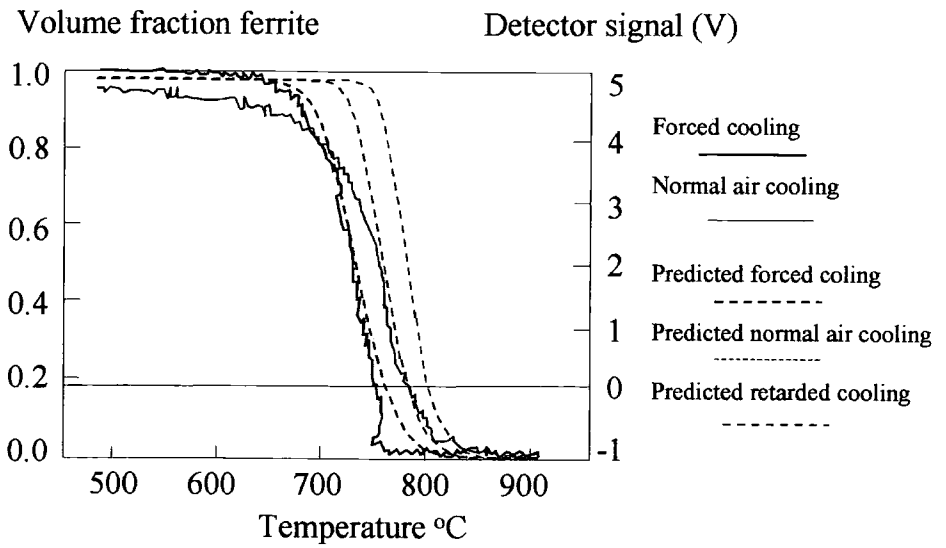

Fig. 8.3.5 **Laboratory results for grade H639.27**

Experiments were not attempted with mild IF steel since it was predicted to transform in the region of 850 to 900°C. Ultrasonic methods are being researched by Dubois[9] et al and Scruby[10], specifically for these grades.

8.3.3 Conclusions

Experiments were carried out with different steel grades, in an annealing furnace at constant lift-off, to identify potential applications for the T-meter. In general, the results confirmed that the Hall sensor was a reasonable representation of the fraction of ferrite present. However, due to the temperature gradient across the sample, it was difficult to accurately define the start of the austenite to ferrite transformation. This was particularly noticeable for low carbon steels, in which the Hall probe detected the transformation starting, while the thermocouple was registering a temperature above the Curie temperature. From the results, two possible applications were identified. The first was to control the transformation more accurately in carbon-manganese steel. The second was eliminate the ambiguity due to converting from temperature to percentage ferrite in the recalescence zone of eutectoid steels.

8.4 Plant trials

8.4.1 Aim of trials

It was found during the hot laboratory tests in section 8.2, that the T-meter could be successfully used to measure the phase transformation in two cases which would give a significant improvement to the mechanical properties of the product.

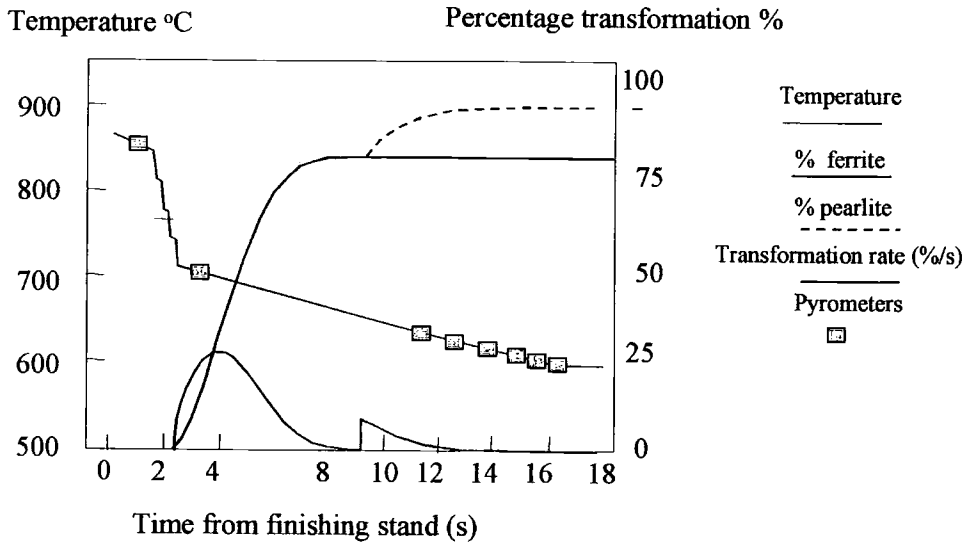

Fig. 8.4.1 **Run out table cooling path and predicted transformation kinetics for CMn grade**

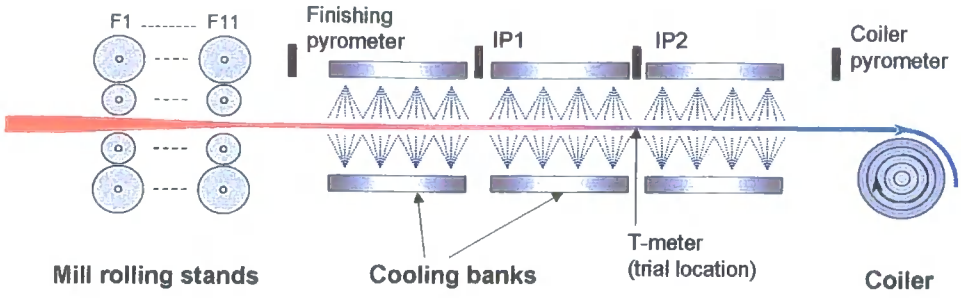

Fig. 8.4.2 **Schematic of the run-out table at Port Talbot hot strip mill**

The first was in the rolling of carbon-manganese steels. The experiments showed that they always transformed below the Curie temperature, which means the T-meter can detect all of the transformation. However, the main benefit is due to the possibility of improved control of the transformation. This is because during the rolling of these products they are rapidly quenched from about 850°C to just above 700°C as shown in fig. 8.4.1 and then cooled at a much slower rate. This is to prevent the ferrite forming until about 700°C. The steel is then cooled much more slowly to enable a high percentage of ferrite to form, before the pearlite is produced. This cooling strategy, however, causes the strip to buckle and hence corrective processing is required downstream.

The second application was in the rolling of high carbon steels, which have a large recalescence during transformation. As mentioned in section 8.3, a single temperature reading can be related to up to 3 different percentage transformations. This means it is difficult to determine whether a steel strip has fully transformed before it is coiled, and therefore severely affects the final properties of the steel.

The plant trials actually carried out included measurements of a variety of steel grades, and then specifically carbon-manganese grades. On Port Talbot hot strip mill (fig. 8.4.2) pyrometers are located at two intermediate positions, IP1 and IP2. It was proposed to place the meter under each of these pyrometers, since the carbon-manganese should have a low ferrite fraction under IP1 and a high ferrite fraction under IP2. To date, only the trials under IP2 have been carried out. Unfortunately, the IP2 temperature output was not suitable since the trigger to the mill logger was inappropriate (it recorded the temperature between coils).

8.4.2 Trial 1(November 1999)

Initially, this trial took place to test the installation and withdrawal procedures of the T-meter head. However, it was subsequently used to give an indication of robustness and usefulness of the output signal. A bracket was manufactured and placed in between the rolls separating banks 14 and 15 (under the IP2 pyrometer). The head was installed by raising the splashguard on the non-drive side and sliding it into position where it was locked in by a retaining plate. The meter was in position for one rolling campaign, where the outputs for over 40 coils were logged. The steel grades rolled during this period varied, but were not carbon-manganese type steels. This resulted in a range of ferrite fractions being presented to the meter. Examples are given in figs. 8.4.3 to 8.4.5.

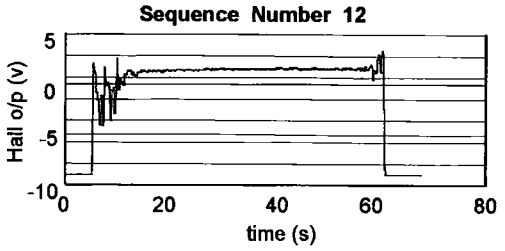

Fig. 8.4.3 **A coil with a large fraction ferrite and temperature below the Curie point**

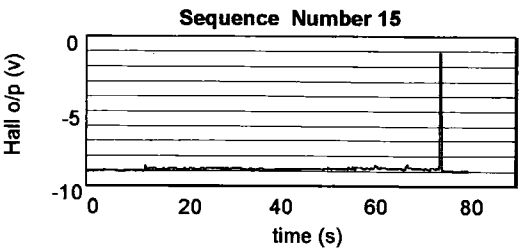

Fig. 8.4.4 **A coil which gives negligible change in the T-meter output**

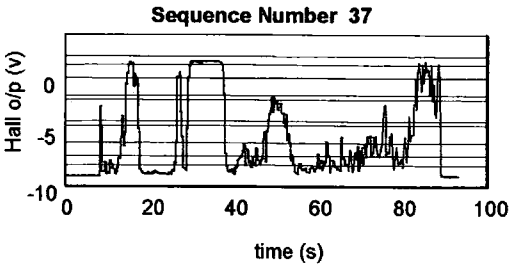

Fig. 8.4.5 **A coil which gives large variations in the T-meter output**

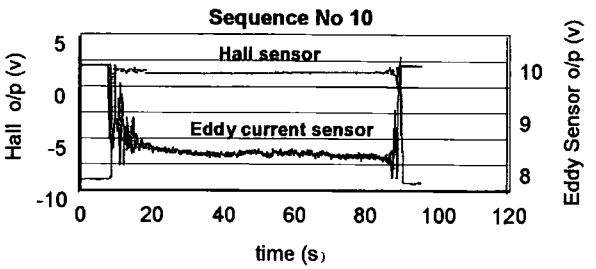

Fig. 8.4.6 **Temperature compensated outputs for grade 1904 steel**

Fig. 8.4.3 shows a temperature compensated trace which is stable when no steel is present. When the steel initially passes over the meter, the signal fluctuates rapidly due to the head end not being under tension, and then settles over 10V higher than the background level until the tail end leaves the finishing stand and the strip end bounces past the meter. This trace indicates that the T-meter has detected the steel, which has a

high ferrite fraction and the strip temperature is below the Curie temperature. To obtain a value for the ferrite fraction, the meter would need to be calibrated to that particular grade of steel.

Fig. 8.4.4 shows a temperature compensated trace in which there is a very small increase when the steel is present. This indicates a steel strip, in which there is a very small fraction of ferrite and the temperature is below the Curie temperature, or ferrite is present and the temperature is above the Curie temperature. Without the IP2 signal it is not possible to distinguish which is the case.

Fig. 8.4.5 shows a highly variable trace when the steel is present. In this case, there are again three possible scenarios due to the lack of temperature data; the first is that the fraction of ferrite present is reasonably constant along the strip, and the temperature is toggling above and below the Curie temperature. The second is that the temperature is always below the Curie temperature, and the lift-off variations are considerable. The third is that the temperature is again always below the Curie temperature and there are severe swings in the fraction of ferrite present. Regardless of the explanation for the changes in the Hall output, it did produce a change which was related to the steel property.

8.4.3 Trial 2(December 1999)

In this trial the T-meter was placed in the IP2 position during the rolling of a carbon-manganese round. Three grades were rolled 1904, 1916 and 1906. The nominal chemical analyses are shown in table 8.4.1.

A typical grade 1904 trace (with temperature compensation) is shown in fig. 8.4.6. The trace initially shows a lot of variation. This is due to the head end of the strip flapping up and down until it reaches the coiler. The Hall voltage then remains around 11V above the background level while the strip is present and has a general upward trend. The eddy current signal similarly shows the initial fluctuations, remains steady when the strip is under tension, but shows a gradual downward trend. Without further analysis, it can be deduced that the steel has significant fraction of ferrite present.

Table 8.4.1

Grade	1904	1906	1916
C	0.13	0.09	0.14
Si	0.069	0.769	0.034
S	0.005	0.002	0.001
P	0.025	0.012	0.021
Mn	0.83	1.19	1.35
Ni	0.019	0.16	0.21
Cu	0.01	0.007	0.013
Sn	0.003	0.003	0.003
N	0.0036	0.007	0.006
soluble Al	0.042	0.038	0.04
Cr	0.027	0.021	0.024
Mo	-	-	-
Nb	-	-	-
Ti	0.002	0.013	0.01
B	-	-	-

Chemistry of Steel Grades Rolled during Trial 2, % Wt.

The results from both the plant trials and laboratory tests suggested that the eddy current sensor was more sensitive to the steel properties than the initial tests had indicated. This resulted in unsatisfactory lift-off compensation. Therefore, a model was developed which accounted for the fact that both the Hall and eddy current sensors were sensitive to fraction ferrite and lift-off.

Hall sensor model

Experiments show that the sensor output can be represented as being proportional to the magnetic property of the target, M(F) and inversely proportional to the square of the lift-off, x. With no sample present the Hall sensor gives a voltage V_b. The magnetic property M(F), of the steel is a function of the fraction transformed, F. Hence,

$$V_{Hall} = V_b + \frac{k_{Hall}.M(F)}{x^2} \qquad (8.4.1)$$

where k_{Hall} is the constant.

Eddy current sensor model

For a given material the eddy current sensor is set up with the manufacturer's calibration equation. Using experimental data the output is also shown to be proportional to the target's change in electromagnetic properties, P(F), the effect of which decreases with distance, following an inverse square law.

$$V_{eddy} = \frac{x}{4} - 2.5 + \frac{k_{eddy}.P(F)}{x^2} \qquad (8.4.2)$$

where k_{eddy} is the constant.

One point to note is that the Hall sensor circuit measures all the way through the sample whereas the eddy current sensor looks through a thin layer whose thickness is determined by the skin depth, δ, which decreases as the sample transforms and becomes more magnetic.

The trial data for grade 1904 were used to estimate the constants for equations (8.4.1) and (8.4.2) using the assumption that

$$k_{Hall}.M(F) = k_h.F \qquad (8.4.3a)$$

and

$$k_{eddy}.P(F) = k_e.F \qquad (8.4.3b)$$

It was also assumed that the steel was 90% ferrite at a distance of 42 mm from the sensor. Using this information and combining equations (8.4.1) and (8.4.2) gives

$$F = \frac{(V_{Hall} + 8.81)}{1130}.\left[V_{eddy} + 2.5 - \frac{(V_{Hall} + 8.81)}{34.0}\right]^2 \qquad (8.4.4)$$

and

$$x = \sqrt{\frac{18100.F}{V_{Hall} + 8.81}} \qquad (8.4.5)$$

These constants could be tuned more accurately using calibration samples placed on a rig or the mill rolls. The samples would need to be large enough to simulate a steel strip.

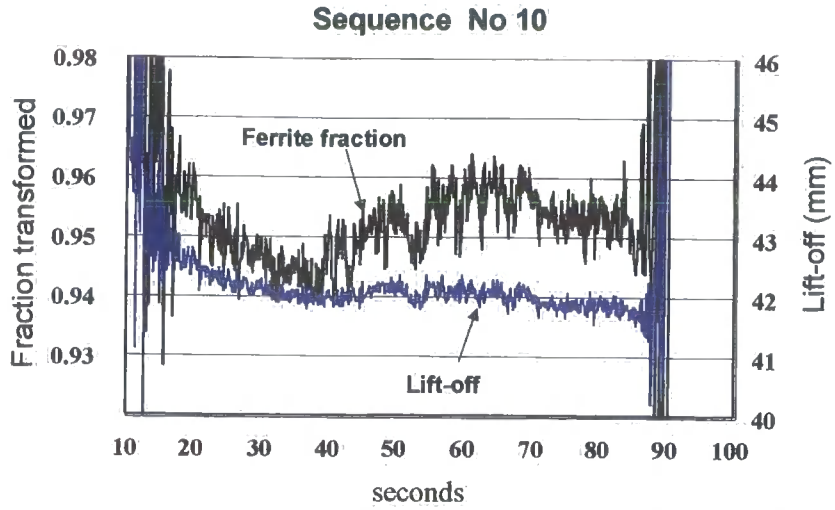

Fig. 8.4.7 **Calculated ferrite fraction and lift-off for grade 1904 carbon-manganese steel.**

The calculated fraction transformed and the lift-off are shown in fig. 8.4.7. The corresponding plant signals (finishing, IP1 and coiler temperatures, and water flow rates) are shown in fig. 8.4.8. The resulting fraction transformed appears to have a negative correlation with the IP1 temperature (IP2 data were not available for this trial), and correlates well with the spray patterns which indicate cooling rate. This is an indication that the output is detecting changes associated with the steel properties. The same analysis was applied to another grade 1904 coil. The results (fig. 8.4.9) again show a correlation between the IP1 temperature, spray patterns and hence cooling rate (fig. 8.4.10), although the ferrite fraction varied less along this coil than in the previous one.

The temperature compensated data for a grade 1916 coil are shown in fig. 8.4.11. When the strip is present there is a lot of variation. This variation could be anywhere along the strip so cannot be solely attributed to the head and tail ends not being under tension. Observations made during the trial and flow rate data show that there was considerable water being forced up under the strip. This could have resulted in large lift-off fluctuations, which would have affected both sensors as shown. It was known that both the Hall and eddy current sensors had different frequency responses. To reduce this effect, a commercial 5Hz anti-aliasing filter was applied to all logged inputs. Despite this, application of the lift-off compensation equation acted to increase the fluctuations. To reduce this effect, the data were smoothed using a 9-point centre averaging technique and then the compensation equation applied. The mill data and the results are shown in figs. 8.4.12 and 8.4.13 respectively.

They show that although a bulk of the lift-off variation, which represented 37% of the signal range, has been removed, there is still a residual variation of about 2%. This is confirmed by the fact that the Hall trace is depressed in the same region as the eddy current sensor output increases. This is consistent with the lift-off increasing.

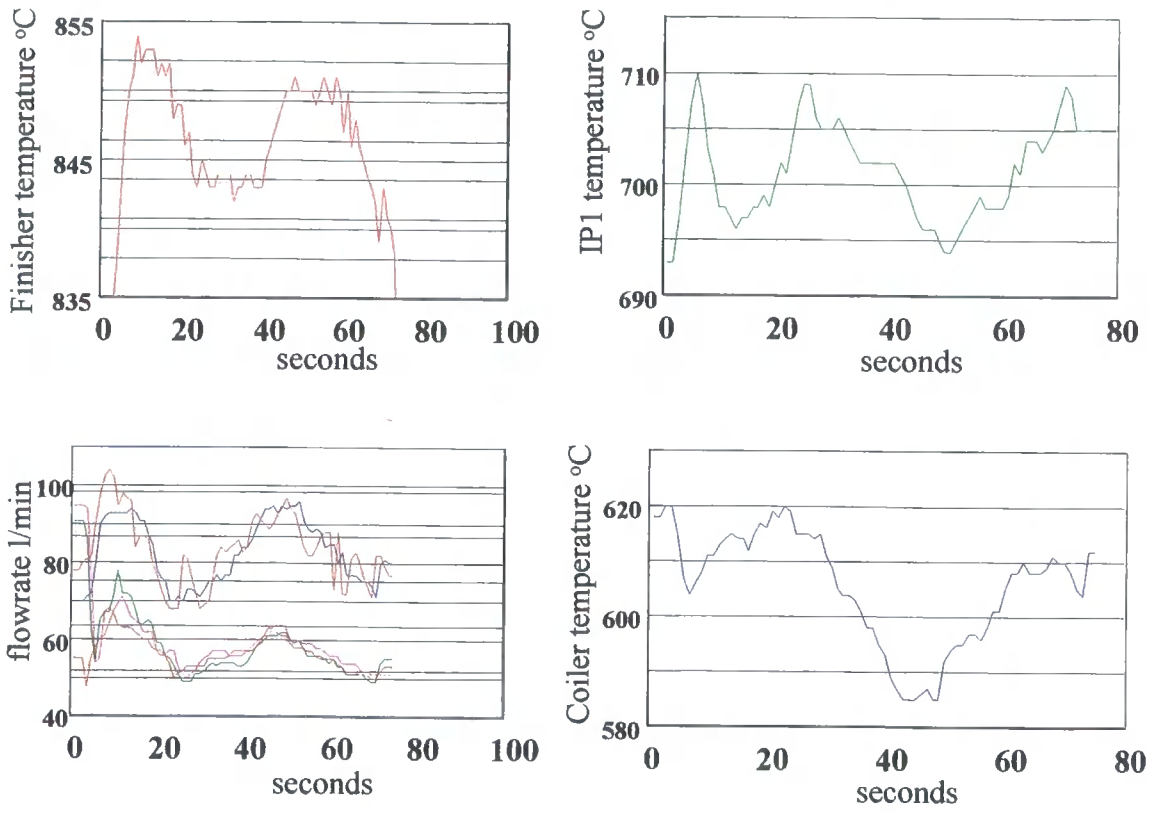

Fig. 8.4.8 Corresponding plant signals for grade 1904 coil, sequence number 10

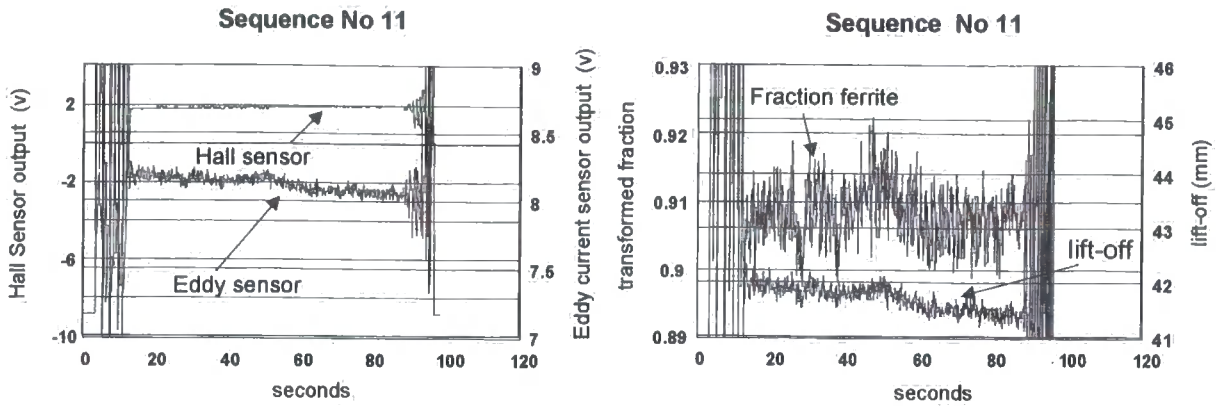

Fig. 8.4.9 Temperature compensated and calculated data for sequence number 11, grade 1904

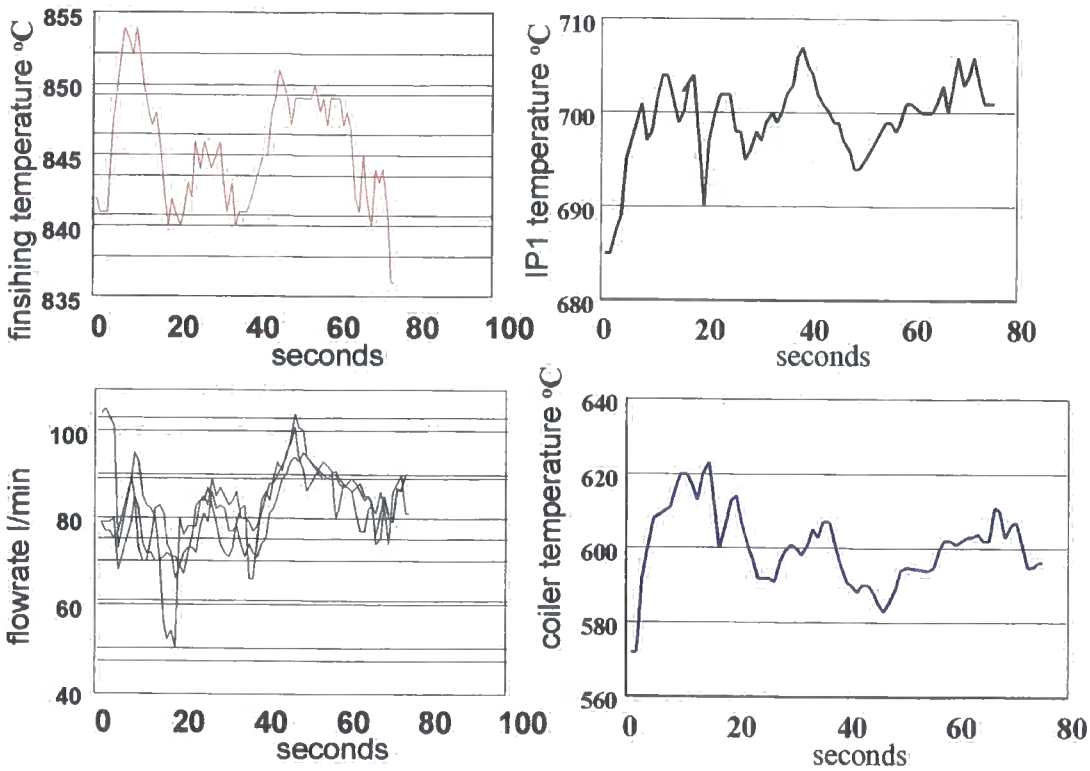

Fig. 8.4.10 Corresponding plant signals for sequence number 11, grade 1904

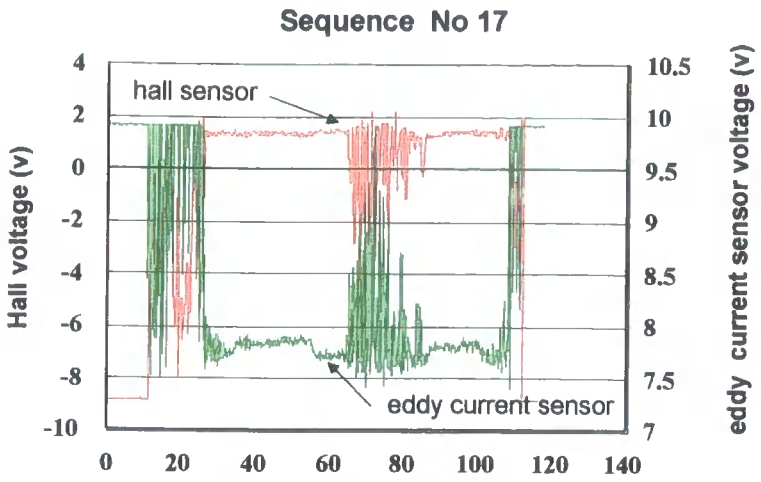

Fig. 8.4.11 **Temperature compensated outputs for grade 1916 carbon manganese steel, sequence number 17**

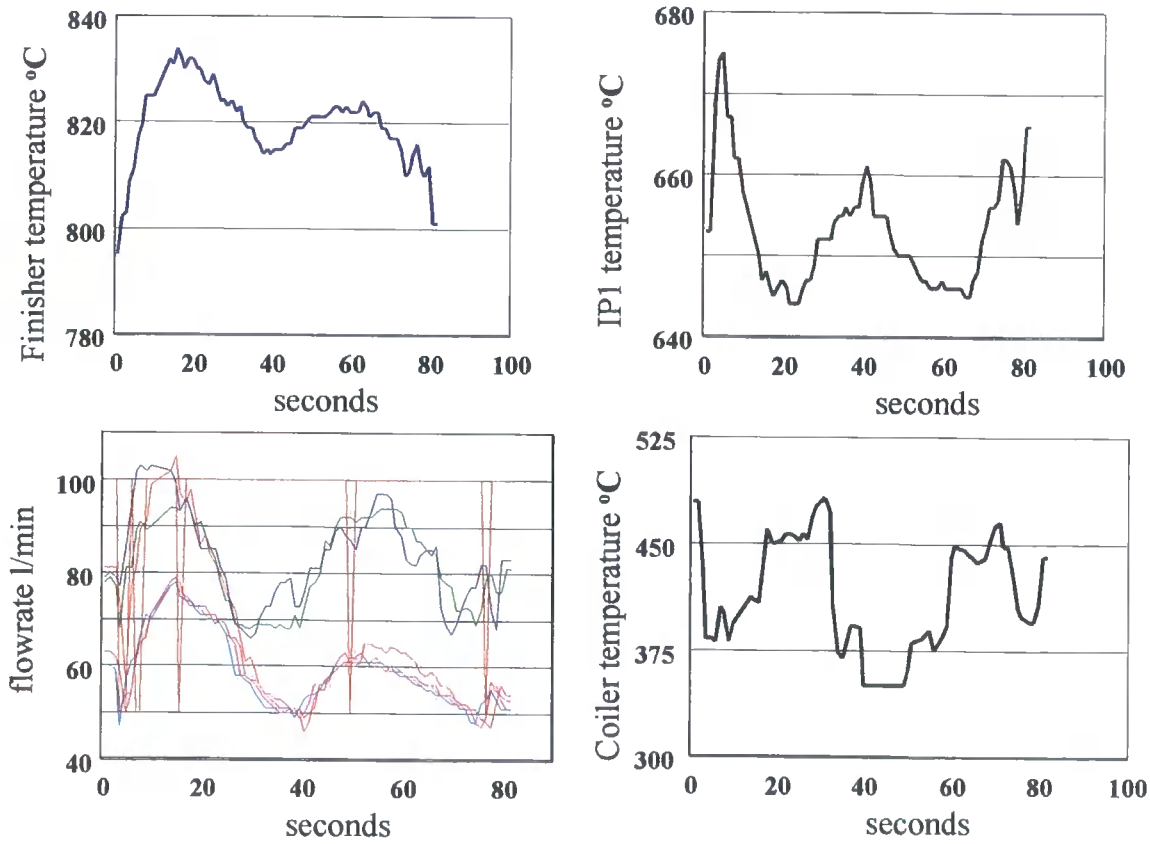

Fig. 8.4.12 **Corresponding plant signals for sequence number 17, grade 1916**

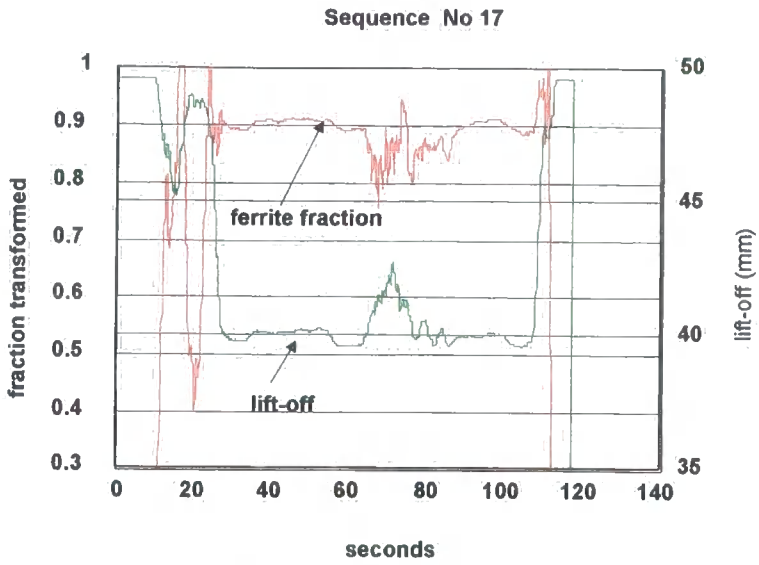

Fig. 8.4.13 Calculated ferrite fraction and lift-off for grade 1916, sequence

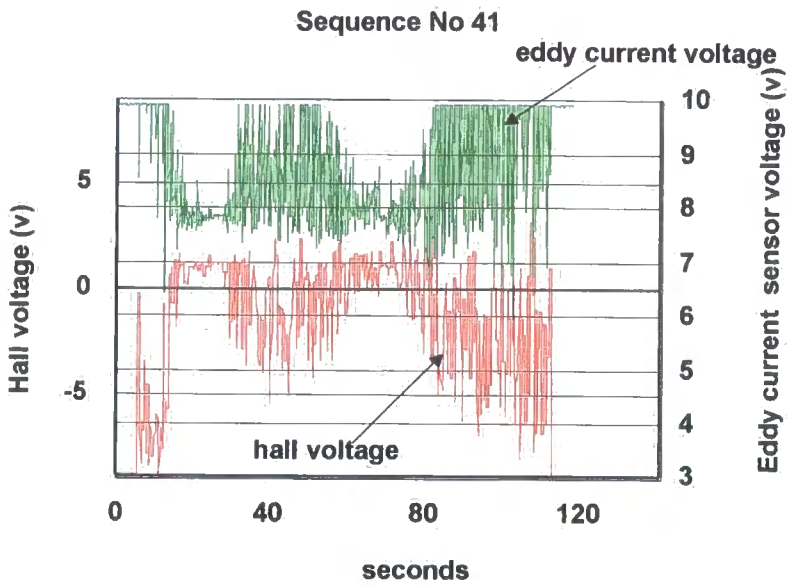

Fig. 8.4.14 Temperature compensated outputs for grade 1916 carbon manganese steel with regions of saturated eddy current sensor output

There are grade 1916 coils in which the fluctuations exist throughout the coil as shown in fig. 8.4.14. In this coil the eddy current sensor repeatedly saturates, therefore invalidating any lift-off compensation. To overcome this, a larger range sensor would be required.

8.4.4 Conclusions

Plant trials were carried out to investigate the relationship between the T-meter output and steel properties. The results revealed that the eddy current sensor was more sensitive to the steel than the initial laboratory experiments had suggested. To account for this, a mathematical model was developed to decouple the ferrite fraction from the lift-off, using both the Hall and eddy current sensor outputs. The model successfully reduced the output variations, due to lift-off fluctuations, for cases where the changes in lift-off and steel properties were slow (less than 3Hz). It should be noted that there was still some correlation observed in the traces, indicating that the compensation was not ideal. For faster variations, the application of the model acted to increase the signal variation. This was due to the different response times of the Hall and eddy current sensors. In an attempt to overcome this, a low pass filter was applied. The net result was to reduce the variation from 37% to 2% of the range. The final limitation of the meter, was the limited measurement range of the eddy current sensor. This was particularly noticeable for the grade 1916 steel.

8.5 References

1 *Johnstone S, Bell C, Morris PF*, 'Metallurgical investigation of the T-meter output for a eutectoid steel', Internal Technical Note, Corus R,D&T, Sept.1999

2 *Johnstone S, Evans P, Lewis O*, 'Evaluation of the T-meter at WTC and Port Talbot hot strip mill', Draft internal Technical Note, Feb. 2000

3 *Samuels L.E*, 'Optical microscopy of carbon steels', American Society for Metals, 1980

4 *Smallman RE, Ashbee KHG*, 'Modern metallurgy, Pergamon Press' 1971

5 *Kitagawa H, Sohmura T*, 'An X-ray diffraction method for quantitative determination of retained austenite in the production line of metastable austenitic stainles steel', Transactions ISIJ, Vol 23 (6), 1983

6 *Lambert N, Colin R, Economopoulos M*, 'Dilatothermy- a new quantitative research method for allotropic transformation', Steel research 58 (1987) No 7

7 *Prior GK*, 'The role of dilatometry in the characterisation of steels', Materials Forum vol 18, pp 265-276

8 *Kop TA, Sietsma J, Vander Zwaag S*, 'Dilatometric analysis of phase transformations in hypo-eutectoid steels', Journal of Material Science, 36, 2001 pp. 519-526

9 *M Dubois, A Moreau, M Militzer, JF Bussiere*, 'Laser-ultrasonic monitoring of phase transformation in steels', Scripta Materialia, Vol 39, No 6 pp 735-741 1998

10 *AEA Technology plc , Irsid, Swedish Institute for Metals Research British Steel plc, Sollac SA Outokumpu Poricopper OY SSAB Tunnplat AB Howmet LTd Exeter Castings*, 'On-line structure monitoring by laser ultrasonics for process control in rolling and heat treatment', Brit/Euram Project No BE96-3349

CHAPTER 9

PROTOTYPE 5 - MAGTRAN

9.1 Introduction

This was the latest prototype to be developed. It was designed to overcome the problems associated with the T-meter, ie the limited range of the eddy current sensor and the different response times of the two sensing technologies. To achieve, this a three-pole electromagnet was used to produce the magnetic field instead of a permanent magnet due to uncertainties about the long term effects of a permanent magnet at high ambient temperatures and difficulties in manufacturing a three pole magnet. High bandwidth Hall probes were used to detect the field changes associated with the steel transforming and/or moving. In this chapter the MagTran is characterised and its performance investigated.

9.2 Instrument Design

A block diagram and photograph of the system are shown in figs. 9.2.1 and 9.2.2. They show that the system consists of 3 components, the sensor head, power supplies and data logger. This section describes the design details, together with proposed final system.

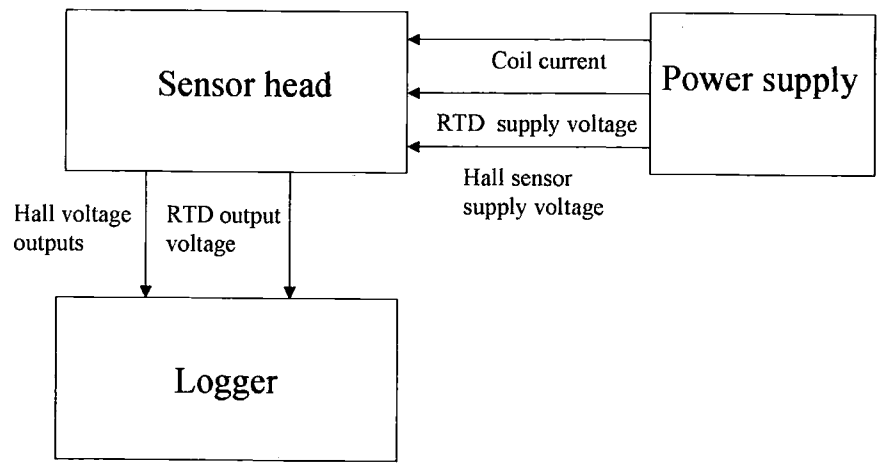

Fig. 9.2.1 MagTran block diagram

9.2.1 The sensor head

This consisted of a 3-pole dc excited electromagnet with Hall sensors located on each pole as shown in fig. 9.2.3. The dimensions were chosen such that the polegap was greater than the lift-off, to increase the sensitivity of the circuit to the sample.

Fig. 9.2.2

Photograph of MagTran system

The polegaps were designed to be significantly different, such that reluctance of the steel in each magnetic circuit was different, thus enabling lift-off compensation. The Hall sensors (KSY14) were procured from Infineon technologies. Their specification is shown in the Appendix A. They were chosen since they do not have built in amplifiers.

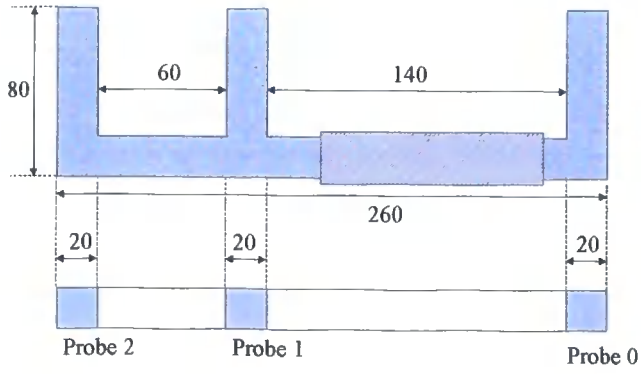

Fig. 9.2.3

Internal design of MagTran

This enabled the design of a sensor, which could generate larger B-fields and hence increase the sensing range. The coil consisted of 2500 windings and was rated to carry a 2A dc current so that the magnetomotive force was about 5000 At. The current was regulated using a constant current source with a sense resistor to give closed loop control. A resistive temperature device (RTD) was included to enable temperature compensation.

The internal components were enclosed in an aluminium case with an encircling water chamber as shown in fig. 9.2.4. Aluminium was chosen because it is a good thermal conductor and is not ferromagnetic; therefore it will enable efficient cooling but will not affect the magnetic circuit. It was designed such that the water enters the base of the chamber and leaves via holes on the sensor top. This produces an insulating layer of water on the sensor, which protects it from radiated heat from the hot steel strip (see fig. 9.2.5). A thin layer of an insulating polymer was also added for extra protection.

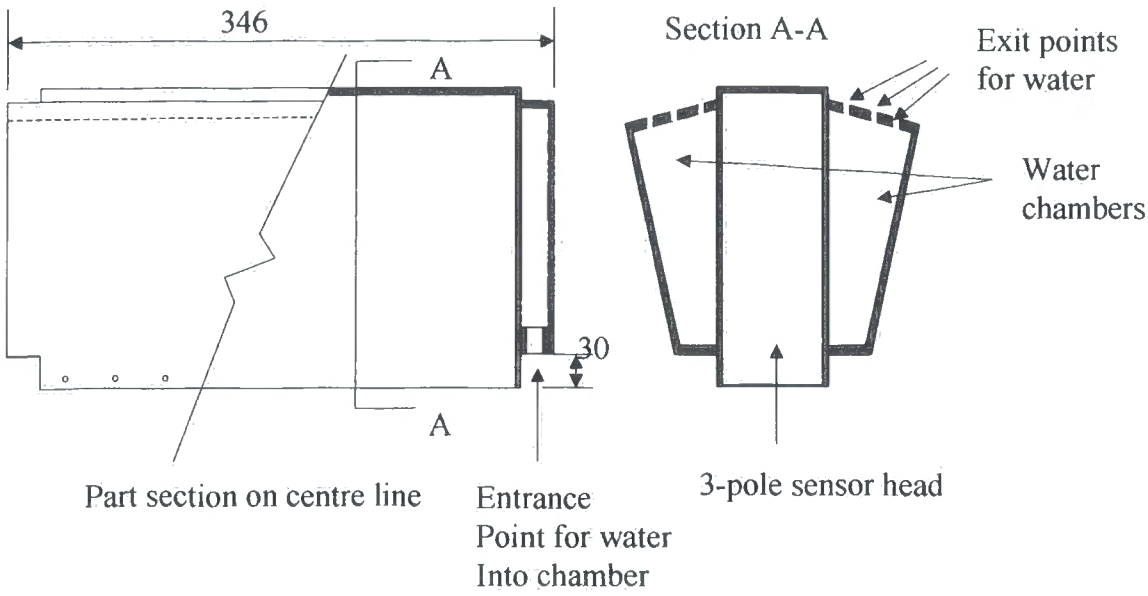

Fig. 9.2.4 Water cooling circuitry

9.2.2 The power supplies

These were housed in a portable cabinet, together with the data logger. A constant 2A dc current source supplied the coil such that a constant magnetic source was achieved. A sense resistor was used to provide closed loop feedback. A 12V dc voltage source was used to produce 3 constant current sources for the Hall probes and power the RTD.

9.2.3 The data logger

A Fluke NetDAQ 2645A was chosen for the system due to its high resolution of 5μV and ease by which it can be networked. A schematic of a networked system is shown in fig. 9.2.6.

Fig. 9.2.5 **Photograph of water cooling**

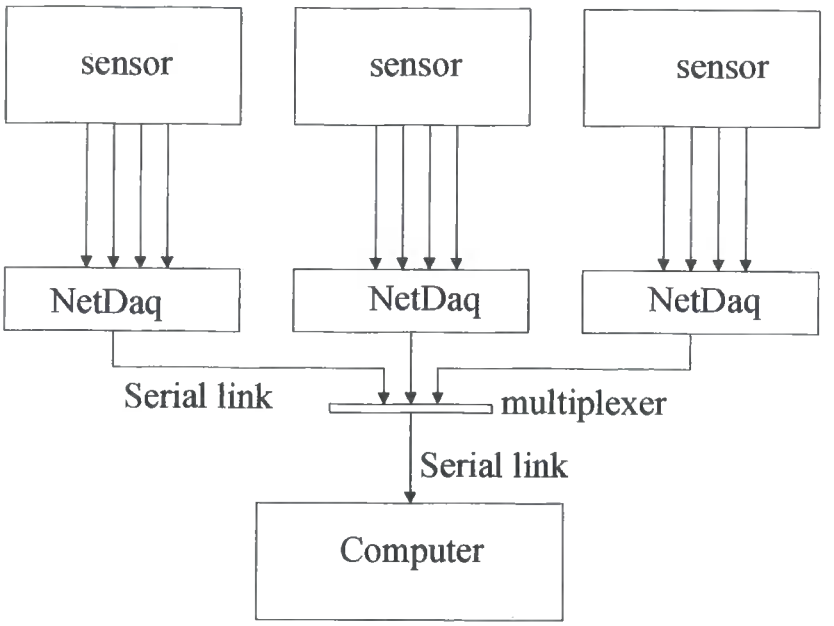

Fig. 9.2.6 **Networked transformation system**

9.3 Lumped circuit model of magnetic circuit

This was developed to identify a suitable specification for the driving coil, and then to assess the feasibility of using a 3-pole device for lift-off compensation. A diagram of the model is shown in fig. 9.3.1, where R_1 and R_2 represent the reluctance of the steel seen by the two sensor circuits, R_A, the air gap reluctance between a pole and sample and R_{p2}, the air reluctances between the poles flanking the coil. The cross-sectional area, A, around the circuit is assumed constant and the ratio of the polegaps is assumed to be 2. The E-core was assumed to have negligible reluctance. This model only gives an indication of the field strengths since it based on the assumption that the air gaps are small when compared with the length of the rest of the circuit. In this sensor this is clearly not the case.

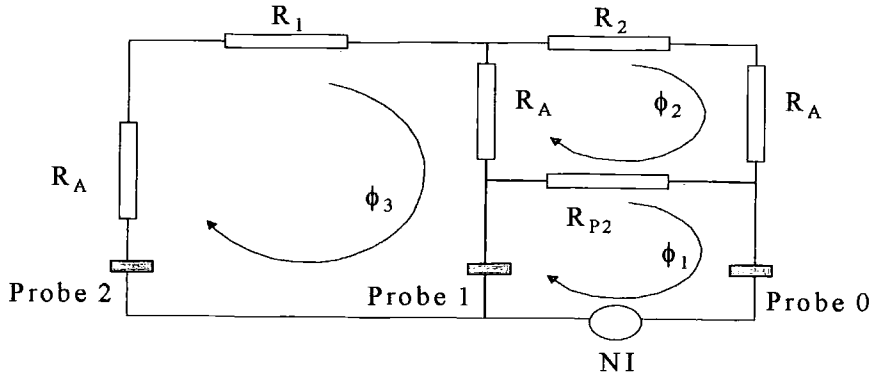

Fig. 9.3.1 **Lumped circuit model for MagTran**

The reluctances are given by

$$R_1 = \frac{l_s}{2\mu\mu_o A}, \quad R_2 = \frac{l_s}{\mu\mu_o A}, \quad R_A = \frac{l_A}{\mu_o A}, \quad \text{and} \quad R_{p2} = \frac{l_s}{\mu_o A}$$

where μ is the relative permeability of the steel.

Summing the H- field.length products around loop 1 gives

$$(\phi_1 - \phi_2)R_{p2} = NI \tag{9.3.1}$$

Rearranging gives

$$\phi_1 = \frac{NI}{R_{p2}} + \phi_2 \tag{9.3.2}$$

Similarly in loop 2

$$\phi_2(R_2 + R_A) + (\phi_2 - \phi_1)R_{p2} + (\phi_2 - \phi_3)R_A = 0 \tag{9.3.3}$$

Giving

$$\phi_2(R_{p2} + 2R_A + R_2) = \phi_1 R_{p2} + \phi_3 R_A \qquad (9.3.4)$$

And in loop 3

$$\phi_3(R_A + R_1) + (\phi_3 - \phi_2)R_A = 0 \qquad (9.3.5)$$

Giving

$$\phi_3 \frac{(2R_A + R_1)}{R_A} = \phi_2 \qquad (9.3.6)$$

Manipulation of (9.3.2), (9.3.4) and (9.3.6) gives

$$\phi_2 = \frac{NI}{(R_{p2} + 2R_A + R_2) - R_A^2(2R_A + R_1)^{-1}} \qquad (9.3.7)$$

This can be substituted into (9.3.2) and (9.3.6) to give ϕ_1 and ϕ_3 respectively.

From these equations the expected range of the B-field at each of the poles was calculated. At a lift-off of 35mm these were found to be about 90-120mT for Hall probe 0, 90-105mT for Hall probe 1 and less than 15mT for Hall probe 2. However, it should be noted that only two independent measurements are made since Hall probe 2 measures the linear combination of the other two probe outputs. Hence, the flux flowing around circuit 2, ϕ_2, is not directly measured.

The Hall probes chosen had approximate sensitivities of around 1-2 mV/mT (see Appendix A). When driven with a 5mA current the output would be expected to change in the region of a few millivolts on background voltages varying from tens to hundreds of millivolts.

The circuit shows that two independent measurements exist, indicating that it is mathematically feasible to decouple the two unknown parameters in the circuit, sample permeability and lift-off.

9.4 Characterisation Tests

As with previous prototypes, the instrument was characterised to compensate for effects which could lead to misinterpretation of the transformation measurement.

9.4.1 Temperature

The sensor head was placed in an environmental chamber and the temperature cycled between 10°C and 70°C which is the recommended highest operating temperature for the Hall probe. The test was carried out with steel samples placed at 45mm and 55mm lift-offs, and the gradients (change in output voltage/change in temperature) averaged. Each Hall probe had its own characteristic; therefore compensation equations were needed for each one. The normal operating temperature of the sensor head without water-cooling was about 40 – 45°C. Therefore, the corrected voltage was assumed to be at 40°C. The resulting compensation equations are

Hall probe 0 $$V_{40} = V_{actual} + 0.1510(T - 40.0000) \quad (9.4.1)$$

Hall probe 1 $$V_{40} = V_{actual} + 0.1171(T - 40.0000) \quad (9.4.2)$$

Hall probe 2 $$V_{40} = V_{actual} + 0.0948(T - 40.0000) \quad (9.4.3)$$

where T is the measured temperature.

It was noted from these tests that the temperature coefficients of each of the probes was greater than that specified by the manufacturer. However, the coefficients took into account all temperature variations in the system (including those of the steel sample) which gives rise to errors.

9.4.2 Speed

This sensor was not specifically characterised with speed because it was assumed that the results would be similar to that of the 2-pole permanent magnet system in the T-meter. Therefore, it was assumed that the relative speed between the strip and the sensor, when the pole center-line and direction of motion are perpendicular, has a negligible effect on the sensor output.

9.4.3 Lift-off

The purpose of this design was to find a suitable method of lift-off compensation. The idea of using a 3-pole device and measuring the magnetic field at each pole has

already been successfully developed for an ac transformation meter developed by Kawasaki[1]. In this research the idea is applied to a dc sensor. This was achieved by placing samples at room temperature on a mock-up of the roller table: In this case the one at Port Talbot as shown in fig. 9.4.1. The sample had to be large enough such that it represented a complete strip. The samples chosen were grades 1904 and 1916, whose compositions are shown in table 9.3.1. Their dimensions were one metre wide (full strip width) and 0.5m long, which was greater than the roll pitch. The basis of the compensation algorithm depended on the following assumptions:

i) The cold samples were 100% transformed, ie there was no retained austenite.

ii) A 0% transformed sample affects the sensor in the same way as a sample infinitely far away, ie when no sample is present.

iii) The intermediate values of fraction transformed form a linear relationship between the 0% and 100% values.

Using these assumptions experiments were carried out in which the sensor was placed a known distance below the pass-line (see fig. 9.4.1) and the carbon-manganese samples placed at known distances above the pass-line using Perspex spacers.

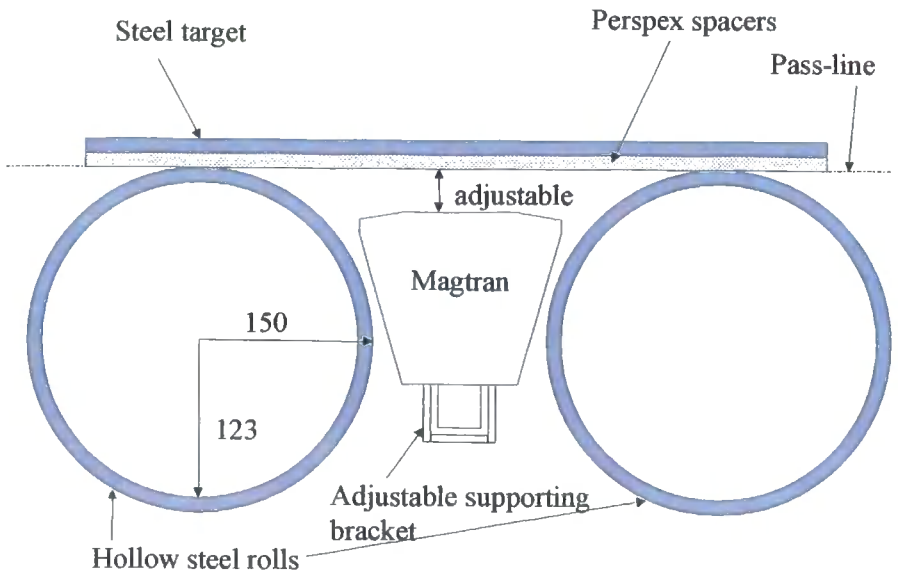

Fig. 9.4.1 **Calibration rig for steel rolled at Port Talbot hot strip mill**

The resulting calibration curves for grade 1916 are shown in figs. 9.4.2 and 9.4.3. They show that the sensor is more sensitive to the transformed state of the sample than variations in the lift-off. The estimated error on fraction transformed due to lift-off is approximately 3%/mm to 4%/mm at 100% transformed. It should be noted that the sensor needs calibrating with sample gauge. The effect of grain size on measurements has not been investigated at this stage but should be considered in future studies.

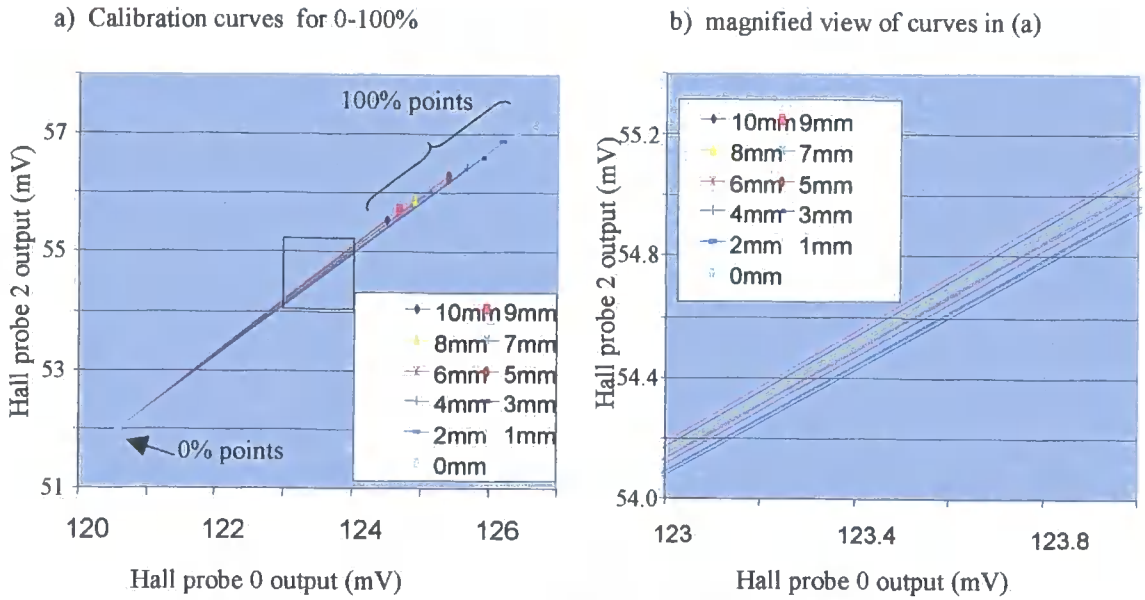

Fig. 9.4.2 **Calibration curves using Hall probes 2 and 0**

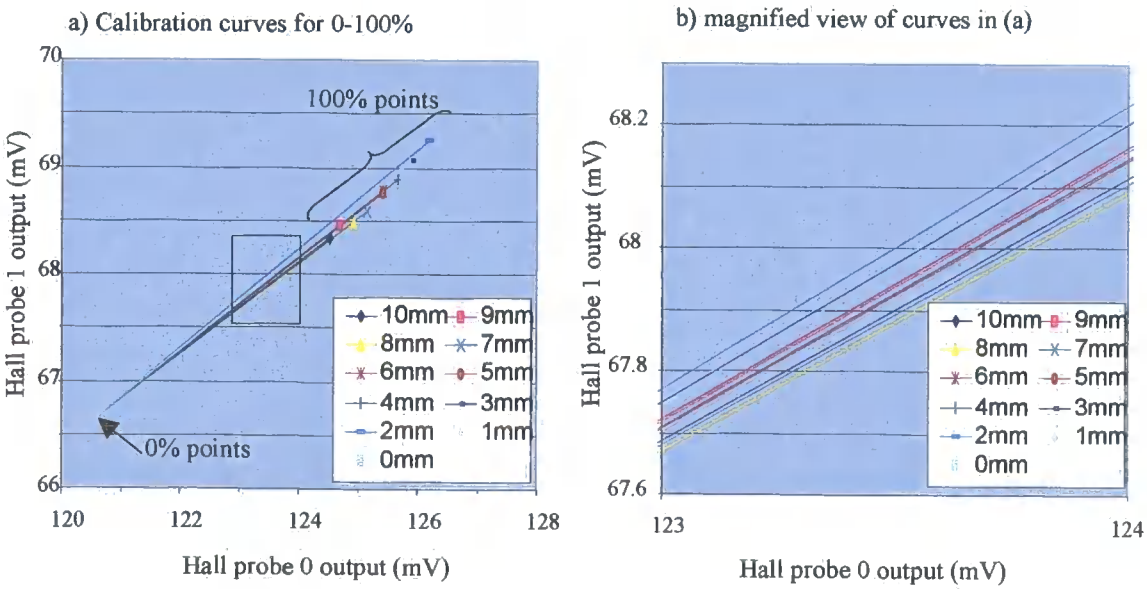

Fig. 9.4.3 **Calibration curves using Hall probes 1 and 0**

As described in section 9.3, only two of the Hall sensor outputs are independent. Therefore, either the graph of Hall probe 1 v Hall probe 0 or the graph of Hall probe 2 v Hall probe 0 should give sufficient information. An algorithm for decoupling lift-off and fraction ferrite is shown in Appendix E. Plant trials are needed to assess the validity of this lift-off compensation method since there is not enough variability in the magnetic properties of cold test samples and .

9.5 Plant trial (December 2000)

9.5.1 Aim of trial

A trial was carried out at Port Talbot hot strip mill with the MagTran in the IP2 position as shown in fig. 8.4.2. The steel grade 1916 was chosen since the previous trial with the T-meter had shown that this grade produced traces with extremely large

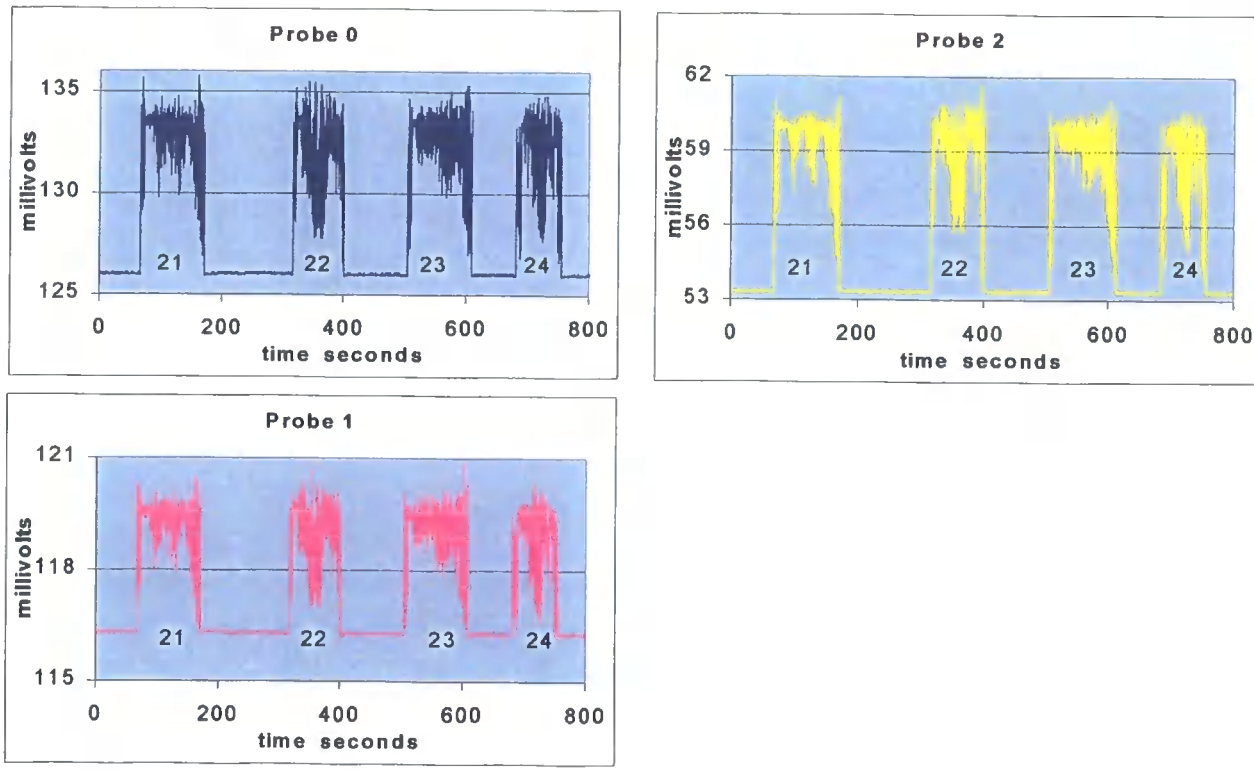

and rapid fluctuations.

Fig. 9.5.1 **Temperature compensated signals from Magtran, November 2000**

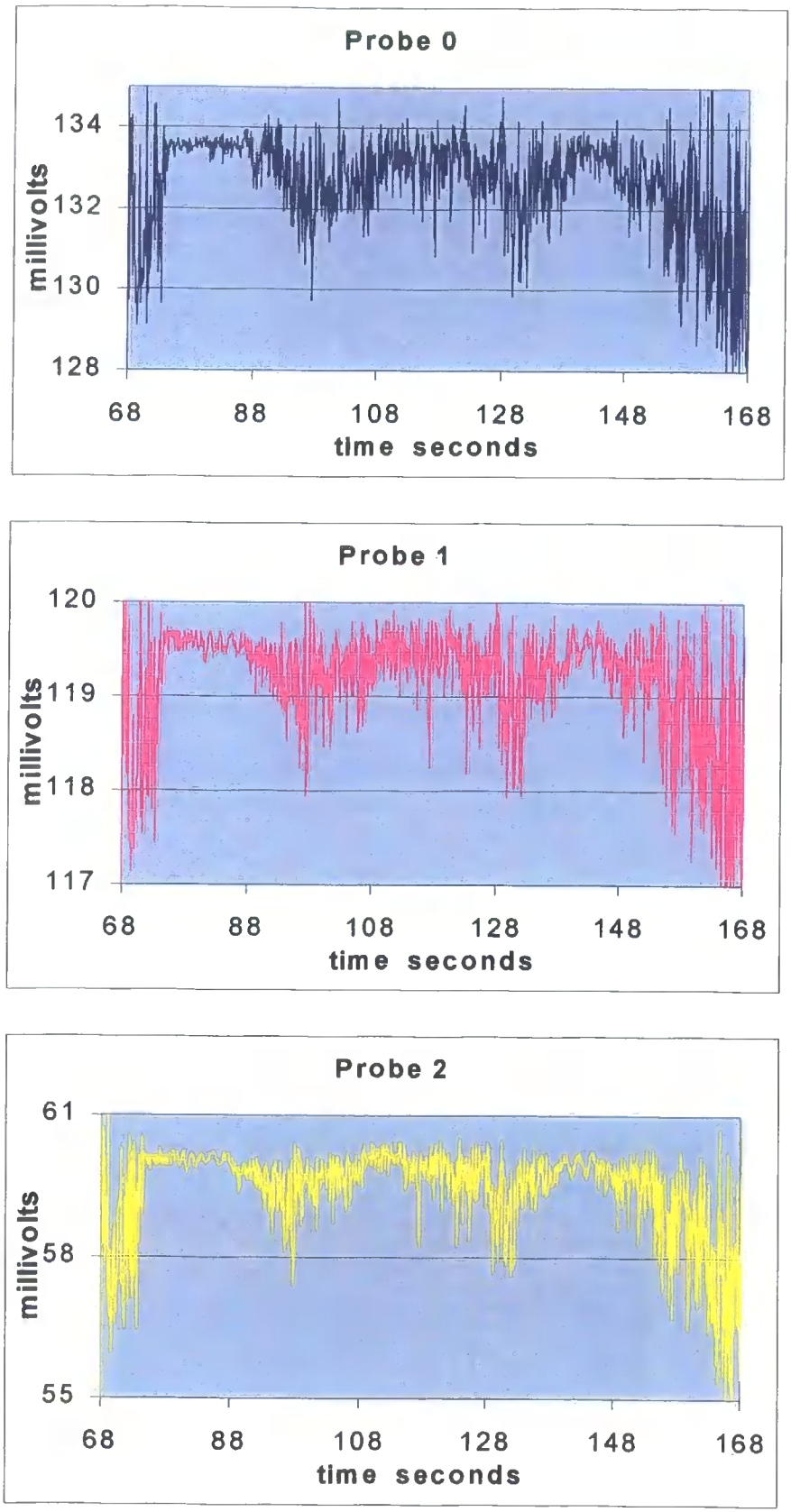

Fig. 9.5.2 **Temperature compensated data for sequence number 21, November 2000**

9.5.2 Results

Over 40 coils were logged. The traces were corrected for temperature using equations 9.4.1 to 9.4.3. The results for four typical grade 1916 coils are shown in fig. 9.5.1. A detailed examination of sequence number 21 (fig. 9.5.2) shows the traces from the three sensors have a high degree of correlation. This was confirmed by carrying out a cross-correlation (fig. 9.5.3) and is as predicted from the equations 9.3.2, 9.3.6 and 9.3.7 since all three measurements are dependent on an algebraic combination of the steel and air gap reluctances.

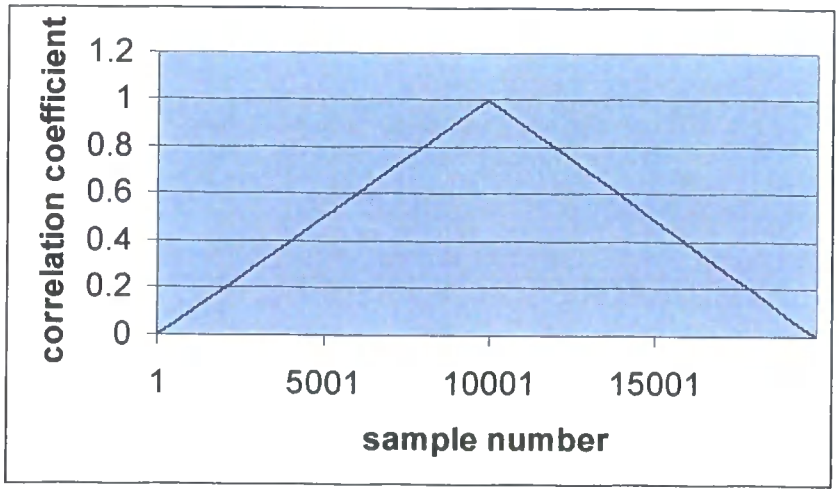

Fig. 9.5.3 **Cross correlation of probe 0 and probe 2 temperature compensated signals for sequence numbers 21 to 24**

Experiments on the rig shown in fig. 9.4.1 were used to produce lift-off curves as described in section 9.4.3. From these curves, a look-up table (table 9.5.1) was produced. The error in measuring the lift-off was +/- 0.2mm due to the manufacture of the Perspex sheet gauges. The probe voltages were logged at 10Hz for about 30s and averaged. The standard deviations were in the region of 0.02mV. Thus, if a noise level of three standard deviations is considered at a lift-off of 3mm, it is equivalent to a lift-off error of 0.3mm or 0.7% transformation at 100% ferrite.

Table 9.5.1

lift-off mm	probe 0 0% mV	probe 0 100% mV	probe 2 0% mV	probe 2 100% mV	gradient
0	123.90	136.12	52.44	61.29	0.74
1	123.90	135.73	52.44	61.12	0.74
2	123.90	135.34	52.44	60.96	0.75
3	123.90	134.95	52.44	60.79	0.76
4	123.90	134.56	52.44	60.62	0.77
5	123.90	134.17	52.44	60.46	0.78
6	123.90	133.78	52.44	60.29	0.80
7	123.90	133.39	52.44	60.13	0.81
8	123.90	133.00	52.44	59.96	0.83
9	123.90	132.62	52.44	59.80	0.85
10	123.90	132.23	52.44	59.63	0.87
11	123.90	131.85	52.44	59.47	0.89
12	123.90	131.46	52.44	59.31	0.91
13	123.90	131.08	52.44	59.14	0.94
14	123.90	130.69	52.44	58.98	0.97
15	123.90	130.31	52.44	58.82	0.10
16	123.90	129.93	52.44	58.65	1.03
17	123.90	129.54	52.44	58.49	1.08
18	123.90	129.16	52.44	58.33	1.12
19	123.90	128.78	52.44	58.16	1.18
20	123.90	128.40	52.44	58.00	1.24
21	123.90	128.01	52.44	57.84	1.32
22	123.90	127.63	52.44	57.68	1.41
23	123.90	127.25	52.44	57.52	1.52
24	123.90	126.87	52.44	57.35	1.67
25	123.90	126.49	52.44	57.19	1.85
26	123.90	126.12	52.44	57.03	2.09
27	123.90	125.74	52.44	56.87	2.44
28	123.90	125.36	52.44	56.71	2.97
29	123.90	124.98	52.44	56.55	3.88
30	123.90	124.61	52.44	56.39	5.80
31	123.90	124.23	52.44	56.23	12.44

Calibration data for lift-off compensation

The plant data were calibrated using a normalisation factor which was calculated by comparing the no steel present and maximum transformed values. The lift-off compensation algorithm was then applied in Matlab. The code is shown in Appendix E.

The algorithm is as follows:

1) Filter the data with a 4-pole Butterworth filter with a 2.5Hz –3dB point.

2) Calculate the gradient of the transformation curve at each sample point using

$$gradient = \frac{measure\ value\ from\ probe 2 - 0\%\ value\ of\ probe 2}{measured\ value\ from\ probe 0 - 0\%\ value\ of\ probe 0} \qquad (9.5.1)$$

3) Locate the lift-off value associated with this gradient using the lookup table

4) Calculate the 100% value associated with this lift-off. To prevent transformations of over 100% being calculated this value was assumed to be 95%. This is a reasonable estimate since there may be retained austenite present in the calibration samples. However, the greatest error will be due to a mismatch in the magnetic circuitry of the rig when compared to the actual mill location.

5) Linearly interpolate to find fraction ferrite present.

The resulting signals are shown in figs. 9.5.4.

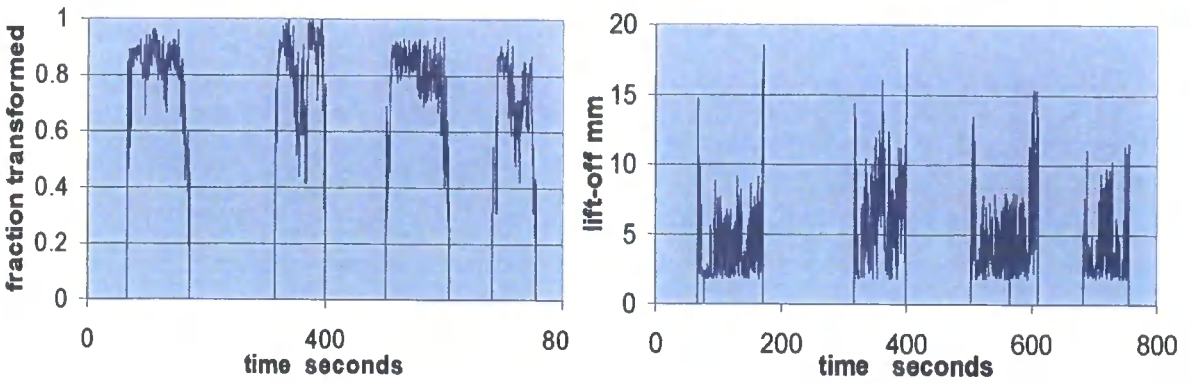

Fig. 9.5.4 Percentage transformation for sequence numbers 21 to 24

The calibration curves in fig. 9.4.3 were used to interpret the plant data. Background testing confirmed the noise levels of the probe signals were unchanged from the laboratory experiements. They indicate that when the steel is only slightly transformed, the probe outputs are not very sensitive to lift-off. Thus, the measurement error of both the fraction ferrite and lift-off is increased at low percentage transformations. However, analysis of the plant data suggests the lift-off values calculated are consistent with observations made during the trial. This is thought to be due to the steel having a large fraction of ferrite present.

The percentage transformation trace shows similar trends with the pre-processed data, however the maximum cross - correlation value with probe 0 data is now in the region of 0.5 to 0.6. The temperature compensated data for probe 0 and the fraction transformed data show similar trends to the temperature recorded by the IP2 pyrometer as shown in fig. 9.5.5.

9.5.3 Discussion

The fluctuations in the signals on both the MagTran and pyrometer traces are particularly severe for this steel grade. The pyrometer trace variations are probably due to obscuration of the steel surface due to the large amount of water present. The MagTran, however, should be able to see through the water. It is thought that its variation in output is due to lift-off fluctuations. This appears reasonable since they are more violent at the coil ends when the coils are not under tension. The lift-off compensation algorithm also predicts higher lift-offs at the ends and lower percentages of ferrite.

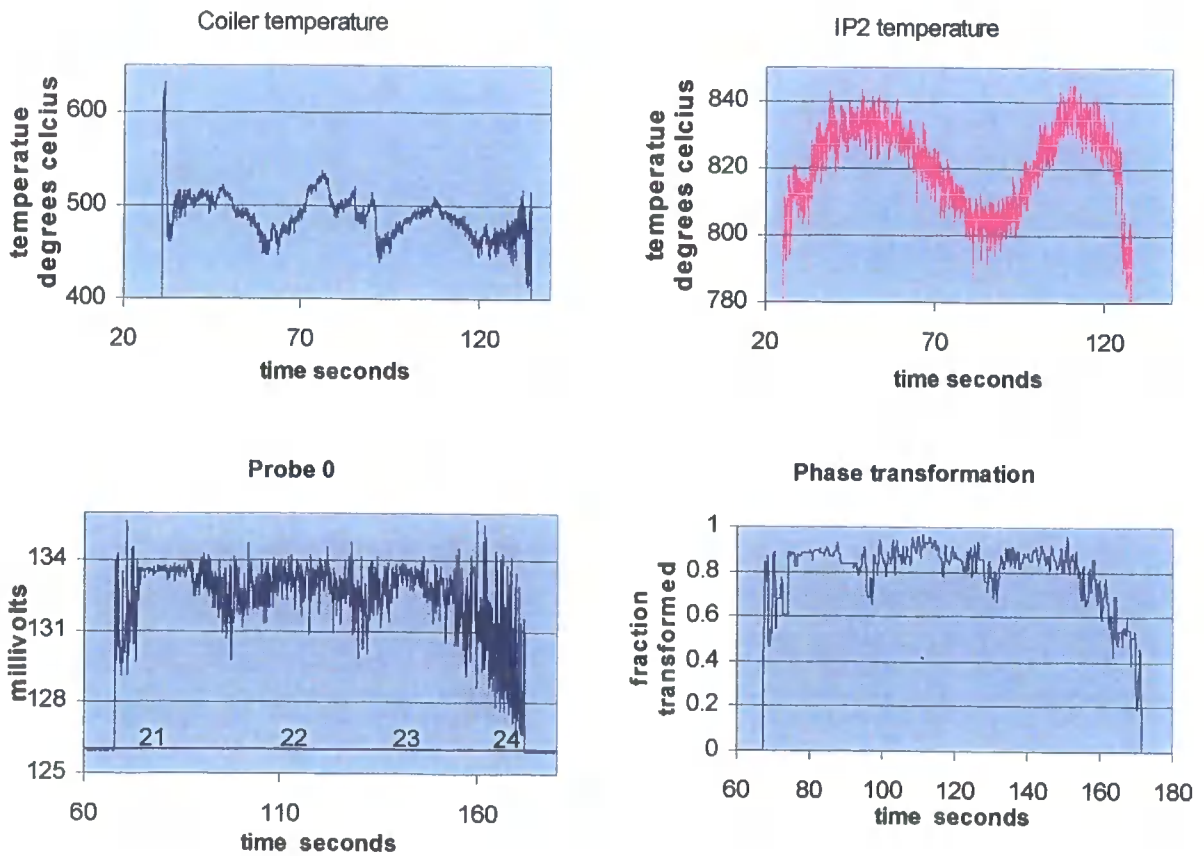

Fig. 9.5.5 MagTran and Pyrometer signals for sequence number 21

It was found that there were close similarities in the traces for phase transformation, the temperature compensated probe signals and the coiler pyrometer signal. Thus, the question of whether the lift-off compensation algorithm improves the phase transformation prediction beyond that from the raw temperature compensated traces was examined. From table 9.5.1 the error in percentage transformation for the uncompensated traces due to 10mm lift-off is 28% for probe 0 and 19% for probe 2. Low pass filtering will act to reduce variations above 2.5Hz. The main point of concern with the lift-off algorithm is that low levels of transformation appear to correlate with high lift-off values. It is not clear whether the algorithm has not compensated sufficiently or if low levels of transformation cause the coil to lift off from the roller table. Evidence to support the latter scenario is the phase transformation trace shows a similar trend to the coiler temperature signal, indicating the changes are due to material property variations. It should be noted, however, that the errors due to lift-off variations are greatest at low levels of transformation. In section 9.6 suggestions are made as to how to assess the accuracy of the decoupled phase and lift-off measurements.

The relationship with the temperature signals was examined. For sequence numbers 21 to 24 the coiler temperature had a positive correlation with both the probe 0 and phase traces. A theory to explain this is put forward below.

The coil had fully transformed by the time it had reached the coiler pyrometer. This can be confirmed by comparing the average temperature of about 500°C with the continuous cooling diagram for grade 1916 steel. Any fluctuations in temperature were therefore due to both variations in composition and process history, including cooling rate. To examine the consequences of these effects, consider the two cases of a steel strip with both a uniform composition and varying cooling rate along its length, and a non-uniform composition with a constant cooling rate.

Uniform composition with a varying cooling rate along its length. The variation in cooling rate could be due to a varying temperature profile before cooling, such that the water flow rates are adjusted to compensate. Here, regions subjected to slow cooling rates will transform at higher temperatures, but more slowly than those exposed to faster cooling rates. The resulting correlation with the coiler temperatures

can be either positive or negative depending on when the strip reaches the transformation temperature associated with the cooling rate.

Non-uniform composition with a constant cooling rate along its length. Here regions of higher carbon content will transform at lower temperatures. The heat produced during the transformation process will distort the cooling profile leading to temperature fluctuations at the coiler which will be correlated with the phase transformation at IP2.

Although the temperature at IP2 was measured, it did not appear to correlate with either the MagTran or any of the other plant signals. This is thought to be due to the fact that the steel was still undergoing the transformation process and releasing heat whilst being cooled at extremely high rates. This is one of the reasons why temperature is not an ideal control measurement for the steel properties. Another point to note is that the IP2 pyrometer is registering a temperature above the Curie temperature. If this was the case, the steel would still be paramagnetic and the MagTran should not detect it. Therefore, explanations as to why this occurred, are needed. The first one considered was the emissivity setting on the pyrometer. This is set to a constant value, usually, 0.8. However, the surface characteristics of the steel change due to the presence of scale, resulting in errors. For example, if the energy density from the steel strip was $100kWm^{-2}$, then the pyrometer would register 911°C with an emissivity of 0.9 and 946°C with a value of 0.8. (These calculations are based on the Stefan-Boltzmann law). Another factor to consider is that the radiation reflects from the mill steelwork. This results in errors which are difficult to quantify. Also, large amounts of water and steam are present. However, since these obscure the view of the pyrometer, the temperature output would be under estimated in this case. The final consideration is that there is a gap in the cooling sprays for this measurement. This allows heat from both recalescence due to the phase transformation, and the residual heat in the bulk of the coil to equalise with the cooler surface. The net result is that a higher temperature is registered.

9.6 Conclusions and further work

The MagTran has been shown to produce measurements which indicate the percentage transformation of steel samples which transform below the Curie temperature. The instrument has been calibrated against temperature and a lift-off compensation algorithm has been developed and assessed within the limits of the plant trials. A more comprehensive assessment could be achieved by producing a rig in which the hot steel sample can be periodically raised and lowered as it cools and transforms.

More informative plant trials could include placing three or more meters together with pyrometers along the run-out table and deriving percentage phase transformation profiles along the length of the coils. Samples from the coils could then be examined and compared with laboratory samples with the same composition, which have undergone identical cooling cycles. This would establish the feasibility of the lift-off compensation algorithm and enable suitable calibration factors to be calculated.

For this measurement to be of use in the steel manufacturing process, the rate of transformation needs to be controlled. The only factor available for this is water flow rate. However, the degree of cooling from the water is dependent on the heat transfer coefficient which itself is temperature dependent. Therefore, it appears unlikely that the transformation meters will replace the pyrometers but will be used in conjunction with them to produce tighter control of the product as suggested by Yahiro et al[(2)].

This magnetic method of transformation measurement is attractive due to its low cost and simplicity. At constant lift-off it gives an output which appears to be directly comparable to the percentage ferrite present. The need to apply lift-off compensation has led to a need for more precise calibrations.

9.7 References

1 *Morita M, Hashiguchi K, Hashimoto O, Nishida M, Okano S*, 'On-line transformation detector for property control of hot rolled steel', Proc Of Met Soc of AIME Symp on Acc Coiling of Steel, Pittsburgh Aug. 1985

2 *Yahiro K, Yamasaki J, Furukawa M, Arai K, Morita M, Obashi M,*
'Development of Coiling Temperature Control System on Hot Strip Mill',
Kawasaki Steel Technical Report No.24 April 1991

CHAPTER 10

PARAMETRIC FINITE-ELEMENT MODELLING OF A PERMANENT MAGNET TRANFORMATION DETECTOR

10.1 Aim

This chapter describes the application of parametric three-dimensional finite-element analysis techniques to accurately model the response of a two-pole transformation meter. The reason behind the investigation is that to calibrate the sensor, a large number of experiments need to be carried out to compensate for factors such as steel grade, gauge and measurement position. This is time-consuming and costly. Also, it complicates the interpretation of measurements when they are used to control the mechanical properties of new products. The aim of this finite-element modeling[1] work is therefore to produce calibrated simulations of a 2-pole sensor when the lift-off is known, such that calibration curve predictors can be produced. The package chosen for this investigation was Ansoft Maxwell ™ using the magnetostatics option. A description of the package is given in section 5.9.

10.2 Experimental setup

The apparatus consisted of an alcomax III™(see Appendix C) magnet with a Lakeshore MMT-6J02-VG Hall probe situated on one pole face. The magnet was bought 'off-the-shelf' and was not specifically designed for this application; it had locating holes through both of the poles. This prevented the Hall probe from being situated in the centre of the pole face. The diameter of the Hall probe was about 1mm, and located such that it measured the B-field perpendicular to the pole face. The output from the Hall probe was conditioned firstly by a Lakeshore model 420 Gaussmeter, and then through two stages of amplification using RDP type 611 dc amplifier modules. These stages were used to reduce the large background field (~160mT) and amplify the much smaller changes due to the presence of the test sample. The apparatus is shown in fig. 10.2.1. Three sets of experiments were carried out.

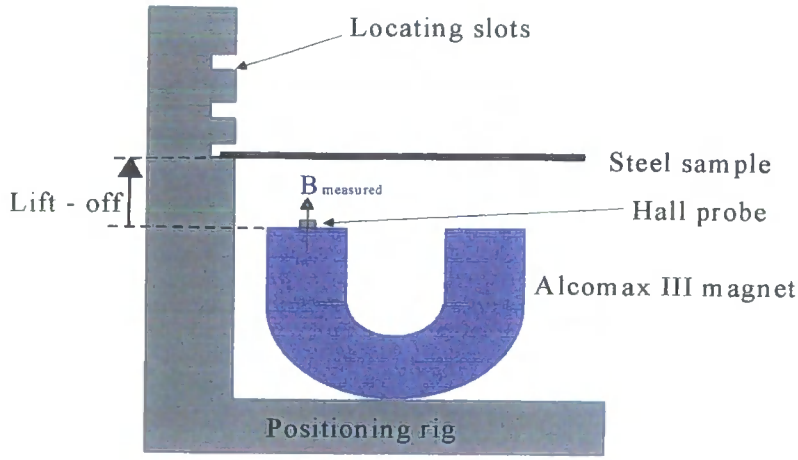

Fig. 10.2.1 Experimental apparatus

10.3 Experiment to determine noise levels

This set was used to determine the noise levels and the characteristic of the Hall probe with distance from the steel sample (lift-off) when fixed in one position. The Hall probe was semi-permanently located as near to the pole centre as was feasible and its location noted. Its orientation was such that it measured the B-field normal to the pole face. Samples were placed in 3 positions (65mm, 75mm and 85mm) and the Hall output logged at 100Hz using an Overpower Monitor logging system. The results including the 'no sample' case are shown in fig. 10.3.1 and table 10.3.1. The range was defined as the difference between the mean output with sample at 65mm and when no sample was present. It was found to be 2.9mT and less than 2% of the range. The noise levels were well below 0.1mT and there was negligible drift. Temperature effects were not taken account of during these tests.

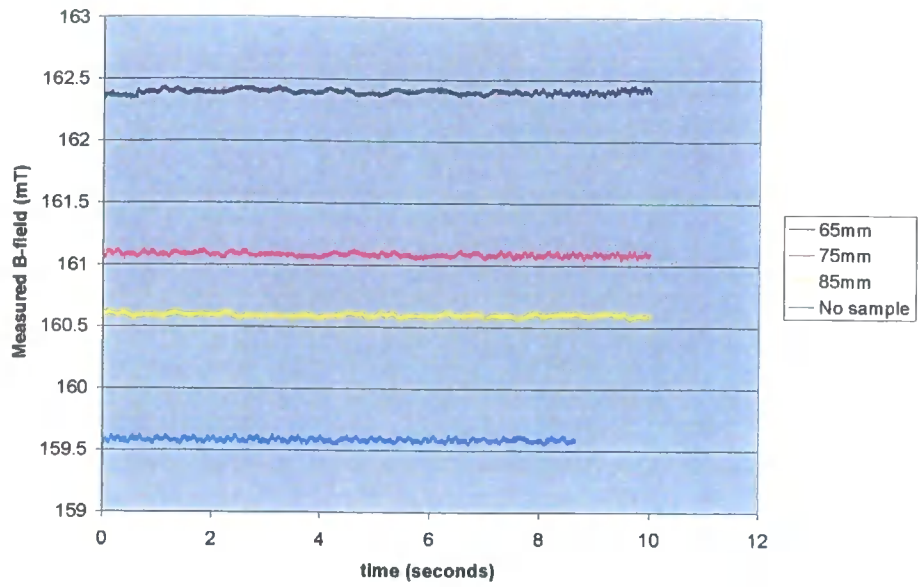

Fig. 10.3.1 Output signals

Table 10.3.1

Lift-off (mm)	Mean of B-field (mT)	Standard Deviation of B-field (mT)
65	162.4	<0.1
75	161.1	<0.1
85	160.6	<0.1
No sample	159.5	<0.1

Summary of Results

10.4 Experiment to characterise Hall probe output with position

This set of tests was used to define the Hall lift-off characteristic with position on the pole face and distance from the sample. The surface of the pole was divided into pole elements 5mm x 5mm as shown in fig. 10.4.1. A two-digit number identified each measurement region on the grid. The first digit identifies the column (0-4) and the second the row (1-5). The grey circle represents the locating hole present in the centre of the pole. With the Hall probe fixed, readings were taken with samples in different positions. A typical set of results is shown in fig. 10.4.2, which plots the change in output from the Hall probe amplifier for a 45mm change in lift-off (40mm to 85mm) with a fully transformed sample. It can be seen that the lift-off characteristic is a function of the Hall probe position.

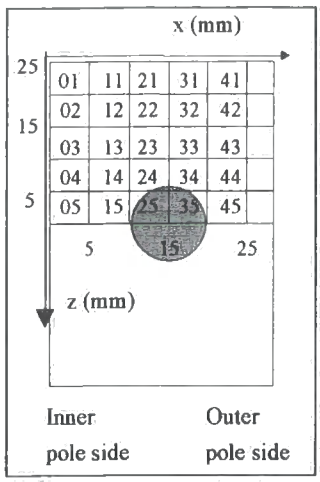

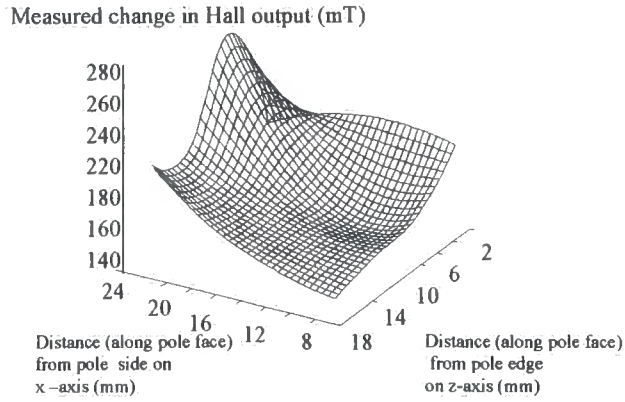

Fig. 10.4.1 Pole measurement positions

Fig. 10.4.2 Lift-off characteristics

10.5 Experiment to define repeatability

These results were used to define the variation in Hall probe output when in a particular element position. With no sample present, the Hall probe was placed in each measurement position as defined in fig. 10.4.1 and spot readings taken. This procedure was repeated ten times. The means and standard deviations are shown in table 10.5.1. The standard deviations were found to be of the same order as the range defined in section 10.3 (2.9mT).

Table 10.5.1

Pole position identifier	Mean of B-field (mT)	Standard Deviation of B-field (mT)
14	145.9056	1.2290
24	151.1785	1.1471
34	175.8945	2.3192
44	201.0292	4.0929
23	160.8601	2.6640
33	164.3559	1.8141
22	160.3739	4.3654
32	186.5350	5.0490
21	215.7575	6.8134
31	242.7897	7.6385

B-fields measured by Hall probe in different locations

10.6 Simulations

The challenge in producing realistic simulations was to be able to simulate changes in the normal pole face B-field of less than 0.2% (10% of the range defined by the experiments). In an attempt to achieve this, full and quarter 3D models were compared, the mesh size examined and a suitable model for the test piece was derived.

10.7 Full 3D simulation

The first model created is shown in fig. 10.7.1. The magnet consisted of three parts; a positive pole, negative pole and the main body. A function was used to sweep the direction of magnetisation around the main body. The package provided a demagnetisation curve for alnico V™ (see Appendix C). This was therefore used in the simulation. In the experiment, the magnet had locating holes. These were not included in the initial models. The Hall probe was defined as a box of side 1mm 'measuring' the B-field normal to the pole face.

$$B_{av} = \frac{\int_{surface} \underline{B} \cdot d\underline{S}}{\int_{surface} d\underline{S}} \qquad (10.7.1)$$

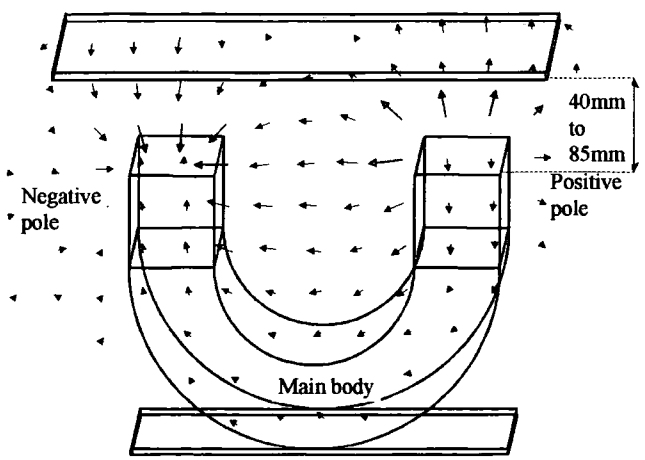

Fig. 10.7.1 **3-D finite element model**

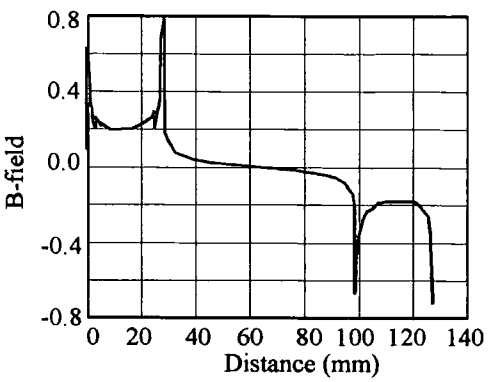

Fig. 10.7.2 **Normal B-field across pole centreline**

To investigate the finite element model validity, the symmetry of the B-field was examined using a mesh size of 106 022 elements. The resulting B-field across the centreline direction from the positive to negative pole is shown in fig. 10.7.2. It shows a slightly non-symmetrical nature. To allow for a closer examination, the average B-field was compared at symmetrical locations on each of the pole faces. The results are shown in fig. 10.7.3. At elements towards the pole centre, differences of up to 15% are present. Towards the edge of the poles, the errors are even greater because of the larger field gradients. These results therefore show that even with large mesh sizes (100k tetrahedra), the full model was not accurate enough to symmetrically simulate this problem.

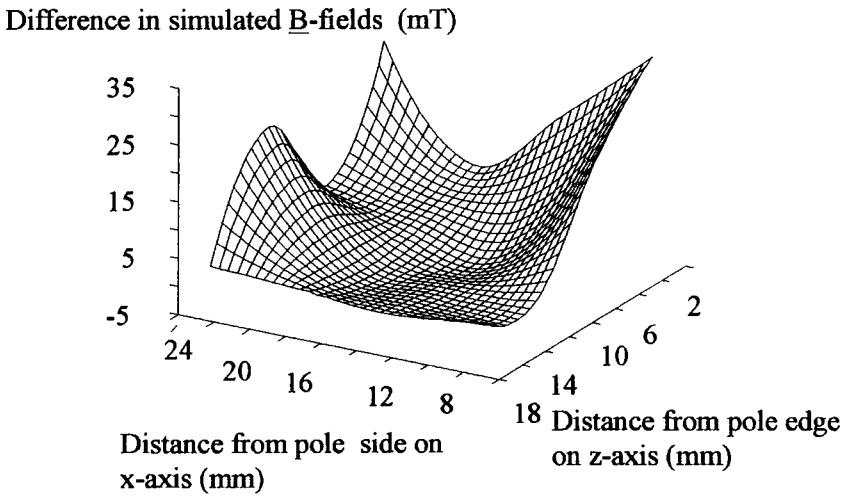

Fig. 10.7.3 Simulation errors between poles in full model

10.8 Quarter model

To reduce the complexity of the model, symmetry was used to reduce it to a quarter model as shown in fig. 10.8.1. The diagram also shows a hole through the pole face. Initially, new meshes were created for the sample in different locations. However, the errors due to different mesh sizes and configurations gave inconsistent results. To overcome this, the model was set up with test pieces in all the required locations. The permeabilities of these pieces could then be varied to define whether they were present in a particular set up, ie to make them invisible, a relative permeability of one

was chosen. The mesh could then be set up for one scenario and subsequently transferred to all the others.

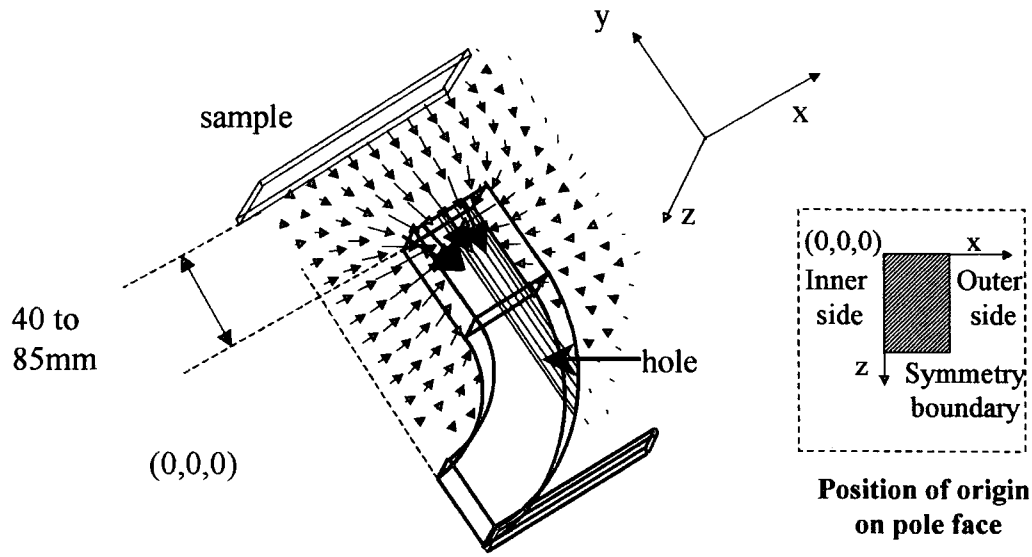

Fig. 10.8.1 Quarter finite element model

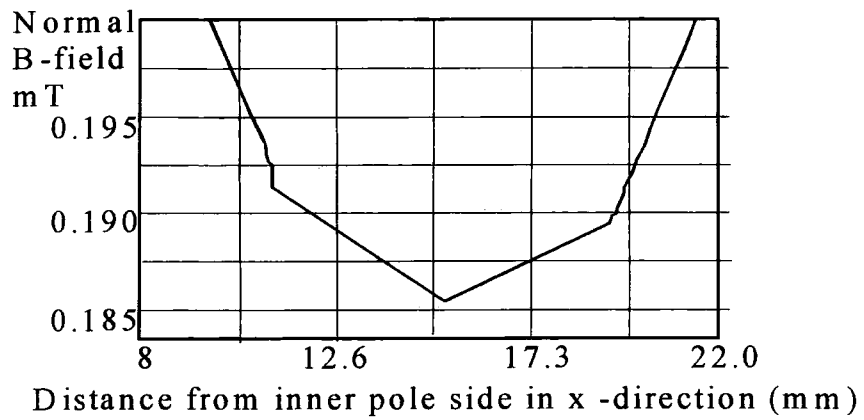

Fig. 10.8.1 Quantisation effect of meshing

10.9 Defining mesh size

A quarter model with no hole was solved for three different mesh configurations. Some of the results for position x=12.5mm, z=17.5mm, are shown in table 10.9.1. Variations of less than 0.01% of the simulated reading were observed between corresponding scenarios with different mesh configurations. This corresponds to about 1% of the simulated range (defined to be the difference between the test sample at 65mm and when no sample is present). Another factor in determining an appropriate mesh size is the quantisation error in the pole region. Fig. 10.9.1 shows

the normal B-field characteristic along the x-axis for mesh size 30,315. The quantisation effect has given a discontinuity of about 0.8mT at the element boundary.

These results show that with meshes containing between 25 000 to 35 000 elements, the mesh must be identical if different scenarios are to be compared. Considering the Hall probe as an area rather than a point does act to reduce the effect of these discontinuity errors. Decreasing the element size in this area will act to reduce these errors but requires considerably more computing power.

Table 10.9.1

Lift-off (mm)	Mesh Size		
	25,685	27,879	30,315
40	192.8844	192.6347	192.3930
45	186.1892	186.1280	185.8884
50	181.1310	181.0656	180.8296
55	177.1629	176.7772	176.8576
60	173.9949	173.8694	173.6924
65	171.1001	171.2683	171.1366
70	169.3608	169.1473	169.1198
75	167.6275	167.4261	167.2653
80	166.0524	165.8571	165.8200
85	164.8478	164.6460	164.6246

Comparison of simulated Hall probe field (mT) for different mesh sizes and lift-offs at probe position, x = 12.5mm, z = 17.5mm

10.10 Defining the test piece

The relative permeability and conductivity of the test-piece were only known approximately from the literature[2] and can be in the region of 500 to 10000 depending on composition, applied field and processing. Therefore, the first aim of the simulation was to identify a suitable maximum permeability for the test samples. Fig. 10.10.1 shows that changing the relative permeability from 2000 to 8000 accounts for about 0.2% of the simulated reading. Therefore, a value of 2000 was chosen as the upper limit.

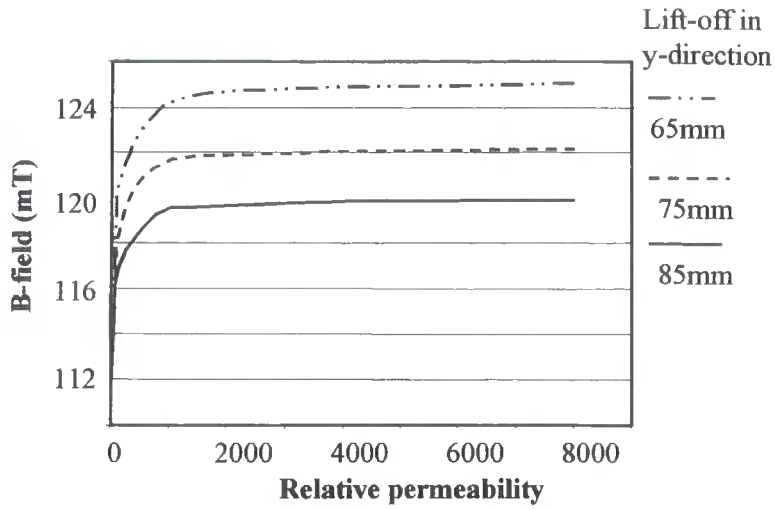

Fig. 10.10.1 **Effect of changing the permeability of the test sample**

10.11 Calibration of simulation

As this part of the investigation a quarter model with a hole was simulated using 35,176 elements. To check the validity of the simulation, the measured (fig. 10.4.9) and simulated (fig. 10.11.1) x - and z- characteristics were compared. The z – traces show the same general trends but the measured data shows some excursions. This is probably due to the magnet not having completely homogeneous properties as assumed in the simulation. This non-homogeneity is more obvious when considering the traces in the x- direction. In this case, the simulated and measured data show very different trends. It can also be seen that the sensitivity of the B-field to location is greater at the pole edges.

The lift-off characteristics were then compared. Typical traces are shown in fig. 10.11.2. For each element the simulated and measured data showed the same trend. However, the mean absolute errors varied upon pole location, with the greatest errors being observed at the pole sides as shown in table 10.11.1. To reduce the errors, a linear regression was applied to the data for each pole element. Table 10.11.2 indicates R^2 values corresponding to good fits. Typical graphs are shown in fig. 10.11.3. The number of points used was limited since the test pieces could not overlap in the model. From these results, it was concluded that general scaling and

offset factors could not be applied to the whole pole face but could be applied to

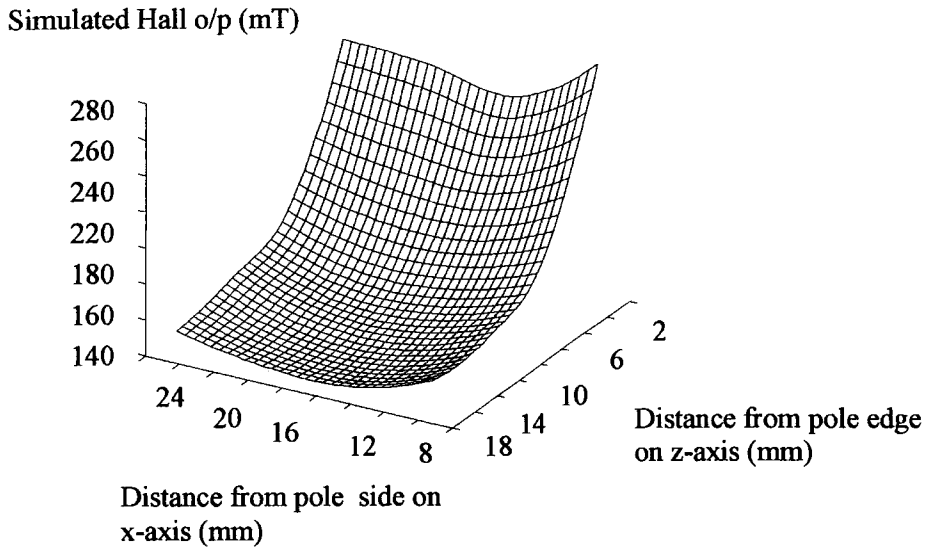

Fig. 10.11.1 Simulated value of the Hall probe output in the x- and z- directions

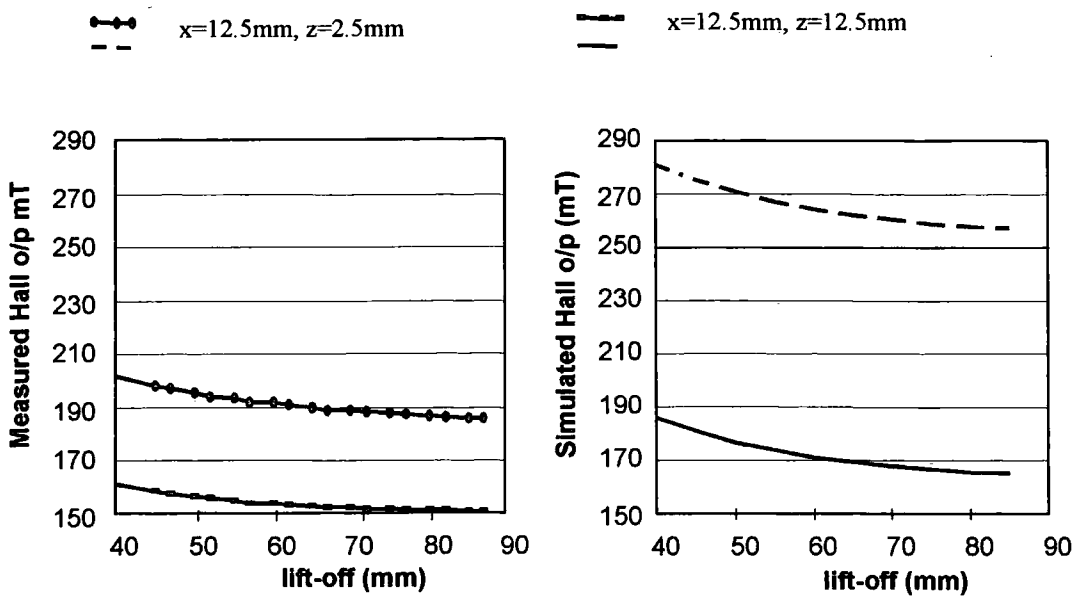

individual measurement positions.

Fig. 10.11.2 Simulated and measured lift-off characteristic

Table 10.11.1

x – position (mm)	7.5	12.5	12.5	12.5	12.5	17.5	22.5	17.5	17.5	17.5
z – position (mm)	17.5	2.5	7.5	12.5	17.5	17.5	17.5	2.5	7.5	12.5
Mean absolute error before calibration (mT)	30.13	38.32	26.44	11.02	11.47	2.73	15.01	42.77	2.01	1.89
Mean absolute error after calibration (mT)	0.13	0.39	0.26	0.10	0.08	0.38	0.36	0.46	0. 24	0.31

Variation of simulation error with position

Table 10.11.2

x - position (mm)	z – position (mm)	Regression		
		Scaling factor (to 4 dp)	Offset constant (to 4 dp)	R^2
7.5	17.5	0.4680	56.5220	0.998
12.5	2.5	0.6530	18.5656	0.995
12.5	7.5	0.5002	56.5913	0.994
12.5	12.5	0.4592	76.9895	0.999
12.5	17.5	0.4716	73.2757	0.999
17.5	17.5	0.4358	99.7165	0.989
22.5	17.5	0.4198	134.9950	0.991
17.5	2.5	0.3960	82.3538	0.986
17.5	7.5	0.3821	115.5202	0.994
17.5	12.5	0.4485	93.1881	0.992

Calibration data

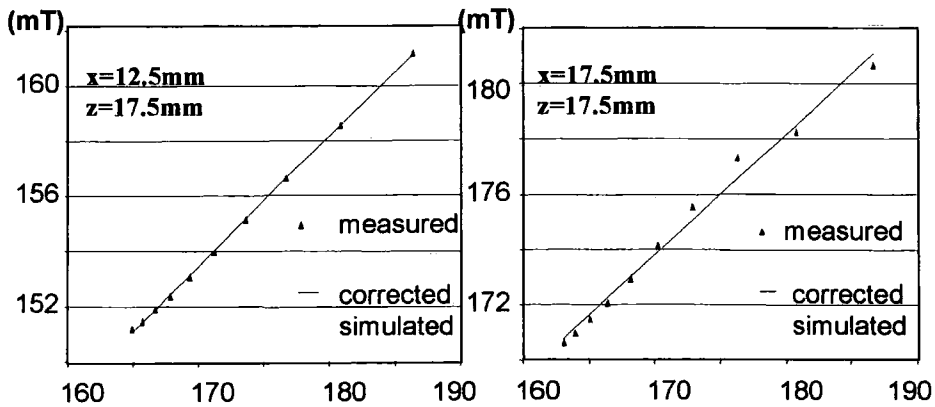

Fig. 10.11.3 Regression fits for measurement positions 24 and 34

10.12 Discussion

This investigation has highlighted some of the main issues with obtaining an accurate repeatable simulation of the experiments. A method has been identified in which the use of a single mesh configuration for all scenarios to be compared is a key factor when using only moderate mesh sizes. The results show that it is not possible to

simulate the actual response to within 0.2% as required, without calibration factors for the mesh sizes investigated. This is thought to be mainly due to the magnet not being completely homogeneous as assumed in the model. This will be partly due to the material itself, but probably also due to the magnetisation process in which the location hole will act to distort the field alignment. Other errors include not knowing the exact location of the probe especially at the pole edges where the sensitivity to position is high and also the imprecise knowledge of the test samples. Increasing the mesh size may reduce the quantisation errors but will not improve on the errors due to assumptions made in modelling the experiments.

The measured and simulated data have a highly linear relationship when individual elements are compared. The degree of linearity is dependent on position and can give errors up to 13% of the range. Further investigation is required to assess whether this is due to the mesh configuration or if optimum elements can be identified to give the most accurate simulations for a particular system. However, the data does show that a calibrated element can be used to predict the normal $\underline{B}$-field to within 0.2% as required. Further work is needed to assess whether this method is still valid for more complicated geometries.

10.13 Conclusions

This chapter has described the use of parametric, three-dimensional finite-element simulation techniques to analyse the response on a magnetic transformation meter developed for use in the steel industry. The study has shown that the raw simulation results are not accurate enough to simulate the experiment to within the required 0.2%. This is mainly due to the assumptions made in the model. However, scaling and offset factors can be used to calibrate the finite element simulation to give errors less than 0.2% provided the mesh configuration and Hall probe locations are not changed, a fixed mesh pattern is used to switch test pieces in and out using their material properties, and symmetry is fully exploited.

It can therefore be concluded that the permanent magnet system can be simulated by a calibrated finite element model for simple geometries. Further work is needed to assess the validity of this method for more complicated geometries.

10.14 References

1 *Johnstone S, Peyton AJ,*' The application of parametric 3D finite element modeling techniques to evaluate the performance of a magnetic sensor system', Sensors and Actuators: A.Physical, Vol. 93/2 pp109-116 Oct 2001

2 *Weast RC,* 'CRC Handbook of chemistry and physics', CRC Press Inc 1986

11.15 Bibliography

Sylvester PP, Ferrari RL, 'Finite elements for electrical engineers', Cambridge University Press, 1983.

McCaig M, 'Permanent magnets in theory and practice', Pentech Press, 1987.

CHAPTER 11

CONCLUSIONS AND FURTHER WORK

The work described in this report is based on the concept that the magnetic properties of steel can be used to infer the state of the phase transformation from austenite to ferrite in steel provided it occurs below the Curie temperature. Based on this, two sets of prototypes have been developed, resulting in the T-meter and MagTran.

The T-meter design is based on a two-pole C-core with a Gaussmeter to measure the magnetic flux density changes due to the steel material properties changing. An eddy current sensor was incorporated to compensate for the fact that the flux density was also a function of the distance between the sensor and the steel. Other factors which could affect the Gaussmeter output were also compensated for; these included temperature changes and strip speed variations.

Tests to compare the T-meter with dilatometry and optical microscopy showed that the T-meter provided a measurement, from which the onset of transformation could be detected for eutectoid steels. The measurements were not as accurate as those from the dilatometer. This is thought to be due to the different sample sizes. It was also found that neither method could accurately locate the end point.

To identify possible applications for the meter, further tests were carried out. These included the control of transformation in carbon-manganese steels and the unambiguous detection of the ferrite fraction in eutectoid steels, where there is a high degree of recalescance. However, when plant trials were carried out, the results suggested that the eddy current sensor was not giving satisfactory lift-off compensation. Therefore, an empirical model was developed, which assumed that both the Gaussmeter and eddy current sensor outputs were sensitive to the steel properties and lift-off. Using this method, the percentage ferrite and lift-off were decoupled. To quantify the success of this method, a carbon-manganese steel was chosen which gave

large fluctuations (37% of range) in the meter outputs. After applying both an analogue anti-aliasing filter and a digital averaging algorithm to overcome difficulties with the different response times of the sensors, the fluctuations were reduced to 2%. However, the range of the eddy current sensor was limited to a lift-off of 55mm. Since the lift-off of the carbon-manganese steel was greater than this, lift-off compensation was not satisfactory for this grade.

The results from this instrument have shown that it is possible to decouple lift-off and steel properties using two different excitation frequencies. The problems with the T-meter were due to the sensors having different response times and sensing ranges. Further work into this could involve designing a single excitation coil driven by the two frequencies and detecting the flux changes using high frequency Hall probes. Although the sensing ranges would still be different, the response times would be the same. Separate mathematical models would need to be developed for each frequency, although the general structure of the equations should be the same.

The MagTran was based on the principle of only using the magnetic properties of the material to infer the percentage ferrite. However, two measurements were again required to decouple the lift-off and material property. To achieve this, two magnetic circuits of different lengths were used. The output was shown to relate to the percentage ferrite in laboratory conditions.

To develop the lift-off compensation algorithm, a linear relationship between the magnetic properties and percentage ferrite was assumed. Using this, a 'cold' calibration method was designed and used in the analysis of plant trials. The traces obtained were similar in structure to the coiler temperature. This suggested they were indicating material property changes. The correlation with the IP2 temperature was not as obvious. This was thought to be due to the different mechanisms affecting the temperature during the accelerated cooling phase.

To investigate the validity of using this sensor arrangement, the calibration method needs to be improved. This could involve performing the cold tests on the mill and noting the correction factors needed to match up the results from those of the mill rig or even finite element models.

To assess either the T-meter or MagTran, more measurement points are required along the roller table, such that the transformation curve for each steel strip can be mapped. Based on this information, operating points can be defined which can be used to control the cooling process.

To use the concept of using magnetic measurements to measure phase transformation on-line, the issue of lift-off needs to be resolved. The two prototypes basically differ by the type of compensation used. A direct measurement is still the preferred option. A device which may be suitable is an ultrasonic pulse echo transceiver which uses water jet coupling.

The final chapter described the difficulties with calibrating finite element models to actual magnetic circuits. The results showed that the raw simulation was not accurate enough (>0.2%), but could be improved using linear scaling and offset factors. However, the corrections were only valid for defined locations. Further simulations are required to investigate whether the conclusions are valid for more complex geometries such as the rolling mill.

The current state of this work is that the MagTran is located on a hot strip mill. Comparison with present research in this field has shown that there have been no reports of on-line systems using magnetic techniques since Lacroix[1], Morita et al [2], Yasohiro et al[3] and Yahiro et al[4], although a pilot plant study, based on a single C-core sensor with no lift-off compensation, was undertaken by Sharif et al[5], along side this work.

The main technique being developed for on-line phase transformation measurement is that of laser ultrasonics[6]. It is a much more costly approach, but could be used effectively in conjunction with the magnetic sensors. Other work presently underway is the use of magnetic Barkhausen noise[7] to measure the martensite phase transformation, and SQUIDs to measure the local remanent magnetisation of different steel phases[8] and correlate it with the underlying microstructure. This second method is useful for 'cold' structures such as bridges, but more difficult to apply to hot steel strip.

11.1 References

1 *M Lacroix, J Abrigo, L Arnault*, 'On line instrument for ferritic transformation control: Inter Conf. On steel rolling', Tokyo, Vol. 2, pp. 1286-1296,1980

2 *Morita M, Hashiguchi K, Hashimoto O, Nishida M, Okano* S, 'On-line transformation detector for property control of hot rolled steel', Proc Of Met Soc of AIME Symp on Acc Coilin g of Steel, Pittsburgh Aug. 1985

3 *M Yasuhiro, A Seigo*, 'Transformation rate-measuring method and device', NKK Corp, Pub. No. 07190991 A, Aug. 1995

4 *Yahiro K, Yamasaki J, Furukawa M, Arai K, Morita M, Obashi M*, 'Development of Coiling Temperature Control System on Hot Strip Mill', Kawasaki Steel Technical Report No.24, April, 1991

5 *Sharif E, Bell C, Morris PF, Peyton AJ*, 'Imaging the transformation of hot strip steel using magnetic techniques', Journal of Electronic Imaging, Vol. 10, No. 3, pp.669-678, Jul. 2001

6 *M Dubois, A Moreau, M Militzer, JF Bussiere*, 'Laser-ultrasonic monitoring of phase transformation in steels', Scripta Materialia, Vol 39, No 6 pp 735-741 1998

7 *Furuya Y, Hagood NW, Tamoto S, Kubota T, Okazaki T*, 'Evaluation of a phase transformation in a ferromagnetic shape memory Fe-Pd alloy using a magnetic barkhausen noise technique', Journal of the Japan Institue of Metals, Vol. 66, No. 1, pp.28-33, Jan. 2002

8 *Shaw TJ, Chan JW, Kang S-H, McDermott R, Morris Jr. JW, Clarke J*, 'Scanning SQUID microscope differentiation of ferromagnetic steel phases', Acta Materialia, Vol. 48, pp 2655-2664, 2000

APPENDIX A

Magnetic field sensor specifications

A. Lohet Hall probe

Supply voltage	8 to 16Vdc
Maximum supply current	19mA
Output (current sourcing)	Ratiometric
Maximum response time	3μs
Magnetic characteristics	
Span (-40mT to +40mT)	6V
Null (offset at 0 Gauss)	6 +/- 0.6V
Sensitivity	50 +/- 2mV/mT
Linearity	+1.5% span
Temperature errors	
Maximum null shift	
-40°C to +150°C	+/-5%
-25°C to + 85°C	+/-3%
0°C to + 50°C	+/-2%
Sensitivity	
-40°C to + 0°C	-0.034%/°C
0°C to +150°C	-0.077%/ °C

Information supplied from RS datasheet 249-4700

B. Lakeshore 420 Gaussmeter

Number of inputs	1
Resolution (+/- 300mT range using MNA-1904-VG probe)	Probe dependent
Electronic DC accuracy	0.45% of reading +/-0.05% of range at 25°C
Drift of DC electronics	0.05% of reading +1 count /°C
AC frequency range	10 – 400 Hz

Overall AC accuracy	+/-5% or better
DC precision	+/-0.1% of range
Analogue output range	+/- 3V
Corrected analogue output accuracy	+/-0.5% of range
Uncorrected analogue output accuracy	Probe dependent

Source: Lake Shore Cryotronics Inc advertising brochure, 64 East Walnut St. Westerville, Ohio 43081-2399

C Axial Hall Probe (to be used with 420 Gaussmeter)

Active area	0.030" diameter
Stem material	Fibreglass epoxy
Frequency range	DC and 10Hz to 400Hz
Corrected accuracy	+/- 0.15% to 3T
Operating temperature range	0°C to 75°C
Zero temperature coefficient	13μT/°C
Calibration temperature coefficient	=/_0.005%/°C

Source: Lake Shore Cryotronics Inc advertising brochure, 64 East Walnut St. Westerville, Ohio 43081-2399

D Infineon KSY 13/14 Hall sensors

The sensors KSY 13/14 are ion-implemented Hall generators made of mono-crystalline GaAs material. If the sensors are operated with a constant supply current, the output Hall voltages are directly proportional to magnetic fields acting on them. For each device the active area is 0.2mm x 0.2mm.

Electrical Characteristics at 25 °C for fields less than 500mT

Nominal supply current	5mA
Open circuit sensitivity	190-260 V/AT
Open circuit Hall voltage	95 – 130 mV
Ohmic offset voltage	less than |20| mV
Linearity	less than 2%
Input resistance at B=0T	900-1200 Ω
Output resistance at B=0T	900-1200Ω
Temperature coefficient of	0.1 – 0.18 %/K

Open circuit Hall voltage	-0.03 - -0.07 %/K
At B=0.1T	
Noise figure	~10dB

Data supplied from datasheet supplied by Infineon Technologies

APPENDIX B

Steel grades

Table containing chemical compositions by percentage weight of steel grades used.

Grade	C	Mn	Si	Nb	Ti	B
H559/6	0.134	0.79	<0.01	-	-	-
H595/1	0.072	1.42	0.12	0.052	-	-
H603/8	0.82	0.72	0.22	-	-	-
H603/9	0.82	0.72	0.22	-	-	-
H604/5	0.16	0.92	<0.01	0.024	-	-
H120/2	0.19	1.55	1.14	-	-	-
H618	0.13	1.22	0.287	-	-	-
H488/5	0.02	0.17	-	-	-	-
H483/3	0.007	0.17	-	-	0.06	
H639/2	0.04	0.25	-	-	-	0.002
3100	0.032	0.211	0.001	-	0.001	-

Information supplied from Corus.

APPENDIX C

Magnetic materials specifications

A Anisotropic sintered ferrite magnet specifications

These type of magnets can only be magnetised in the direction of the preferred magnetic axis.

MDL Grade	Remanence B_r (mT)	Coercive force, H_c (kA/m)	Intrinsic coercive force, jH_c (kA/m)	Maximum energy product, BH_{max} kJ.m^3	Magnetising force (minimum) (kA/m)	Maximum working temperature (°C)	Density (x10^3 kg/m^3)	Reversible temperature coefficient of Br% (°C), 20-100°C
FER1	220	136	220	8	600	250	4.8	-0.19
FER2	400	160	185	28	800	250	5.0	-0.19
FER 3d	350	155	160	24	800	250	5.0	-0.19
FER 3w	370	240	260	28	800	250	4.9	-0.19
FLEX6	163	110	240	4.5	800	75	3.7	-0.19
FLEX11	225	159	222	9.5	800	75	3.7	-0.19

Information supplied by Magnet Developments Ltd (MDL), Magnet House, Swindon,Wiltshire.

B Alcomax III (AlnicoV)

Magnetic properties

MDL Grade	Remanence B_r (mT)	Coercive force, H_c (kA/m)	Intrinsic coercive force, jH_c (kA/m)	Maximum energy product, BH_{max} kJ.m^3	Magnetising force (minimum) (kA/m)	Maximum working temperature (°C)	Density (x10^3 kg/m^3)	Reversible temperature coefficient of Br% (°C), 20-100°C
Alcomax III	1260	52	53	43	240	240	7.3	-0.02

Information supplied by Magnet Developments Ltd (MDL), Magnet House, Swindon,Wiltshire

Composition

Al	Ni	Co	Cu	Nb	Ti	B_r (T)	$(BH)_{max}$ kJm^{-3}	H_c (kAm^{-1})
8	12	23	3	0	0	1.2	41	46
9	16	26	4	1	0	1.3	44	52

Nominal compositions (% Weight) and magnetic properties of grade A2 permanent magnet alloys

Alnico V and Alcomax III are the USA and UK trade names for a grade A2 magnet.

Note: there are two sets of values corresponding to different manufacturers

Information supplied by M McCaig, 'Permanent Magnets in Theory and Practice', Pentech Press, 1987

APPENDIX D

RDP amplifier specification

Supply voltage	120 or 240V AC +10%, -22%, 47-400Hz
Output	+/-15V at 2A, limited at 2.2A
Load regulation	0.5% (10-90% Iout)
Supply regulation	0.2% (+10%/-15% Vin)
Ripple	20mV at full load
Input power	80W at full load

APPENDIX E

Matlab function to decouple lift-off and ferrite fraction

```
function [time,phase,dist, probe0,probe2]= phase_detect(inputs)

%     function [time,phase,dist]= phase_detect(inputs)

%      This algorithm takes in the raw data from the MagTran (
Probe0,
%     Probe1, Probe2) and separates percentage ferrite from lift-off
%     It is a 3 column matrix
%     The matrix caldata.dat contains the required calibration data
as
%     a series of column data
%     [Lift-off (mm)  (Probe0 x Probe1)/Probe1(average)(0%),
%     (Probe0 x Probe1)/Probe1(average)(100%),
%     (Probe2 x Probe1)/Probe1(average)(0%)
%     (Probe2 x Probe1)/Probe1(average)(100%)
%     m= col2-col1/col4 - col3]

%     VERSION 1.0
%     SHERRI JOHNSTONE
%     SCHOOL OF ENGINEERING
%     UNIVERSITY OF DURHAM



%     Define the measurements and display
probe0      =     inputs(:,1);
probe1      =     inputs(:,2);
probe2      =     inputs(:,3);
time        =     [0:0.1:length(inputs)./10]';
time        =     time(1:length(probe0));
figure(1)
plot(time,probe0)
xlabel('seconds');
ylabel('mV');
title('Probe0 raw')
figure(2)
plot(time,probe2)
xlabel('seconds');
ylabel('mV');
title('Probe2 raw')


%     Design  and apply low pass filter then display
[b,a]       =     butter(4,0.25);   %this gives a 2.5Hz -3dB point
probe0      =     filtfilt(b,a,mult0);
probe2      =     filtfilt(b,a,mult2);
figure(3)
plot(time,probe0)
xlabel('seconds');
ylabel('mV');
title('Probe0 filtered')
figure(4)
plot(time,probe2)
```

```
xlabel('seconds');
ylabel('mV');
title('Probe2 filtered')


%     initialise vectors to store fraction ferrite(phase) and
%     lift-off(dist)
dist=[]; phase=[];

%     give access to calibtation data (Table 10.5.1)
load caldata.dat

%     For each sample
%     a) check it is above the threshold for a coil to be present
%     b) calculate the gradient of the transformation curve at a
%     constant lift-off
%     c) locate the lift-off using the lookup table caldata.dat
%     d) calculate the 95% transformed value associated with the
%     lift-off curve
%     e) calculate the fraction transformed

for i = 1: length(probe0)

%     check that signal is above threshold at IP2 location
  if (probe0(i) > 124.5)

%     calculate the gradient of the transformation line
    gradient=(probe2(i)-caldata(1,4))./(probe0(i)-caldata(1,2));

%     check if out of range
      if(gradient < 0.7435)
       phase=[phase;phase(i-1)];
       dist=[dist;dist(i-1)];

%     check again to see if out of range
      elseif (gradient> 12)
       phase=[phase;0];
       dist = [dist;32];
    else

%     if in range locate the calibration gradient lines either side
      bottom      =     min(find(caldata(:,6)>gradient));
      top         =     max(find(caldata(:,6)<gradient));

%     interpolate to find actual lift-off
      x1          =     (gradient-caldata(top,6)).*caldata(bottom,1);
      x2          =     (caldata(bottom,6)-gradient).*caldata(top,1);
      diff  =     caldata(bottom,6)-caldata(top,6);
      dist  = [dist;((x1+ x2)./diff)];
```

```
%     Thus the percentage ferrite can now be calculated assuming
linear
%     relationship
      probe0_90   =    ((gradient-caldata(top,6)).*caldata(bottom,3)
      + (caldata(bottom,6)-
      gradient).*caldata(top,3))./(caldata(bottom,6)-caldata(top,6));

      range             =          probe0_90-caldata(1,2);
      phase             =          [phase; (probe0(i)-
      caldata(1,2))./ range.*0.9];

    end
 else phase = [phase;0];      dist  =     [dist;0];

 end

end


%     Display the results
figure(5)
plot(time, dist)
xlabel('seconds');
ylabel('distance mm');
title('Lift-off measurement')
figure(6)
plot(time,phase)
xlabel('seconds');
ylabel('% ferrite');
title('Percentage ferrite measurement')
```

APPENDIX F

Publications

Johnstone S, Peyton AJ, 'The application of parametric finite element modeling techniques to evaluate the performance of a magnetic sensor system', Sensors and Actuators A 93(2001) pp109-116

Johnstone S, Binns R, Peyton AJ, Pritchard W, 'Using electromagnetic methods to monitor the transformation of steel samples' Transactions of the Institute of Measurement and Control Vol23, No 1, 2001 pp21-29

Johnstone S, Binns R, Morris P, Peyton A, Pritchard W, 'Developments in the use of electromagnetic methods to monitor the transformation of steel samples', Presented at Institute of Materials Conference on 'Are you getting the most of your instrumentation',at Birmingham, May 2000.

Johnstone S, Binns R, Mallinson S, Meydan T, Peyton AJ, Walker T, Pritchard WDN, 'Using electromagnetic methods to monitor the transformation of steel samples' (Presented at Institute of Materials Conference, 'Measuring up to customers needs: Advances in on-line instrumentation for finishing processes in strip production' , London 27th April 1999)

ELSEVIER

Sensors and Actuators A 93 (2001) 109–116

SENSORS AND ACTUATORS A PHYSICAL

www.elsevier.com/locate/sna

The application of parametric 3D finite element modelling techniques to evaluate the performance of a magnetic sensor system

S. Johnstone[a,*,1], A.J. Peyton[b]

[a]*Teesside Technology Centre, Corus Research Development and Technology, PO Box 11, Eston Road, Middlesbrough TS6 6UB, UK*
[b]*Engineering Department, Lancaster University, Lancaster LA1 4YR, UK*

Received 27 October 2000; received in revised form 6 March 2001; accepted 29 March 2001

Abstract

This paper describes the application of parametric three-dimensional (3D) finite element analysis techniques to accurately model the response of a new industrial electromagnetic sensing system. The study focuses on a magnetic transformation detector for hot steel strip, which is capable of measuring the austenite-to-ferrite phase transformation fraction of hot steel on-line as the material cools below the Curie temperature.

This sensor presents several challenges with regard to modelling its response. First, small changes (~0.3 mT) in the measured magnetic field must be detected against a much larger background value (~160 mT). Second, the response of the sensor to variation in lift-off must be accurately determined so that changes in lift-off could be subsequently rejected using an appropriate compensation algorithm. Finally, an accurate model (error <0.2%) of the sensor was essential to avoid the need for extensive laboratory testing. The paper describes a number of approaches to address these issues.

The paper presents an overview of the sensor and its application, together with a summary of the models used. A number of different approaches were used to improve the accuracy of the modelling process including, mesh configurations, model definition and output calibration, which are also described. Outputs from the model are then compared with the measurement values.

This study demonstrates the feasibility of using calibrated simulations to describe the response of the sensor to the required accuracy and repeatability for symmetrical geometries. Further work is needed to assess the feasibility of the calibration method for more complex systems.

Keywords: Finite element; Phase transformation; Steel; Electromagnetic

1. Introduction

In recent years finite element modelling techniques have become widely accessible due to advances in both computer processing power and the available software tools. At the same time, research in this area has also produced more computationally efficient algorithms enabling simulations with greater detail and accuracy. Consequently, relatively complex systems can be now simulated in reasonable time periods and at a more affordable cost. In the steel industry for example, modelling work has been reported for the measurement and control of a number of key processes. These include, for instance, continuous casting systems [1–3] in order to improve the control of solidification process; and hot strip rolling for mechanical property prediction, including stress and strain modelling [4].

To date, research in the area of electromagnetic properties in hot strip rolling has been limited mainly to experimental work [5–9]. However, this experimental approach has severe limitations because a single application can involve calibrating the electromagnetic sensor system with a large number of steel products, with different gauges and chemical compositions, at a range of temperatures between 600 and 850°C and different lift-off values. This can be a lengthy and tedious procedure. Consequently, there is a need to use simulation techniques to reduce the size of the required measurement set in order to determine accurately the transfer function of the sensor system. Therefore, a combined simulation and measurement course can significantly reduce calibration time and cost. In this paper, some of the key issues associated with calibrating parametric three-dimensional (3D) finite element simulations of electromagnetic

* Corresponding author. Tel.: +44-191-374-3915; fax: +44-191-374-7492.
E-mail address: sherri.johnstone@durham.ac.uk (S. Johnstone).
[1] Present address: School of Engineering, University of Durham, South Road, Durham DH1 3LE, UK.

0924-4247/01/$ – see front matter
PII: S0924-4247(01)00647-1

sensor systems will be discussed and as a case study, a novel sensor will be examined. This sensor has been recently developed to measure the percentage phase transformation of hot steel strip as it cools [10].

2. Background

An overview of a hot strip mill is shown in Fig. 1. When hot steel strip leaves the last rolling stand, it is usually in the hot austenite phase. As it cools, it transforms to a ferrite type phase. The microstructure of this final phase and the temperature at which the ferrite starts forming, i.e. the transformation temperature are dependent on the composition and cooling rate. These are at present inferred by measuring the surface temperature of the strip using pyrometers in a limited number of positions and then applying mathematical models to deduce the progression of transformation along the run-out table. Unfortunately, temperature is only an assumed parameter, which is used to determine transformation. Work has been reported on electromagnetic transformation detectors, which have been realised using specialised coil arrangements [11,12]. However, with advances in material technology and magnetic field detection, the authors have researched the use of permanent magnets for on-line transformation detectors [9]. The sensor investigated consists of a C-shaped permanent magnet with a Hall probe to detect changes in the magnetic field, which in turn can be related to the percentage phase transformation of the steel. Low-cost and ease of maintenance are of prime importance when designing a commercial instrument in this environment. For phase transformation detection, the sensor is placed between steel rolls upon which steel strip of widths in excess of 1 m will travel as shown inset in Fig. 1.

The final magnetic circuit will involve all of the surrounding steel work including the rolls. Therefore, to calibrate the device, an identical structure needs to be produced in the laboratory so that every test position can be tested. This is costly and time consuming. In addition, it may not be possible to obtain the range of samples needed to produce a complete set of calibration data. A more simple option is to calibrate a simulation for each instrument using a single set of laboratory data and then applying the resulting calibration equation obtained to subsequent geometries. The work described in this paper considers some of the issues with calibrating such as, permanent magnet sensor system.

3. Physical principles

The sensor is a permanent magnet system, which can be defined using a demagnetisation curve. The magnetic field generated by the permanent magnet can be represented as follows [13]. Consider an element of hard magnetic material of area dS, length dL and magnetisation M. The associated magnetic dipole is $(M\,dL)\,dS$. This can be represented, in terms of a set of equivalent surface current densities, J_s, as a current loop dipole moment of $(J_s\,dL)\,dS$.

Therefore, for each element

$$J_s = M \tag{1}$$

By considering the vector potential A at a distance r from a current loop dipole it can be shown that a magnetised material can be represented as source volume, and surface current densities, J_v and J_s

$$J_v = \nabla \times M, \quad J_s = M \times a_n \tag{2}$$

In a two-dimensional (2D) simulation, the z-component of the vector potential is first calculated by solving the scalar Poisson equation

$$J_z(x,y) = \nabla \times \left[\frac{1}{\mu}\right] \nabla \times A_z(x,y) \tag{3}$$

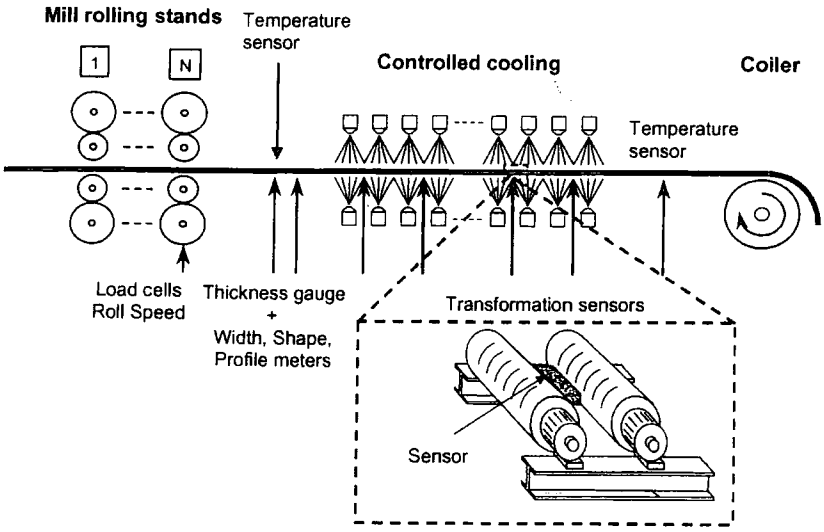

Fig. 1. Location of an on-line magnetic sensor.

where μ is the permeability. $\underline{B}$ and $\underline{H}$ are then calculated using

$$\underline{B} = \nabla \times A, \quad \underline{B} = \mu \underline{H} \tag{4}$$

In a 3D simulation, the magnetic fields are solved directly using the simultaneous field equations

$$\nabla \times \underline{H} = J, \quad \nabla \cdot \underline{B} = 0, \quad \underline{B} = \mu \underline{H} \tag{5}$$

4. Experimental

Commercially available components were used to provide a low-cost system with low maintenance costs and delivery times. The major components were an Alcomax III™ (see Appendix A) magnet, with standard locating holes through both of the poles, and a Lakeshore MMT-6J02-VG Hall probe, which was situated on one pole face. The diameter of the probe was about 1 mm and located such that it measured the $\underline{B}$-field perpendicular to the pole face. The probe could not be placed at the pole centre due to the presence of the locating hole. The output from the Hall probe was conditioned firstly by a Lakeshore model 420 Gaussmeter and then through two stages of amplification using RDP type 611 dc amplifier modules. These stages were used to reduce the large background field (~160 mT) and amplify the much smaller changes due to the presence of the test sample. The apparatus is shown in Fig. 2.

Experiments were performed to determine the noise levels and the characteristic of the Hall probe with distance from the steel sample (lift-off) when fixed in one position. The results including the 'no sample' case are shown in Table 1.

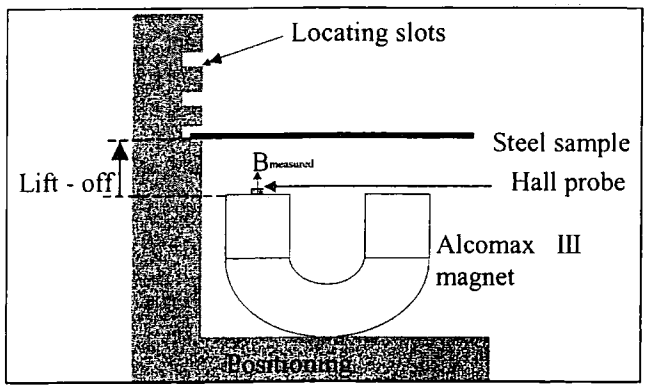

Fig. 2. Experimental apparatus.

Table 1
Noise levels of the Hall probe at varying lift-offs

Lift-offs (mm)	Mean of B-field (mT)	S.D. of B-field (mT)
65	162.4	<0.1
75	161.1	<0.1
85	160.6	<0.1
No sample	159.5	<0.1

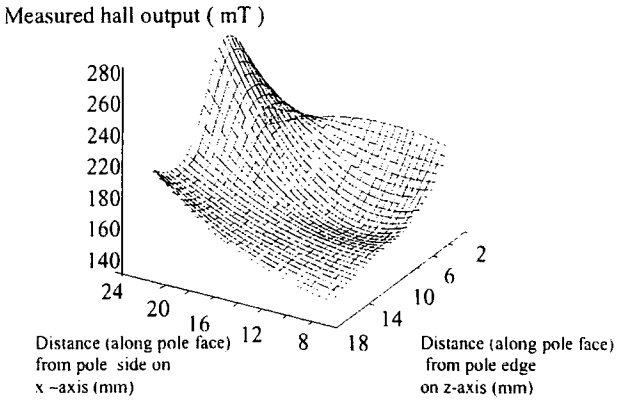

Fig. 3. Measured Hall output as a function of pole position.

The range was defined as the difference between the mean output with a fully transformed sample at a lift-off of 65 mm and when no sample was present. It was found to be 2.9 mT and less than 2% of the range. The noise levels were well below 0.1 mT and there was negligible drift. Temperature effects were not investigated at this stage. Calibration factors to correct for thermal drift were determined in later tests.

The lift-off characteristics for the Hall probe in different positions on the pole face were also examined. A typical set of results is shown in Fig. 3, which plots the output from the Hall probe amplifier with a fully transformed test sample at 40 mm lift-off. As can be seen the lift-off characteristic is a function of the Hall probe position.

The errors associated with positioning the Hall probe were also investigated by placing the probe several times on each element and noting the mean and standard deviation (S.D.). The S.D. ranged from 1.2 to 2.4% of the mean reading depending on probe location. However, when compared to the range of 2.9 mT (i.e. 0–100% transformation at the nominal lift-off of 65 mm) the S.D. was far in excess of 100% of the actual signal range. This experiment shows the importance of securely positioning the Hall probe and gives an indication of the accuracy required from the simulations.

5. Simulation

The challenge in producing realistic simulations was to be able to simulate changes in the normal pole face $\underline{B}$-field of less than 0.2% (10% of the range defined by the experiments).

5.1. Full 3D simulation

One of the first models created is shown with the corresponding $\underline{H}$-vectors in Fig. 4. In this case no attempt was made to exploit the symmetry of the problem. The magnet consisted of three parts a positive pole, a negative pole and a main body. A function was used to sweep the direction of magnetisation around the main body and the magnetisation curve for Alnico V™ (see Appendix A) was used for all the

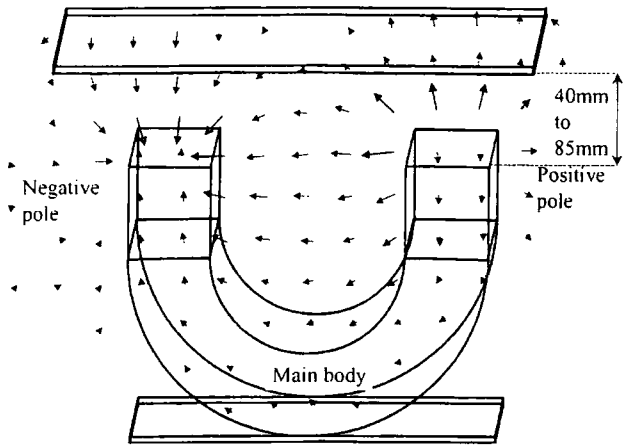

Fig. 4. 3D finite element model.

magnet components. In the experiment, the magnet had locating holes, however, for simplicity these were not included in the initial stages. The Hall probe was defined as a box of side 1 mm 'measuring' the average $\underline{B}$-field normal to the pole face using Eq. (6).

$$B_{av} = \frac{\int_{surface} \underline{B} \cdot d\underline{S}}{\int_{surface} d\underline{S}} \quad (6)$$

To investigate the FE model validity, the symmetry of the $\underline{B}$-field was examined using a mesh size of 106,022 elements. The resulting $\underline{B}$-field across the centre-line direction from the positive to negative pole is shown in Fig. 5. It shows a slightly non-symmetrical nature. To allow for a closer examination, the average $\underline{B}$-field was compared at symmetrical locations on each of the pole faces. The results are shown in Fig. 6. At elements towards the pole centre, differences of up to 15% are present. Towards the edge of the poles the errors are even greater because of the larger field gradients. These results therefore, show that even with large mesh sizes (100,000 tetrahedra), the full model was not accurate enough to symmetrically simulate this problem.

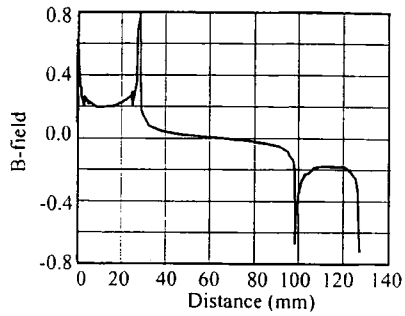

Fig. 5. Normal $\underline{B}$-field across pole centre-line.

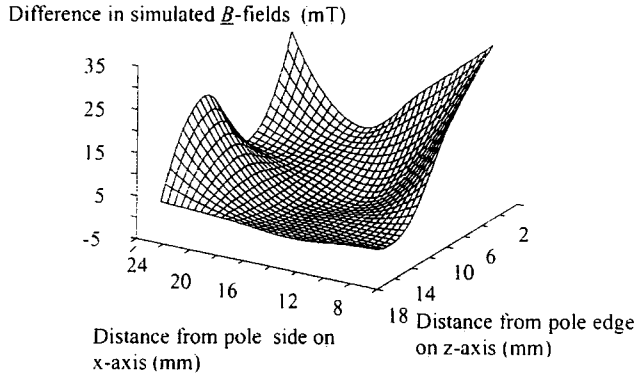

Fig. 6. Simulation errors between poles in full model.

5.2. Quarter model

To reduce the complexity of the model, symmetry was used to reduce it to a quarter model as shown in Fig. 7. The diagram also shows a hole through the pole face. Initially, new meshes were created for the sample in different locations. However, the errors due to different mesh sizes and configurations gave inconsistent results. To overcome this the model was set-up with test pieces in all the required locations. The permeabilities of these pieces could then be varied to define whether they were present in a particular

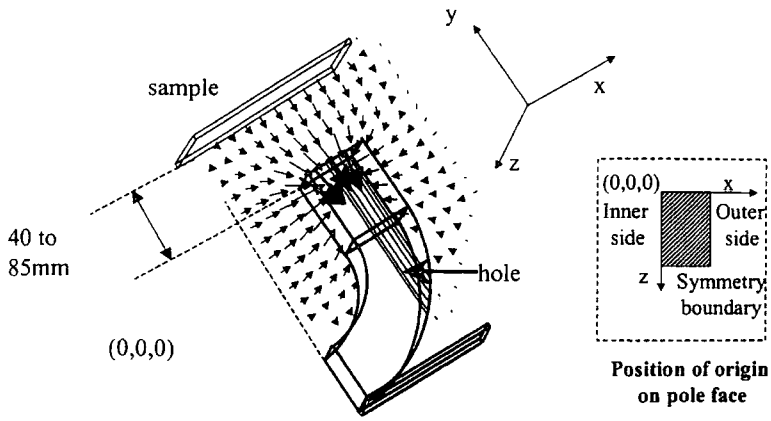

Fig. 7. Quarter finite element model.

Table 2
Comparison of simulated Hall probe field (mT) for different mesh sizes and lift-offs at probe position, $x = 12.5$ mm, $z = 17.5$ mm

Lift-off (mm)	Mesh size		
	25,685	27,879	30,315
40	192.8844	192.6347	192.3930
45	186.1892	186.1280	185.8884
50	181.1310	181.0656	180.8296
55	177.1629	176.7772	176.8576
60	173.9949	173.8694	173.6924
65	171.1001	171.2683	171.1366
70	169.3608	169.1473	169.1198
75	167.6275	167.4261	167.2653
80	166.0524	165.8571	165.8200
85	164.8478	164.6460	164.6246

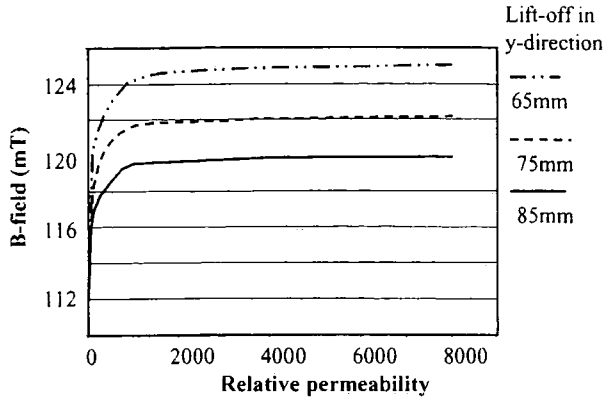

Fig. 9. Effect of changing the permeability of the test sample.

set-up, i.e. to make them invisible a relative permeability of one was chosen. The mesh could then be set-up for one scenario and subsequently transferred to all the others.

5.3. Defining mesh size

A quarter model with no hole was solved for three different mesh configurations. Some of the results for position $x = 12.5$ mm, $z = 17.5$ mm, are shown in Table 2. Variations of less than 0.01% of the simulated reading were observed between corresponding scenarios with different mesh configurations. This corresponds to about 1% of the simulated range (defined to be the difference between the test sample at 65 mm and when no sample is present). Another factor in determining an appropriate mesh size is the quantisation error in the pole region. Fig. 8 shows the normal $\underline{B}$-field characteristic along the x-axis for mesh size 30,315. The quantisation effect has given a discontinuity of about 0.8 mT at the element boundary.

These results show that with meshes containing between 25,000 and 35,000 elements, the mesh must be identical if different scenarios are to be compared. Considering the Hall probe as an area rather than a point does act to reduce the effect of these discontinuity errors. Decreasing the element size in this area will act to reduce these errors but requires considerably more computing power.

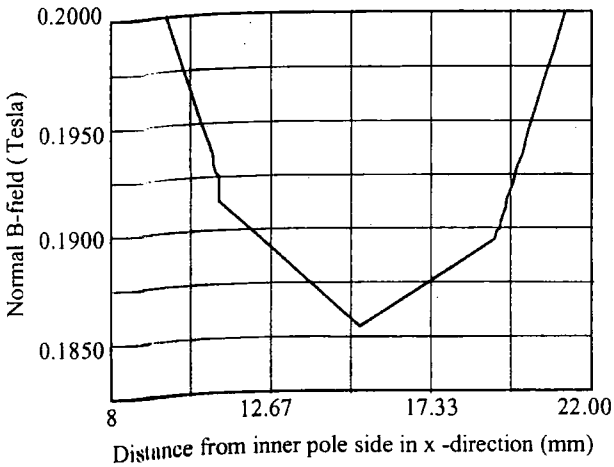

Fig. 8. Quantisation effect of meshing.

5.4. Defining the test piece

The relative permeability and conductivity of the test piece were only known approximately from [14] and can be in the region of 1000–10,000 depending on composition and processing. Therefore, the first aim of the simulation was to identify a suitable maximum permeability for the test samples. Fig. 9 shows that changing the relative permeability from 2000 to 8000 accounts for about 0.2% of the simulated reading. Therefore, a value of 2000 was chosen as the upper limit.

5.5. Calibration of simulation

As this part of the investigation a quarter model with a hole was simulated using 35,176 elements. Simulations were carried out to determine the lift-off characteristics for Hall probes in different positions on the pole faces. A typical set of results is shown in Fig. 10. To check the validity of the

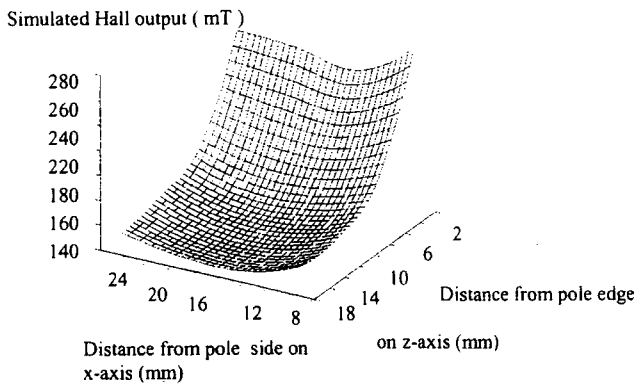

Fig. 10. Simulated value of the Hall probe output in the x- and z-directions.

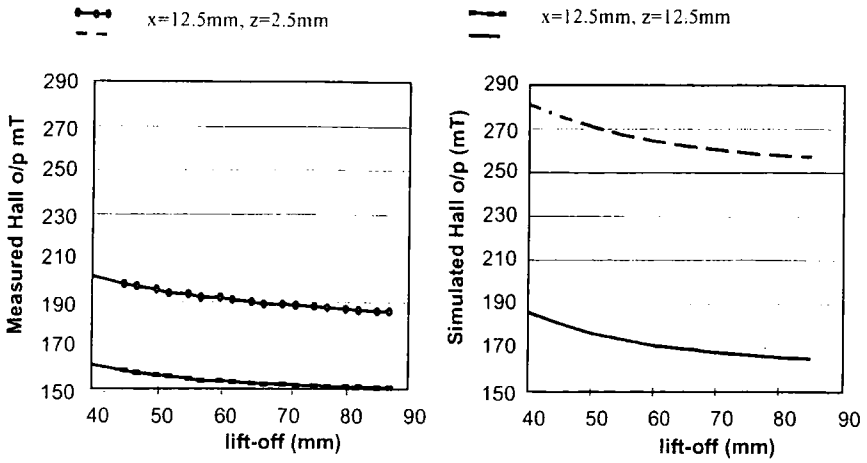

Fig. 11. Simulated and measured lift-off characteristic.

simulation, the measured (Fig. 3) and simulated (Fig. 10) x- and z-characteristics were compared. The z-traces show the same general trends but the measured data shows some excursions. This is probably due to the magnet not having completely homogeneous properties as assumed in the simulation. This non-homogeneity is more obvious when considering the traces in the x-direction. In this case, the simulated and measured data show very different trends. It can also be seen that the sensitivity of the $\underline{B}$-field to location is greater at the pole edges.

Table 3
Variation of simulation error with position

x-Position (mm)	z-Position (mm)	Mean absolute error (mT)	
		Before calibration	After calibration
7.5	17.5	30.13	0.13
12.5	2.5	38.32	0.39
12.5	7.5	26.44	0.26
12.5	12.5	11.02	0.10
12.5	17.5	11.47	0.08
17.5	17.5	2.73	0.38
22.5	17.5	15.01	0.36
17.5	2.5	42.77	0.46
17.5	7.5	2.01	0.24
17.5	12.5	1.89	0.31

Table 4
Calibration data for finite element model

x-Position (mm)	z-Position (mm)	Regression		
		Scaling factor (4 dp)	Offset constant (4 dp)	R^2
7.5	17.5	0.4680	56.5220	0.998
12.5	2.5	0.6530	18.5656	0.995
12.5	7.5	0.5002	56.5913	0.994
12.5	12.5	0.4592	76.9895	0.999
12.5	17.5	0.4716	73.2757	0.999
17.5	17.5	0.4358	99.7165	0.989
22.5	17.5	0.4198	134.9950	0.991
17.5	2.5	0.3960	82.3538	0.986
17.5	7.5	0.3821	115.5202	0.994
17.5	12.5	0.4485	93.1881	0.992

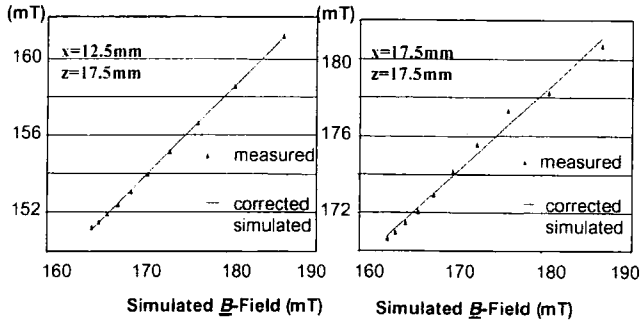

Fig. 12. Regression fits for two typical locations on the pole face.

The lift-off characteristics were then compared. Typical traces are shown in Fig. 11. For each element the simulated and measured data showed the same trend, however, the mean absolute errors varied upon pole location with the greatest errors being observed at the pole sides as shown in Table 3. To reduce the errors a linear regression was applied to the data for each pole element. Table 4 indicates R^2-values corresponding to good fits. Typical graphs are shown in Fig. 12. The number of points used was limited since the test pieces could not overlap in the model. From these results it was concluded that general scaling and offset factors could not be applied to the whole pole face but could be applied to individual elements.

6. Discussion

This investigation has highlighted some of the main issues with obtaining an accurate repeatable simulation of the experiments. A method has been identified in which the use of a single mesh configuration for all scenarios to be compared is a key factor when using only moderate mesh sizes. The results show that it is not possible to simulate the

actual response to within 0.2%, as required, without calibration factors, for the mesh sizes investigated. This is thought to be mainly due to the magnet not being completely homogeneous as assumed in the model. This will be partly due to the material itself, but probably also due to the magnetisation process in which the location hole will act to distort the field alignment. Other errors include not knowing the exact location of the probe especially at the pole edges where the sensitivity to position is high and also the imprecise knowledge of the test samples. Increasing the mesh size may reduce the quantisation errors but will not improve on the errors due to assumptions made in modelling the experiments.

The measured and simulated data have a highly linear relationship when individual elements are compared. The degree of linearity is dependent on position and can give errors up to 13% of the range. Further investigation is required to assess whether this is due to the mesh configuration or if optimum elements can be identified to give the most accurate simulations for a particular system. However, the data does show that a calibrated element can be used to predict the normal $\underline{B}$-field to within 0.2% as required. Further work is needed to assess whether this method is still valid for more complicated geometries.

7. Conclusions

This paper has described the use of parametric, 3D finite element simulation techniques to analyse the response on a magnetic transformation meter developed for use in the steel industry. The study has shown that the raw simulation results are not accurate enough to simulate the experiment to within the required 0.2%. This is mainly due to the assumptions made in the model. However, scaling and offset factors can be used to calibrate the finite element simulation to give errors less than 0.2% provided the mesh configuration and Hall probe locations are not changed, a fixed mesh pattern is used to switch test pieces switched in and out using their material properties, and symmetry is fully exploited.

It can therefore be concluded that a calibrated finite element model for simple geometries can simulate the permanent magnet system. Further work is needed to assess the validity of this method for more complicated geometries.

Acknowledgements

The author wishes to thank Ansoft Corporation for providing the software, Ansoft Maxwell™, and associated technical support required to undertake this investigation.

Appendix A.

Alnico V™ and Alcomax III™ are the USA and UK trade names for a grade A2 magnet the properties of which are given below in Table 5 [15].

Table 5
Nominal compositions (wt.%) and magnetic properties of grade A2 permanent magnet alloys

Al	Ni	Co	Cu	Nb	Ti	B_r (T)	$(BH)_{max}$ (kJ m^{-3})	H_c (kA m^{-1})
8	12	23	3	0	0	1.2	41	46
9	16	26	4	1	0	1.3	44	52

Note: there are two sets of values corresponding to different manufacturers.

References

[1] E. Takeuchi, M. Zeze, H. Tanaka, H. Harada, S. Mizoguchi, Novel continuous casting process for clad steel slabs with level dc magnetic field, Iron making Steel making 24 (3) (1997) 257–263.
[2] T. Toh, E. Takeuchi, M. Hojo, H. Kawai, S. Matsumura, Electromagnetic control of initial solidification in continuous casting of steel by low frequency alternating magnetic field, ISIJ Int. 37 (11) (1997) 1112–1119.
[3] M. Nakada, S. Okimoto, T. Meikan, S. Kumagai, S. Nishioka, T. Osako, Initial solidification control in horizontal continuous casting using high frequency magnetic field, NKK Tech. Rev. 77 (1997) 14–17.
[4] A. Howe, F. Beckitt, Z. Hussain, D. Farrugia, P. Ingham, G. Watts, Control of microstructure and properties of wrought transformable steels', European Commission Technical Steel Research Report, EUR 14789 EN, 1997.
[5] J.F. Bussiére, On-line measurement of the microstructure and mechanical properties of steel, Mater. Evaluation 44 (1986) 540–564.
[6] É.V. Aronson, G.V. Bida, V.M. Kanardin, M.N. Mikheev, L.Z. Samokhvalova, Possibility of magnetic testing of the impact strength of low-carbon and low-alloy steel rolled products, Defektoskopiya 6 (1978) 66–72.
[7] R. Langman, Measurement of the mechanical stress in mild steel by means of rotation of magnetic steel strength, NDT Int. (1981) 255–262.
[8] U. Fiedler, M. Kroning, W.A. Theiner, Non-destructive evaluation of material parameters using neural networks, Mater. Sci. Forum 210–213 (1996) 343–348.
[9] S. Johnstone, R. Binns, A.J. Peyton, W.D.N. Pritchard, Using electromagnetic methods to monitor the transformation of steel samples, Trans. Inst. Measurement Control 23 (1) (2000) 21–29, submitted for publication.
[10] S. Johnstone, A.J. Peyton, R. Binns, P. Morris, W.D.N. Pritchard, Developments in the use of electromagnetic methods to monitor the transformation of steel samples, in: Proceedings of the Conference on Are You Getting the Most of Your Instrumentation?, Institute of Materials, Midlands Engineering Centre, Austin Court, Birmingham, UK, 2000.
[11] Detection on-line du point de transformation alpha-gamma, European Commission Technical Steel Research Report, IRSID, MCA RCA 91318, 1991.
[12] M. Morita, K. Hashiguchi, O. Hashimoto, M. Nishida, S. Okano, On-line transformation detector for property control of hot rolled steel, in: Proceedings of the Metallurgical Society of AIME Symposium on Accelerated Cooling of Steel, Pittsburgh, 1985.
[13] P.P. Sylvester, R.L. Ferrari, Finite Elements for Electrical Engineers, Cambridge University Press, Cambridge, 1983.
[14] R.C. Weast, CRC Handbook of Chemistry and Physics, CRC Press, Boca Raton, 1986.
[15] M. McCaig, Permanent Magnets in Theory and Practice, Pentech Press, Plymouth, 1987.

Biographies

S. Johnstone obtained a BSc (Hons) in electronics from Durham University in 1992. She then worked in the Research and Development function at Corus (formerly British Steel) for 8 years where she has specialised in developing and implementing new and novel measurement solutions for the steel making process. In 2001 she returned to Durham University as a lecturer. Her main research interests include sensor systems and instrumentation with particular emphasis on material property measurement using electromagnetic methods.

A.J. Peyton graduated with a BSc (Hons) in electrical engineering and electronics from UMIST, 1983. He received his PhD in medical instrumentation from UMIST, 1986 and then went on to work for Principal Engineering Kratos Analytical Ltd. until 1989 where he developed precision electronic instrumentation systems for magnetic sector and quadruple mass spectrometers. He returned to UMIST as a lecturer in 1989 and moved to Lancaster University in 1996 to take up the post of senior lecturer. His main research interests include instrumentation, sensor systems, and in particular electromagnetic systems for imaging inspection and tomography.

Transactions of the Institute of Measurement and Control 23,1 (2001) pp. 21–29

Using electromagnetic methods to monitor the transformation of steel samples

S. Johnstone[1], R. Binns[2], A.J. Peyton[2] and W.D.N. Pritchard[1]

[1]Teesside Technology Centre, Corus UK, Teesside TS6 6UB, UK
[2]Engineering Department, Lancaster University, Lancaster LA1 4YR, UK

This paper describes several electromagnetic sensing arrangements for measuring the percentage of austenite, which has transformed into ferrite in hot rolled steel as it cools. The results from laboratory experiments are presented. These indicate that all the sensors produce outputs, which are associated with the percentage transformation. Using the knowledge gained from this work it is proposed to build an on-line trial sensor for use in a hot strip mill.

Key words: austenite; electromagnetic; ferrite; phase; steel; transformation.

Introduction

In the production of steel strip, the temperature distribution and cooling rates along the mill run-out table have a significant effect on the steel microstructure and hence on final material properties of the strip such as tensile and impact strengths. Consequently, demands for improved product consistency and an increasing diversity of sophisticated steel grades have increased the requirements for tighter control of these process conditions.

Traditionally, the cooling rate is controlled by measuring the surface temperature of the steel strip after it has been hot rolled and then applying large quantities

Address for correspondence: S. Johnstone, Teesside Technology Centre, Corus UK, P.O. Box 11, Eston Rd, Grangetown, Middlesborough TS6 6UB, UK.

 0142-3312(01)TM006OA

of water to both the top and bottom surfaces of the steel. The temperature is measured using noncontacting optical pyrometers due to the high temperature of the strip, which is usually in the range of 500–1000°C. Unfortunately, obscuration due to steam and surface emissivity irregularities adversely affect the accuracy of these sensors. The optical pyrometers are therefore positioned outside the quenching zone and mathematical models are used to interpolate the condition of the steel strip during cooling. In addition, temperature is only used as an assumed indicator of microstructure and only the surface of the steel is measured. Ideally, the control of cooling rate should take account of the progress of the change in microstructure, i.e., the dynamic transformation at a particular point rather than the strip temperature alone. A transformation monitoring system used in conjunction with optical pyrometers, as shown in Figure 1, would therefore represent a significant step forward in this respect.

Phase transformation

Steel consists primarily of iron and a low percentage of carbon which is typically less than 0.8%. The phases of this binary system are shown in Figure 2. When a hot steel strip leaves the last rolling stand, it is usually in the hot austenite phase. As it cools, it transforms firstly to the ferrite phase and finally to a combined ferrite and cementite phase (Bozorth, 1951). The microstructure of this final phase and the temperature at which ferrite starts forming (the transformation temperature), are dependent on both the percentage of carbon present and the rate of cooling. Figure 3 shows the effect of cooling rate on the austenite-to-ferrite transformation temperature for a pearlitic steel.

Background

A number of approaches have been proposed and studied for monitoring transformation on-line, including X-ray diffraction (Kitagawa and Sohmura, 1983), X-

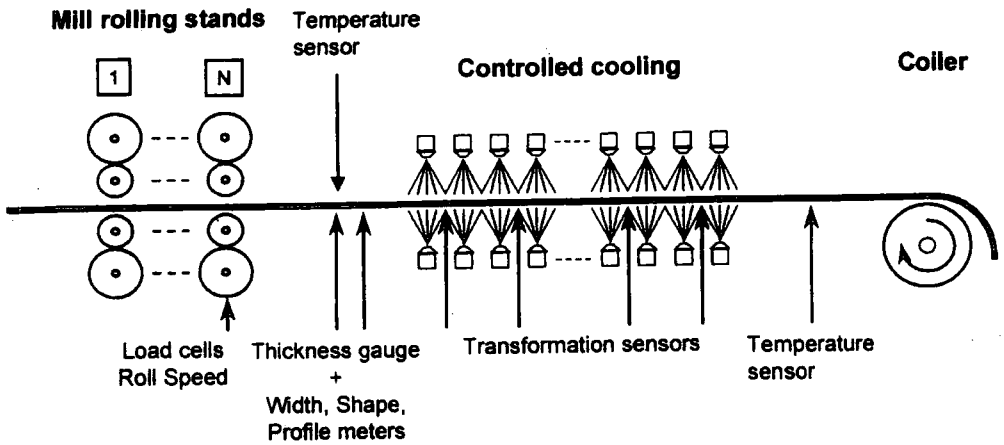

Figure 1 Schematic of a hot strip mill

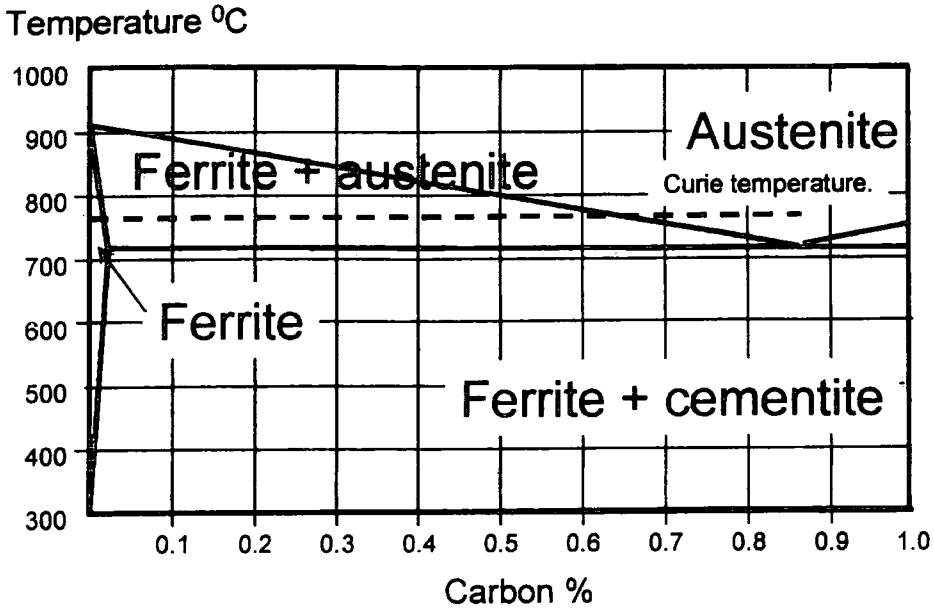

Figure 2 Iron–carbon phase diagram

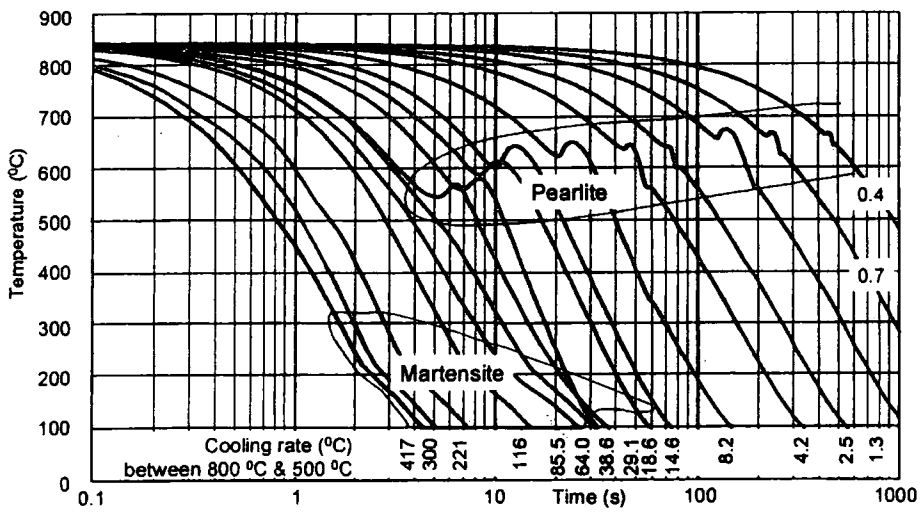

Figure 3 Continuous cooling diagram for a pearlitic steel

ray attenuation to monitor density change (Gaujé, 1990), laser ultrasonics, thermal (Bodin and Marchal, 1994) and electromagnetic.

The electromagnetic technique was chosen for this development because it has several potential advantages. The magnetic field is unaffected by water and any nonmagnetic material used to protect the sensor. In addition, the field acts at a distance and requires no contact with the hot strip.

Any transformation monitoring system requires a multi-sensor array, which will

be situated in a hostile environment. Therefore, each sensor head should be low cost, robust and easily maintainable. The electromagnetic technique was considered to fit this remit.

There are several reports of the successful use of electromagnetic sensors to monitor transformation both in the laboratory and on the run-out table (Ishibashi *et al.*, 1987; Morita *et al.*, 1987; Kim *et al.*, 1990; Yahiro *et al.*, 1990).

Measurement principle

It is well known that the electromagnetic properties of steel change significantly as the material progresses through transformation (Bozorth, 1951). The austenitic phase is always paramagnetic but the ferritic phase is only paramagnetic above the Curie temperature and is always ferromagnetic below. The Curie temperature is usually around 770°C but depends on the chemical analysis of the steel. Any austenite to ferrite transformation occurring below the Curie temperature may therefore be detected by the ferromagnetic transformation of the ferrite.

In an equilibrium state the iron–carbon phase diagram shows that, for steels with a carbon content less than 0.6%, the austenite-to-ferrite transformation starts above the Curie temperature (see Figure 2). The ferrite thus formed is paramagnetic and cannot be detected magnetically. However, in practice, accelerated cooling systems on the run-out tables of strip mills can reduce the austenite-to-ferrite transformation temperatures to below the Curie temperature as shown for the pearlitic steel in Figure 3. Thus microstructural changes can be detected and monitored using magnetic sensors. The phase transformations have been previously studied using thermal analysis techniques (Bodin and Marchal, 1994).

Experiments

Laboratory experiments have been conducted using a number of electromagnetic sensors operating at d.c. and excitation frequencies including 1 kHz, 10 kHz, and 1 MHz. To date, there are very few reports of the electromagnetic properties of hot steel during transformation and there are even fewer reports conducted at different frequencies. Figure 4 shows a typical test set-up, including the lift-off,

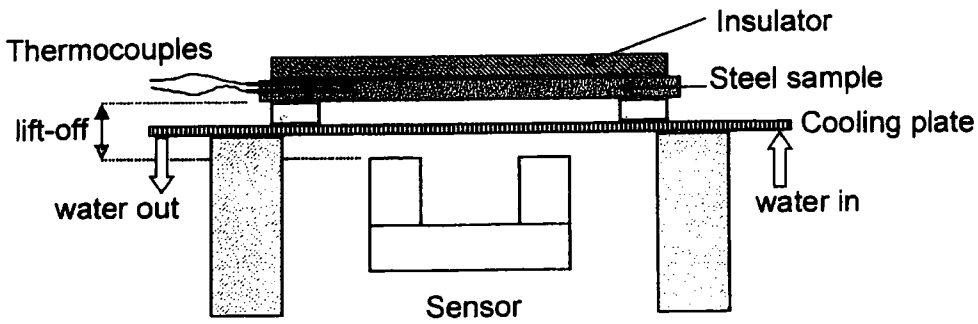

Figure 4 Experimental set-up

the cooling plate, and a C-cored based sensor. Figure 5 illustrates the difficulties with the actual mill location, which include space limitations, the effects of magnetic coupling to the rollers, lift-off variations and the effects of Faraday induction in the fast moving strip.

The effects of lift-off were measured and simulated using parametric finite element (FE) analysis (Maxwell, Ansoft Corp.) in order to determine the most appropriate sensor geometries. Figure 6(a) illustrates some of these results and shows the effects of lift-off for two d.c. electromagnetic sensor designs. The pole gap is one of the most important factors, and generally as the pole gap increases, so does the lift-off response (Macovschi and Poupot, 1990). In practice, space limitations between the rollers will limit the pole gap and hence determine the maximum lift-off. Figure 6(b) shows the lift-off characteristic of a permanent magnet-based sensor with a pole gap of 115 mm.

As an initial approximation, the percentage transformation is assumed to be proportional to the output voltage at a known lift-off. If the arrangement shown in Figure 6(b) is considered at a lift-off of about 40 mm, it would have to be stable to better than 0.1% of its full scale output to resolve a 5% change in transformation. Such a long-term stability would be quite demanding; however, a practical system could use an auto-zero technique in between strip runs to compensate for offset drift.

Figure 7 shows results obtained from a low-carbon steel with a Hall probe, measuring a d.c. magnetic field, and a 1 MHz Kaman (type 10CU) eddy current probe, arranged such that there was no interaction between them. Clearly, both probes register the transformation. The output of the eddy current device reduces after transformation due to the change in relative permeability, which is a complex function of both temperature and frequency. The eddy current sensor is also affected to a lesser extent by the resistivity of the steel, which also changes during transformation.

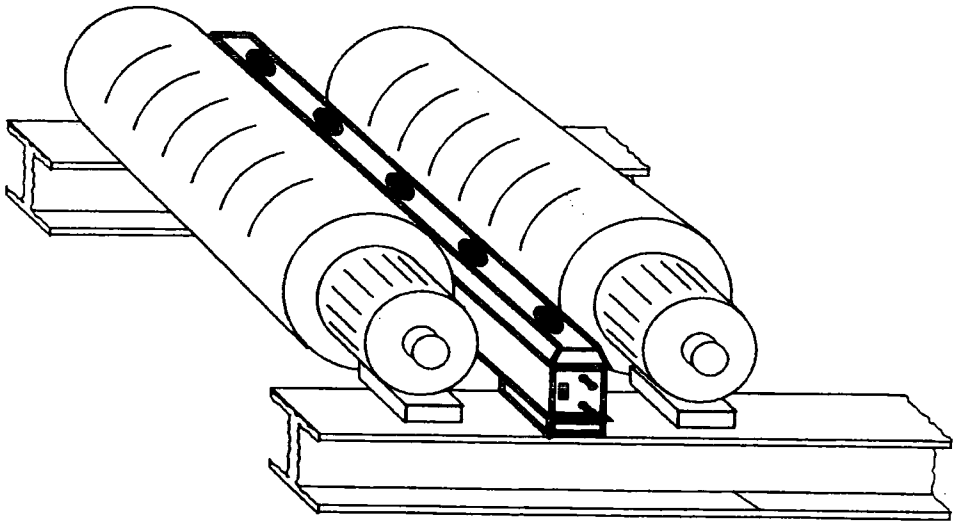

Figure 5 Proposed sensor array in mill

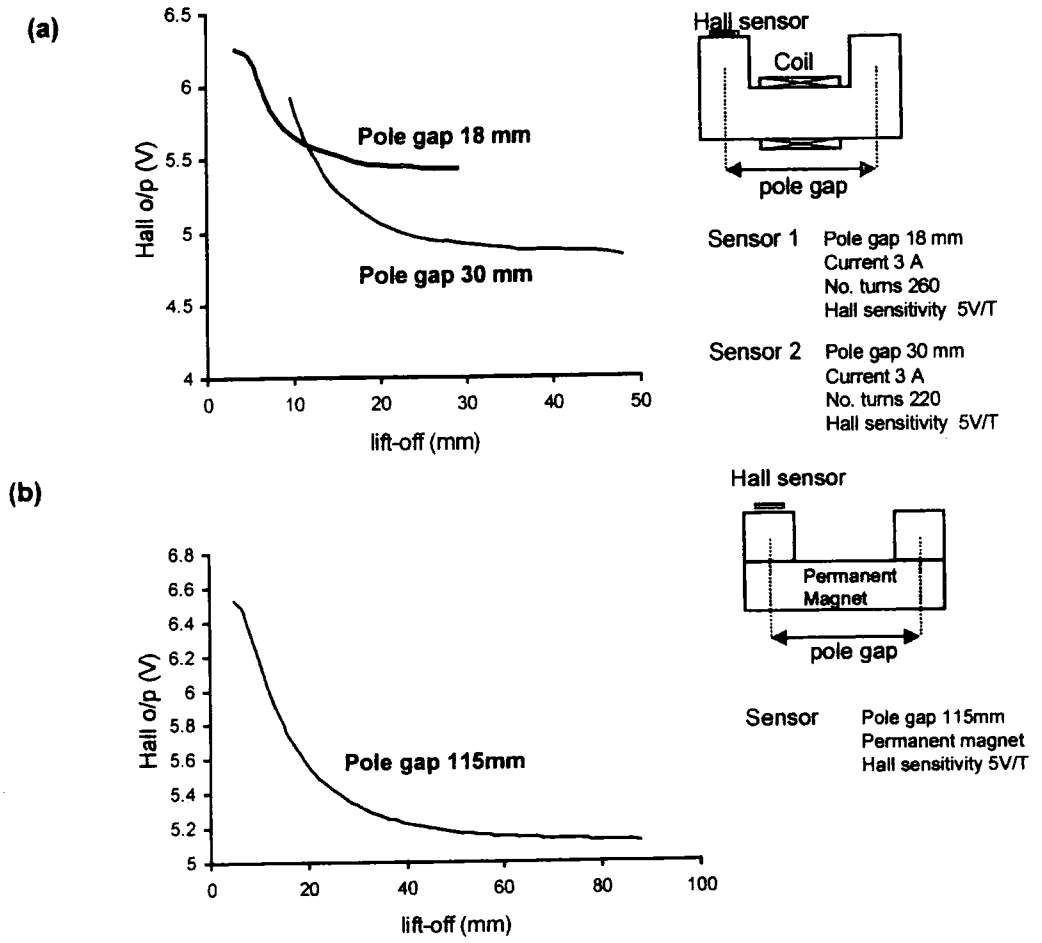

Figure 6 Effects of lift-off

Figure 8 shows the outputs of a different eddy current sensor based on the transformer principle at frequencies of 1 and 10 kHz, on a similar steel sample. These frequencies were chosen such that they were:

1) high enough to produce a measurable output;
2) separated enough to identify trends;
3) low enough for the magnetic field to penetrate sufficiently into the steel sample.

The in-phase coupling is shown in Figure 8(a), which displays similar curves to the previous graph. Note at 10 kHz, the coupling starts to reduce after transformation; this effect was also seen more distinctly for the 1 MHz Kaman sensor.

The quadrature (90°) component of the coupling is shown in Figure 8(b). This component is caused by any eddy current and magnetization losses in the steel. The quadrature component passes through a maximum during transformation when the relative permeability rapidly increases. This causes the skin penetration depth to reduce and, when the skin depth is comparable to the thickness of the

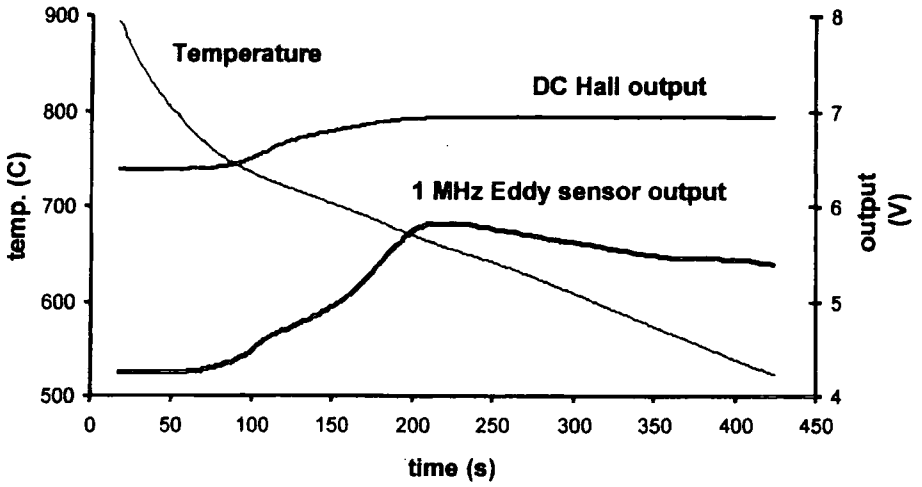

Figure 7 Test results from d.c. and 1 MHz sensors

steel sample, the eddy current losses are a maximum. Both curves also contain a minimum at approximately 740°C. Below this temperature, the magnetization losses increase especially at the higher frequency of 10 kHz. A plot of the simulated sensor response versus permeability using a two-dimensional model is shown in Figure 8(c), that confirms the trend for the in-phase component.

Discussion

A selection of results from laboratory experiments on steel samples, with a range of excitation frequencies from d.c. to 1 MHz has been presented. All the experiments yielded responses indicative of the transformation effects and further confirm the potential of this approach.

The choice of sensor design to pursue is application dependent. The d.c. type device has the potential of measuring the average percentage phase transformation through the steel strip. It would therefore be suitable for a thin strip (2–5 mm).

The a.c. types only have the potential to measure the transformation of the outer skin of the steel as determined by the frequency. This could be suitable for thicker steel plate (10 mm or higher), where an average value would yield limited information due to differing transformation rates between the centre and surface of the plate.

Each steel type will have its own transformation curve. In order to implement any of the sensor designs, further work is required in understanding and defining the relationship between the sensor outputs and these curves.

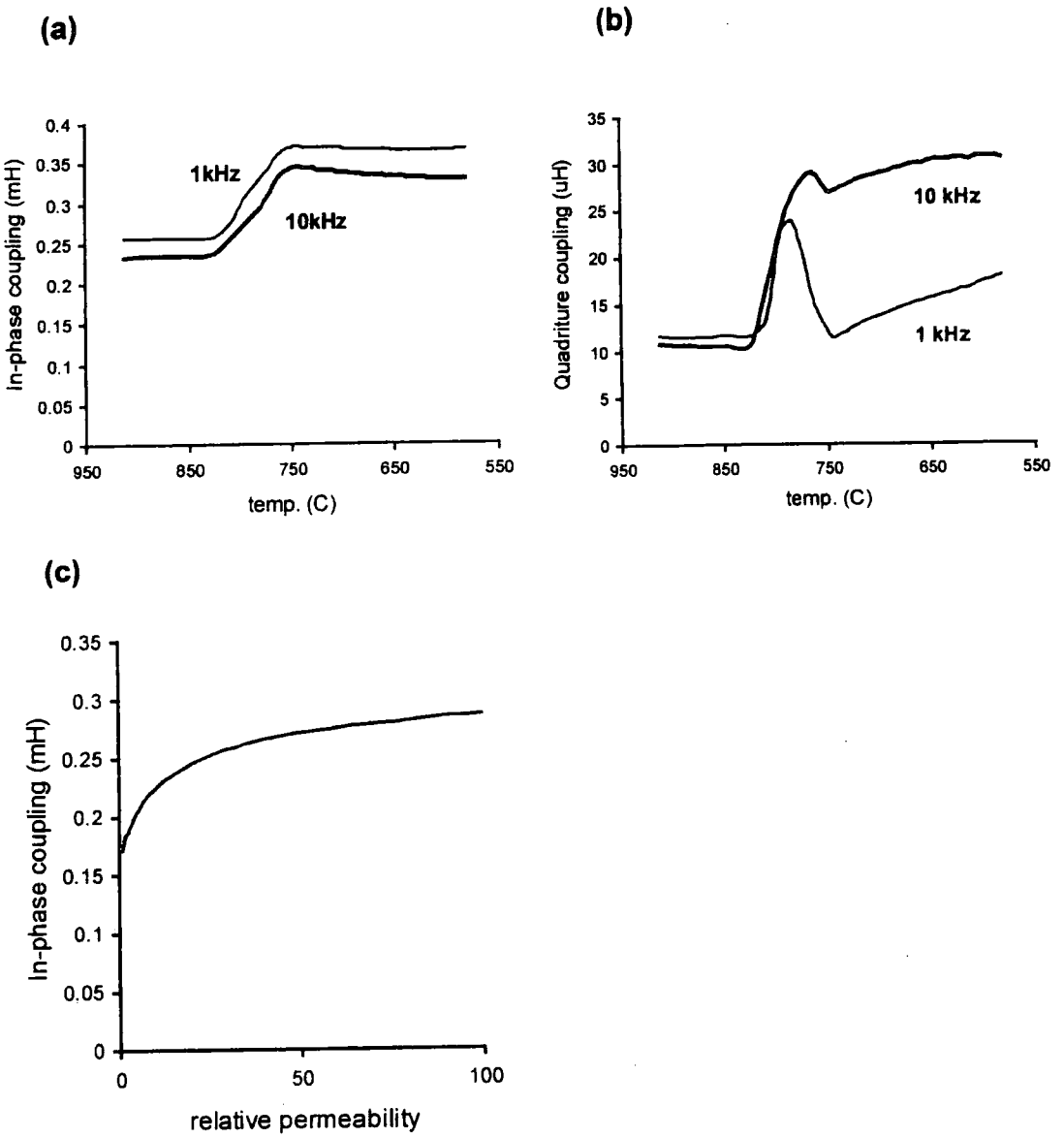

Figure 8 Response of a two-coil eddy current sensor at 1 and 10 kHz

Conclusions

The present method of controlling the microstructure and hence mechanical properties of steel is to measure the surface temperature of the strip using optical pyrometers and use mathematical models to calculate the amount of cooling required. Temperature is an indirect measurement of microstructure and has limited accuracy due to the environment.

Several other methods of measuring phase transformation on-line have been considered. Electromagnetic methods were found to be potentially most suited to the environment and of lowest cost.

Laboratory tests indicated that all the sensor configurations gave responses indicative of phase transformation.

The sensor design to pursue is application dependent. Direct current and low frequency devices are more suitable for thin products whereas higher frequency sensors could be used for thicker products.

The relationship between sensor outputs and each steel grade output would need to be researched for any of the sensor designs.

The results of this research have given the authors sufficient confidence to build an on-line unit for test measurements at a hot strip mill.

Acknowledgements

The authors would like to thank S. Mallinson, Mallinson Eng, T. Walker, Lancaster University, and T. Meydan, Cardiff University, for their contributions in this project. The authors would also like to thank Dr R.B. Smith, Research Director, Teesside Technology Centre, Corus UK for permission to publish this paper which was originally presented at the IoM conference on 'Measuring up to Customer Needs' in April 1999.

References

Bodin, A. and **Marchal, P.D.** 1994: The use of thermal analysis techniques for the validation of phase transformation models. *Steel Research* 65, 103–9.

Bozorth, R. 1951: *Ferromagnetism*. New York: Van Nostrand.

Gaujé, P. 1990: Measure de densité par absorption de rayonnements ionisants. Application à la caractérisation des aciers. *La Revue de Métallurgie CIT*, 1145–50.

Ishibashi, N., Morita, M., Sakata, K., Hashiguchi, K. and **Okano, S.** 1987. Method for measuring strip temperature with magnetic sensor. *Transactions of the Iron and Steel Institute of Japan* 27, B-54.

Han-Soo Kim, Il-han Park, Sang-Bong Wee, Song-Yop Hahn and **Min-Koo Han.** 1990: Eddy current methods for evaluating the transformed fraction of metals by voltage source. *IEEE Transactions on Magnetics* 26, 505–8.

Kitagawa, H. and **Sohmura, T.** 1983: An X-ray diffraction method for quantitative determination of retained austenite in the production line of metastable austenitic stainless steel. *Transactions of the Iron and Steel Institute of Japan* 23, 543–49.

Macovschi M. and **Poupot C.** 1990: Study of variable inductance transducers as proximity sensors: I. Computer aided design. II. Experimental study using C-type magnetic circuits. *Measurement Science and Technology* 1, 1031–40, 1291–96.

Morita, M., Hashiguchi, K., Hashimoto, O., Nishida, H. and **Okana, S.** 1987: Development of on-line transformation detector for property control of hot rolled steel. Proceedings of the Materials Society AIME Symposium on Accelerated Cooling of Steel, Pittsburgh.

Yahiro, K., Yamasaki, J., Furukawa, M., Arai, K., Morita, M. and **Obashi, M.** 1990: Development of coiling temperature control system on hot strip mill. *Kawasaki Steel Giho* 22, 12–18.

Memo

To	Gerard Gleijm, Jaap Rengersen
From	Edwin Snoeks
Reference	CO 0009 EP/Sn/01136/A
Date	13 November 2001
cc	Tim Leek, Gédo Kuiper, Roger Hammond, Brian Smith, Peter Drake, Sherri Johnstone (by letter)

Corus Intellectual Property Department
PO Box 10000
1970 CA IJmuiden
The Netherlands

T +31 (0) 251 491605 (direct)
F +31 (0) 251 470252
edwin.snoeks@corusgroup.com

Re: Filing of a patent application in Europe in the name of Corus Technology BV

On 2 November 2001, a patent application was filed with the European Patent Office entitled "Device and method for detecting magnetic properties of a metal object, use of the same in producing a hot rolled metal strip, and hot rolling mill comprising such a device" to which application the filing number 01204185.1 has been allotted.

The patent application has been filed in the name of Corus Technology BV.

Kind regards,

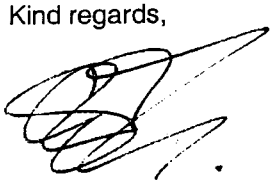

Edwin Snoeks

Enclosure: text as filed

DEVICE AND METHOD FOR DETECTING MAGNETIC PROPERTIES OF A METAL OBJECT, USE OF THE SAME IN PRODUCING A HOT ROLLED METAL STRIP, AND HOT ROLLING MILL COMPRISING SUCH A DEVICE

The invention relates to a device for detecting magnetic properties of a metal object, in particular for detecting phase transformation of a hot rolled metal strip, comprising generating means for generating a magnetic field intersecting a measurement plane in which measurement plane the metal object under investigation is to be located, and detecting means for detecting a portion of the magnetic field and producing a detection signal in relation to the portion of the magnetic field, and means for processing the detection signal.

In the context of this patent application, metal object is to be understood to comprise metal strip and metal bar. Metal strip is to be understood to comprise metal plate or metal sheet. The typical thickness range of steel strip is understood to be 0.8 to 25 mm.

When hot steel strip leaves a finishing hot rolling stand in a hot rolling mill, the steel strip may be in the hot austenite phase. As it cools, the phase transforms to ferrite based phases such as pearlite, bainite, or martensite phases, depending on the cooling rate and composition of the steel. Austenite is paramagnetic at all temperatures, while ferrite is paramagnetic above the Curie temperature and ferromagnetic below the Curie temperature. Therefore, as the austenite phase transforms to ferrite below the Curie temperature, the fraction of austenite and ferrite present in the steel strip can be detected by measuring the magnetic permeability of the steel. Thus, the magnetic properties of the steel strip can be related to the fraction of phase transformation. More details are disclosed in, for example, European patent application published under number EP 0 177 626 A1.

A device for detecting magnetic properties of a metal strip is known from EP 0 177 626 A1. The known device comprises an exciting coil for generating an alternating magnetic field by feeding alternating current through the coil. The exciting coil is arranged on one side of a steel strip when the strip is in a measuring position. Two detecting coils are arranged in the vicinity of the steel strip, at positions different in distance from the exciting coil. The detecting coils are each induced with the alternating magnetic field of the exciting coil, resulting in individual detection signals. When the

steel strip is in its measuring position, part of the alternating magnetic field that induces the detecting coils has passed through the steel strip. The induced signals are analysed and processed using an arithmetic unit.

In practice, the known device is said to be used for on-line detection of a transformation value. When used in an industrial hot mill, it is highly desirable to protect the device from external influences such as dust, magnetisable dust, and water vapour.

It is a drawback of the known device, that only electrically insulating materials, such as ceramic materials, can be used to shield the device from the metal object to be investigated. Most of these materials are unsuitable for usage in an industrial hot mill, because they are fragile and often they are not sufficiently impermeable for water vapour.

It is an object of the invention to provide a device for detecting magnetic properties of a metal object, which can be shielded from the exterior using a metallic shield.

It is yet another object of the invention to provide a device of the above-mentioned type, that is suitable for use in a heavy industrial environment, in particular in conjunction with a hot rolling mill.

It is yet another object of the invention to provide a device of the above-mentioned type, is advantageous for use for on-line detection of magnetic properties of a metal strip being produced in a hot mill.

According to the invention, one or more of these objects are achieved with a device for detecting magnetic properties of a metal object, generating means for generating a magnetic field intersecting a measurement plane in which measurement plane the metal object under investigation is to be located, and detecting means for detecting a portion of the magnetic field and producing a detection signal in relation to the portion of the magnetic field, and means for processing the detection signal, whereby the generating means are continuous magnetic field generating means, and the detecting means are means suitable for detecting at least a continuous component of the magnetic field.

Because of the continuous nature of the magnetic field, no eddy currents result in conducting materials on which the magnetic field is incident. The device according to

the invention can therefore be shielded using a metal shield, in particular using a non-magnetisable metallic shield. Examples of metals that can now be used for shielding are stainless steel and aluminium.

The metal shield may even be placed between the device and the metal object under investigation, i.e. between the generating means and the measurement plane, because the continuous magnetic field may penetrate though the entire thickness of the shield. Therefore, the metal shield can be of advantage also as supporting means for supporting the metal object during investigation, including holding the metal object in the measurement plane.

An additional advantage of the invention is that the continuous magnetic field penetrates through the entire thickness of hot rolled products. Even for thick metal objects under investigation, the detection signal is therefore conveniently independent of skin depth, which renders the detection signals less complicated to analyse and obtain meaningful information.

The detecting means should be capable of detecting the continuous magnetic field.

Continuous magnetic field is to be understood in any case to include a magnetic field having a DC-component such as a DC magnetic field or a DC-biased magnetic field that may additionally contain AC-components. Continuous magnetic field may be understood to also include a slowly varying magnetic field, as long as the frequency is low enough to not cause a significant contribution to the detection signal from the metal shield. A maximum allowable frequency may be frequency 15 Hz for metal objects up to several mm thickness gauge. Preferably, the frequency is less than 5 Hz, more preferably it is less than 1 Hz.

It is remarked, that in EP 0 177 626 A1 it is said to be generally known that the skin depth of the magnetic field into the metal object depends upon the frequency of the magnetic field. Nonetheless, this prior art teaches that the frequency of the magnetic field should preferably not be less than 30 Hz.

Several devices or methods can be suitable for detecting the continuous magnetic field. In one preferred embodiment, the detecting means comprises a Hall sensor. Hall sensors are commercially available against negligible cost. Delicate sensors such as Hall sensors are not known to be used in a heavy industrial environment such as

an industrial hot rolling mill. Hall sensors can typically withstand a temperature of approximately 150 °C. Thus, the demand for cooling power is not so critical, which makes them suitable for use in a run out table of a hot rolling mill.

The continuous magnetic field generating means can be formed by a permanent magnet. However, it is preferred that continuous magnetic field generating means are switchable. This has the advantage that the magnetic field can be switched off. Magnetic particles that might be attracted to the magnet will then fall off, so that the need for manual cleaning is reduced with respect to a permanent magnet.

A switchable permanent magnet can be used, but a transmitter coil connected to a DC power source, or optionally a DC-biased power source, is found to be more convenient as switchable continuous magnetic field generating means.

The detection of a portion of the magnetic field by the detection means depends not only on properties of the metal object that is investigated, but also on the distance between the metal object and the device, which is referred to as the lift off distance. In a hot rolling mill, the lift off distance may even fluctuate, due to bends and waves in the metal strip being hot rolled. To take into account the effect of the lift off distance, it is possible to provide additional means for monitoring the lift off distance. Such means can be for instance a commercially available eddy current sensor, or preferably ultrasonic distance measuring means because the lift off determination using the eddy current sensor is complicated by the dependence of eddy currents on the magnetic properties of the metal strip.

However, it is preferred that the detecting means comprise two units, each placed at a position different in distance from the continuous magnetic field generating means. Having at least two such units, a simultaneous measurement of both the magnetic properties and the lift off distance is possible, since two independent detection signals are provided from which the means for processing the signal can extract two unknown entities, i.e. the magnetic property of the metal object and the lift off distance. Therefore, a separate unit for monitoring the lift off distance is not needed.

In an embodiment of the invention, the means for processing the detection signal comprises input means for receiving a thickness signal that contains independent thickness information of the metal object and means for using the thickness signal in processing the detection signal. Herewith it is achieved that the thickness gauge of the

metal object under investigation can be taken into account. Since the magnetic field probes the entire thickness of the metal object under investigation, the detection signals will be dependent not on the penetration depth but rather on the thickness gauge of the object.

Such input means can, for instance, be connected to a device on which the thickness gauge is entered manually and transformed into a thickness signal that is related to the thickness gauge. However, it is preferred to have provided a measurement device for generating the thickness signal. Herewith it is achieved that thickness variations in the metal object can be accounted for. Such measurement device may be a known X-ray thickness gauge measurement device.

In a second aspect, the invention relates to a method of detecting magnetic properties of a metal object, in particular of detecting phase transformation of a hot rolled metal strip, wherein a magnetic field is generated and the metal object to be investigated is positioned such that the magnetic field is incident on the metal object, and wherein a portion of the magnetic field is detected and a detection signal is produced in relation to the portion of the magnetic field that is detected, and wherein the detection signal is processed.

According to this aspect of the invention, the magnetic field is generated as a continuous field, and the portion of the magnetic field is detected using suitable means.

This method may be carried out using the device in accordance with the description above. The advantages are achieved as explained above, in particular the advantage that a conducting shield may be present in the magnetic field to protect the device, and the further the advantage of obtaining a measurement that is independent of skin depth.

In another aspect, the invention relates to a process of producing hot-rolled steel strip with a certain desired fraction of ferrite and austenite phases, wherein a slab is hot rolled at a temperature where the austenite phase forms, to produce an intermediate steel strip, and wherein the intermediate steel strip is subsequently cooled to a temperature below the Curie temperature and whereby the austenite phase transforms into the ferrite phase, during which cooling the amount of transformation is monitored.

According to this aspect of the invention, the process is characterised by monitoring the amount of transformation using the device or method according to an embodiment of the first aspects of the invention.

The information that is obtained by this process, by processing the detection signal, can be utilised for improved process control. This is advantageous since the transformation state is of influence on the strength of the hot rolled product. Also, a higher homogeneity and reproducibility of the mechanical properties of the hot rolled product is achieved.

The result of the monitoring can be used as a basis for feedback information to regulate the cooling power. Herewith, more control is achieved over the quality of the obtained hot rolled product.

In yet another aspect, the invention relates to a hot rolling mill for hot rolling of metal strip, comprising at least a finishing hot rolling stand and a trajectory for passing the metal strip through the hot rolling mill.

According to this aspect of the invention, the hot rolling mill is characterised in that the device according to any embodiment of the first aspect of the invention is provided in the vicinity of the trajectory, for on-line detecting the magnetic properties of the metal strip.

In an embodiment, the means for processing the detection signal is provided with output means to produce a feedback signal, which output means is connected to regulation means for regulating the hot rolling mill.

The invention will now be illustrated with reference to the drawing wherein

FIG. 1 is a schematic view of an embodiment of the device according to the invention;

FIG. 2 is a schematic view of another embodiment of the device according to the invention;

FIG. 3 is a schematic view of yet another embodiment of the device according to the invention;

FIG. 4 is a diagram showing the effect of the lift off distance on the detection signals;

FIG. 5 is a schematic view of a hot rolling mill provided with the device according to the invention; and

FIG. 6 is a diagram showing a signal from the device according to FIG. 1 as a function of time during cooling down of a steel strip.

FIG. 1 shows a device for detecting magnetic properties of a metal object 1. This embodiment is based on a permanent magnet 2. At least one of the poles is provided with a Hall sensor 3. Both poles are equally well suited. In fact the Hall sensor does not even have to be located on a pole, as long as it is picking up magnetic flux. Means (not shown) is provided for processing the signal that is produced by the Hall sensor 3. During operation, the magnetic poles of magnet 2 are aimed at the metal object 1 under investigation.

The resulting magnetic field lines 4 at least in part pass through the metal object 1. The magnetic field that passes through the Hall sensor 3 thus depends on the magnetic permeability of the metal object 1. The Hall sensor 3 responds to the incident magnetic field with a detection signal, which is a voltage signal that is proportional to the incident magnetic field.

The magnetic permeability of a paramagnetic metal is 1, and that of a ferromagnetic metal is higher than one. Thus, the higher the fraction of the metal that is in a ferromagnetic state, the higher the permeability of the metal object as a whole. This affects the magnetic field that is incident on the Hall sensor 3, and consequently, the produced detection signal. The magnetic field on the Hall sensor is higher if the fraction of ferromagnetic material in the metal object is higher.

The magnetic field that is incident on the Hall sensor, is also dependent on the distance D between the magnetic poles and the metal object (often referred to as the lift off distance), as well as on the thickness of the metal object. Additional devices may be used to measure D and/or the metal object thickness gauge in concurrence. The means for processing the detection signal can be provided with input means for receiving a lift off signal and/or a thickness signal, and means for using one or both of these signals in processing the detection signal.

FIG. 2 shows an embodiment similar to that of FIG. 1, whereby the permanent magnet is replaced by a magnetisable core 7 having coil 5 wound around it. The coil is connected to a DC power supply 6, which typically delivers an electric current. The U-shape of the core contributes to the detection efficiency of the Hall sensor 3, which is placed on a leg of the U-shaped core. The core can consist, of for instance, iron or transformer steel.

Optionally, the coil may be connected to a DC-biased current. In this case, the detection signal could for example be filtered to separate the DC-component from unwanted AC-contributions in the signal.

FIG. 3 shows yet another embodiment. It has a forked core 8, with a generating leg 8a two receiving legs 8b and 8c. One of the receiving legs (8c) is located at a longer distance from the generating leg 8a than the other receiving leg (8b). The coil 5 is wound on the generating leg 8a or in a section between the generating leg and the nearest receiving leg 8b. The coil is connected to a DC power supply 6. Both receiver legs are provided with detection means (3,3'), each providing mutually independent detection signals.

With the embodiment of FIG. 3, both the magnetic properties of the metal object, and the lift off distance can be determined using the two independent detection signals from detection means 3 and 3'. Details of the procedure are given in EP 0 177 626 A1. An example is given in FIG. 4, where the continuous line represents the Hall sensor signal S_b of the first receiving leg 8b (which is the closest to the generating leg 8a) is plotted as a function of lift off distance. The dashed line gives the ratio between the detection signals of the first receiving leg and the second receiving leg. As can be seen, this ratio varies with lift off distance.

It should be noted that the sum of the magnetic field lines passing legs 8b and 8c should theoretically add up to the field lines passing through leg 8a. Therefore, the embodiment as shown in FIG. 3, can be used equally well when one of the detection means 3 or 3' is located on the generating leg 8a instead of a receiving leg. The flux on the pole having no detection means can then be determined by subtraction of the two detection signals.

Also shown in FIG. 3 is a metallic protective shield 14, which is located in the magnetic field 4 between the poles of the magnet 8 and the metal object 1 that is under investigation. The shield may be part of an encasement of the device.

FIG. 5 shows a schematic view of a steel hot rolling mill. It comprises hot rolling stands 9 to hot roll a metal slab into a metal strip 1. Following a finishing hot rolling stand, there is provided a run out table 10, which can be provided with an accelerated cooling section having water cooling units 11 for accelerated cooling. The run out table comprises rollers 15 for supporting the strip 1. A coiler 12 can be provided for coiling

the cooled metal strip or sheet 1. The device 13 for detecting magnetic properties of the metal strip is arranged in the vicinity of the trajectory of the metal strip 1. The device 13 can be arranged after the last water-cooling unit, or within the accelerated cooling section, or both.

As the hot steel strip leaves the finishing hot rolling stand in the hot rolling mill, the steel strip may be in the hot austenite phase. As it cools, the phase transforms to ferrite based phases such as pearlite, bainite, or martensite phases, depending on the cooling rate. Austenite is paramagnetic at all temperatures, while ferrite is paramagnetic above the Curie temperature and ferromagnetic below the Curie temperature. Therefore, as the austenite phase transforms to ferrite below the Curie temperature, the fraction of austenite and ferrite present in the steel strip can be detected by the device according to the invention.

If the rollers 15 are spaced relatively far apart from each other, the metal strip can vibrate significantly and thus result in varying lift off distance. With the invention, it is possible to provide a metallic support between the device 13 and the metal strip 1.

To demonstrate the device, a steel strip of 1.9 mm thickness gauge and alloyed with 1.35 wt.% Mn and 0.14 wt.% C, was heated up to 900°C, and subsequently cooled by natural air cooling. The Curie point of this steel is thought to be at about 768°C. FIG. 6 shows, as a function of time, the average temperature of the strip (dashed line) and the Hall sensor signal (continuous line), which was measured using the embodiment having a permanent magnet as shown in FIG. 1.

As can be seen in FIG. 6, the temperature over all decreases with time, and also the Hall sensor signal changes gradually with time. The Hall signal changes in a smooth S-curve. Around $t = 25$ s, the effect of heat release due to the transformation from austenite to ferrite can be seen on the temperature. The temperature may even temporarily increase due to said heat release. This coincides with the highest rate of change in the Hall sensor signal. This shows that temperature is not unambiguously related to the transformation fraction of the metal strip.

The transformation fraction is, at least in good approximation, linear with the Hall sensor signal, because the skin depth of the continuous magnetic field is constant and much larger than the thickness gauge of the steel strip. For reference, it is remarked that would a magnetic field be used that was generated in a coil excited with a 50 Hz

current, the skin depth would have changed from 10 mm to 3 mm during the transformation. Even with a 1.9 mm thickness gauge, that would have resulted in a significant deviation from the linear relation between the detection signal and the transformation fraction. The device according to the invention can thus be advantageously used to monitor the transformation fraction of the steel strip.

The invention has been set out mainly in conjunction with use of the device in a hot rolling mill. While this indicates particular suitability of the instrument for use in such an environment, it will be appreciated by the person skilled in the art, that the device can also be used advantageously in other environments.

CLAIMS

1. Device for detecting magnetic properties of a metal object, comprising generating means for generating a magnetic field intersecting a measurement plane in which measurement plane the metal object under investigation is to be located, and detecting means for detecting a portion of the magnetic field and producing a detection signal in relation to the portion of the magnetic field, and means for processing the detection signal, characterised in that, the generating means are continuous magnetic field generating means, and the detecting means are means suitable for detecting at least a continuous component of the magnetic field.

2. Device according to claim 1, characterised in that the detecting means comprises a Hall sensor.

3. Device according to claim 1 or 2, characterised in that the continuous magnetic field generating means comprises a transmitter coil connected to a DC power source.

4. Device according to any one of the preceding claims, characterised in that the detecting means comprise two units, each placed at a position different in distance from the continuous magnetic field generating means.

5. Device according to any one of the preceding claims, characterised in that the means for processing the detection signal comprises input means for receiving a thickness signal that contains independent thickness information of the metal object and means for using the thickness signal in processing the detection signal.

6. Method of detecting magnetic properties of a metal object, wherein a magnetic field is generated and the metal object to be investigated is positioned such that the magnetic field is incident on the metal object, and wherein a portion of the magnetic field is detected and a detection signal is produced in relation to the portion of the magnetic field that is detected, and wherein the detection signal is

processed, characterised in that the magnetic field is generated as a continuous field, and the portion of the magnetic field is detected using means suitable for detecting at least a continuous component of the magnetic field.

7. Process of producing hot-rolled steel strip with a predetermined fraction of ferrite and austenite phases, wherein a slab is hot rolled at a temperature where the austenite phase forms, to produce an intermediate steel strip, and wherein the intermediate steel strip is subsequently cooled to a temperature whereby the austenite phase transforms into the ferrite phase, during which cooling the amount of transformation is monitored, characterised in that the monitoring of the amount of transformation is performed using the device according to any one of claims 1 to 5, or using the method according to claim 6.

8. Hot rolling mill for hot rolling of metal strip, comprising at least a finishing hot rolling stand and a trajectory for passing the metal strip through the hot rolling mill, characterised in that the device according to any one of the claims 1 to 5 is provided in the vicinity of the trajectory, for on-line detecting the magnetic properties of the metal strip.

ABSTRACT

Device for detecting magnetic properties of a metal object, comprising generating means for generating a magnetic field intersecting a measurement plane in which measurement plane the metal object under investigation is to be located, and detecting means for detecting a portion of the magnetic field and producing a detection signal in relation to the portion of the magnetic field, and means for processing the detection signal, characterised in that, the generating means are continuous magnetic field generating means, and the detecting means are means suitable for detecting at least a continuous component of the magnetic field.

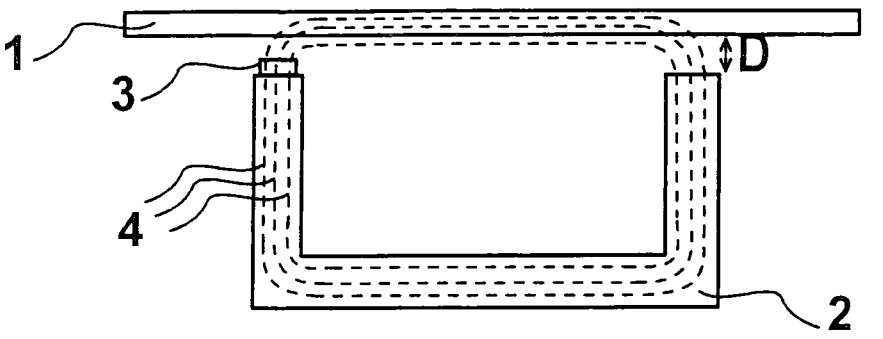

Fig. 1

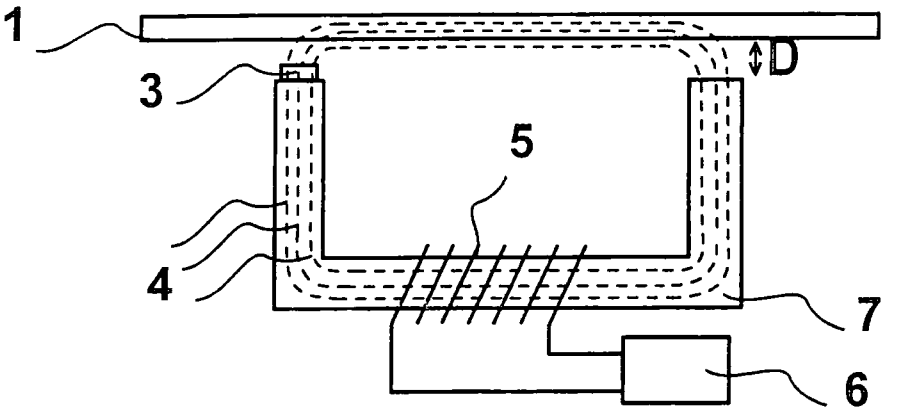

Fig. 2

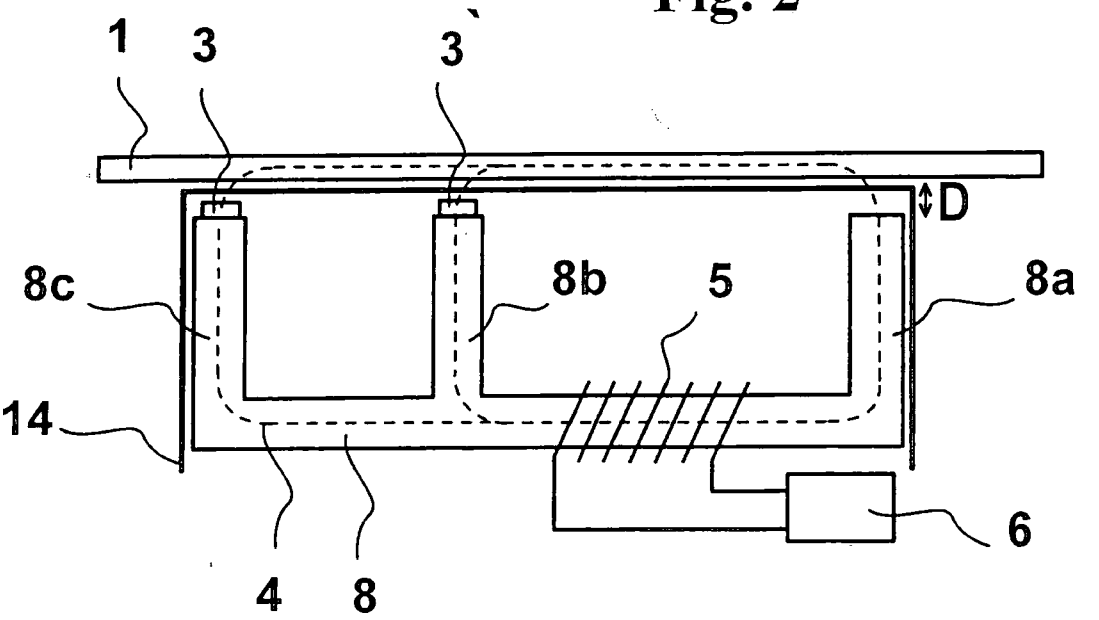

Fig. 3

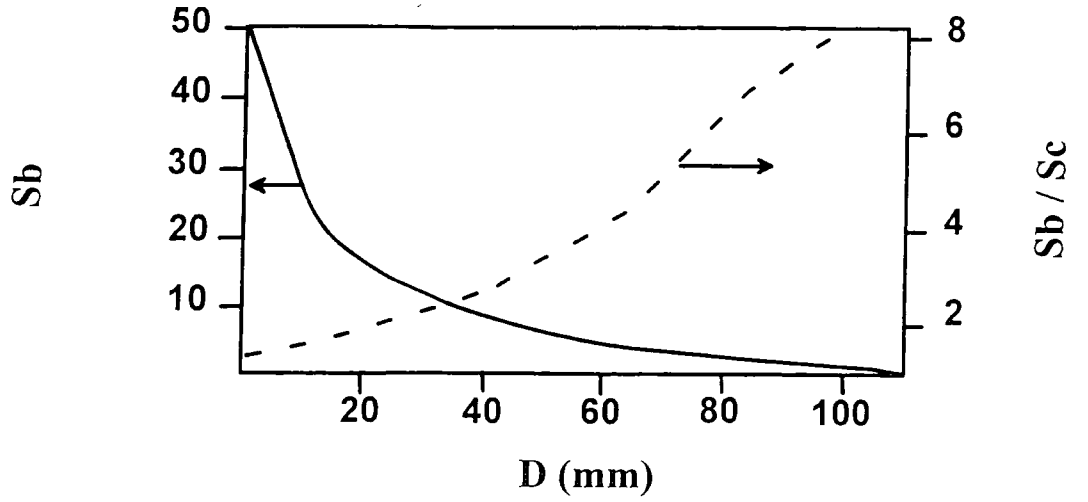

Fig. 4

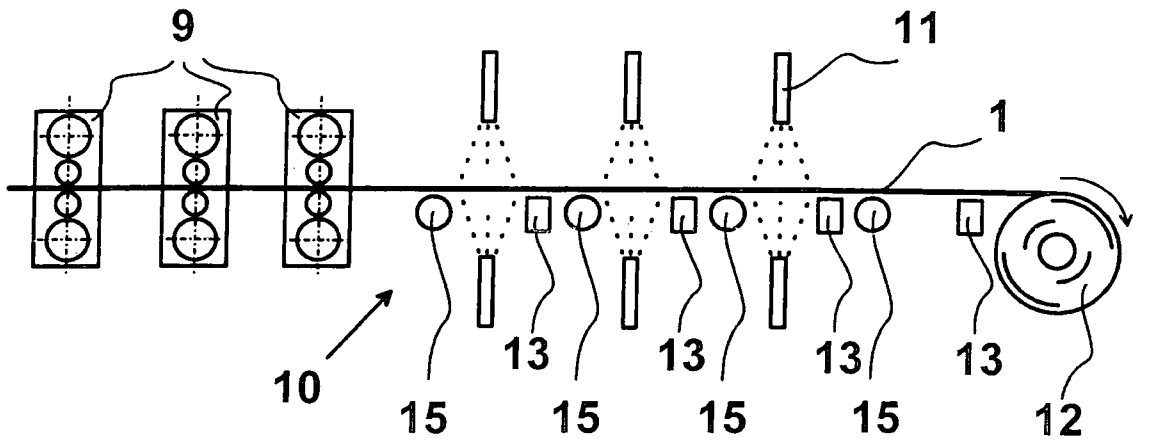

Fig. 5

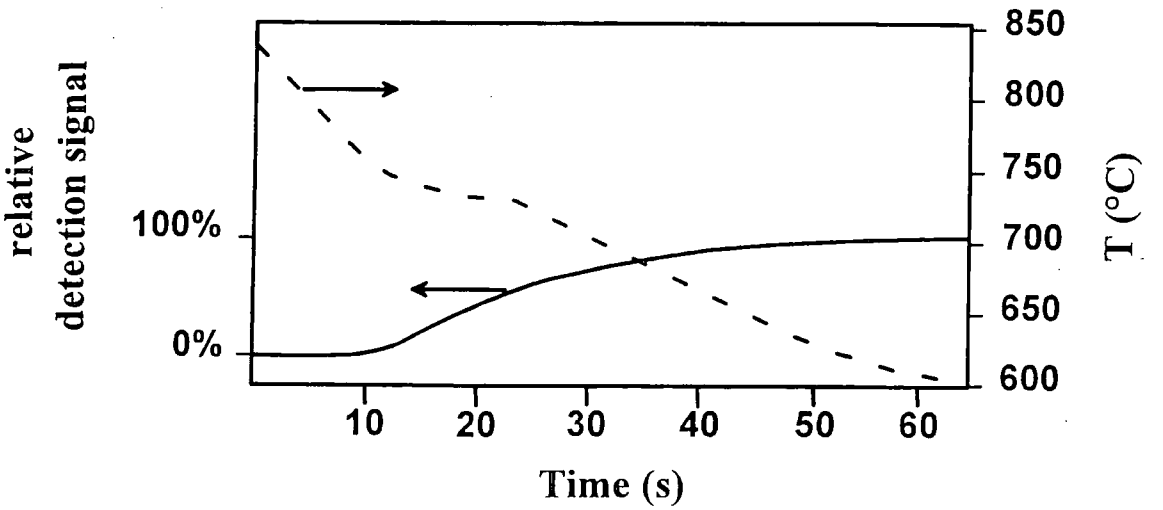

Fig. 6